FABRICATION OF MICROFLUIDIC DEVICES FOR YEAST CULTURING

by

Sevde Üçpınar

B.S., Chemical Engineering, Yildiz Technical University, 2014

Submitted to the Institute for Graduate Studies in
Science and Engineering in partial fulfillment of
the requirements for the degree of
Master of Science

Graduate Program in Chemical Engineering

Boğaziçi University

2016

to my beloved family…

ACKNOWLEDGEMENTS

I would like to thank all people who support me all the time during my thesis study. I would first like to thank to my thesis advisor Prof. Kutlu ÜLGEN who has supported me throughout my thesis work with her patience and knowledge. I attribute the level of Masters degree to her encouragement and effort and she consistently allowed this thesis to be my own work, but steered me in the right direction. I want to express my thanks to my thesis co-advisor Assoc. Prof. Şenol Mutlu. The door of his office was always open whenever I had a question about my research.

Also, I would like to thank to the rest of my thesis committee: Assoc. Prof. Elif Özkırımlı Ölmez, Assist. Prof. Melikhan Tanyeri and Assoc. Prof. Kerem Uğuz for their insightful comments about my thesis.

I must express my very profound gratitude to my family members, my mother Ayşe Üçpınar, my father Süleyman Üçpınar and my brother Burak Üçpınar for providing me with unfailing support and continuous encouragement throughout my years of study in my life. I would like to thank to Fatih Puza for being always with me in my hardest times and promoting me with eternal support. This accomplishment would not have been possible without them.

During the period of these two years, there have been some exclusive friends whom I would like to express my deep gratitude. Firstly, I have to acknowledge Elif Gençtürk and İrem Ezgi Dayan in our laboratory KB440 for their endless friendship, for the stimulating discussions and especially for the sleepless nights we were working together during the experiments where we had lots of fun.

I am grateful to Simge Acılıoğlu for her lasting friendship, for being my supporter and being with me during my undergraduate and master studies. I would also like to thank to my friends Hatice Eyvaz and Çağla Uzunuoğlu for their friendship and kindness.

I would like to thank to Emre İşeri, from the department of Electrical and Electronics Engineering, for his assistance during the studies I had done in the clean room.

Lastly, I thankfully acknowledge that this thesis has been financially supported by Boğaziçi Research Fund through project 9701R and The Scientific and Technological Research Council of Turkey (TUBITAK) through 2210C Priority Areas Scholarship Program for Graduate Study.

ABSTRACT

FABRICATION OF MICROFLUIDIC DEVICES FOR YEAST CULTURING

Microfluidic technology has appreciated extensive success in recent years. Microfluidics is a well understood physic domain and can be used to develop tools for a wide range of platforms comprising engineering, biological applications and biotechnology. Some of the driving advantages for increased usage of microfluidics are small volumes of reagents and consumables, parallel processing, reduced processing time and high-throughput. Therefore, well-controlled microfluidic devices were designed for cell growth experiments. *Saccharomyces cerevisiae* has been an important model for studying cell biology in higher eukaryotic systems. Within the scope of this thesis, the fabrication of microfluidic devices for yeast culturing was achieved successfully. The microbioreactor was designed by L-Edit software to serve the purpose of cell trapping. Fabrication was done by hot embossing and thermo-compression bonding techniques. The microfluidic devices were fabricated from PMMA, COP and PEN polymers by optimizing the fabrication parameters for each of them separately. COMSOL Multiphysics3.5a program was used to simulate velocity, concentration and pressure distribution within the device. The main aim was to visualize the growth kinetics and expression of the GFP tagged Sld7p (YOR060C) of *S.cerevisiae* under environmental stress by changing nutrient media and the glucose concentration. The cell growth experiments were performed using either YNB (2% and 0.2% glucose contained) or YPD (2% glucose contained) media. During the experiments, brightfield and fluorescence microscope images were captured by Nikon Eclipse-T inverted microscope at regular time intervals and then processed via ImageJ-Fiji software. The results of cell count, area, perimeter and integrated density values were analyzed and used further to calculate the specific growth rates of yeast cells. The duration of budding and G1 phases in cell cycle were determined precisely. Using the in house fabricated Lab-on-a-Chip platform, cell culturing in the microbioreactor was achieved.

ÖZET

MAYA KÜLTÜRLENMESİ İÇİN MİKROAKIŞKAN CİHAZLARIN ÜRETİMİ

Mikroakışkan teknolojisi son yıllarda geniş çaplı başarısı ile takdir görmüş bir teknolojidir. Fizik alanında iyi anlaşılmış mikroakışkanlar, içerisinde mühendislik, biyolojik uygulamalar ve biyoteknolojiyi de içeren birçok alanda gelişim sağlamak için kullanılabilmektedir. Mikroakışkanların kullanımının yaygınlaşmasında etkili olan avantajlardan bazıları; az miktarda reaktif ve sarf malzeme gereksinimi, eş zamanlı işlem yapabilme, azalan işlem zamanı ve yüksek çıktıdır. Bu yüzden hücre kültürlenmesi deneyleri için iyi kontrol edilen mikroakışkan cihazlar tasarlanmıştır. *S. cerevisiae* gelişmiş ökaryotik sistemlerde hücre biyolojisi çalışmaları için önemli bir modeldir. Bu tez kapsamında maya kültürlenmesi için mikroakışkan cihaz başarı ile üretilmiştir. Cihaz tasarımı L-Edit programı ile, maya hücrelerini yakalama amacına yönelik olarak yapılmıştır. Mikroakışkan cihazlar PMMA, COP ve PEN polimerlerinden, fabrikasyon parametreleri ayrı ayrı optimize edilerek üretilmiştir. COMSOL Multiphysics programı kullanılarak cihaz içerisindeki hız, konsantrasyon ve basınç dağılımı simülasyonu yapılmıştır. Asıl amaç *S.cerevisiae* mayasının besiyeri ve glikoz konsantrasyonu değiştirilerek çevresel strese maruz bırakılmasıyla oluşan büyüme kinetiği ve yeşil flüoresan ile işaretlenmiş Sld7p (YOR060C) proteinini üretme kapasitesinin incelenmesidir. Hücre kültürlenmesi deneyleri YNB (2% ve 0.2% glikoz içeren) ve YPD (2% glikoz içeren) besiyeri kullanılarak gerçekleştirilmiştir. Deney boyunca ışık ve floresan görüntüleri Nikon Eclipse-T ters mikroskobu ile düzenli aralıklar ile çekilmiş ve sonrasında Image-J-Fiji programı ile işlenmiştir. Hücre sayısı, alanı, çevresi ve floresan ışıması yoğunluğu sonuçları analiz edilmiş, veriler maya hücrelerinin spesifik büyüme hızlarının hesaplanmasında kullanılmıştır. Hücre döngüsünde bölünme ve G1 evreleri için geçen süreler belirlenmiştir. Kurum içinde fabrikasyonu yapılan Çip-üzerinde-Laboratuvar platformu kullanılarak mikrobiyoreaktör içinde maya kültürlenmesi gerçekleştirilmiştir.

TABLE OF CONTENTS

LIST OF FIGURES

LIST OF TABLES

LIST OF SYMBOLS

c	Concentration
D	Diffusion coefficient
F	External forces
h	Height
L	Length
P	Pressure
Rh	Hydraulic resistance value
u	Velocity
w	Width
x_i	Weight fraction
x_v	Concentration of viable cells in medium
X	Cell count
y	Statistical movement of a molecule
P	Product concentration
ρ	Density
η	Dynamic viscosity
μ	Specific growth rate
μ_{max}	Maximum specific growth rate
ρ_{mix}	Mixture density
γ	Thermodynamic activity coefficient
τ	Shear stress
Ω	Resistivity

LIST OF ACRONYMS/ABBREVIATIONS

2D	Two dimensional
3D	Three dimensional
BSA	Bovine serum albumin
CFD	Computational fluid dynamics
CFP	Cyan fluorescent protein
CNC	Computer numerical control
COP	Cyclo olefin polymer
D1	First new design
D2	Second new design
DIC	Differential interference contrast
E1	Experiment done without yeast cells (2% glucose YPD)
E1Y	Experiment with yeast cells (2% glucose YPD)
E2	Experiment done without yeast cells (0.2% glucose YPD)
E3Y	Experiment done with yeast cells (2% glucose YPD)
E4Y	Experiment done with yeast cells (2% glucose YNB)
E5Y	Experiment done with yeast cells (0.2% glucose YNB)
FBC	Fraction of total budded cells
GFP	Green fluorescent protein
IPA	Isopropyl alcohol
MEMS	Microelectromechanical systems
MMS	Methyl methanesulfonate
OD	Optical density
PALM	Photoactivated localization microscopy
PDMS	Poly (dimethylsiloxane)
PEN	Poly (ethylene naphthalate)
PMMA	Poly (methyl methacrylate)
PP	Poly (propylene)
SC	Synthetic complete
SEM	Scanning electron microscope

SD	Synthetic defined
Tb	Time of budding
Td	Duplication time
Tg	Glass transition temperature
TμC	Tesla microchemostat
WT	Wild type
YES	Yeast extract-sucrose
YEPD	Yeast extract-peptone-dextrose
YFP	Yellow fluorescent protein
YNB	Yeast nitrogen-base
YPD	Yeast extract-peptone-dextrose
YPDA	Yeast extract-peptone-dextrose-agar
YPG	Yeast extract-peptone-glycerol

1. INTRODUCTION

In recent years, microfluidic devices have become popular because of its numerous advantages as research tools. Microfluidics is a multidisciplinary field intersecting with micrometer-sized channels. In these systems, at least one dimension of the channel should be at the order of micrometer. The microfluidic devices were first developed in 1980s by producing silicon based microfluidic devices, MEMS, and it gave rise to industrial microfluidic applications. The applications of MEMS in biology, chemistry and biomedical fields were investigated in 2000s and all the processes have been integrated on a single microfluidic chip, so 'Lab-on-a-chip' devices have been developed [1].

Microfluidic technologies offer the usage of small volumes for high-throughput reaction, separation and detection processes and decrease the cost of analysis by necessitating small amounts of samples and reagents. Microfluidics also exploits its characteristics such as large surface area to volume ratio providing good heat and mass transfer in the devices. Laminar flow characteristics of these devices has numerous advantages on flow control by pumps, valves, electrodes in micro channels. Due to the fast reactivity at microscale, the environment of a chemical reaction can be controlled in real time and this leads to more controlled results. Micro channels can be integrated so that tens or thousands of analyses can be done simultaneously.

The fabrication of microfluidic devices are cheaper than those of other conventional systems. Commonly, soft lithography and photolithography techniques are used to produce the microfluidic devices from polymers such as PDMS, PMMA or COP [2]. The polymer structures and properties such as optical transparency, mechanical strength, biocompatibility and ease of fabrication allow scientists to create microfluidic devices for their research studies.

Lab-on-a-chip devices are widely used for biological applications and many organisms can be studied by these devices including yeast, bacteria and micro-algae [3]. Microfluidic cell culturing has significant advantages over conventional culturing

methods. The design of the microfluidic device can be tailored to the needs of cell types or the aim of the study. The co-culture can be controlled by automatization and the real-time analysis can be done on-chip. The contamination risk is also reduced by reduced consumption of reagents. The conventional well-plate or batch systems used for cell experiments takes long time and do not enable to monitor the behavior of cells during budding or environmental stress. In a microfluidic system, a low number of cells is sufficient for analysis. An overview of both macroscopic and microfluidic cell culture is given in Figure 1.1.

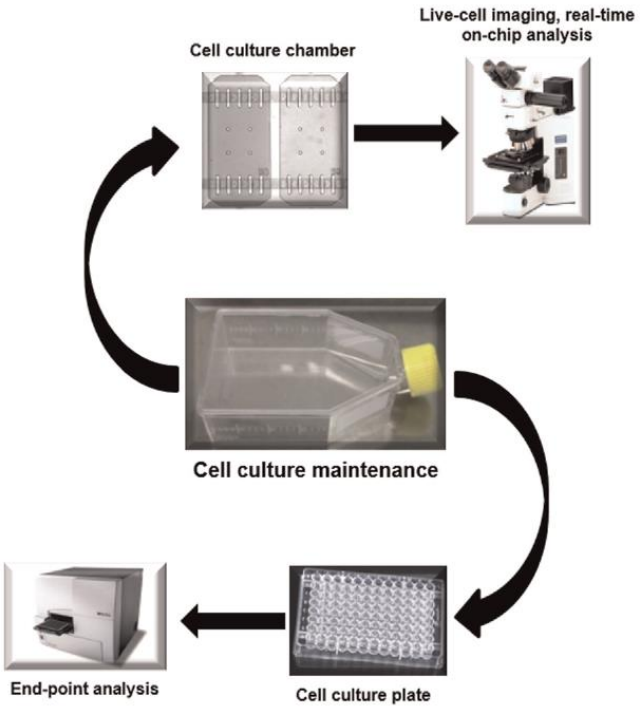

Figure 1.1. Overview of both macroscopic and microfluidic cell culture [4].

Yeasts are commonly used for biomolecular engineering applications, and they duplicate asexually by budding and the time of duplication is around 90-120 minutes. Studying yeast cells in a microfluidic device (microchemostat) provides convenient conditions to visualize the reactions within the cells, in their natural environment unlike conventional bioreactors [4].

For the applications of yeast cells, cell trapping has an important role on visualizing single cell or a colony during their lifespan for relevant studies. Trapping methods are classified as contact based (active) and noncontact based (passive) trapping. The contact based methods are further classified as hydrodynamic and chemical-gel matrices, and noncontact based methods include immobilization of cells by optical, electrical, acoustic and magnetic fields [5]. The cell trapping in microfluidic devices becomes state-of-the-art to visualize microbial cells at a single-cell level or as a colony during their lifespan for aging, genetic interaction, cell growth, replicative lifespan, gene expression, environmental response, metabolic and physiologic activities [6].

In this thesis, a microfluidic device was designed and fabricated for yeast culturing applications. The design was modelled by L-Edit software, the device was to serve as a passive cell-trapping device and simulated by COMSOL Multiphysics3.5a program. The master mold for the fabrication was produced via photolithography and electrochemical wet etching techniques. The fabrication of the microfluidic device was performed via different polymers as PMMA, COP and PEN by hot embossing and thermal bonding techniques. Yeast cells were trapped in the 0.13 nL c-shaped trapping regions and culturing experiments were performed successfully in the COP made microfluidic device. Brightfield and fluorescence microscope images were processed by ImageJ-Fiji software. The main aim is to follow the growth kinetics of the cells and expression of the GFP tagged Sld7p (YOR060C) of *S.cerevisiae* under environmental stress by changing the glucose concentration.

To provide an insight about fabrication of microfluidic devices and their applications on yeast cells, the second chapter is designated as “Theoretical Background”. In the “Materials and Methods” section, the fabrication steps, yeast culturing procedure and image processing steps are explained in detail. In the fourth chapter, computational simulations, critical points about the fabrication process, experiments done by the microfluidic device and insights from the experiments are given. The optimized fabrication steps, growth and product formation kinetics of the cells are examined and the role of Sld7p in cell cycle is discussed. The last chapter consists of the conclusions gained from this study and recommendations for future work.

2. THEORETICAL BACKGROUND

2.1. Yeast Culturing Applications Using Microfluidic Devices

In recent years, microfluidic devices are preferable for cell experiments due to their low cost and high-throughput characteristics. Most of the experiments related to cell biology have been done with yeast cells as a model system for human biology. The studies with pioneering designs reported in literature in the last 10 years are summarized below and listed in Table 2.1.

Groisman *et al*. (2005) developed microfabricated elastomer chips to demonstrate the growth of bacterial and yeast colonies in shallow microscopic microchamber arrays [7]. The device consisted of 16 flow through symmetric channels and 340 chambers. This two layer PDMS device was fabricated by using soft lithography and sealed by a coverglass. Silicon wafer was used as master-mold then it was spin-coated with PDMS prepolymer at 80°C. The first layer was for cells and medium and the second layer was the water circulation layer. The walls of the chambers were designed as impassable for cells, but allowed diffusion of chemicals and capillaries and become permeable at high pressure. They used the advantage of height differences between channels and capillaries to grow the colonies in each chamber. Figure 2.1 shows the design and operation of microfluidic device. Depths of capillaries were increased by gauge pressure by using the advantage of high flexibility of PDMS. The flow in the chambers was at least 1000 times weaker than that of in channels (0.1 μm/s to 100 μm/s). The same pressure was applied to two inlets, and each of inlet was connected to vents, a short distance upstream of the T-junction. Hence, the medium in the array can be replaced by applied driving pressure quickly. Thermostatic water circulator was set to 37 °C and the temperature profile along a line through the center of the device was measured by an infrared camera.

Cell colony growths were determined for three different chamber widths and two different temperatures by using three different chips at each temperature. The increase of GFP (fluorescence) intensity by growth was measured to understand the cell proliferation

rates through the chambers. Fluorescence, bright-field and phase-contrast images were captured by epifluorescence microscope at 3 minute intervals then colonies were calculated by summing the intensity of all pixels in the chamber image and subtracting the background noise.

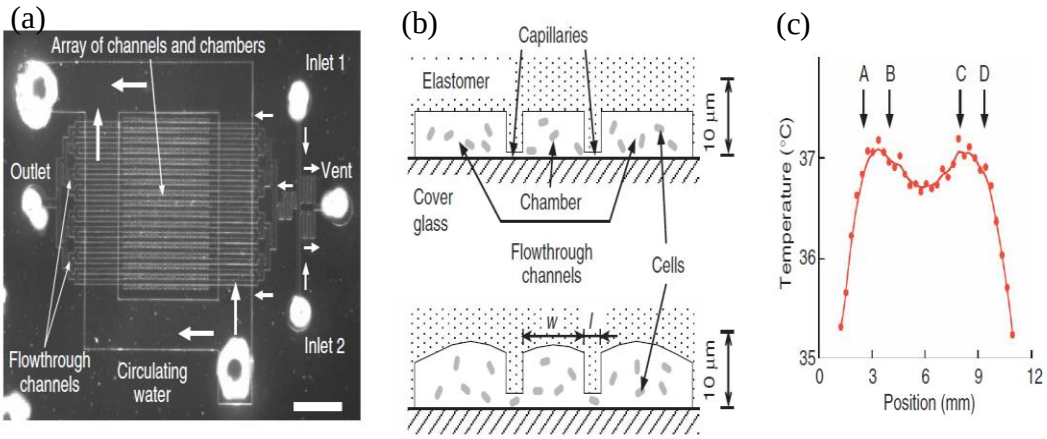

Figure 2.1. Chip design (a) micrograph of the PDMS device (b) schematic drawing of a cross-section of the array showing two channels at low gauge pressure (c) capillaries depth at high gauge pressure (d) temperature profile along a line [7].

Cookson *et al.* (2005) illustrated the operation of the Tesla microchemostat (TμC) with single yeast cells and run the analysis of fluorescence data over many generations [8]. The cells could be observed for long period of times and the division periods were also determined for both young and old cells. The classic Tesla diode loop was made of a single PDMS layer to visualize growth of cells in a monolayer in 4μm height chambers for long time periods. The chip was created with channels and microstructures from a silicon wafer template and treated with oxygen plasma. The chip had ports for cell loading, medium supply and waste. Thermal lines (T1 and T2) were used to maintain the device at an optimum temperature by running temperature-regulated water through lines. The strong flow created a momentum to carry the cells into the region against resistance. Once cells are loaded, flow was reversed to run both cell and waste ports to minimize the clogging (Figure 2.2). Cells received nutrients via diffusion and advection. The device was mounted to the microscope stage and optimal growth temperature was set to 30°C. Images were

captured with epi-fluorescent inverted microscope outfitted with a hardware-based autofocus controller and analyzed by using a written LabVIEW software program.

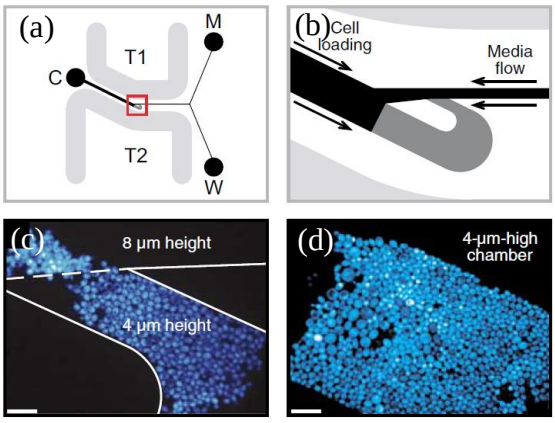

Figure 2.2. Chip design (a) ports for cell loading, medium and waste (b) a zoomed diode loop (c) trapping regions confine cells to a monolayer (d) TµC full of cells after 24 hour growth [8].

Another study on yeast application in microfluidic device was performed by Ryley *et al.* (2006) [9]. A microfluidics-based flow cell design was used to trap the yeast cells in yeast jails. The aim of this study is to improve the previous trapping methods, as micromanipulation on agar cannot be used to trap mother cells and remove the daughter cells by media flow at the same time. In this study, different jail designs were compared for tracking the mother cells (two different color tagged yeast strains). The most convenient jail design for eliminating mother cells from daughter cells and for observation of most jails per field of view was determined as three squared posts (Figure 2.3b). Yeast cells were also chosen in this study because of their well-known ageing model. The device was created by a software, and then a negative image in silicon wafer was used to create the mold for the PDMS. The design included five devices on one wafer, each device contained 9 arrays, 400 individual yeast jails. There were 3600 yeast jails for single cell trapping per device. The timing of the inlet flows were controlled by a pump at the same flow rate for forward and reverse phases of media flow. Single drops of medium containing the suspended yeast cells were placed into each jail, and after budding the mother cell was

kept in the jail and daughter cells were removed by media flow (Figure 2.3). The device was mounted on the microscope stage and the fluorescence and bright-field images were captured at 15 minute time intervals by inverted microscope equipped with camera. Image correlations, shading and background corrections were performed by a software program. Normalized fluorescence values were used to compare the yeasts and non-biological fluorescence microspheres. Heat shock responses of budding yeasts were also determined.

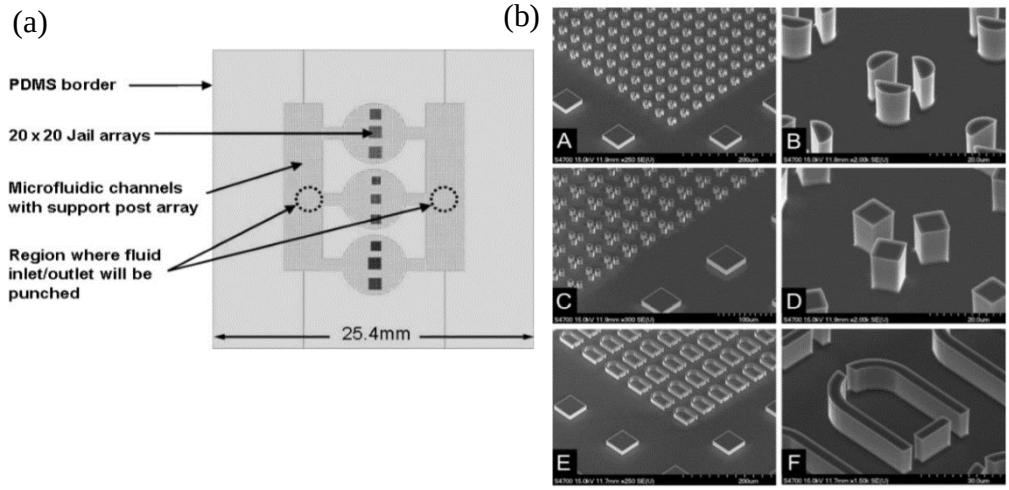

Figure 2.3. Chip design (a) schematic view of the device (b) negative silicon masters of PDMS devices showing various jail designs [9].

A microfluidic imaging platform, developed by Luo *et al.* (2009), was used for monitoring the diffusion based yeast monolayer cell culturing and determining the distribution of patterning ratio as functions of injection times and cell cavity areas [10]. The device was made of PDMS to use the advantage of gas absorption property for fast and simple cell patterning. PDMS devices were fabricated by soft lithography technique on the master mold, this one consisted of two layers as cell cavities and main channel. For the first layer 100 square cavities with the different side lengths of 100,125,150,175 and 200 μm; or side lengths of 150 μm and width of 40 μm, thickness of 4 μm were created. The PDMS layer for cell cavity was created with a thickness of 10 μm and height of 4 μm which is smaller than the size of the yeasts to limit the growth of the cells in a monolayer colony. Figure 2.4 shows the 2-layer fabrication and views of the microfluidic device. The

working principle of yeast cell patterning was based on the changes of cell cavities by the applied high velocity. Initially, yeast cell suspension was loaded at a high velocity (1000µl/h), cell cavities plump up due to high pressure and that resulted in a higher volume for the culture. Also, the capillary depth was increased by this pressure and allowed cells to pass as shown in Figure 2.4c. After the first loading, gas was injected into the main channel to keep the pressure at 1.1-1.2 atm and with the cavities deflating, cells were trapped. If cell injection was repeated, the cell cavities were loaded with a certain volume of cells which has the difference between the expanding volume and the original volume. Pictures of each 100 cavities were taken every 20 minute to visualize the colony growth and to determine the patterning ratio in order to understand the relation between length changes of yeasts by time.

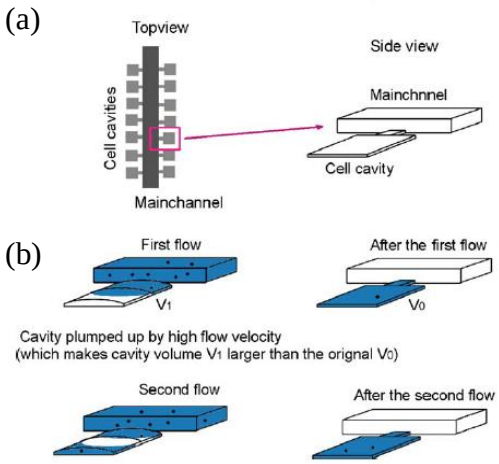

Figure 2.4. Chip design (a) the top and side views of device (b) cell loading process into cavities [10].

In the study of Falconnet *et al*. (2011), a high-throughput microfluidic system for tracking single yeast cells over multiple generations was presented [11]. The GFP tagged yeast cells were immobilized by using mechanical clamping and polymerization on agarose gel and visualized over multiple generations. The main aim of this study was to demonstrate yeast signaling response dynamics across various kinds of genotypes under several different conditions. To achieve this goal, the matrix architecture system was

designed as 8 columns and 16 rows for a total 128 chambers, which allowed simultaneous live cell imaging experiments for different strains (Figure 2.5). Firstly, cell suspension including agarose gel and media was introduced to column channels, and column valves were actuated to prevent contamination of strains. Then row valves were actuated to stop the flow of cells and to isolate each chamber. Fluidic multiplexer was used to deliver reagents to specific rows. The flow of media was continued to flush excess cells and agarose out. Each row had their waste channel above the chambers to eliminate the possible contamination. By using this device, 60,000 individual yeast cells from 8 strains were monitored and response data were collected. A written MATLAB code was used to analyze the large number of bright-field, fluorescence and DIC images captured during the experiments.

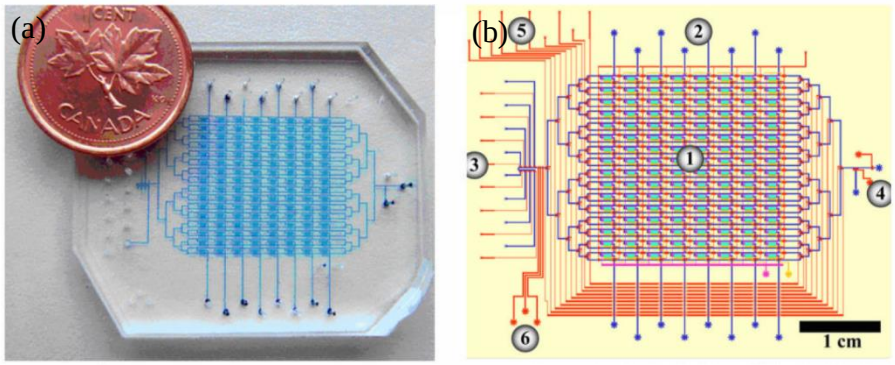

Figure 2.5. Chip design (a) image of microfluidic device (b) working area of the device (1) array of 128 chambers (2) column inlets (3) chemical inlets (4) outlet ports (5) fluidic multiplexer (6) integrated peristaltic pump [11].

In the study of Lee *et al*. (2011), cellular polarization of budding yeast was measured by a developed single-cell assay platform [12]. The platform allowed the analysis of single cell chemotaxis, subcellular microscopic imaging and analysis of marked proteins. Finding the molecular regulatory mechanism of chemotaxis in yeast cells will serve as a paradigm to understand cancer metastasis. Polarized signaling response of two types of cells, wild type and mutant, were compared. The device was made of PDMS by soft lithography technique. The PDMS and a glass piece were bonded after UV ozone treatment. The designed device was used to generate morphogenetic gradients across the cell culture

chamber. These gradients were formed by diffusion of high and low concentrations of α-factors flowing through the channels which were located above and below the cell culture chamber (Figure 2.6a). Convection barriers were used to reduce the flow across the cell culture chamber. Feeder wells were delivered to the cell culture chamber by compressed air pressure at high and low concentrations. To control the gradient profile in cell culture chamber the pressure ratios ($\Delta P_H/\Delta P_L$) were changed via controlling the volume of media introduced to the channel. The chamber was loaded with medium before loading the cells. Flow rate in the cell culture chamber was determined by COMSOL simulations. The device was mounted on the stage of an inverted microscope and the temperature was set to 30°C. Image analysis and data extraction were done by using a MATLAB script. Time-lapse fluorescence microscopy imaging of yeast cells exposed to α-factor concentration gradients were performed to see the polarization direction.

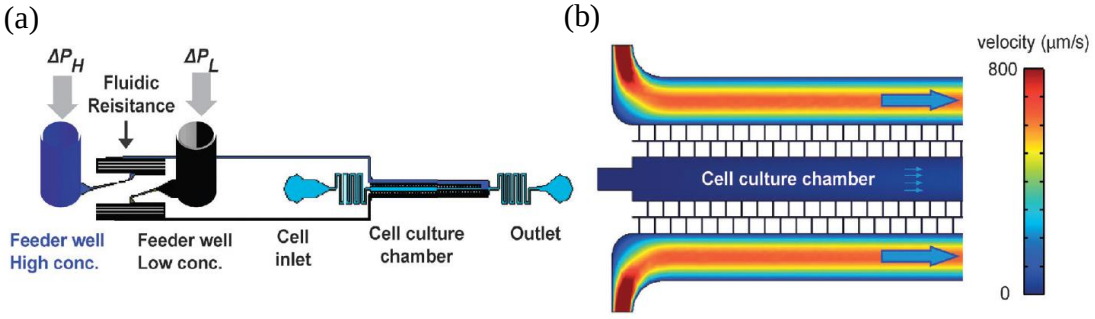

Figure 2.6. Chip design (a) overview of the microfluidic setup (b) COMSOL simulation of flow velocity in cell culture chamber [12].

Zhang *et al.* (2012) reported a microfluidic device consisted of four independent modules operating in parallel channels with arrays of pensile columns to physically trap mother cells at the gap while washing out the daughter cells by flow of fresh media [13]. Columns were created of 40 μm by 40 μm dimension and with a trapping gap of 4 μm which allowed to trap only mother cells and remove daughter cells efficiently. Bridges were added to connect the main channel with the two side channels (Figure 2.7). The mold for the chip was fabricated by the standard multilayer photolithography processes, the PDMS device was then created by soft lithography technique, after treating with oxygen

plasma. Lifespan curves of long and short-lived mother cell mutants are determined without surface labeling and stress response between mother and daughter cell was reported as a function of mother age. Initially yeast cell suspension was injected at high velocity (1000μL/min). Later, the velocity was lowered and cells were started to trap under the pensile columns. Each column can take 1-2 mother cells throughout their lifespan and in each functional module 100 cells can be tracked. Mother cells' bright-field images were taken continuously at 10 minute time intervals by Nikon TE2000 time-lapsed microscopy which makes it possible to study cell division dynamics throughout the entire lifespan of 100 mother cells in typically 2-3 days. Fluorescence images were taken every 2-4 hours for single cell gene expression analysis and at 10 minute intervals for stress response analysis. The total fluorescence signal of a cell normalized by its area was used to calculate the fluorescence intensity. The timing of budding yeast was determined by using convenient plugin of ImageJ and processed by MATLAB software program.

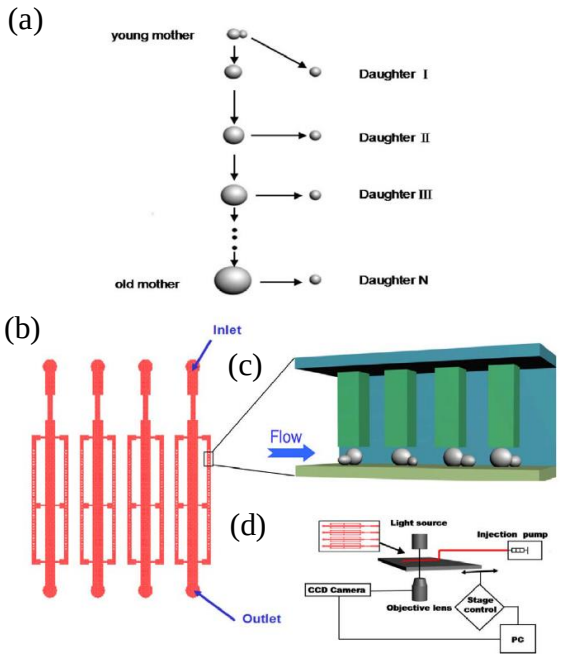

Figure 2.7. Chip design (a) a schematic of the replicative aging of a yeast cell (b) the design of the microfluidic chip (c) mother cells are physically trapped in the gap (d) The experimental setup [13].

Denervaud *et al.* (2013) reported a parallel microchemostat array system for yeast growth and observed 1152 yeast strains at the single cell level with 20 minute time resolution [14]. Protein abundance and localization changes were measured in GFP-tagged strains, and 576 GFP strains were analyzed under five additional conditions. Cell size and growth of cells were also observed by this microfluidic system. The microfluidic device was designed as an array of 1152 microchemostats which were divided into three independent sections (Figure 2.8). Medium supply could be done by two sources and nutrients were supplied by diffusion to each chamber. The device was composed of two layers; a flow layer and a control layer which were fabricated on separate molds by using standard photolithography processes.

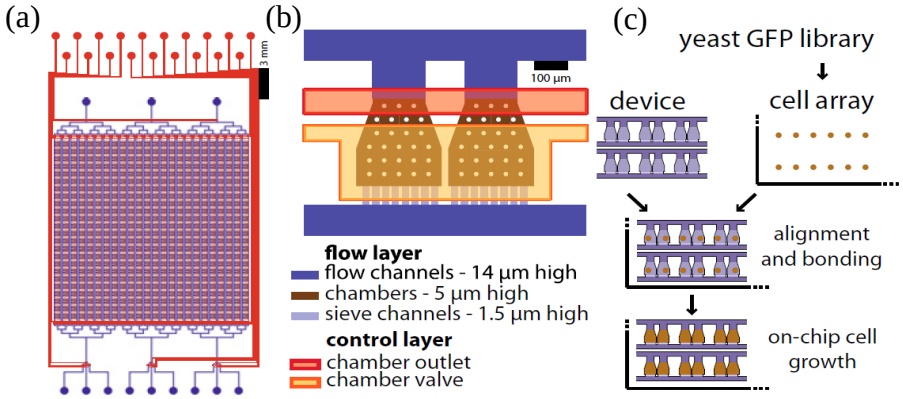

Figure 2.8. Chip design (a) design of the parallel microchemostat array for culturing 1,152 yeast strains (b) schematic of a pair of microchemostats (c) the chip programming process [14].

This mold consisted of flow channels (15 µm high), 260x300 µm small microchemostats (5 µm high), and shallow sieve channels (1.7 µm high). Channels were used for creating microvalves, and the chamber outlet valve was utilized for avoiding the contamination of cells during the experiment. By using a DNA array spotter, yeast strains were arrayed on a microscope coverslip as shown in Figure 2.8c. When the arrayed cells started to divide, in order to avoid crowding in the microchemostat, they were carried away by the medium stream and eluted from the device. Pressure difference across the chamber was generated by chamber button to force cells to grow in a monolayer and sieve channels

were used to trap the cells, and hence cells could not go out from the bottom of the chemostat. For imaging, a Visual Basic program was written to control the automated fluorescence microscope and images were taken at 20 minute time intervals. The time consumed for imaging the growth of cells and the switch of media was 6 and 7 hours, respectively. After the experiment, chamber and cell segmentation, background correction, signal deconvolution and protein localization analysis were done at single cell level via custom written image analysis software.

Park *et al.* (2013) introduced a microchemostat array with two-depth chamber design. This design was ensured small-volume replenishment of culture medium at 1% per replenishment region in a 250 nanoliter volume [15]. The system had an array of 8 microchemostats on a 40 × 60 mm^2 footprint and operated automatically by a single controller unit. The unique two chamber design minimized the fluctuation in cell density and gave the opportunity to monitor and quantify budding yeast at different dilution rates and two different cell densities (single-cell resolution). Saccharomyces cerevisiae strain was used and cultured in synthetic carbon-limited medium. A smooth slope profile was created between two depth regions, 100 µm deep culture chamber and 20 µm deep replenishment region. These two slope profiled depth difference avoided cells from accumulation at the interface area where depth of chambers was changed. Circulation of cells was controlled by peristaltic pumps and replenishment was controlled by two valves (Figure 2.9) which were controlled by a custom LabVIEW software program for automation of the system.

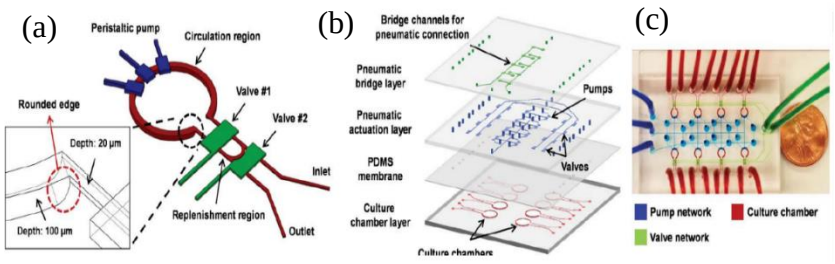

Figure 2.9. Chip design (a) a schematic illustration of replenishment microchemostat unit (b) an illustration of the 8-unit microchemostat array (c) a photographic image showing an array of eight microchemostats [15].

By using these two controlled valves, the replenishment region was disconnected from the main loop, and inlet/outlet ports and the replenishment region were arranged (Figure 2.10). This 8-unit microchemostat was controlled by a single 5-channel pneumatic controller. The PDMS made chip was consisted of four layers, which were bridge channels for pneumatic connection, pneumatic bridge layer, actuation layer and culture chamber layer. PDMS molds were made by conventional photolithography technique and fabricated layers were treated with oxygen plasma before assembled under optical microscope. The microscopic images were captured every 10 minutes, counted and converted into cell density.

Crane *et al.* (2014) designed a long-term culturing and trapping system, a microfluidic device which allows to monitor budding yeasts [16]. Cell cycle dynamics, replicative life span and history dependent behavior in the response to stress were studied on up to 1000 single cells. The principle of this single cell trapping was based on the design of the device. By using the advantage of this design 90% of cells were trapped by continuous flow during the cell loading. The device had three inlet ports, middle inlet was used to load cells and other two inlets were used for media flow. General design of the chip is shown in Figure 2.11a.

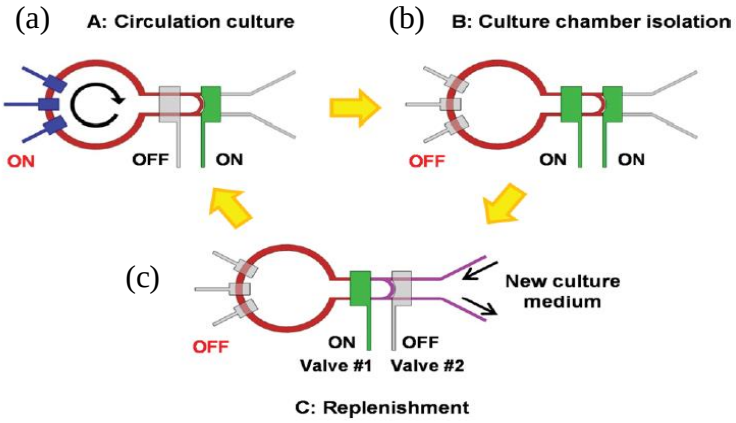

Figure 2.10. Culture chamber design (a) growth under continuous circulation using peristaltic pumping (b) isolation of the replenishment region from the culture chamber (c) replenishing cells and old culture medium with fresh culture medium [15].

Daughter cells were loaded to device by programmable syringe pumps and they were trapped by two traps as shown in Figure 2.11a. Here the trapping principle was based on the hydrodynamic pressure difference. While daughter cells were trapped, the hydrodynamic resistance of pillars was increased and this caused a pressure difference across the chamber from the top to the bottom. By this method mother cells are kept by pillars and budded daughter cells were removed by continuous media flow. Daughter cells were pushed away by two ways which depends on the polarity of mother cell. Bud could be oriented towards the top of the trap and moved to the side by diverted flow to remove the daughter cell. Secondly, the bud could be formed downstream of the mother cell during the completion of cytokinesis as shown in Figure 2.12.

Cell cycle dynamics for each single cell was determined by following the localization of Whi5p-GFP protein. Also, stress response was shown by glucose limitation effects on Msn2p-GFP proteins using three periodic pulses. Heat-chock protein Hsp 104p-GFP was used to determine the budding period by the help of kymographs which showed gene expressions during budding. For the experiments yeast GFP clone was used and cells were cultured in 2% glucose in synthetic complete medium (SC).

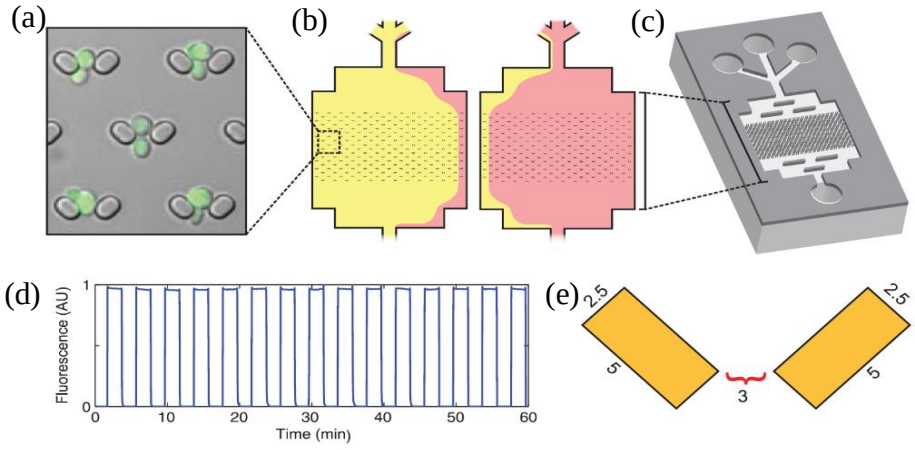

Figure 2.11. Chip design (a) a DIC image of the cell traps (b) a schematic depicting fluid flow in the flow cell during media switching (c) overview of the microfluidic device (d) the switching rate and reliability of media switching in traps (e) schematic showing trap dimensions in microns [16].

Device fabrication was made by using soft-lithography techniques and AutoCAD software was used for chip design. After the design was completed, it was printed to a chrome-on-glass mask and mold was fabricated. The microfluidic devices were made by using PDMS, holes were punched and devices were bonded by using oxygen plasma treatment. Nikon Eclipse Ti inverted microscope was controlled by MATLAB script written for micromanager for taking bright-field and fluorescence images. In addition to image segmentation, the cell tracking and data extraction processes were also performed by using a customized MATLAB code.

Jo *et al*. (2015) developed a microfluidic device called "High throughput yeast aging analysis" chip [17]. Particular changes in cell morphology such as critical cell size, terminal morphology and protein subcellular localization were determined by using this efficient device by trapping 8000 individual single yeast cells. The microfluidic device was fabricated with soft lithography of PDMS and oxygen plasma was used to activate both PDMS and glass side surfaces before PDMS replica was bonded to glass side.

In the device, 16 parallel discrete channels were grouped into 4 modules, each channel consisted of 520 cup-shaped single-cell trapping structures (Design and working mechanism of the chip for studying aging in yeast is shown in Figure 2.13). Four different strains could be tested by four different media by using the advantage of multiple module design. The height and the depth of the traps were determined as 12 μm and 12μm, respectively. Firstly, culture media were introduced to main channel then the desired cell suspensions were loaded through the subinlets at a lower flow rate. After the mother cells were started to budding, the daughter cells were washed out of the device by a slower medium flow than that of cell loading. Daughter cells could be removed from the small outlet opening or larger opening against the flow without losing trapped mother cells.

With this method, the retention rate achieved was 90%, which allowed the high-throughput analysis of replicative aging. Replicative life spans, cell cycle times and critical cell size correlations were determined for selected yeast strains and shown as a marker for longevity of yeast. Also terminal morphologies of yeast strains were shown by categorizing them as budded and unbudded strains at the end of their lifespans and localization of GFP-

tagged proteins were followed by using the merged images of fluorescence and bright-field microscopy. For visualization, chip was mounted onto the stage of an inverted microscope and time-lapse images were captured at 10 minute intervals for 96 hours. Images were analyzed with ImageJ software to determine budding events, cell size, morphology and localization changes. The results were consistent with those of conventional microdissection method.

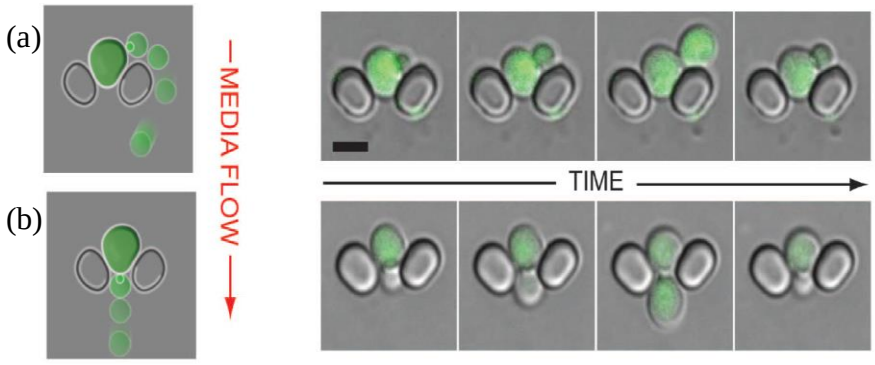

Figure 2.12. Chip design principle (a) the removal operation of a daughter cell by the media flow when the mother buds at the top of the trap or (b) at the bottom [16].

Hansen *et al.* (2015) introduced a multiplexed microfluidic device to measure the dynamic gene expression response of individual yeast genes by single cell analysis [18]. Thousands of cells could be monitored by performing up to 20 different experiments per day. The required silicon wafer master mold was fabricated by photolithography technique, and the replica molding of PDMS was done by soft lithography. The device consisted of 400 μm wide, 100 μm wide channels separated by 150 μm wide walls. Schematic view of the device and two channels separated by walls are shown in Figure 2.14b and Figure 2.14c. All 5 microfluidic channels for cell growth could be controlled independently which gives the opportunity to test different strains by multiple conditions simultaneously (Figure 2.14a). The budding yeast transcription factor Msn2 nuclear localization was determined and controlled by a specialized molecule, which behaves as an inhibitor of kinases to study the drug response. The gene was tagged by cyan fluorescence protein (CFP) and yellow fluorescence protein (YFP) in diploid cells. For flow control, solenoid valves were used

for each channel and controlled by a written MATLAB code. After cells were loaded into channels, microfluidic device was mounted on the microscope stage and set to 30 °C. Tubings for inlets, outlets and valves were inserted and the flow was started by pulling the 20 gauge needle syringe into the tubing which allowed 1µl per second per channel flow rate for each channel in 4 hour experiments. Time lapse microscopy was used for visualization and each channel was captured from 5 fields of view by microscope software to see the separation between positions.

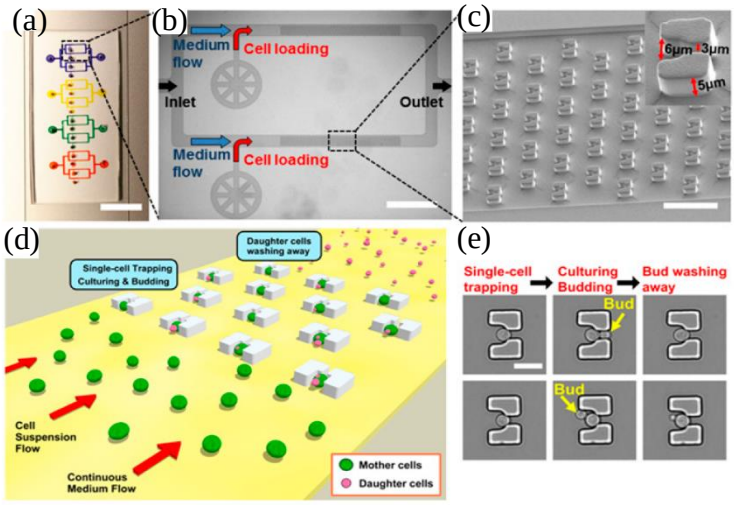

Figure 2.13. Chip design (a) optical image of the chip (b) microscopic image of branched trapping channels (c) SEM of trap arrays in the chip (d) chip working mechanism (e) a single yeast cell showing the working mechanism procedure [17].

In the study of Bell *et al.* (2013), they designed a basin-style microfluidic device for trapping single fission yeast cells of *S. pombe* [19].The aim was to demonstrate normal growth and fission of *S. pombe* cells with highly controlled and reversible immobilization by providing their natural environment. The device was fabricated by channel and control layers and consisted of 69 rows, each with 28 basins along it, and each device has 7728 trapping sites (Figure 2.15). The working principle was based on hydrodynamic pressure difference. While the cells were flowing through channels, they trapped individually in small wells. The cells were prevented from external forces in deep small wells and the bulk flow passed through the wells without effecting buried cells. The device was designed for effective Photo-activated Localization Microscopy (PALM) imaging of fission yeast.

There were three fluidic inlets to feed four trapping regions, and temperature was controlled by rapid circulation of heated or cooled water through the device. The cells were pumped into the device by a syringe pump at a velocity of 10L/h. The flowing cells were trapped one by one and automatically scanned.

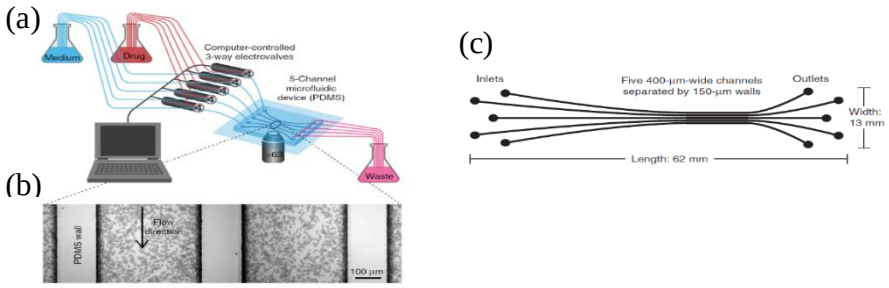

Figure 2.14. Chip design (a) microfluidic setup (b) brightfield image of budding yeast cells in microfluidic channels (c) device design [18].

The simulation of image trapping was also done by Comsol Multiphysics 4.0a. The pressure drop and flow velocity profiles were obtained as expected (Figure 2.15b and 2.15c). The flow velocity and pressure values were lower in trapping sites. The results were matched with Poiseuille's model used for hydrodynamic flow resistances. The white light transmission and single-molecule fluorescence super-resolution images were captured with an inverted microscope automatically by a written MATLAB code, and each cells position was replotted via custom written ImageJ. Table 2.1 below summarizes some of the yeast applications of microfluidic devices from literature.

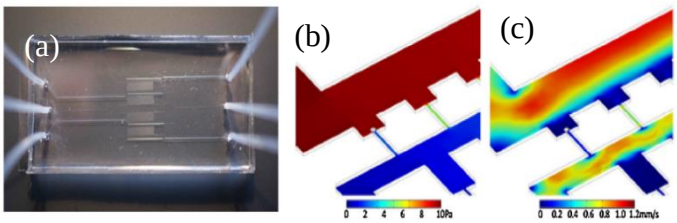

Figure 2.15. Chip design (a) image of fabricated device with fluidic interconnections (b) simulation of pressure difference through flowing (c) flow velocity (d) flow velocity over 11 rows [19].

Table 2.1. Yeast applications with microfluidic devices.

Reference	Device material	Active /Passive	Duration	Microscopy	Yeast & medium	Parameters	Image Processing system	Single/ Multiple
[5]	PDMS	Flow was driven by pressure differences (open to atm for 0-12 psi pressure difference) (Passive)	14-25 h	Nikon Eclipse TE2000 epifluorescence microscope -Fluorescence, bright field, phase-contrast micrographs - 20X, 40X,60X	-Bacterial and yeast species -E.coli cells -GFP tagged	-Three different chips are used at 20 and 35^{o}C -Cell density -Chamber sizes Temperature	3 minute intervals	Multiple
[6]	PDMS	Passive	20 h	Nikon Diaphot TMD epi fluorescent inverted microscope -autofocus controller -Fluorescence	*S.cerevisiae* strain K699 -YFP tagged -Synthetic drop out (SD) medium	-Gene expression over generations -Cell tracking with respect to time -Cell division period -Cell sizes	Not announced	Single 119 cells
[7]	PDMS	Passive	-18 h for RAS2-YFP -5 h for HSP104-GFP	-Zeiss AxioVert 200M inverted microscope (200X and 400X) -Fluorescence and Bright field images	-RAS2-YFP -HSP104-GFP -SC medium (contains 2% glucose)	-Two different tagged proteins -Different jail designs -Expression levels -Heat shock response of each cell	15 minute intervals for up to 20 hours	Single cell (3600 yeast jails per device)
[8]	PDMS	Solution is injected by a syringe pump (PASSIVE)	4h-10h	-Inverted fluorescent microscope (Olympus IX 71) -Bright field image	-Budding yeast *S.cerevisiae* -*S. pombe* -YPG solution (2%glucose)	-Cavity sizes -Repeating times of injection	20 min intervals	Multiple

Table 2.1. Yeast applications with microfluidic devices (cont.).

[9]	PDMS	Active (valves inside the system)	-136 min (fluorescence experiments) -1600 min (cell counting) -400 min (GFP concentration)	- Leica DMIRE2 fluorescent microscope -Bright field images -Fluorescence images - (DIC) images	*S. cerevisiae* (GFP tagged) -low melting temperature agarose -YPD medium	-Tracking single cells over multiple generations in 28 experiments -Response across 8 genotypes and 16 conditions	5 min intervals 15 min- 256 DIC& 512F images	Single 100 cells
[10]	PDMS-glass	Passive	240 min	Inverted fluorescence microscope (Eclipse Ti, Nikon Instruments)	-Wild type and far1-H7 mutant cells (YFP tagged) -Synthetic defined media with 2% glucose	-Intracellular protein localization -Cellular polarization (by using α factors) -Cellular morphology	5 min intervals up to 250 mins	Single cell
[11]	PDMS	Passive	40-60 hours	Nikon TE2000 time-lapsed microscopy (40X, 60X)	B74741 background Ptef2-RFP YEPD medium	-Replicative lifespan, cell cycle, stress response	10 min (stress response), 2 or 4 h (gene experiments)	Single 100 cells
[12]	PDMS	Active (Valve control)	-6h (for imaging growing) -7h (for media switch)	-Inverted epi-fluorescence microscope (Nikon Eclipse Ti-E) -4X, 20X, 60X -Phase contrast and fluorescence images	1152 yeast-GFP tagged strains -High MMS, low MMS, Sorbitol	-Protein abundance -Localization -Cell size -Growth parameters -Media switch	20 minute intervals	Single 1152 cells
[13]	PDMS membrane layers	Active (Syringe pumps & solenoid valves)	0-40 hours imaging every 8 hours -140 hrs for cell density	-Optical microscope (Nikon America Inc., NY) -Bright field	*S. cerevisiae* culture -synthetic Carbon limited medium	-Two different initial cell densities -Dilution rates	10 min intervals	Multiple

Table 2.1. Yeast applications with microfluidic devices (cont.).

[14]	PDMS	Passive (By hydro dynamic pressure change)	10-60 hours	-Nikon Eclipse Ti inverted microscope -60X, 100X Fluorescence, bright field images	Yeast GFP clone -2% glucose in SC media (synthetic complete medium)	-Comparison of two devices -Different GFP tagged proteins -Trap length and gap -Cell cycle dynamics under stress	15 min intervals	1000 single mother cells
[15]	PDMS and glass	Passive	96 h - 72h	-Olympus Inverted Microscope -60X, 40X -Brightfield and Fluorescence images	Yeast strains with BY4741 background (GFP tagged) -YPD medium	-Critical cell size -Protein localization, replicative life spans	20 min intervals	Single 8000 cells
[16]	PDMS	Active	100-150 min	Time-lapse -Phase-contrast, Bright-field, fluorescence images	*S.cerevisiae* (Msn2-mCherry, CFP, YFP) -Low fluorescent medium)	-Nuclear localization of the budding yeast transcription factor	10 min intervals	Singles thousands of cells
[17]	PDMS	Passive	Not announced	-Olympus IX71 Inverted microscope -Oil immersion	*S. pombe* YES media	-Growth and division of *S. pombe* cells	60 min intervals	Single 7728 cells

2.2. Protein Characterization in Yeast Strains Using Microfluidic Devices

Some studies are focused on the localization changes, hyphal growths and lipid accumulations of specific yeasts to determine their functions and genetics. In most of these studies, fluorescent tag is used for labelling and detection of the molecules. Some of the pioneering studies in the literature done by fluorescently tagged yeast strains are given below.

In the study of Bouchez *et al.* (2015), to find the role of Rab upon interaction with other organelles was studied [20]. The goal was to identify new proteins associated with both vacuole and LDs (lipid droplets) using proteomic, biochemical and microscopic

approaches. Immunoblot experiments were done by using the Rab7-like Ypt7p yeast protein as the marker of the vacuole and late endosome. Yeasts were grown in YNB with low C/N until the early stationary phase. A modified strain (GFP-MYC-YPT7) was used for microscopic visualization and the results were compared with another strain (ERG6-RFP), which was associated with LDs. A partial co-localization was observed by epifluorecence microscope by using these two strains (Figure 2.16). The study was also showed the relationship between vacuole/endosome and LDs. Then biochemical analysis and proteomics on LD's were done to confirm these observations. A deletion mutant (ypt7Δ) was used for genetic studies, to determine the role of YPT7 in LD dynamics.

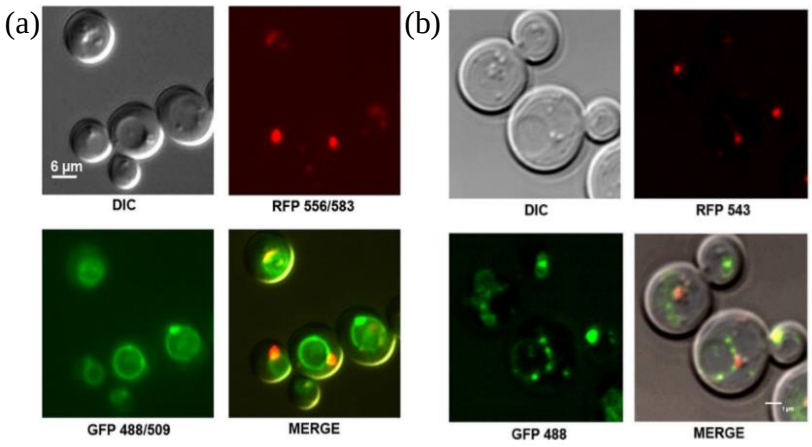

Figure 2.16. Erg6p-RFP and GFP-Ypt7p in the GFP-YPT7/ERG6-RFP strain partly co-localize (a) epifluorescence (b) confocal fluorescence microscopy images [20].

In the study of Breker *et al.* (2013), different kinds of external stimuli were used to describe the dynamics of proteins [21]. Breker's group was focused on the regulation of protein levels and localization under three different stress conditions: DTT (dithiothreitol), H_2O_2 and nitrogen starvation (Figure 2.17). Characterization of 5330 yeast proteins at single cell level was studied by using the GFP-tagged yeast library. Cytosolic mCherry was inserted into every strain of the yeast by using "Synthetic Genetic Array". By this method, images were segmented into single cell objects via extracting GFP intensity in a single cell resolution.

The images of hundreds of individual cells were captured during their growth under control conditions (logarithmic growth in SD) and three stress conditions. The scatter plot of median fluorescence values (r^2 values) of two different experiments showed high reproducibility of the system and were also in agreement with literature. After the determination of subcellular localization, new 72 proteins localizations were investigated among, which 21 proteins were essential [21]. The abundance changes under stress were expressed as the $\log_2$ fold change, i.e. nitrogen starvation of up-regulated, down-regulated and bi-modal distributed relative abundances. Survival strategies of each strain (Bet Hedging) was represented for two types of GFP tagged strains (Pre3 and Ssb1). Low and high GFP expressing fractions were sorted after one day nitrogen starvation. The results of these experiments showed unique morphological characteristics for each strain.

Protein of unknown function (Pin3) was also studied to determine a new cellular function by using the changes in protein localization. Proteins selected by their similarity of localization change under the same stress condition (DTT treatment). The localization shift under stress and four new connections of Pin3 protein were demonstrated. The changes in protein localization was used to identify new cellular functions.

3. MATERIALS AND METHODS

3.1. Chip Fabrication

3.1.1. Polymers Used for Microfluidic Device Fabrication

The design and fabrication of the microfluidic device differ based on its application area which may be genetic analysis, cell manipulation and culturing, diagnostics or tissue engineering. Different polymeric materials are used for the fabrication depending on their specific characteristics related to the aim of the study. For most of the biological applications on cell analysis, specific polymers are chosen to control the transport of the cells as well as to immobilize them in certain trapping regions.

In our study, the main aim is to trap the cells in C-shaped region without trapping in channels or clogging. Also highly optical transparent polymers need to be used for better imaging of cells. To achieve these goals, three different polymer types were tested to find the best one for yeast culturing. These polymers and their material properties are given in Table 3.1.

Table 3.1. Properties of polymers used for fabrication [22].

Name	Trade Name	Density (g/cm^3)	Tg (°C)	Resistivity ($\Omega\ cm^{-1}$)	Water adsorption (%)	Thermal Expansion Coefficient ($10^{-6}/K$)	Young's (Tensile) Modulus (MPa)
PMMA	Polymethyl-methacrylate	1.18	85-165	$1x10^{15}$	2%	80	1800-3200
COP	Cyclic Olefin Copolymer	1.02	70-180	$> 1x10^{17}$	0.01%	70	2400
PEN	Polyethylene naphthalate	1.36	122	$1x\ 10^{15}$	0.4%	20-21	5200

The stability and resistance properties against solvents and organic solvents are important in fabrication process and also when dealing with cell applications. PMMA is a hydrophobic polymer and it is resistant against media of diluted acids and bases, but it does not show resistance to alcohols, acetone, benzole and UV radiation [23]. Acetone, benzene or dichloromethane solvents can damage this polymer. COP polymer is also resistant against acids and bases and it has the lowest water absorbency among all plastics. Therefore COP polymer has good dimensional stability which is not changed under high moisture conditions, and has an excellent structure for microfluidic device fabrication [24].

PEN polymer is in the class of biocomponent binder fiber materials and it was tested because of its good bonding properties in thermal compression bonding process. The polymer has good resistivity for concentrated and diluted acid solutions, alcohols and alkalis [25]. The designed microfluidic device for yeast cell culturing was fabricated by using these three polymers. Biocompability, background fluorescence and yeast cells' response to these polymer structures were tested as the first step of this study.

3.1.2. The Improvement of the Previous Design

A microfluidic bioreactor was successfully designed by Gençtürk E. (2015), to grow yeast cells, as a part of her MSc Thesis [26]. The previously created model of Gençtürk E., has a diameter of 400 μm trapping region, which is not totally appropriate to observe all of a chamber shape in captured images with inverted microscope under 40X objective [26]. To solve this problem, the design dimensions need to be changed.

The area to be seen under the microscope was determined by following spatial calibration procedure. A stage micrometer image of ruler was used for calibration and the image was captured under 40X objective lens of Nikon Eclipse E200 Microscope. This area is then used to measure the area seen under the microscope and to determine the proportions for downscaling. The steps of calibration process are as follows;

(i) The stage micrometer image was selected as captured image of 40X magnified objective ruler in Fiji.

(ii) By using the line selection tool, a line of known length was drawn on the stage micrometer image.

(iii) 'Analyze – Set Scale' menu was opened.

(iv) The known distance was drawn as a line and set in the 'Know Distance' Field. The tool knows how many pixels long was the line you drew.

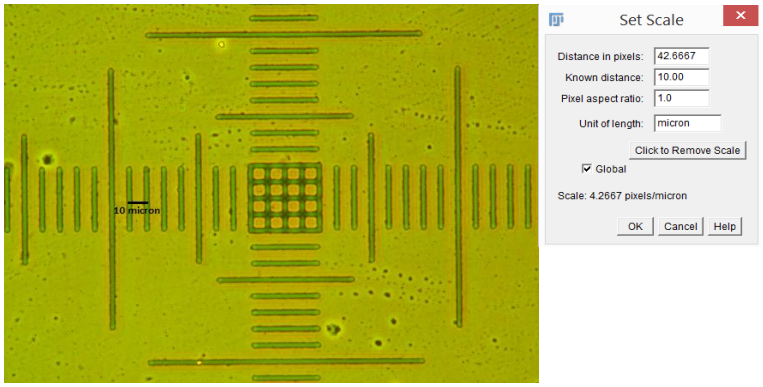

Figure 3.1. 40X objective stage micrometer and 'set scale'.

(v) The units of the measurement were set (μm, mm etc.).

(vi) The 'Global' option was turned by clicking the check box, so all open images take the same spatial calibration when you click 'OK'.

All the area captured are given in terms of microns and written automatically at the left top of the screen of images when opened. For our case under 40X objective the area was 300 x 225 microns^2. In the previous c-shaped chamber the trapping region had a diameter of 400 μm. The captured image under 40X objective only showed a part of the c-shaped region. This situation had numerous disadvantages. First of all, it was very difficult to capture the same area each time and to unite the partial images of the chamber (to see the chamber as one piece) and consequently led the cell counting results to be non-uniform. By using these dimensions, the area seen in two designs are compared in Figure 3.2. The possible areas seen under 40X objective lens are marked with grey rectangle. The improved design offers the visualization of the trapping region along with the c-shape at the same time.

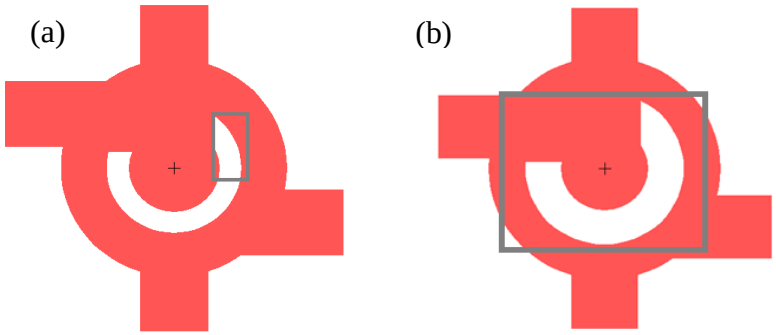

Figure 3.2. The area seen under the microscope by using 40X objective (a) previous design (b) improved design.

The dimension reduction through the etching process should also be taken into account. During the isotropic etching process, the channel widths, chamber diameters and c-shape widths are reduced in determined technical orders taking additional size reduction in etching process into consideration. In a conventional etching process, the objects get smaller and the amount of change is approximately 15% of material thickness. In the light of these criteria, new dimensions are given in Table 3.2 and Figure 3.3. R1, R2 and R3 refer to the radii of the chambers, respectively. The width values are same for all channels.

Table 3.2. Dimensions of previous and new designs.

Dimensions (microns)	**Previous Design**	**New Design**
R1 (radius of the inner chamber)	500	60
R2 (radius of the middle chamber)	200	110
R3 (radius of the outer chamber)	300	160
w (widths of the channels)	300	90
Height of the reactor	12	10
c-shape thickness	100	50

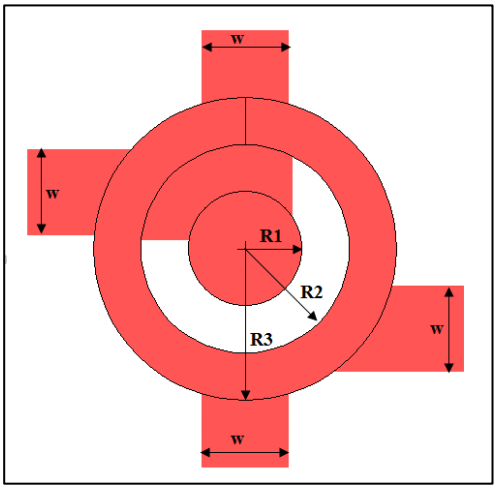

Figure 3.3. The dimensions of a c-shaped region.

3.1.3. Creating the Mask

To start the fabrication of a microfluidic device, the most important step is to design a useful device to achieve the aim. In this case, the microfluidic device was designed to investigate the molecular function of an uncharacterized protein in yeast. 8 chambers along 2 rows with inlet and outlet channels are designed. The number of chambers was taken same as the previous design made by Gençtürk E., 2015. The number of outlet ports was reduced from six to two for taking all sample from one port at each row. The c-shaped regions were created to trap GFP and RFP tagged yeast cells and to visualize the localization of protein of interest during the cell-cycle process.

The design was modelled by L-Edit software program in two dimensional form (Figure 3.4). The diameter of the trapping region is 120 µm and c-shape thickness is 50 µm. The inlet channels for yeast and nutrient supply, outlet channels for waste solvent and side channels for carrying the excess flow to main channels, all have 90 µm width and 8-10 µm depth.

When the drawing was finalized, the file format was converted into .pdf and it is sent to a high resolution printer (Çözüm Tanıtım, Ankara) to be printed on an acetate paper. Printed mask is then used for photolithography process.

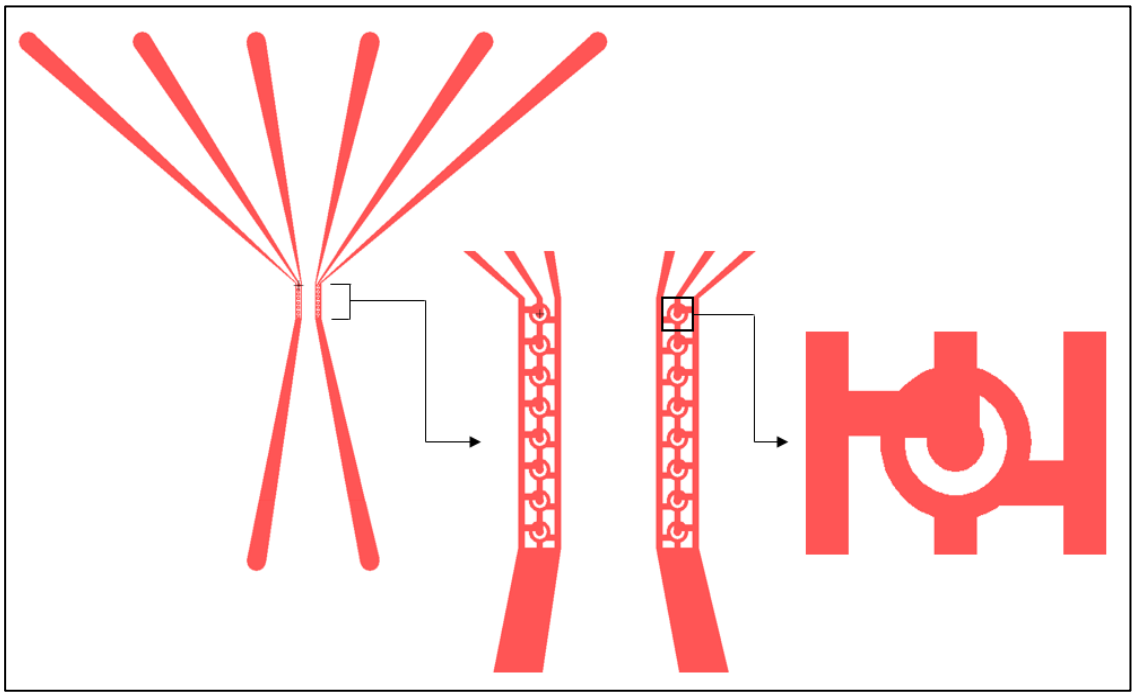

Figure 3.4. General view of mask and chambers.

3.1.4. Photolithography

Photolithography process is an important technique for microscale fabrication and it is limited to 2 dimensional lateral structures. A photosensitive emulsion layer is used to transfer the desired pattern from a transparent mask to the substrate. Three steps of photolithography process is; positioning, exposure and development [27]. First of all, the substrate should be coated with resist and then substrate and mask are laterally positioned. Here the distance between mask and substrate is an important parameter to achieve the desired pattern. There are two types of resists used in this process; positive and negative. Obtaining the desired resist type depends on the solubility characteristics of resist under UV light exposure. The second step of the process is to expose the resist layer to UV-light or X-ray. Usually a UV light of 254-365 nm wavelength is used. In positive photoresists, exposure process changes the chemical structure of the exposed area of the resist and it becomes more soluble in water, the process works inversely for negative photoresist. At the end of this process, patterns are transferred to photoresist layer as shown in Figure 3.5.

The development process is done by dissolution or etching of the resist pattern by a developer solution for negative or positive photoresists, respectively.

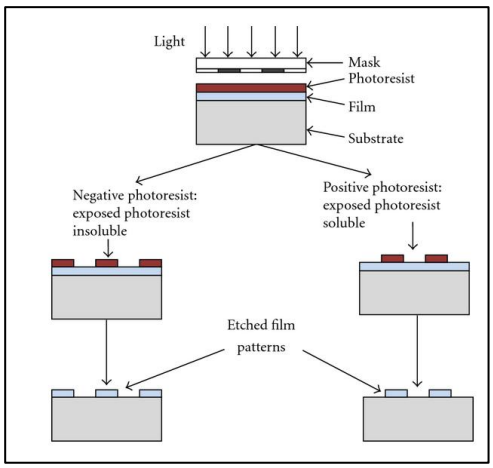

Figure 3.5. Photolithography process by using negative or positive photoresist [28].

In our case, the photolithography process was applied by using a 10x10 cm stainless steel as the substrate. The aim is to obtain a positive photoresist mask to further create a mold. First the steel plate was cleaned with acetone, isopropyl alcohol and distilled water. Then dried by pressurized nitrogen to remove the dusts on the surface. The spots on the surface was again cleaned by acetone, washed by distilled water and then dried. The steel plate was positioned on the middle of the spin coater (SPS SPIN 150, Netherlands) and fixed with vacuum. PR-1828 photoresist was poured on the middle of the plate and spread over the plate to achieve uniform distribution on the square shape. The bubbles on the surface was cleaned before starting the process. The rotation speed and time was based on the photoresist type used. Here, for the PR-1828 photoresist, the spin coater was set to 2000 rpm for 30 seconds. The spin coater started to rotate at 500 rpm for 10 seconds, then the process was completed after rotating at 2000 rpm for 30 seconds. After the spin coated steel was soft baked at 95°C for 2 minutes, the curing process of the mask was applied under UV lamp for 2 minutes. Here, the mask was put on the steel plate under UV light and the areas exposed to light were cured at the end of the process. The development of the mask was done by AZ-726 developer solution for 45 seconds. The cured steel was submerged into the developer and UV light exposed and cured areas were dissolved in this

solution. Then the steel was cleaned by distilled water and the shape of the design was checked under the microscope. After all, the steel plate shaped with the design was hard baked at 110°C for 3 hours. The general scheme of the process is given below (Figure 3.6).

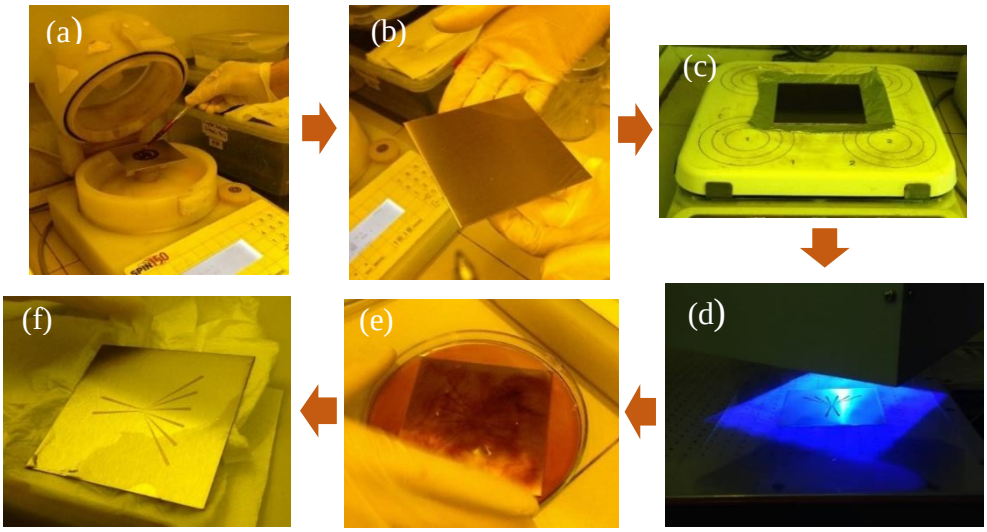

Figure 3.6. Photolithography process (a) applying photoresist in spin coater (b) photoresist coated steel plate after spin coating process (c) soft baking (d) UV light exposure (e) development (f) drying mask before hard baking.

3.1.5. Creating Mold by Electrochemical Etching

Electrochemical (Electro) etching process is the etching process of metals via using an electrolyte solution, an anode and a cathode. DC power is used to create a direct electric current. The stainless steel metal piece to be etched is connected to the positive pole of a source (anode) and another stainless steel metal piece is connected to the negative pole of the source (cathode). These two pieces are submerged into an electrolyte solution. When the current is started, the metal of the anode is dissolved and an equal amount of the cation is deposited on the cathode. Electrolyte solvent and distance between two metal pieces are determined according to the properties of solvent and metal pieces. At the end of the process a mold is created [28]. A schematic description of the process is shown in Figure 3.7.

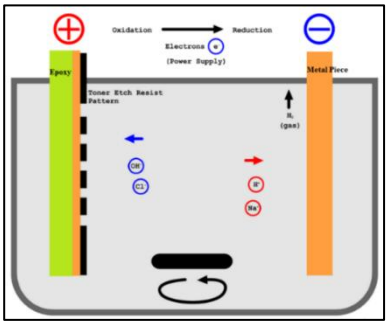

Figure 3.7. Schematic view of electrochemical etching process.

For the wet etching of the steel plate with the design on it, NaCl : Distilled water (20:80 w/w) solution was used as the electrolyte solution. The solution was prepared by adding 8 liters of water to 2 kilogram of NaCl and mixed. The corners of the steel plate was covered by insulating tape to reduce the etchant area and direct the flow on the designed part uniformly. The steel attached insulator plate was the cathode electrode which is positioned in container, the electrolyte solution was poured up to the level, where the steel plate was submerged. The steel plate, which was the anode electrode, was submerged into the container right across the cathode electrode. DC power supply was set to 60A to create the current for electrochemical etching and applied for 35 seconds. The isotropic etching setup was designed to create a 10 μm depth in the steel plate. The setup and the mold before the process are shown in Figure 3.8.

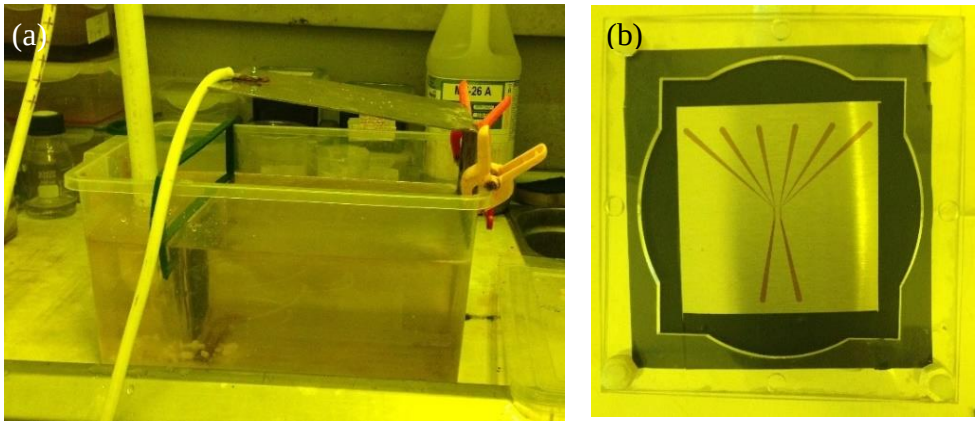

Figure 3.8. Electrochemical etching process (a) experimental setup (NaCl solution, connections of power supply) (b) steel plate before etching.

The steel mask took the form of the desired shape and the created mold under the microscope is shown in Figure 3.9.

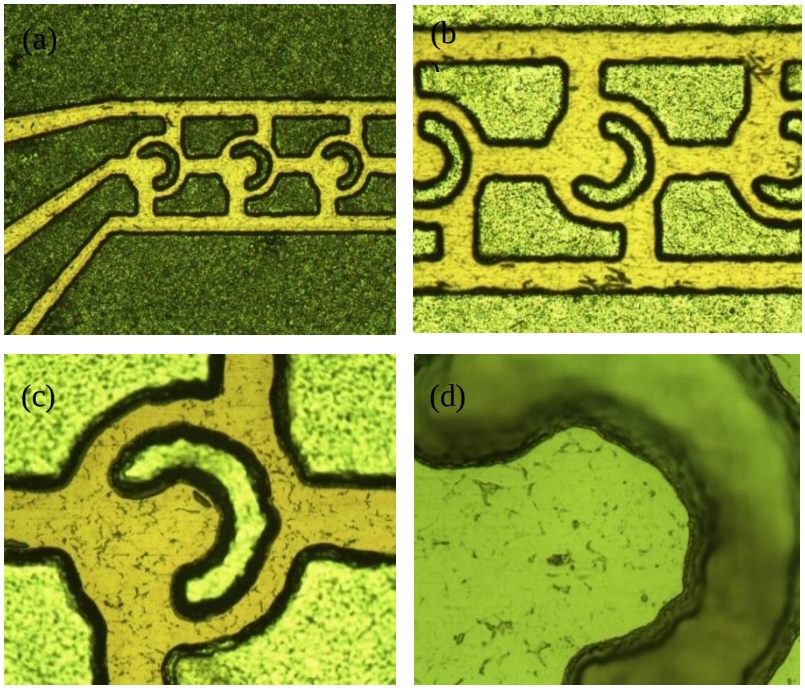

Figure 3.9. Microscope images of etched steel plate (a) left channel inlets (b) channels (c) c-shape of an entire chamber (d) trapping region of an entire c-shape (40X objective).

3.1.6. Hot Embossing

Hot embossing process is a widely used process for the fabrication of polymer based microstructures. This process is a simple and straightforward process with low cost, and thus large range of materials can be used. There are two parameters taken into account; temperature and pressure. The aim is to apply the pattern from the mask to the material by using optimum pressure and temperature values.

Thermoplastics are reshaped near their glass transition temperatures (Tg). The process consists of three steps. Firstly, Carver's temperature is set higher than the transition temperature of the selected polymer and it is placed on the middle of the lower hot plate which is heated to just above the glass transition temperature of the polymer. The mold is also heated to the same temperature and pressed into the polymer at an optimum pressure.

After the process is done (approximately 10 minutes later), two substrates are isothermally cooled below the transition temperature and demolded [22]. Simple schematic view of the process and Carver machine used in experiments are shown in Figure 3.10.

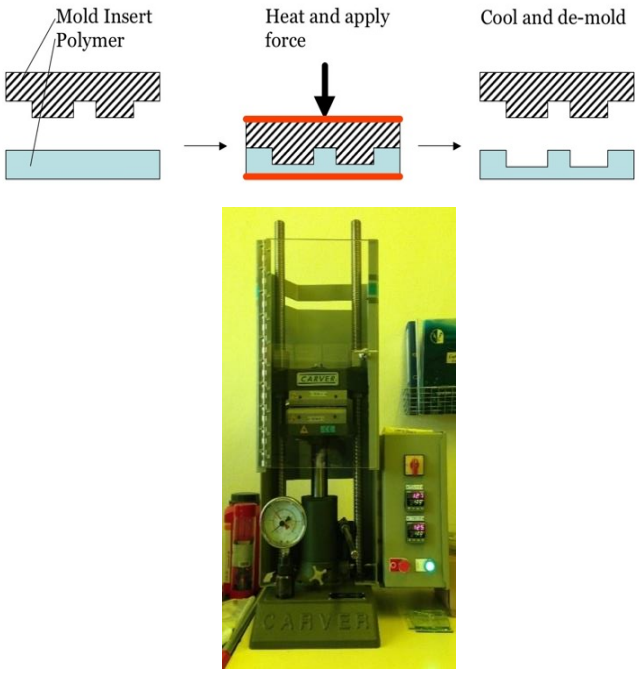

Figure 3.10. Schematic view of hot embossing process and hydraulic press machine (Carver).

In the hot embossing process, the master mold created by the previous steps was used to generate microchannels on polymer sheets. 3 cm x 5 cm PMMA (Polymethyl methacrylate, commonly known as plexi) sheets with 3 mm thickness are used. Firstly, the PMMA piece was cleaned by water, IPA and distilled water, respectively and dried by pressurized N_2 gas. The temperature of the upper and lower hot plates of Carver machine was set to 120°C, which is slightly higher than the glass transition temperature of PMMA (T_{gPMMA} = 105°C). The PMMA piece was put on the steel mold and covered by aluminium foil. The covered polymer piece and mold was put between the hot plates and pressurized at 1250 lbs for 10 minutes. Then the temperature was set to 65°C and polymer piece inserted mold was cooled under pressure. The polymer and the mold were separated (demolded) when the temperature reached 65°C. PMMA alignment on steel plate and channel formation after demolding is shown in Figure 3.11.

Hot embossing process for COP was carried out at 130°C which is also higher than the glass transition temperature of COP (T_{gCOP} = 100-102°C). Firstly, the COP piece was washed by acetone, IPA and distilled water, respectively and dried by pressurized N_2 gas. The hot embossing step was done on the 3cm x 4 cm COP piece and the piece was pressurized at 130°C by 1330 lbs pressure for 10 minutes by using the same aluminum covering and demolding procedure of PMMA. The PEN sheets cleaning step was different than those of PMMA and COP materials. The PEN sheets were cleaned by Chloroform:Ethanol (1:1 volume/volume) mixture and dried by pressurized N_2. The 3 cm x 5 cm PEN sheet was pressurized at 135°C under 3800 lbs pressure and demolding was done at 60°C.

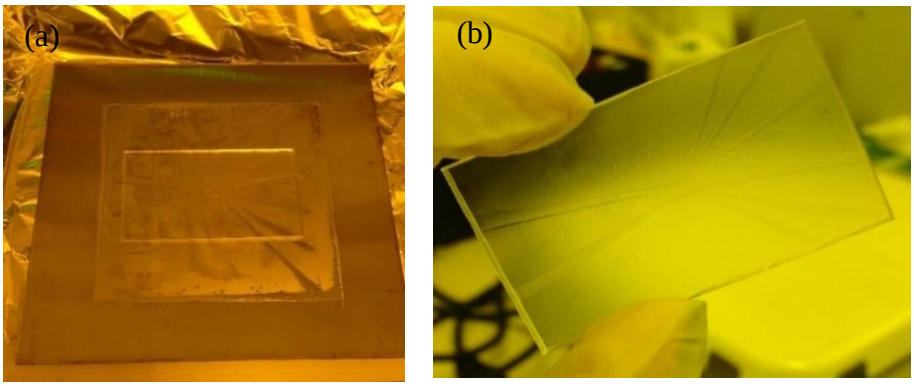

Figure 3.11. Hot embossing process (a) PMMA alignment on steel mold (b) channel formation by using PMMA polymer.

3.1.7. Thermo-compression Bonding

Thermo-compression bonding is a useful method for bonding of two polymer pieces. For a successful bonding, selected polymers should have convenient properties for sticking together. Because of this, before the bonding process, polymer surfaces are usually activated by the methods of specialized solvents, oxygen plasma, atmospheric plasma or UV/ozone treatment [22]. Thereafter, glass-glass or glass-polymer pieces are aligned and bonding is done at optimum temperature and pressure and cooled to room temperature. This method is used to cover the microfluidic pattern keeping its original shape without

deformation, so optimum temperature, pressure and duration time are important. This process is done by Hydraulic Press Machine (Carver).

Bonding strength is an important parameter and related to some factors such as polymer type and surface properties, bonding temperature and pressure. Bonding strength can be increased by hot press, post annealing or applying solvents. If hot press, without using any solvent, results in weak bonding strength, the surface activation is usually done by using a solvent for PMMA experiments. Bonding parameters such as temperature, pressure, duration time and solvent applied on polymer were tested and optimized. The tested parameters for these three polymers are given in the results section.

3.2. Yeast Culturing in Liquid Medium

The strain used in all the experiments is wild type BY4741 yeast strain and its YOR060C gene was tagged with GFP (an Aequorea Victoria GFP (S65T) tag at the C-terminus end) to visualize the protein expression. The GFP fusion proteins are integrated into the chromosome of yeast via homologous recombination and the proteins are expressed by endogenous promoters. The GFP tagged strain was kindly provided by Prof. Steve Oliver from University of Cambridge, Department of Biochemistry, Functional Genomics and Systems Biology Laboratory.

For sterilization of the equipment, the capped erlenmayers flasks of different sizes (50 mL, 100 mL, 1L and 2L) and micropipette tips were placed in autoclave and sterilized at 121°C for 15 minutes. To prepare the YPD medium, 2% glucose containing YPD medium was used to grow the cells. 6 gr yeast extract and 3 gr peptone was dissolved in 210 ml purified water and sterilized in autoclave at 121°C for 15 minutes. 6 gr glucose were dissolved in 90 ml purified water and sterilized in autoclave at 121°C for 3 minutes. Two solutions were left for cooling at room temperature under sterile hood. The yeast extract-peptone and glucose solutions were mixed with the help of hand vortexing in 500 ml erlenmayer flask.

The next step was to prepare the pre-cultures. 20 ml YPD medium was put into two 100 ml erlenmayer flasks. Previously prepared yeast cells grown on the solidified YPDA medium were taken from the refrigerator at 4°C and used to inoculate liquid medium at room temperature. The inoculation loop was sterilized at the tip of the flame (Bunsen burner) and cooled down by pressing onto the edge of the solidified YPDA medium. A colony of yeast cells with the help of the inoculation loop were scraped from the agar plates and dipped into the 20 ml YPD medium in the erlenmayer flask. Same procedure was done for the second 20 ml erlenmayer flask containing YPD medium. The liquid cultures containing GFP tagged YOR060C strain were placed in the shaker at 28°C and 180 rpm, and kept till exponential phase of growth. The time required for their growth was between 1-2 days overnight. They were then kept in the refrigerator at 4°C until their usage. The grown yeast culture needed to be diluted before using in the experiment. The OD measurements were done by spectrophotometer at fixed wavelength of 600 nm. The 2% glucose containing YPD medium was used as blank and yeast culture was diluted to an OD of 0.5.

For the second set of experiments (Caloric restriction), the pre-culture was grown in 2% glucose containing YPD medium and then in microbioreactor experiments 0.2% glucose containing YPD medium was used. To prepare the YPD medium (0.2% glucose), 0.6 gr glucose was dissolved in 90 ml purified water and sterilized. 6 gr yeast extract and 3 gr peptone were dissolved in 210 ml purified water and sterilized. Two solutions were mixed and used for medium loading step in microbioreactor. For the third and fourth set of experiments, a new GFP YOR060C tagged strain was grown in low auto-fluorescence YNB medium without histidine. To prepare the YNB medium (2% glucose), 20 gr glucose was dissolved in 300 ml purified water and sterilized. 3.5 gr ammonium sulfate, 0.07 gr leucine, 0.014 gr methionine and 0.014 gr uracile were dissolved in 700 ml purified water and sterilized. Two solutions were mixed and used for both yeast culturing and medium loading into the microbioreactor. For the last set of experiments, the YNB medium contained 2% glucose was diluted to 0.2% glucose and used for the experiment. The new strain grown in YNB medium reached the exponential phase faster than the older strain grown in YPD medium. The size of the cells are compared in Figure 3.12. The size of the cells grown in YNB and YPD mediums are 2-2.5 μm and 3-5 μm, respectively.

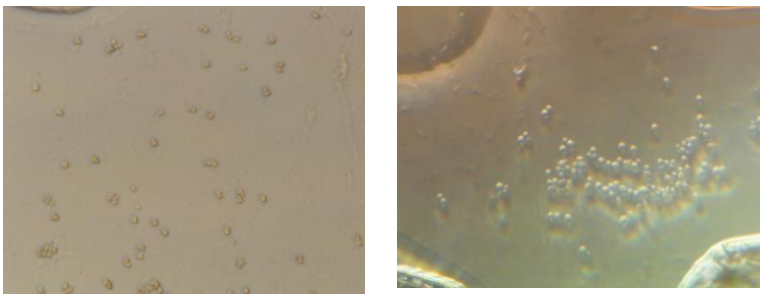

Figure 3.12. The cells grown in YPD vs. YNB medium.

3.3. Image Processing

3.3.1. Brightfield Image Processing

Brightfield images of yeast cells taken during the experiments were analyzed and processed by using Fiji - ImageJ software. The program was started and the image of a chamber was opened. The region of interest (ROI) should be determined at the beginning. For this aim, the interested area was drawn with *Polygon selection* in tool box and *Edit* → *Clear Outside* was used to eliminate the images out of the interested area. Thereafter, the selected area was processed by using Process menu. This menu lists all commands related to image processing, including point operations, filters, and arithmetic operations between multiple images. *Process* → *Smooth* command was used to blur active image by replacing each pixel with the average of its 3x3 neighborhood. *Process* → *Sharpen* tool increased contrast and accentuated detail in the image or selection, but may also accentuate the noise. *Process* → *Filters* → *Variance* sequence was applied for 4.0 pixel radius to highlight the edges in the image by replacing each pixel with the neighborhood variance. *Process* → *Math* → *Subtract* command was used and the value was entered as 25. *Process* → *Enhance Contrast* was used to make images clear by contrasting it with the background. Figure 3.13 shows the image filtering steps of the process.

The images were opened in RGB format which was not suitable for putting threshold. In this case the image was transformed into 8- bit image by *Image* → *Type* → *8-bit* commands. Threshold tool was used to set lower and upper threshold values, segmenting grayscale images into features of interest. *Image* → *Adjust* → *Threshold*, *Otsu Threshold*

with *Red* was selected and *Dark Background* was chosen. There were some noises on images and *Process* → *Filters* → *Median* with 3.0 pixel radius was used to avoid these noises.

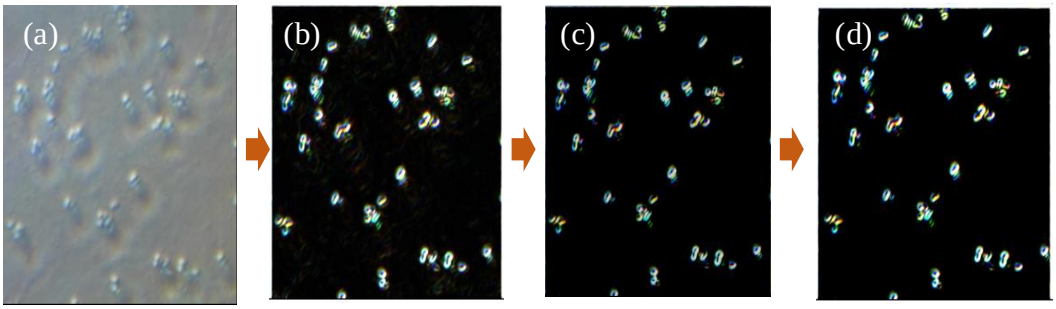

Figure 3.13. Image filtering steps (a) the selected area (b) 2 pixels radius variance (c) Subtract entered as 50 (d) the contrast is enhanced.

The outline of the images were cleared by using the shaped tool in tool box and then *Edit* → *Clear* was chosen. The threshold application steps are shown in Figure 3.14. The last step of the procedure was to analyze and count the cells in this processed area. In this part, measurements were needed to be set by using *Analyze* → *Set Measurements* tool. The area, minimum and maximum gray value, mean gray value and perimeter were chosen. To analyze the number of cells in the ROI, *Analyze* → *Analyze Particles* tool was used, the size was arranged between 30- infinity and it was adjusted to show outline. Display results, clear results, summarize and add to manager options were chosen. If the cells are in cluster form, the results are not reliable and these clusters should be divided into cells. Therefore, *Process* → *Binary* → *Watershed* tool was used to divide cluster cells into separate cells.

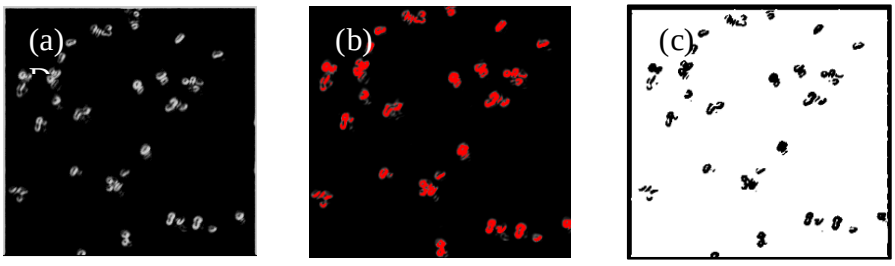

Figure 3.14. Threshold adjusting steps (a) image converted to 8-bit (b) otsu threshold is selected (c) after applying threshold.

3.3.2. Macro for Brightfield Images

The processing steps of brightfield and fluorescence images were automated by writing macro codes. For a brightfield image, firstly the undesirable area of image was cleaned. Then, for each image, the same procedure was followed by writing a macro code as shown in Figure 3.15.

```
run ("Smooth");
run ("Sharpen");
run ("Variance...", "radius=4");
run("Subtract...", "value=25");
run("Enhance Contrast...", "saturated=0.4");
run("8-bit");
setAutoThreshold("Otsu dark");
//run("Threshold...");
//setThreshold(64, 255);
setOption ("BlackBackground", false);
run("Convert to Mask");
run("Set Measurements...", "area mean min perimeter display redirect=None decimal=3");
run("Analyze Particles...", "size=30-Infinity show=[Overlay Outlines] display
```

Figure 3.15. Macro for brightfield images.

3.3.3. Fluorescence Image Processing

Fiji – ImageJ software was used to count the cells and see the cell integrated density, perimeter and area. The image was in RGB format and the channels need to be splitted for fluorescence image. This step, splits an RGB image (or stack) into three 8–bit grayscale images containing the red, green and blue components of the original. To split the channels *Image* → *Colour* → *Split channels* commands were followed. The window names were appeared as ‘red’, ‘green’ and ‘blue’. Since the yeasts used in experiments were tagged by green fluorescence, green channel image window was chosen for further steps. *Process* →

Sharpen tool was selected to increase the contrast and emphasize details in the selected area of the image. To perform grayscale dilation on non-thresholded images, *Process* → *Filters* → *Maximum* was applied and the Maximum was selected, the radius was entered as 2.0 pixels.

To highlight edges in the image by replacing each pixel with the neighborhood variance *Process* → *Filters* → *Variance* commands were followed. After clicking the Variance, radius value was set as 2.0 pixels same as Maximum filter value. Then the Process (active image or selection. Image J uses a Sobel edge detector to do this. The commands in Math submenu added (subtract, multiply, etc.) a constant to each pixel in the active image or selection. To apply this property in image, *Process* → *Math* → *Subtract* steps were followed to subtract a constant from the image. Here, subtract value was set to 50. Image filtering steps is shown in Figure 3.16.

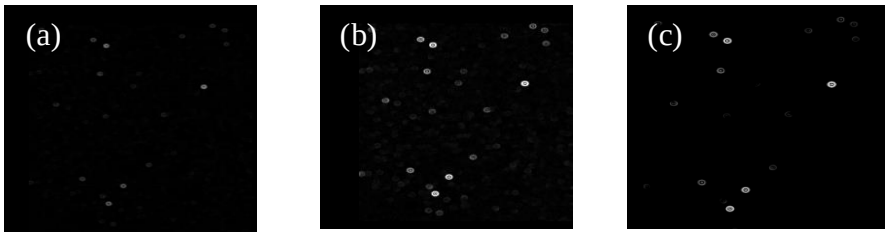

Figure 3.16. Image filtering steps (a) 2 pixels radius variance (b) after find edges command used from process tool bar (c) subtract entered as 50.

Image section was used to apply a threshold and after *Image* → *Adjust* → *Threshold* steps, the threshold type was selected as *Otsu* and color was *Red*. The resulting image appeared after clicking the *Dark Background* button. The thresholding steps are shown in Figure 3.17. As the last step, analyses and measurements were done by *Analyze* tool → *Analyze Particles* tool. The size was selected as 0-Infinity, circularity 0.00-1.00 and Show Overlay outlines was selected in the Show section. Also the Display results, Clear results, Summarize and Add to Manager were selected. *Analyze* → *Set measurements* commands were used to specify the measurements such as area, minimum and maximum gray value, integrated density, mean gray value and perimeter. After Analyze particles was selected, a

summary window appeared which showed the counted cell number, total area, average size, perimeter and integrated density (intensity) values. In the Results section, all properties of the cells were written individually and the specific cell from ROI manager was selected to see its features.

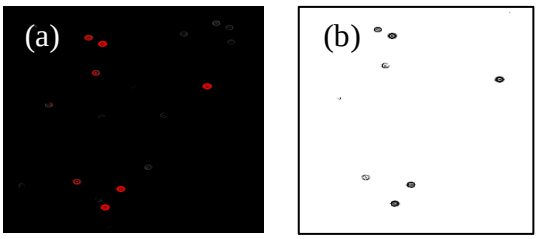

Figure 3.17. Threshold adjusting steps (a) otsu threshold is selected (b) after applying threshold.

3.3.4. Macro for Fluorescence Images

For a fluorescence image, channels were split by using *Image* → *Color* → *Split Channels* tools and then green channel was used for each image. After this step, a macro code was written to follow the same steps for each image as shown in Figure 3.18.

```
run("Sharpen");
run("Maximum...", "radius=2");
run("Variance...", "radius=2");
run("Find Edges");
run("Subtract...", "value=50");
//run("Threshold...");
setAutoThreshold("Otsu dark");
setOption("BlackBackground", false);
run("Convert to Mask");
run("Set Measurements...", "area mean min perimeter integrated display redirect=None decimal=3");
run("Analyze Particles...", "size=100-Infinity show=[Overlay Outlines] display
```

Figure 3.18. Macro for fluorescence images.

3.4. Procedure of CFD Simulation Studies by COMSOL Multiphysics

The designed microfluidic platform was drawn by COMSOL Multiphysics 3.5a software to simulate the computational fluid dynamics (CFD) in the micro bioreactor. For this aim, MEMS Module (Microelectromechanical Systems) was used as working module integrated with 'Incompressible-Navier Stokes' and 'Convection and Diffusion' modules. Velocity and pressure distribution, glucose concentration distribution were determined by these selected modules, respectively. The procedure is as follows;

(i) Start COMSOL Multiphysics and set space dimension to 3D.

(ii) MEMS Module → Microfluidics → Flow with species Transport → Incompressible Navier Stokes → Steady State analysis→ Add.

(iii) MEMS Module → Microfluidics → Flow with species Transport → Convection and Diffusion → Steady State analysis→ Add, click OK to start the program.

(iv) Draw menu → Work-Plane Settings. The xy-plane at z=0 is clicked in the quick work plane.

(v) By using 'Options menu' add the constants of the model, click 'Apply' and 'OK'. The values of the constants such as density, diffusivity, initial concentration and initial velocities for main and side channels were written in constants box as shown in Figure 3.19.

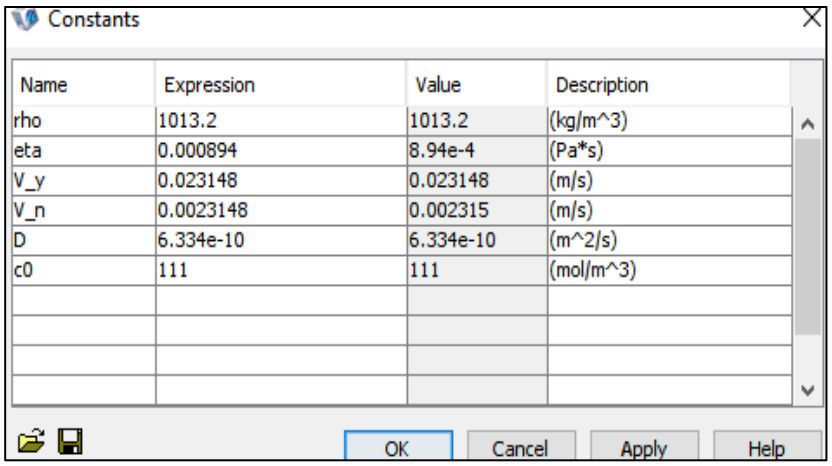

Figure 3.19. The constants of the model.

(vi) Draw the model in 2D and extrude it to 3D by using draw menu and enter the height of the reactor as $4x10^{-6}$ meters (half of the channel height).

(vii) Right click the Navier Stokes mode at left side and enter the 'Subdomain Settings'. Write density and viscosity values as 'rho' and 'eta' by their expressions.

(viii) Enter the 'Boundary Settings' and write down the boundary conditions as shown in Table 3.3.

Table 3.3. Boundary settings of incompressible Navier Stokes mode.

Boundary Definition	**Boundary Type**	**Boundary Condition**	**U_0**
Inlets of main and side channels	Inlet	Velocity	V_n or V_y
Outlets of main and side channels	Outlet	Pressure, no viscous stress	0
Upper and lower sides of the surfaces	Symmetry boundary	-	-
All others	Wall	No slip	

(ix) Right click the 'Convection and Diffusion' mode and enter the 'Subdomain settings'. Select D (isotropic) and write 'D' as defined in constants.

(x) Enter the boundary settings of this mode as given in Table 3.4.

Table 3.4. Boundary settings of convection and diffusion mode.

Boundary Definition	**Boundary Condition**	**Quantity**	**Value/Expression**
Main channel Inlet	Concentration	c_0	c0
Side channels	Concentration	c_0	0
Outlets	Convective flux	-	-
Upper and lower sides of the surfaces	Insulation/Symmetry	-	-
All others	Insulation/Symmetry	-	-

(xi) Use Post processing menu→ Plot parameters to select predefined quantities as velocity or pressure.

(xii) Use Solve menu → Solver manager → Solve for and initially solve for the Navier Stokes mode to see the velocity and pressure profiles.

(xiii) Select 'Initial value' tab and click 'Initial value expression' and 'Use setting from initial value frame' and click 'Solve'.

(xiv) To see the concentration profile, change the selected quantity to concentration in post processing menu.

(xv) Go to 'Solver manager' and solve for both 'Navier Stokes mode' and 'Convection and Diffusion mode'.

(xvi) Select 'Initial value' tab and click now 'Initial value' and 'Current Solution' and click 'Solve' to see the concentration profile in the reactor.

Multiple inlet velocities were tested to optimize the flow behavior in side channels and to trap the cells in c-shaped regions efficiently.

3.5. Simulation Studies by LT-Spice

The aim is to calculate the flow in channels as resistances in order to see how the design works and how the flow is distributed throughout the channels. To achieve this aim, the hydraulic resistances for each channel (flow) portion were calculated. There are several factors that affect fluid resistance such as area and length of the pipe and type of fluid flowing (μ). To validate the design at each point, the flow was cut at each intersection point and nodes were defined on these cut points. Hydraulic resistances between each node were calculated. These nodes are determined as shown in Figure 3.20. The hydraulic resistances were calculated using the hydraulic resistance formula given for a rectangular pipe.

In equation 3.1, η (N.s/m^2) is dynamic viscosity of the fluid, L (m) is length, w (m) is width and h is the height.

$$R_h = \frac{12\eta L}{wh^3(1 - 0.630h/w)} \tag{3.1}$$

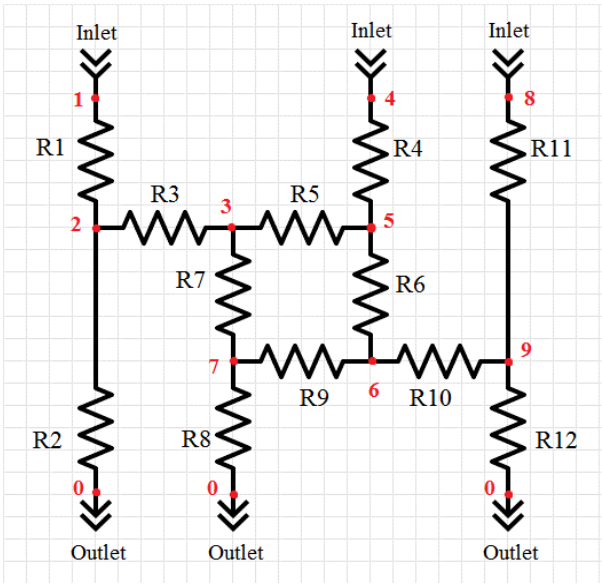

Figure 3.20. Resistances and nodes of the first chamber.

The resistance values calculated for each portion of the channel are given in Table 3.5.

Table 3.5. Resistance values of each portion.

	R1=R12	**R2=R11**	**R3=R10**	**R4=R8**	**R5=R9**	**R6=R7**
Length (m)	0.00018	0.00028	0.00013	0.00007	0.00018	0.00025
Width (m)	0.00009	0.00009	0.00009	0.00009	0.00005	0.00005
Height (m)	0.000008	0.000008	0.000008	0.000008	0.000008	0.000008
Viscosity (N.s/m2)	0.000894	0.000894	0.000894	0.000894	0.000894	0.000894
Rh (Pa.s/m3)	4.44E+13	6.91E+13	3.21E+13	1.73E+13	8.39E+13	1.17E+14

The calculated resistance values were used to determine the flow direction and proportion from inlet to outlet by using LT-Spice program. The calculated values were entered to program as shown in Figure 3.21. As it can be seen from Figure 3.20, starting from the second line in the workspace, resistance name, inlet point, outlet point and calculated resistance values were written one by one for each hydraulic resistance. Thereafter, the flow values (I1, I2, I3) for each of the three inlets were written, and to end

up the code –op and –probe commands were used. When the file was run, another window appeared on the screen showing the current values (I(Rh)) for each resistance as displayed in Figure 3.20.

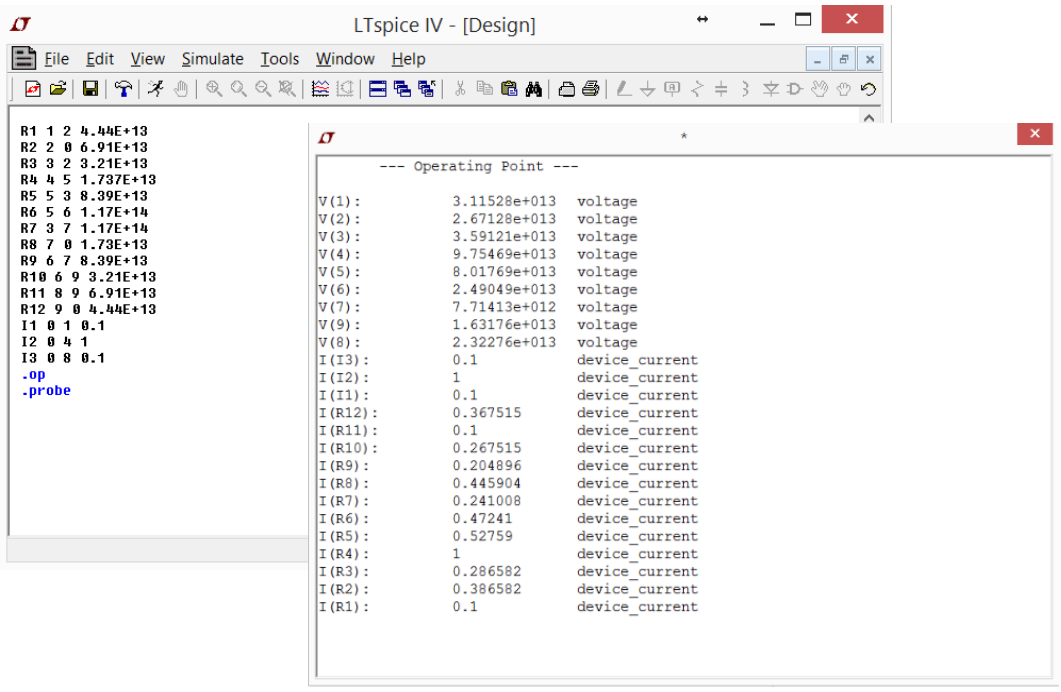

Figure 3.21. Workspace and operating point window of LT-Spice.

4. RESULTS AND DISCUSSION

One aim of this thesis was to improve the created design by Gençtürk E. (2015) and fabricate the microfluidic device by using different polymers as PMMA, COP and PEN. These microfluidic devices were used to visualize the budding yeast and investigate the unknown function of SLD7 protein by using this platform.

4.1. Design of the Microfluidic Device

The developed microfluidic system was shown in Figure 4.1. In this system, 3 inlets were used for cell and nutrient loading and one outlet was used to remove the waste, to avoid contamination in each symmetric side. The device was used to trap the yeast cells in the c-shaped regions and remove the excess flow by using the side channels. The device has 8 µm height to achieve the monolayer growth of the cells and all channels have 90 µm width. The chambers have a diameter of 320 µm and the c-shaped region's diameter is 120 µm. The microfluidic devices were made from PMMA, COP and PEN polymers bu using different bonding parameters and techniques.

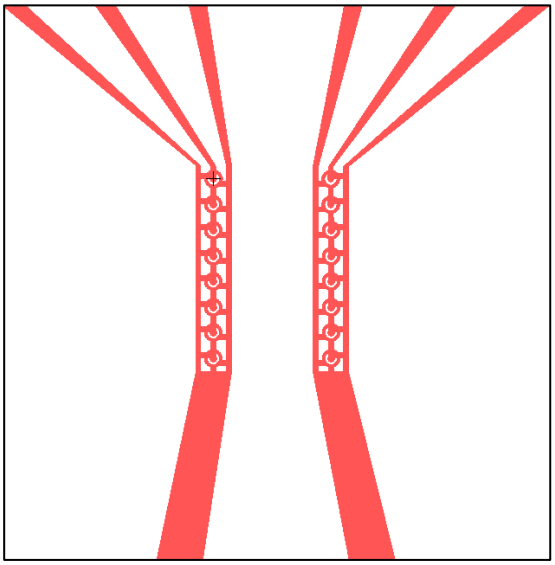

Figure 4.1. The developed microfluidic device.

4.2. Simulation Studies by COMSOL Multiphysics

The microfluidic device was modeled by COMSOL Multiphysics 3.5a software and various fluid dynamic computational fluid dynamics (CFD) simulations were used to optimize the fluid flow within the chambers and the side channels. Microelectromechanical Systems (MEMS) module was used with 'Incompressible Navier Stokes' and 'Convection and Diffusion' modes. Incompressible Navier Stokes mode was employed to identify the velocity distribution and pressure drop inside the chambers, and Convection and Diffusion mode was performed to elucidate the glucose concentration distribution within the device. The fluid density was assumed to be constant during the process. Navier Stokes equation (equation 4.1) and the equation of continuity (equation 4.2) were applied to run the simulations using the conservation of mass assumption. The Navier Stokes equation governs the motion of fluids.

$$\rho\left(\frac{\partial \mathrm{u}}{\partial \mathrm{t}} + u.\nabla u\right) = -\nabla P + \nabla.(\eta(\nabla \mathrm{u} + (\nabla \mathrm{u})^{\mathrm{T}}) + F \tag{4.1}$$

$$\nabla.u = 0 \tag{4.2}$$

In equation 4.1, u is the fluid velocity (m/s), P is the pressure (Pa), η is the dynamic viscosity (Pa.s) and ρ is the density (kg/m^3), and the gradient terms correspond to different forces. $\rho\left(\frac{\partial u}{\partial t} + u.\nabla u\right)$ corresponds to the inertial forces, $-\nabla P$ is the pressure force, $\nabla.(\mu\,(\nabla u + (\nabla u)^T)$ is the viscous force and F shows the effect of external forces applied to the fluid, but it was taken as zero during the simulations.

"Convection and diffusion" mode was selected for solving the equation 4.3 and hence for understanding the effect of both of them on mass transfer rate of species. Mass transport equation (4.3) was used with selected boundary conditions. For the walls and outlets, boundaries were set to no-slip (u=0) and convective flux ($\nabla.(-D\nabla c) = 0$) condition, respectively. At the channel outlets, the pressures were set to zero.

$$\nabla.(-D\nabla c + cu) = 0 \tag{4.3}$$

D represents the diffusion coefficient (m^2/s) and c is the concentration (mol/m^3). In the simulations, the inlet concentration value was set to zero in two side channels and an inlet glucose concentration of 2% of the weight (20 g/L, 111 $gmol/m^3$) was set at the middle channel. The density, dynamic viscosity and diffusion constant between glucose and water values were calculated according to the inlet glucose concentration and they were found as 1013.2 kg/m^3, 0.000894 Pa.s and 6.334×10^{-10} m^2/s respectively. Calculation of parameters is shown in Appendix A. The cell and nutrient loadings were simulated in the models and optimum values of velocity, pressure and concentration were determined.

4.2.1. Determination of Optimum Inlet Flowrates for Channels

The aim of this simulation was to trap the yeast cells in all c-shaped regions efficiently. In order to achieve this aim, several inlet flow rates were tested and the flow profile inside the device was analyzed. Table 4.1 shows the summary of flow profiles which were tested to identify the optimum velocity values for the middle and the side channels.

Table 4.1. Summary of inlet flow rates and velocities in the simulated models.

Model	Flow rate in the middle channel (μL/min)	Flow rate in side channels (μL/min)	Chamber 8 velocity at the middle of the chamber (m/s)	Flow in C-shaped region
1	1	1	1.91×10^{-3}	Rapid
2	0.1	0.1	1.91×10^{-4}	Rapid
3	0.01	0.1	1.33×10^{-4}	Inefficient
4	0.01	0.001	7.6×10^{-6}	Inefficient
5	0.1	0.01	7.6×10^{-5}	Efficient
6	1	0.1	7.6×10^{-4}	Efficient

In the first model, same inlet velocity of 1 µL/min was used for all the three inlets. The general velocity field, first and last chambers' velocity distribution and the velocities inside the c-shaped regions of the chambers are shown in Figures 4.2, 4.3 and 4.4, respectively.

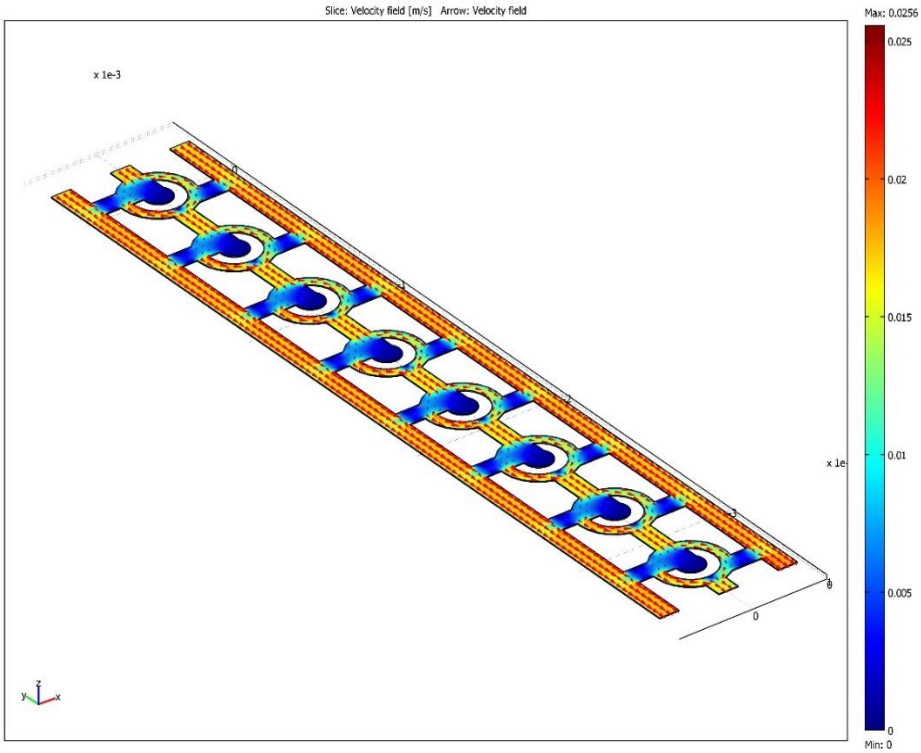

Figure 4.2. Velocity field of Model 1.

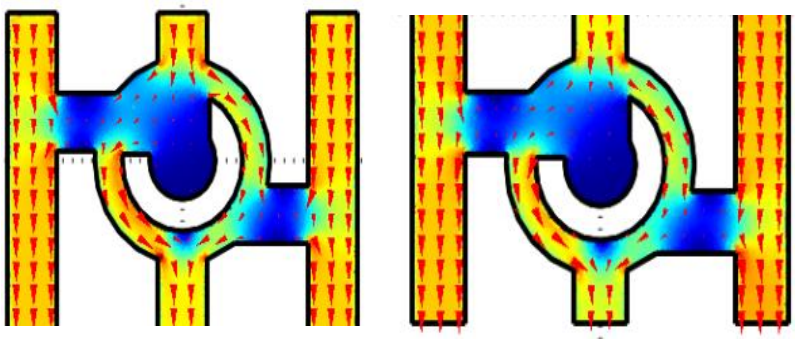

Figure 4.3. Velocity field of the first and the last chambers for model 1.

In the light of the simulation using Model 1, the colors inside the channels (orange color) showed that the flow in two side channels were too rapid. The rapid flow inside the channels and around the perimeter of the c-shape can cause the cells to be flushed away from the trapping region which is not a preferred situation. The coordinates of the first chamber is shown in Figure 4.4a for a clear explanation of the dimensions. Figure 4.4b shows that the speed at c-shaped region (x=0) was around $2x10^{-3}$ m/s and this speed may cause the cells not to enter the trapping region efficiently.

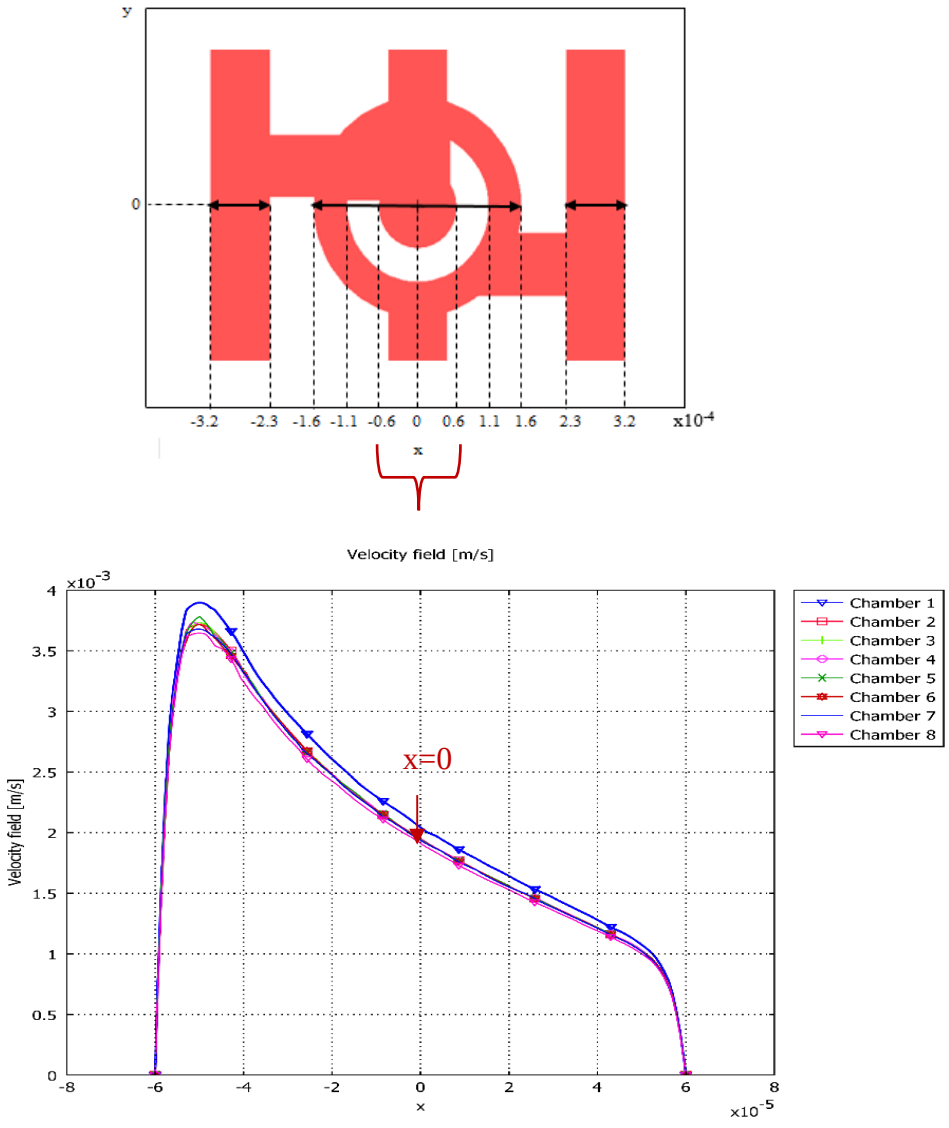

Figure 4.4. The velocities inside the c-shaped regions of the chambers for model 1.

The existence of small arrows close to the c-shaped region indicated that there was still minor flow in this region ($3x10^{-3}$ m/s) and that flow may cause already trapped cells to be flushed away. The right and left bridge channels (channels which connect the chambers and side channels) are blue colored indicating that they did not carry the excess flow to the side channels, despite their mission. Also, the number of arrows were less (seen rarely) in these bridge regions supporting this comment. For this reason, inlet speed of 1 µL/min was not efficient for nutrient and cell loading.

In Model 2, inlet flow rates were decreased by 10 fold and same inlet velocities (0.1 µL/min) were used for all the inlets. The velocity field of Model 2 is shown in Figure 4.5 and the profile is nearly same as Model 1. It was again not a suitable model because of the risk of flushing out of the cells from c-shaped trapping region without immobilization. The velocities inside the c-shaped regions are shown in Figure 4.6 and Figure 4.7. The speed at the center of the c-shaped region was around $2x10^{-4}$ m/s in all the chambers and these speed values were still too high for cell trapping.

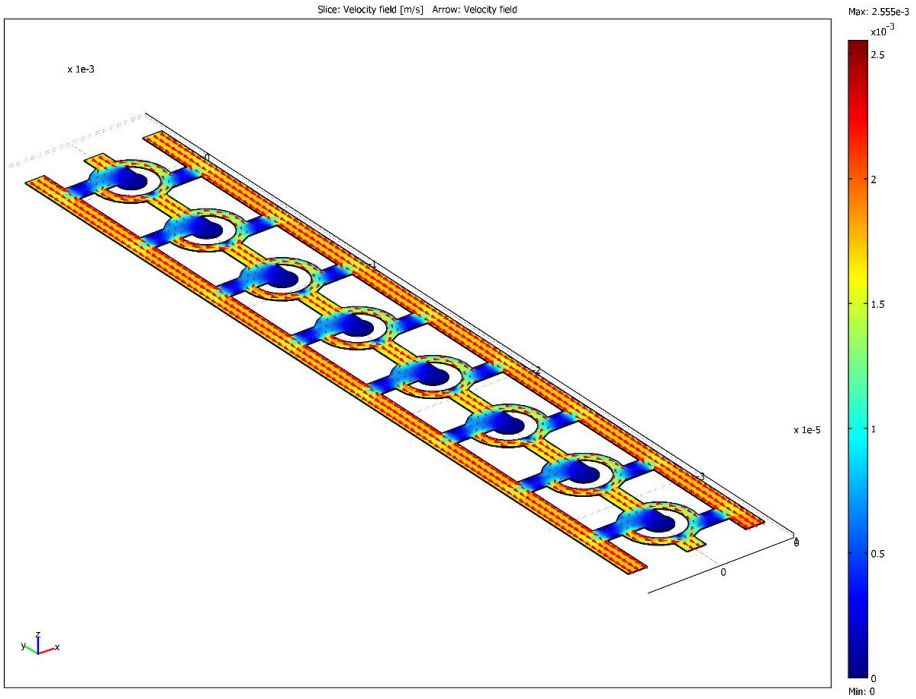

Figure 4.5. Velocity field of model 2.

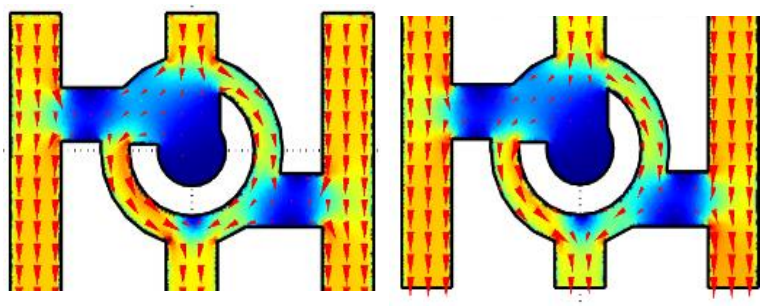

Figure 4.6. Velocity field of the first and the last chambers for model 2.

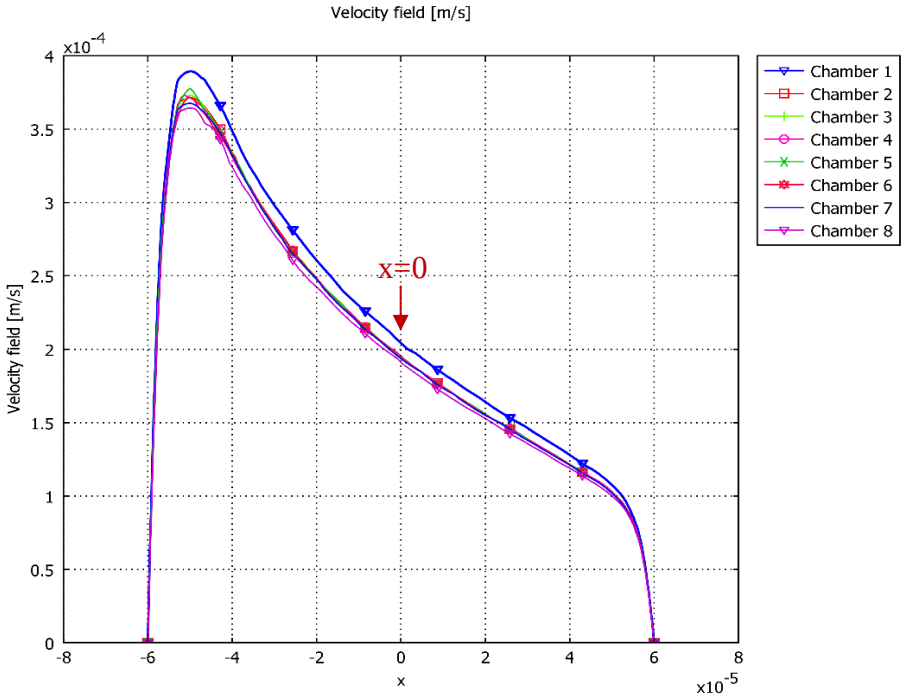

Figure 4.7. The velocities inside the c-shaped regions of the chambers for model 2.

In order to see the effect of higher speed values of side channels than the middle channel, 10 fold higher velocities than the main channel were used at the side channels in Model 3. The inlet velocities are 0.01 µL/min and 0.1 µL/min for middle and side channels, respectively. The velocity field is shown in Figure 4.8. The flow distribution in the microbioreactor showed that the speeds at the side channel inlets started to decrease at the inlet of the first chamber and remained constant until it reached the last chamber. The

bridge channels between side channels and chamber regions did not work effectively and the flow around the external perimeter of the c-shaped region was too rapid as shown in Figure 4.9. This rapid flow might prevent the trapping of cells in determined region. Figure 4.10 shows the velocity profiles, in all the chambers, including c-shaped regions. In the first chamber, the velocity was around zero and this made the first chamber useless. There was no flow entering into this chamber. The other seven chambers' speeds are around 1.33×10^{-4} m/s as shown in Figure 4.10. This profile was more preferable than the first two models' profiles, but still the flow rates in last seven chambers were too high and there was a risk of flushing out. Therefore, this model was also not convenient for cell trapping.

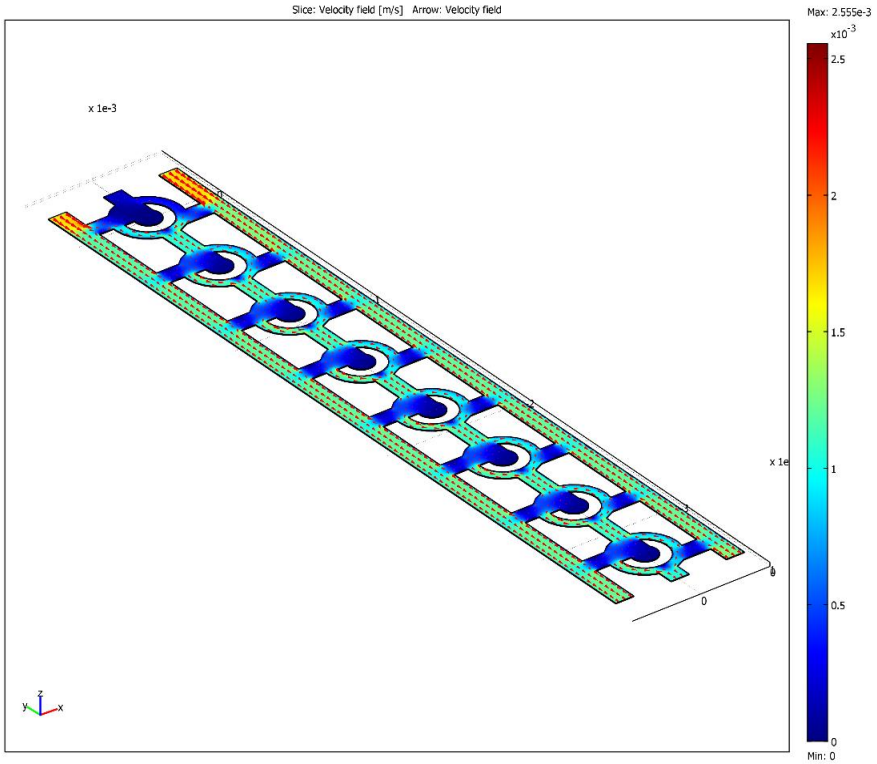

Figure 4.8. Velocity field of model 3.

In order to direct the flow into the c-shaped regions, the inlet velocity at the middle channel was increased to a level which is greater than the side channels' inlet velocity values. In Model 4, the flowrates at middle channels and side channel were determined as 0.01 µL/min and 0.001 µL/min, respectively. Figure 4.11 and 4.12 show the flow profiles in the device. In this model, flow distribution from the entrance to the end of the device is

more uniform than those obtained by the first three models. The excess flow within the chambers was carried efficiently by bridge channels but this carriage was decreased from the first to the last channel. Figure 4.12 also shows the flow directions by arrows at the first and last chambers (Model 4) and no arrows are seen in the last bridge channels. Figure 4.13 shows the velocities inside the c-shaped regions of the chambers. The speed at the center of the first chamber (x=0) was around 2.25×10^{-5} and higher than the speeds obtained in other seven chambers (at x=0 around 0.76×10^{-5} m/s). This model was more reliable than the first three models for cell loading and flushing out the untrapped cells by side channels but still not the optimized one.

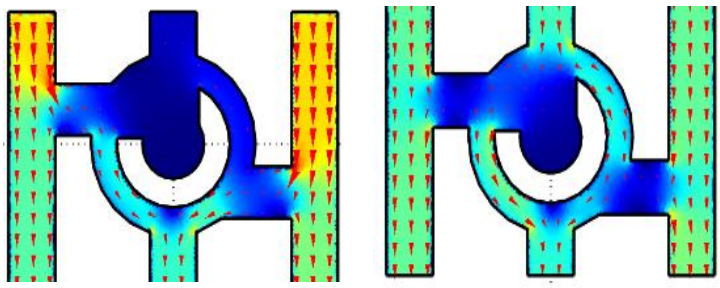

Figure 4.9. Velocity field of the first and the last chambers for model 3.

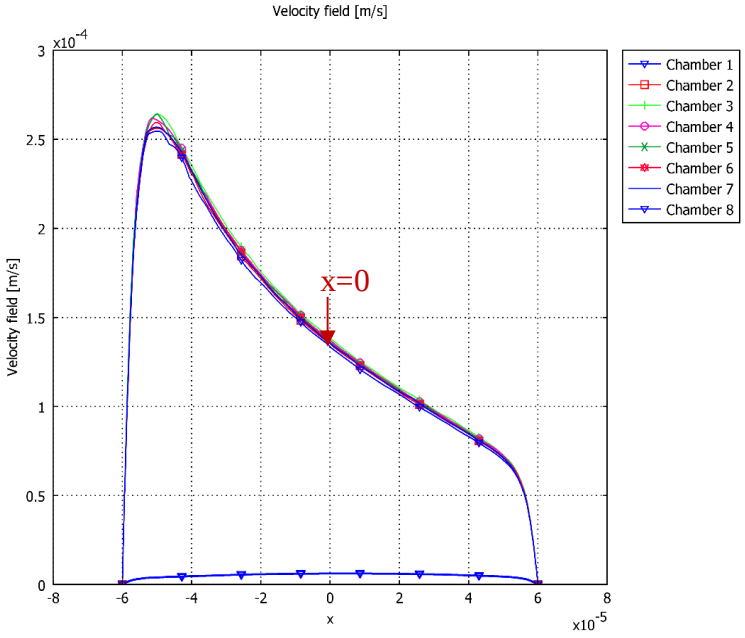

Figure 4.10. The velocities inside the c-shaped regions of the chambers for model 3.

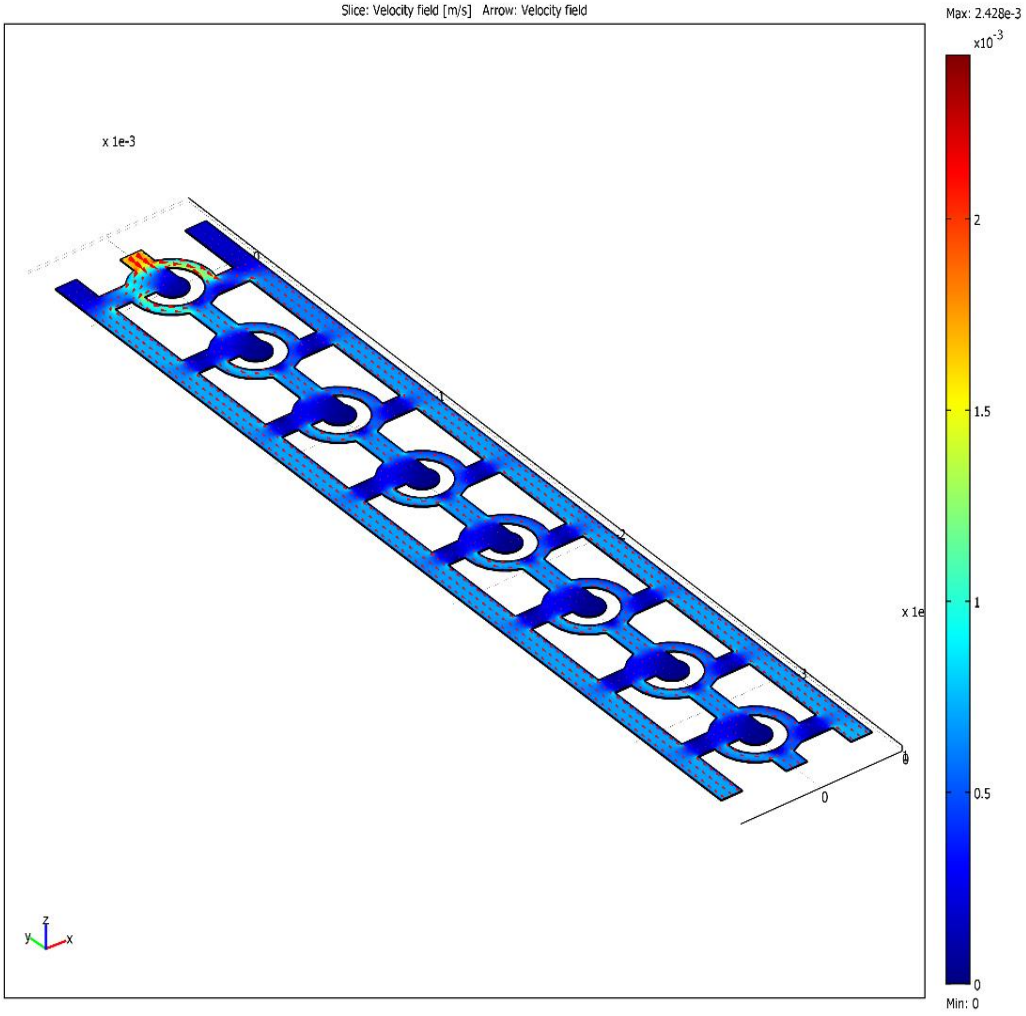

Figure 4.11. Velocity field of model 4.

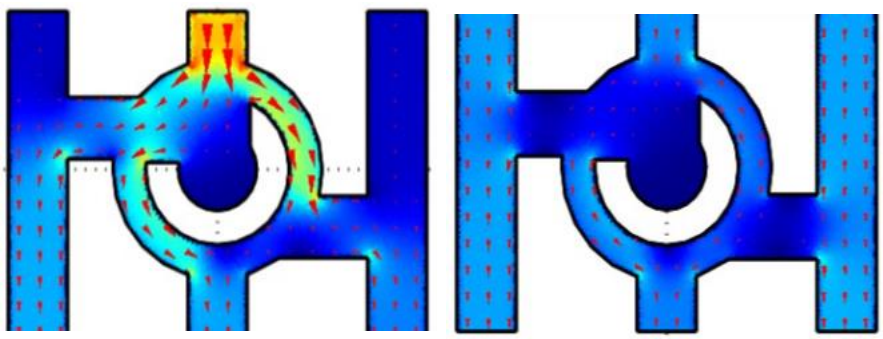

Figure 4.12. Velocity field of the first and the last chambers for model 4.

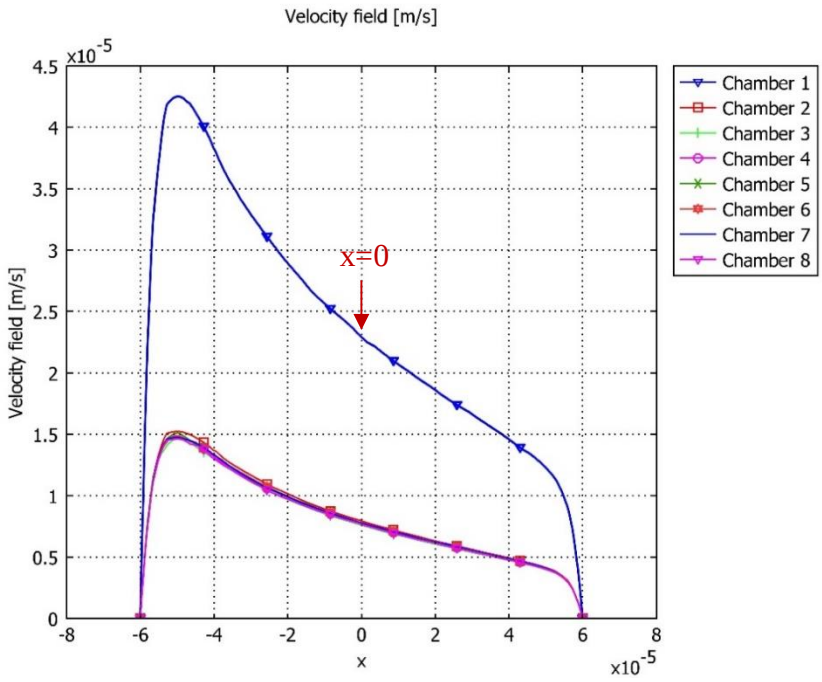

Figure 4.13. The velocities inside the c-shaped regions of the chambers for model 4.

In Model 5, the side and channel inlet values were increased by 10 fold for a faster loading process, i.e. the velocity values for middle and side channels were determined as 0.1 µL/min and 0.01 µL/min, respectively. The general velocity field profiles were looked very similar in Figures 4.11 and 4.14. From these similar profiles, the more convenient one for efficient cell trapping was determined by analyzing the velocity values at the center of the chambers and concentration profiles within the devices and velocity fields in all chambers. For the most efficient trapping, low speed values at the center of the chambers were necessary to immobilize the cells in the determined trapping region. In this model, the speed value at the center of the first chamber was around 2.3×10^{-4} m/s and the speed values at the center of other chambers were 0.76×10^{-4} m/s as shown in Figure 4.16. The velocity distribution profile in Model 5 was selected as the most efficient flow profile for cell trapping. The speed differentiation between the trapping region (c-shaped region) and around its external perimeter was not high (Figure 4.15). Additionally, the velocity values at the center of all the chambers were very small. The velocity field arrows also showed that fluid did not enter the trapping region rapidly but the excess flow was efficiently carried to the side channels by the bridge channels throughout the device.

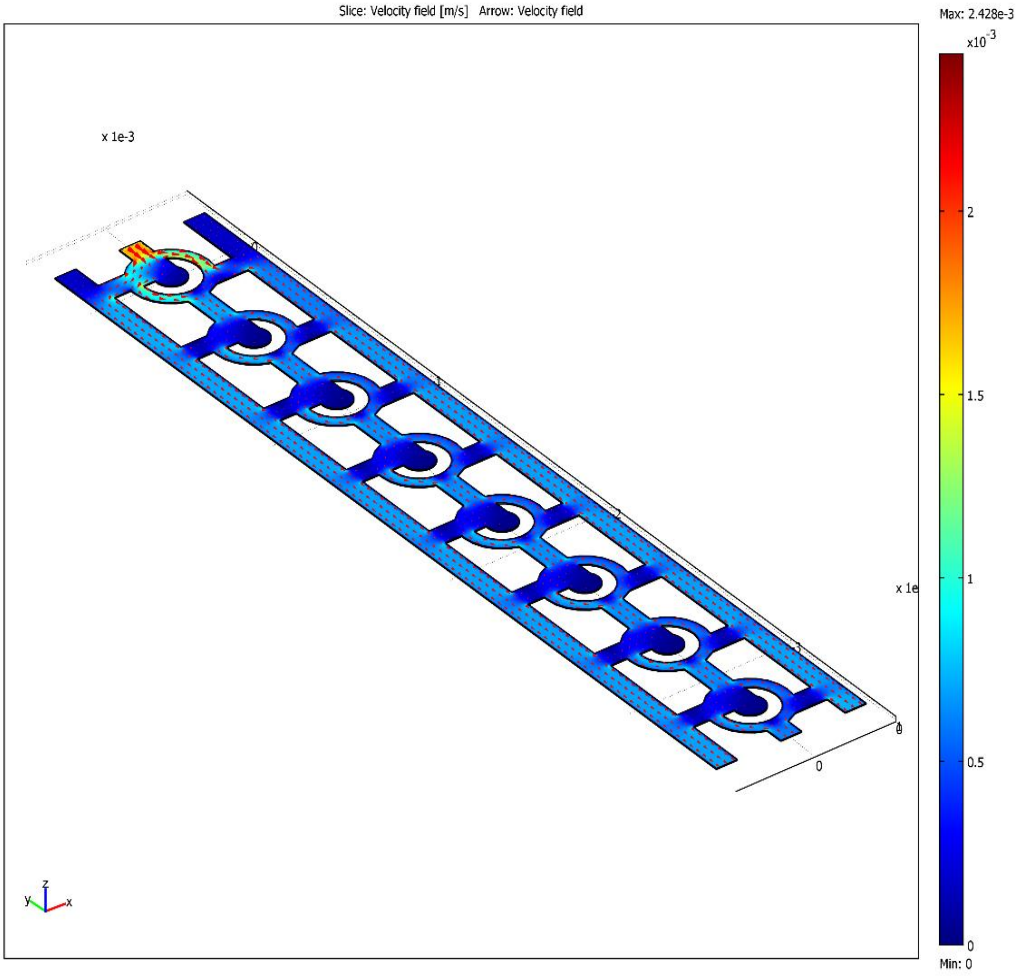

Figure 4.14. Velocity field of model 5.

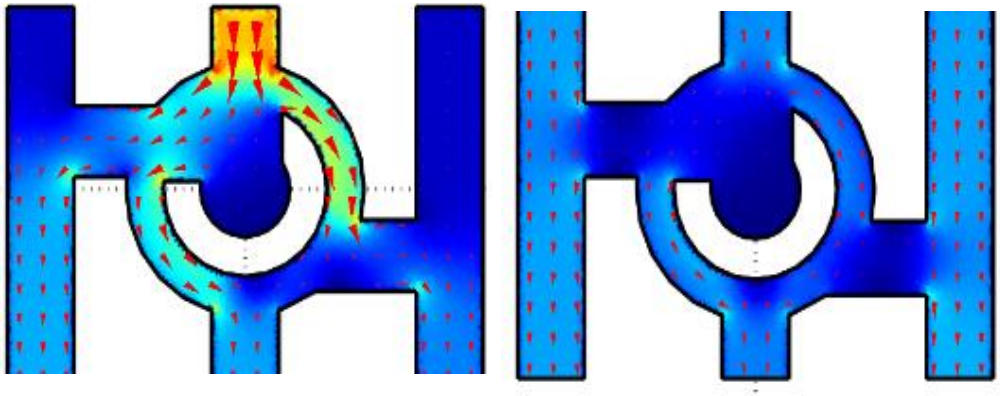

Figure 4.15. Velocity field of the first and the last chambers for model 5.

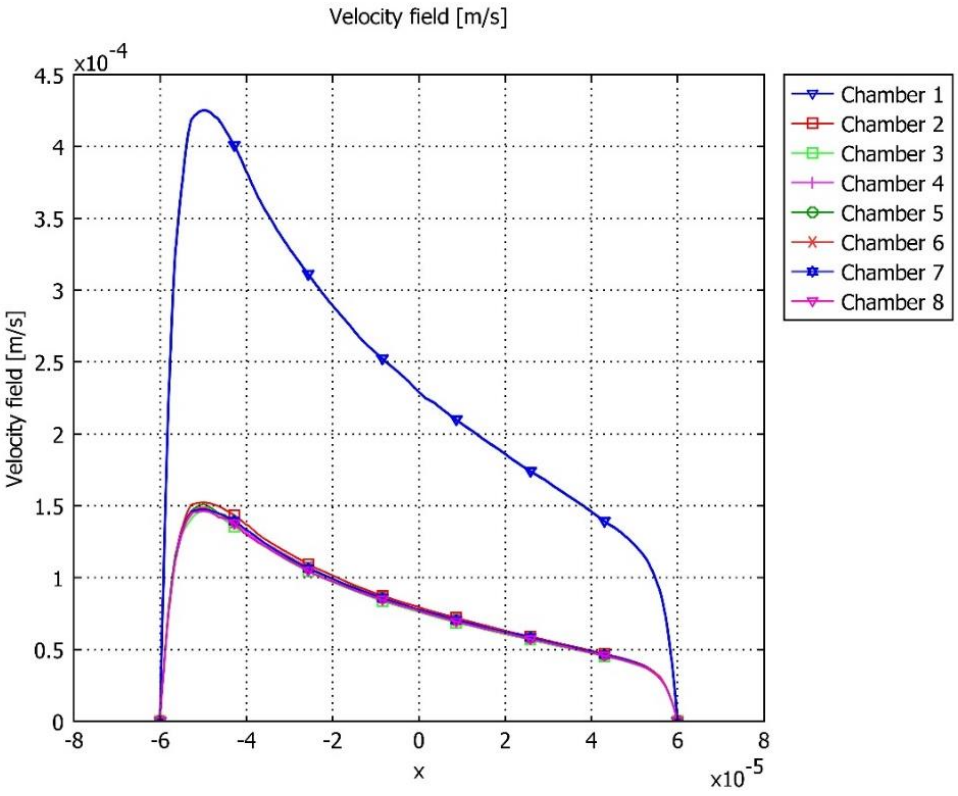

Figure 4.16. The velocities inside the c-shaped regions of the chambers for model 5.

In Model 6, the velocity values in Model 5 was increased by 10 fold. The inlet velocities for side and middle channels were selected as 0.1 µL/min and 1 µL/min, respectively. The flow profile and first and last chambers' velocity fields are shown in Figure 4.17 and Figure 4.18. The velocity distributions in Model 4, 5 and 6 are very similar according to their velocity field profiles and arrows. The speed values in the c-shaped regions are also small enough in Model 6.

The velocity values at the center of all chambers are shown in Figure 4.19. The speed value is around 2.3×10^{-3} m/s for the first chamber and it decreases to 7.6×10^{-4} m/s for last seven chambers. The speeds inside the c-shaped regions and around its perimeter were very similar and velocity values at the center of the chambers were also low. In the light of these velocity profiles, the last three models were found to be convenient for the nutrient

and cell loading processes. By considering the syringe pumps properties, Model 6 was selected for the operation.

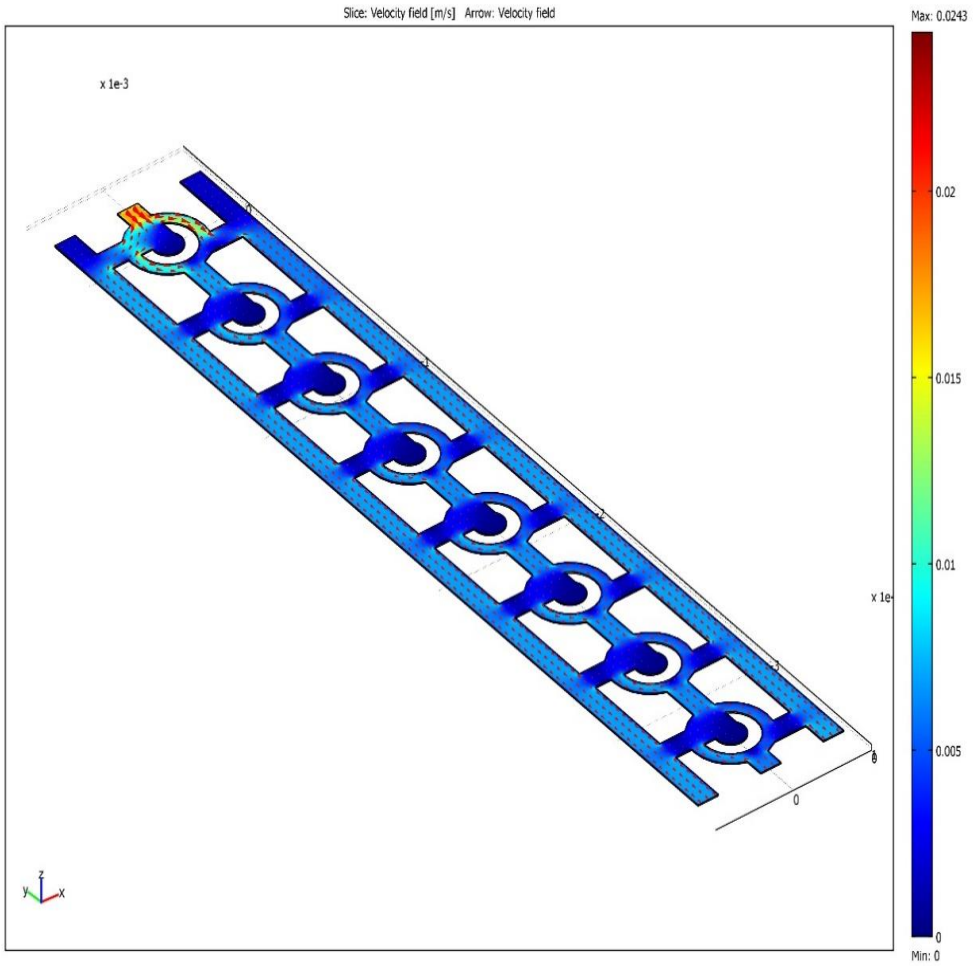

Figure 4.17. Velocity field of model 6.

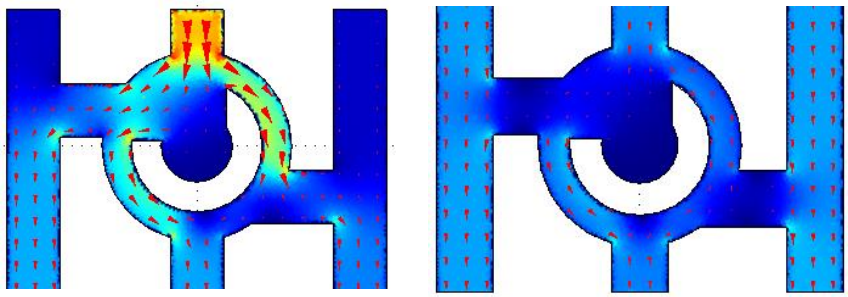

Figure 4.18. Velocity field of the first and the last chambers for model 6.

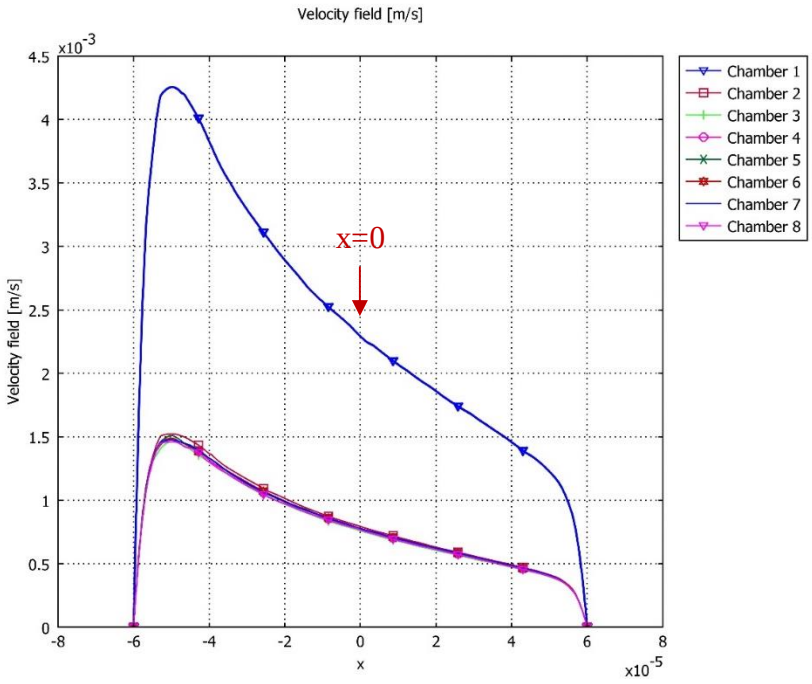

Figure 4.19. The velocities inside the c-shaped regions of the chambers for model 6.

4.2.2. Radial Velocity Distribution in the Microbioreactor

Some other analysis were next done to ensure that the optimized inlet velocity values are appropriate for cell loading. The inlets of the side channels were cut into 5 sections to see the velocity distribution through the inlets. The velocity profiles of the left and right entrances of all the chambers are shown in Figure 4.20. For the left inlet of the microbioreactor (Section 1 and 2), the velocity profile of the first chamber was different than those of other seven chambers. The velocity increased very rapidly at the beginning and after a short time period it increased exponentially until it reached the entrance of the chamber. When the fluid entered into the trapping region, the velocity started to decrease linearly (Section 3). This showed that the velocity inside the trapping region was slow enough to trap the cells and keep the trapped cells in this region.

For other seven chambers, the velocity first increased rapidly and then after a short time period, it started to decrease exponentially (Section 1) till the starting point of the bridge channel (the channel between the side channel and the chamber). As shown in

Figure 4.20, in Section 2, the velocity increased slightly. This velocity was small enough to carry the fluid efficiently to the trapping region, i.e. the fluid was coming to the trapping region as expected. In the third section, the velocity (speed) started to decrease again to achieve an efficient trapping in this region. At the right entrance of the first chamber, the velocity profile was again different than those obtained in the other seven chambers. First, the velocity increased very rapidly for a short time, followed by a slight increase until reaching the entrance of the chamber (Section 4). In Section 5, the velocity started to decrease slowly again. For the other seven chambers, the velocity profile significantly changed. In the side channels (Section 4), the velocity values increased very rapidly in a short time and then started to decrease exponentially until the entrance of the chamber. In Section 5, the fluid coming from the side channels met with the fluid coming from the main channel and velocity values increased as expected.

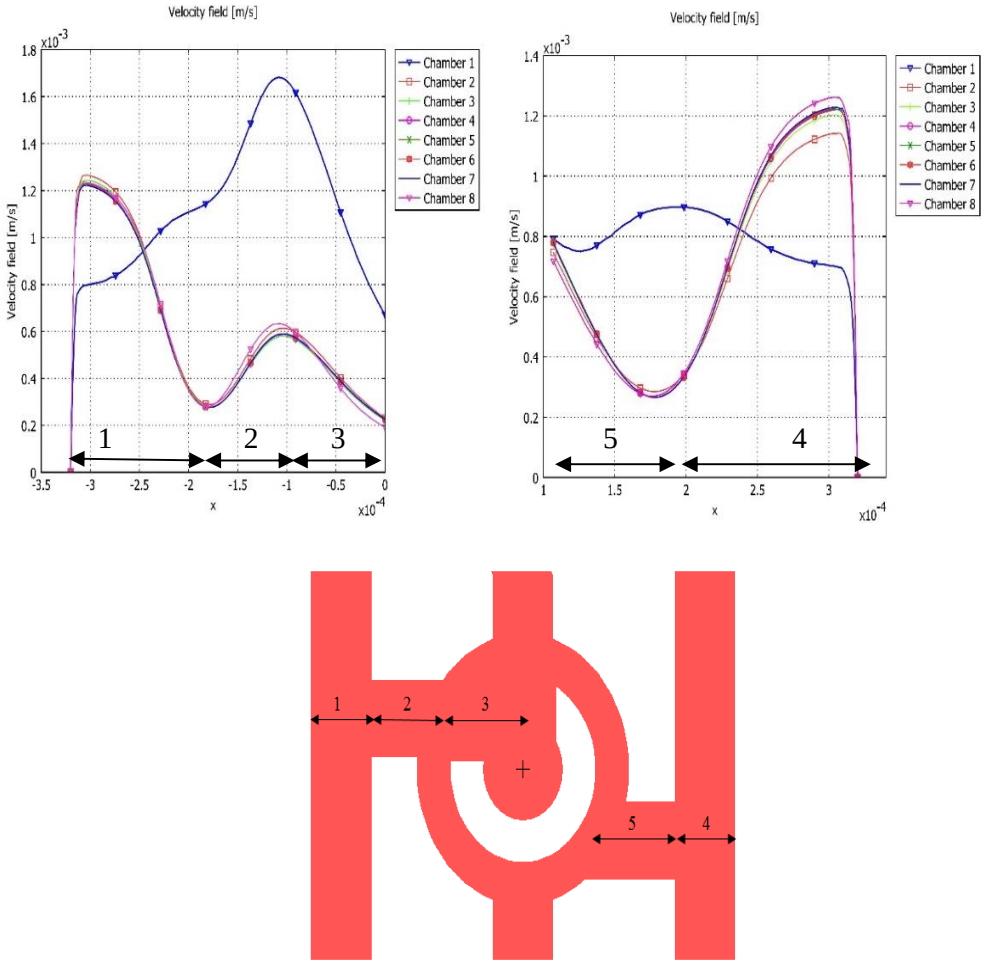

Figure 4.20. The velocity profiles of left and right entrances of all chambers.

4.2.3. Pressure Distribution in the Microbioreactor

The pressure profile was created via using the optimized inlet velocity values (1 µL/min middle inlet, 0.1 µL/min side inlets) as shown in Figure 4.21. At the 'Incompressible Navier Stokes' operation mode, the boundary conditions for the outlets of the main and side channels were selected as 'Pressure, no viscous stress' and the outlet pressure value was set to zero and the result of the simulation verified this for the flow rates of 0.1 µL/min at the entrance of the middle channel and 0.01 µL/min at the entrance of side channels. The pressure drop was found to be around 550-600 pascal, which is a suitable value for a microfluidic system.

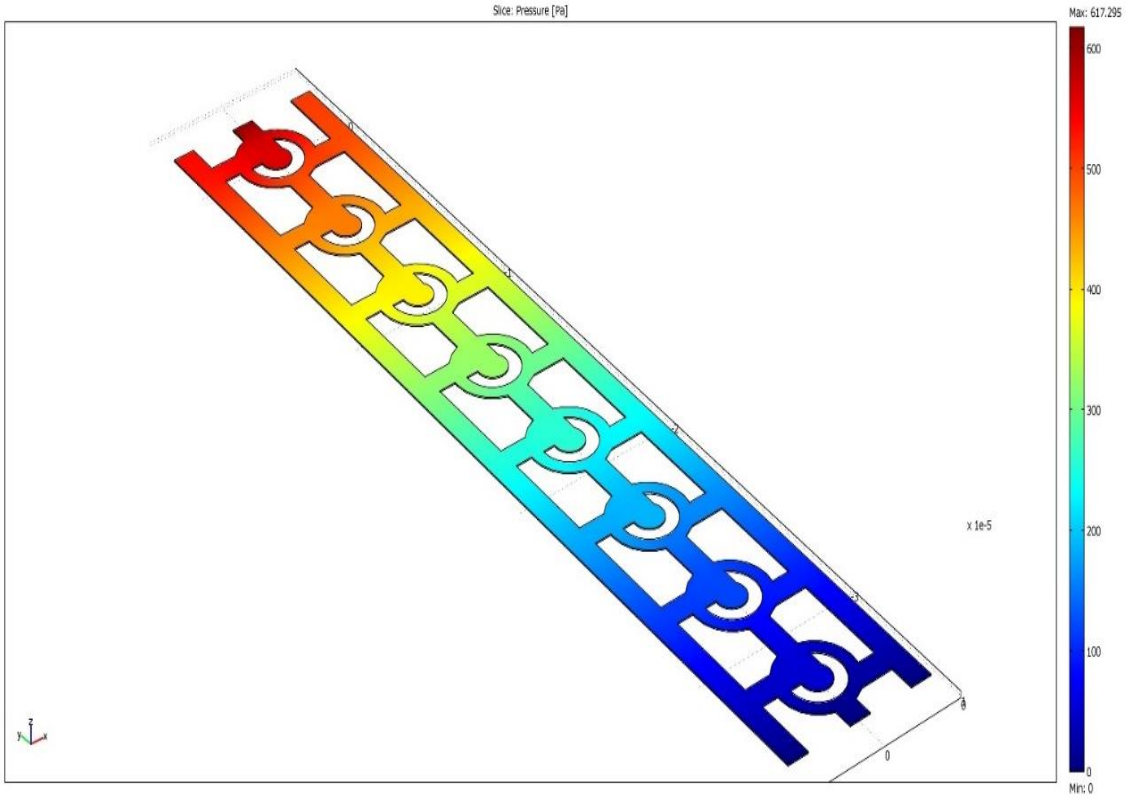

Figure 4.21. The pressure profile of the microfluidic device.

Figure 4.22 shows the pressure drop in the microbioreactor in the vertical direction. The pressure drops occurred in middle and side channels were around 600 and 500-550 Pa, respectively. At the outlets of the channels, the pressure values were almost zero.

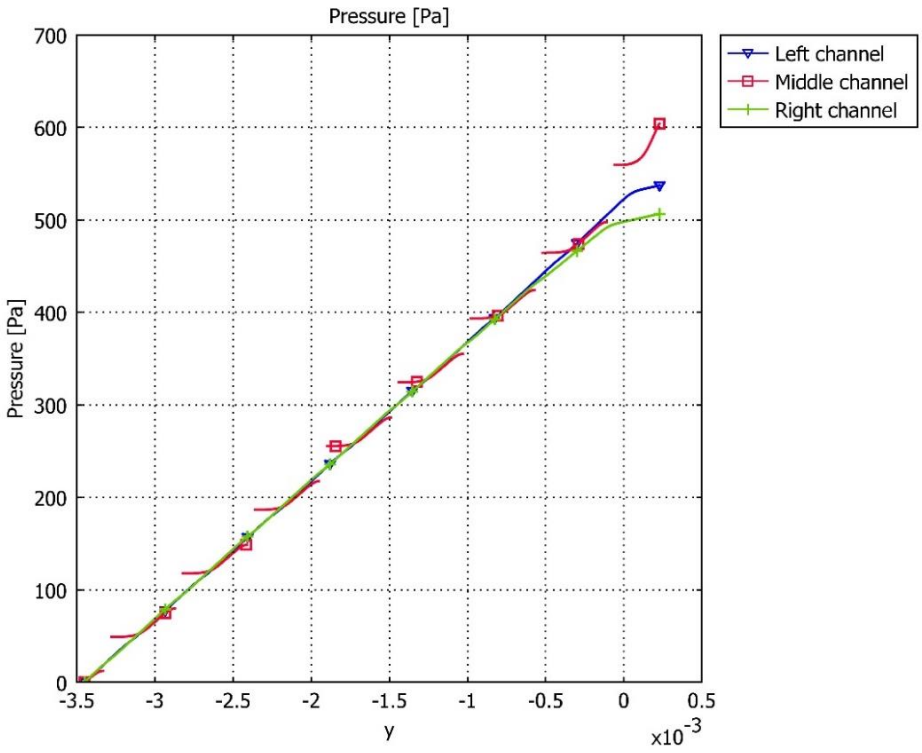

Figure 4.22. Pressure drop throughout the microfluidic device (y-vertical distance) (y=0, inlet).

4.2.4. Nutrient Distribution in the Microbioreactor

The concentration profile of the nutrient (glucose) was simulated in addition to the velocity and pressure profiles. In the simulation, the nutrient was fed through the middle channel only, however it will be fed from all the inlets in experiments. This simulation was performed to see the concentration distribution of glucose along the device. For this aim, 2% by weight concentrated glucose was fed through at 0.1 µL/min inlet flow rate through the middle channel. The side channels' flow rate was 0.01 µL/min and concentration value was zero. The concentration distribution of glucose in the microbioreactor is shown in Figure 4.23. The uniform red color in all the chambers showed that the glucose concentrations in all the trapping regions of the chambers were same. In fact, all c-shaped trapping regions' immobilization behavior need to be same and concentration profile in all these areas need to be uniform to achieve the best nutrient distribution efficiency. Figure 4.23 shows that the concentration distribution in all the trapping regions were almost the

same (shown with red color). Figure 4.24 shows the concentration profiles in both vertical and horizontal directions. In the vertical direction, the concentration values in first six chambers were almost the same and it was 111 mol/m^3, which was entered as the initial concentration value of the middle inlet in simulations. In the last three chambers, the value was decreased to 108.46 mol/m^3 until it reached the last chamber. The decreased values showed that there was a concentration lost of 2.2% of the initial value. This small decelaration was not an effective one, so all concentrations in all chambers were assumed to be uniform in horizontal and vertical directions. The concentration analysis for both vertical and horizontal directions were depicted in Figure 4.24. Additionally, the analyses of concentration profiles were done for the left and right entrances of all the chambers.

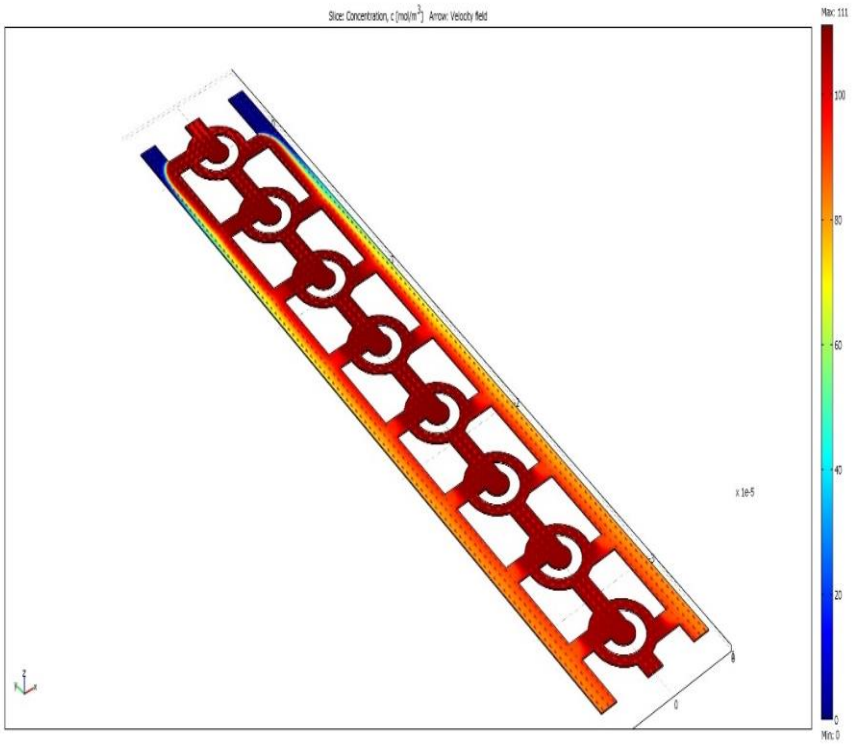

Figure 4.23. The concentration profile of the microfluidic device.

Figure 4.25 shows that for both sides, the concentration values in side channels were small and started to increase through the chambers and remained constant in the trapping regions of each chamber. At the entrance of side channels, the nutrient concentration values

were set to zero. After passing through the second chamber, some mixing occurred and concentration values in the side channels were increased to some extent.

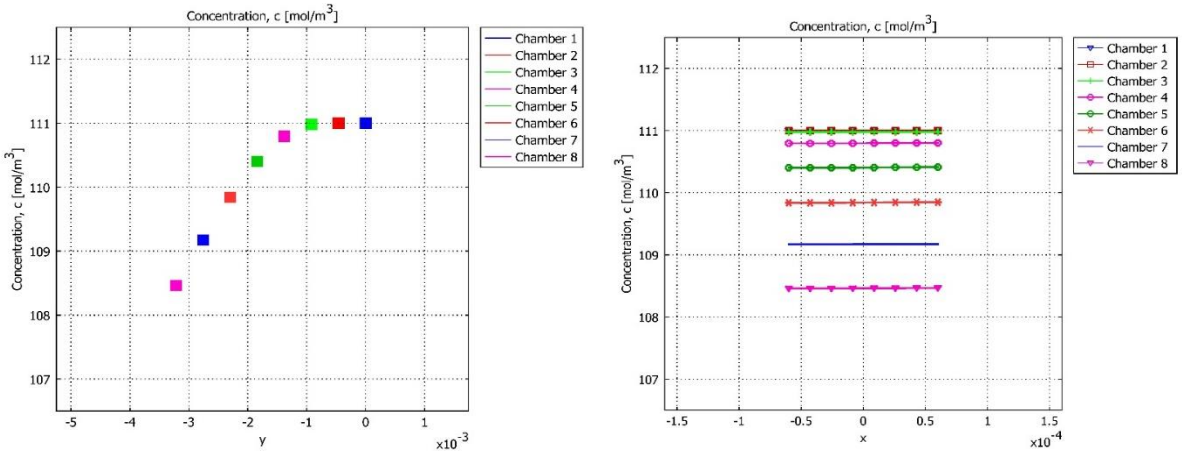

Figure 4.24. The concentration profiles in vertical and horizontal directions (y=0, inlet).

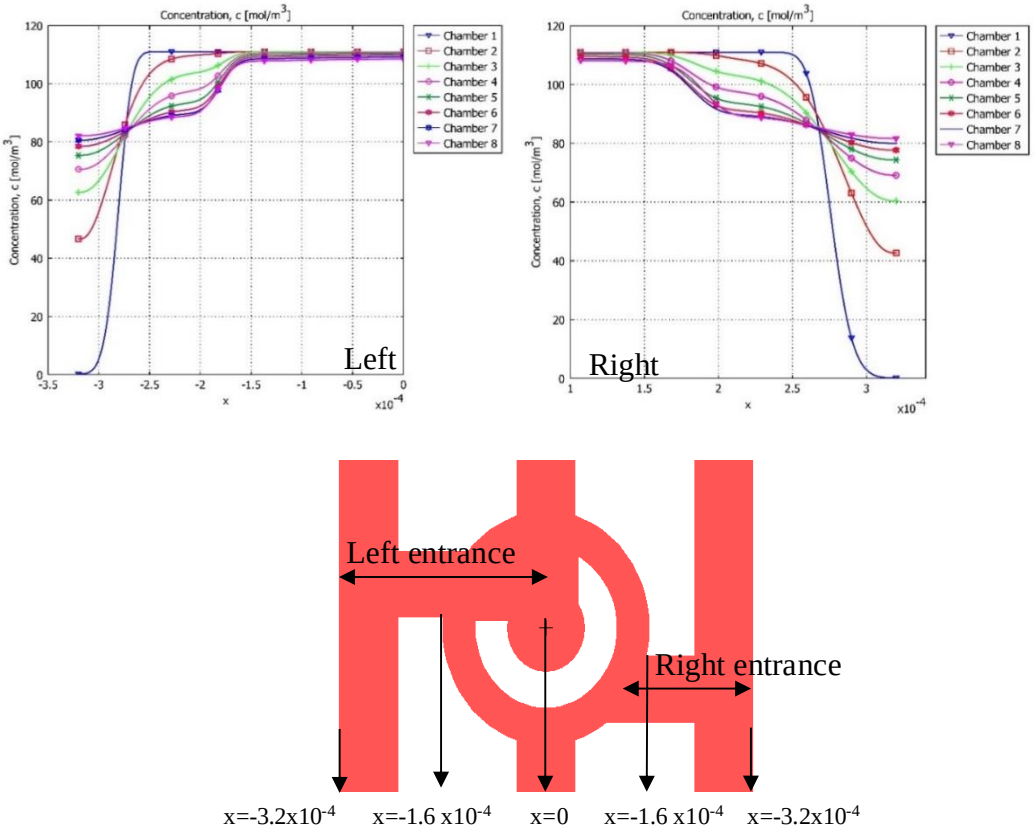

Figure 4.25. The concentration profiles of the left and right entrances of all chambers.

The concentration value of the nutrient remained same after entering the c-shaped region. The concentration profiles at different heights (z=0, $2x10^{-4}$, $6x10^{-4}$ μm) were analyzed for Chamber 1 (Figure 4.26). The high concentration of nutrient loaded through the middle channel was diluted by the fluid coming from side channels, the concentration started to decrease. However, it stayed constant in the trapping region. This process was same for different heights and it showed that concentration values were not changed at different heights (Figure 4.26).

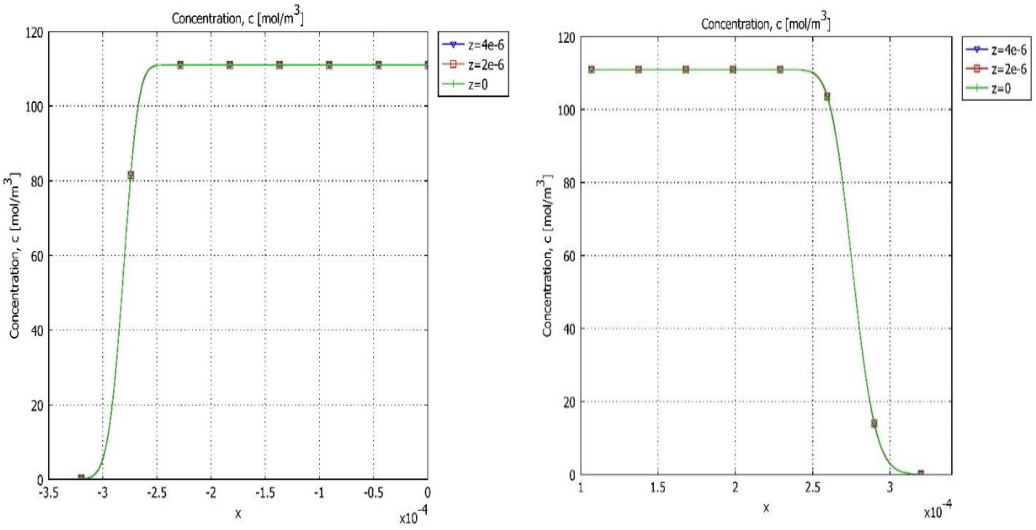

Figure 4.26. The concentration profiles of left and right entrances of chamber 1.

4.2.5. Discussion on the Optimized System

In the COMSOL simulation, six models were first tested to optimize the velocity distribution within the microbioreactor. The inlet flow rates of 0.1 μL/min and 0.01 μL/min were selected for cell loading and nutrient loading, respectively. The aim was to trap the cells in the c-shaped regions efficiently and remove the untrapped cells without flushing out all fluid from the region by the side channels. The velocity fields of Model 4, Model 5 and Model 6 were convenient to achieve this aim (Figure 4.11, Figure 4.14 and Figure 4.17). The velocity values at the center of the c-shaped regions of all the chambers were small enough to immobilize the cells. This value should not be zero because this means there was no entrance to that chamber. In the Model 3 the problem of zero speed occurred

and the first chamber was useless because of no flow. The outer perimeters of the c-shaped regions were also analyzed to prevent cells from flushing out via fast fluid flow.

In first three models, the velocities in side channels and around the outer perimeter of c-shaped regions were very high and carried the risk of flushing out. The inlet velocity pairs of 1 μL/min and 1 μL/min, 0.1 μL/min and 0.1 μL/min, 0.01 μL/min and 0.001 μL/min for middle and side channels were inefficient, respectively. After the optimization of velocity distribution, concentration profiles of nutrient were simulated for all the models. Figure 4.23 shows the optimized concentration profile which belongs to Model 5. Figure 4.14 and Figure 4.11 show that the velocity profiles of these two models were very similar. Figure 4.27 shows the concentration profiles of these two models which had close velocity profiles. For Model 4, after loading the cells and nutrients, mixing began from the second chamber. The concentration of the fluid was set to almost 97.21 mol/m^3 in all the chambers. Because of this huge concentration drop in Model 4, it was not selected as the optimized one.

The concentration was nearly same at all chambers in Model 5 and Model 6. In model 5, the mixing occurred in the last two chambers but the diversion from the initial value of 111 mol/m^3 was only 2.2% (Figure 4.24). In model 6, the diversion from the initial value was only 2.1%. Also the velocity profiles at the left and right entrances of the side channels showed that the possibility of flushing out of the cells was nearly zero (Figure 4.25). The concentration characteristics at different heights were also same (Figure 4.26). Besides, pressure profile of the microbioreactor was simulated at the optimized velocities (1 μL/min at middle channel, 0.1 μL/min at side channels). The pressure was set to zero at outlets open to air and the pressure drop in all the channels were very small (500-600 Pa) in the device (Figure 4.22).

As a conclusion, the inlet velocities were determined as 1 μL/min for the middle channel, 0.1 μL/min for the side channels for the cell feeding. For the nutrient feeding, all the inlet velocities were determined as 0.1 μL/min. In these COMSOL simulations, role of beads or yeast cells was neglected. The optimized parameters were expected to guide for

a better loading process in experiments and they provided an insight into possible future problems in the microbioreactor.

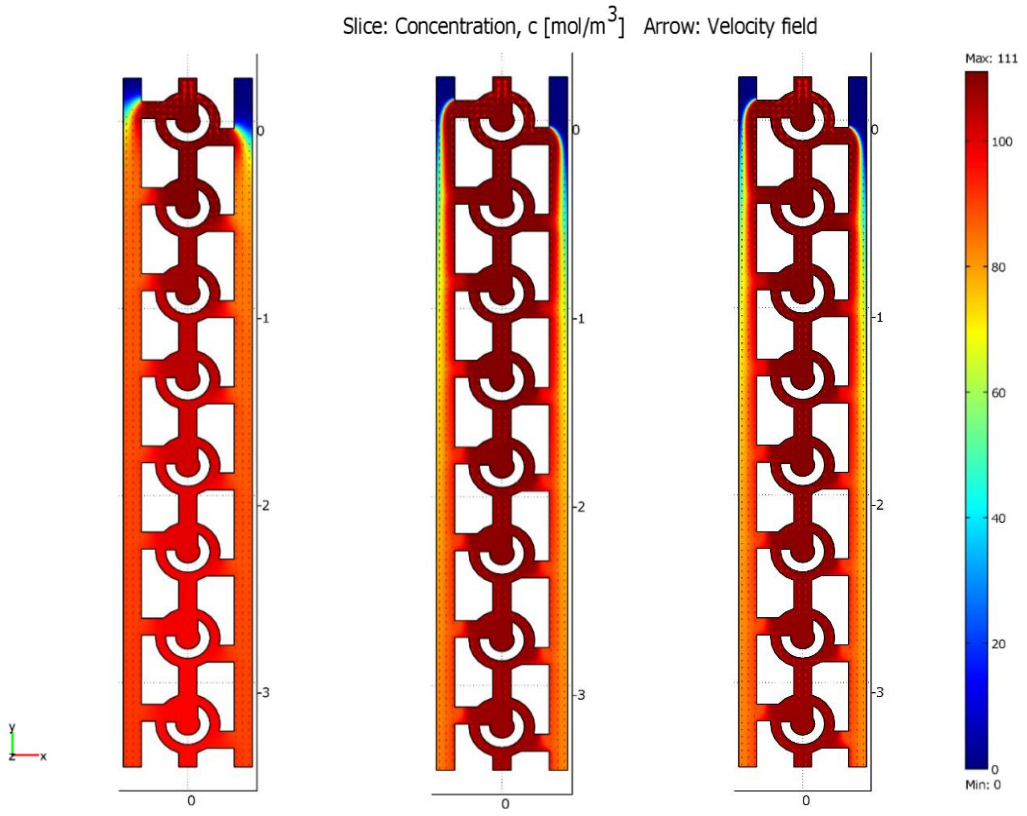

Figure 4.27. The concentration profiles of model 4, model 5 and model 6.

4.3. Validation of the Flow Profile by LT-Spice

In order to estimate the flow direction and distribution in the microbioreactor, LT-Spice was used to calculate the hydraulic resistances in the channels and at the perimeter outside of the c-shaped region. The nodes were located to the possible inlets of the flow and an electric circuit was drawn according to these nodes.

The flow profile was estimated for the first chamber only. The channels and flow paths were assumed to have rectangular cross section, and hydraulic resistances for each

cross section were calculated via using the equation. The hydraulic resistances and their locations in the first chamber are shown in Figure 4.28.

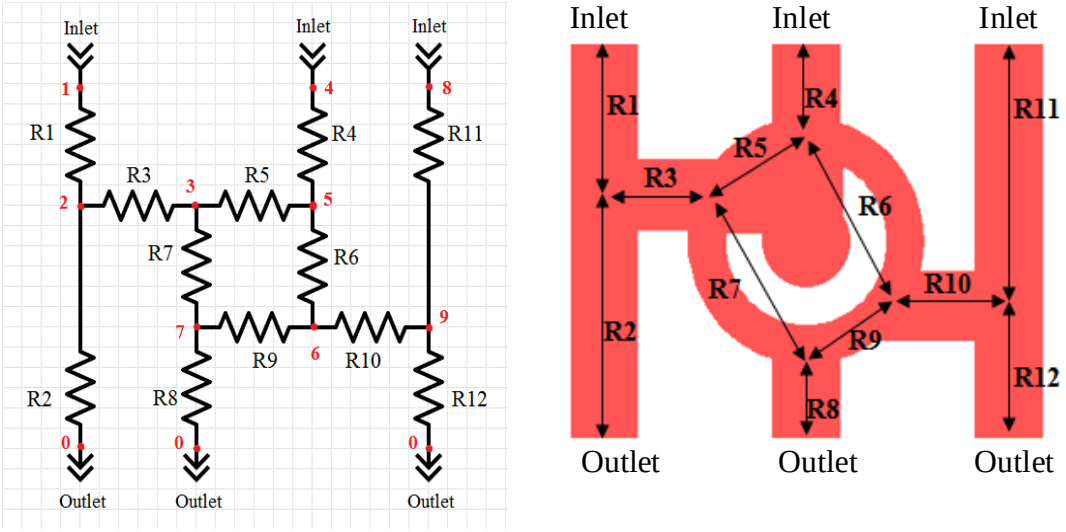

Figure 4.28. The resistances of the first chamber.

$$R_h = \frac{12\mu L}{wh^3(1 - 0.630h/w)} \tag{4.4}$$

In the equation 4.4, μ (N.s/m^2) is the viscosity, L(m) is the total length, h(m) is the height and w(m) is the width. The calculated resistances are shown in Table 4.2.

Table 4.2. Resistance values of each portion.

	R1=R12	**R2=R11**	**R3=R10**	**R4=R8**	**R5=R9**	**R6=R7**
Length (m)	0.00018	0.00028	0.00013	0.00007	0.00018	0.00025
Width (m)	0.00009	0.00009	0.00009	0.00009	0.00005	0.00005
Height (m)	0.000008	0.000008	0.000008	0.000008	0.000008	0.000008
Viscosity (N.s/m2)	0.000894	0.000894	0.000894	0.000894	0.000894	0.000894
Rh (Pa.s/m3)	4.44E+13	6.91E+13	3.21E+13	1.73E+13	8.39E+13	1.17E+14

The calculated resistance values were used to determine the flow direction and proportion from inlet to outlet by using LT-Spice program. The current distribution shows the direction of the flow which is important for cell trapping. The schematic representation of the current distribution in the first chamber is shown in Figure 4.29. The back flow through the inlets did not occur and the side channels were removing the excess flow efficiently according to the calculated values in LTSpice.

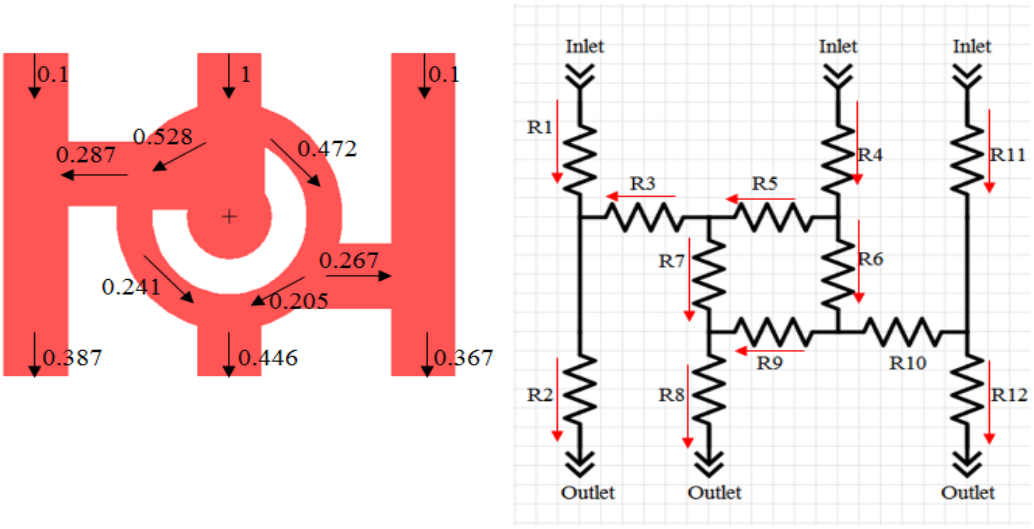

Figure 4.29. The current distribution in the flow (µL/min).

4.4. Experiments Done by New Design

In order to demonstrate the functionality of the developed microbioreactor for cell culturing, yeast (*Saccharomyces cerevisiae*) was used as the model organism. The yeast strain used in this study was obtained from Prof. Steve Oliver, Cambridge University, Department of Biological Sciences, UK. The wild type (WT) BY4741 strain was derived from the parental S288C strain and has the following base genotype: MATa *his3Δ1 leu2Δ0 met15Δ0 ura3Δ0*. The WT strain was transformed with the genome coding for enhanced green fluorescent protein (GFP) and GFP tagged YOR060C strain was obtained by proper biological construction.

The materials used for fabrication of the microbioreactor were selected according to their chemical properties such as the stability and resistance properties against solvents, water absorption properties and thermal expansion coefficients as mentioned in Section 3.1.1. The thermal bonding parameters for each polymer (PMMA, COP and PEN) were optimized. The flow in channels were tested by water for PMMA, by acetone for COP and by ethanol for PEN made microbioreactors, respectively.

After ensuring the channels were open enough for the flow of the medium, experimental setup was started to be prepared. The connections of channels on the fabricated microfluidic device were arranged with 20 µL sterile pipette tips (ExPellPLUS, CAPP Denmark), silicon tubings (SCI, Micro Medical Tubing, 0.86 mm ID x 1.52 mm O.D.) and epoxy (BISON 5 minute epoxy). First, the pipette tips were cut until they tightly fitted the drilled inlet hole. Then, the intersection of the pipette tip and the polymer were connected with the help of epoxy and let to dry at room temperature. Here, the sizes of the pipette tips were properly adjusted to the size of the holes, which were drilled by hand. This process was applied for 6 inlet and 2 outlet holes, respectively. The silicon tubings were connected to these tips by the help of the pipette tips, and used as yeast and nutrient inlets and outlets. Figure 4.30 shows the inlet and outlet connections of the microbioreactor. The timing of all the process is given in Table 4.3.

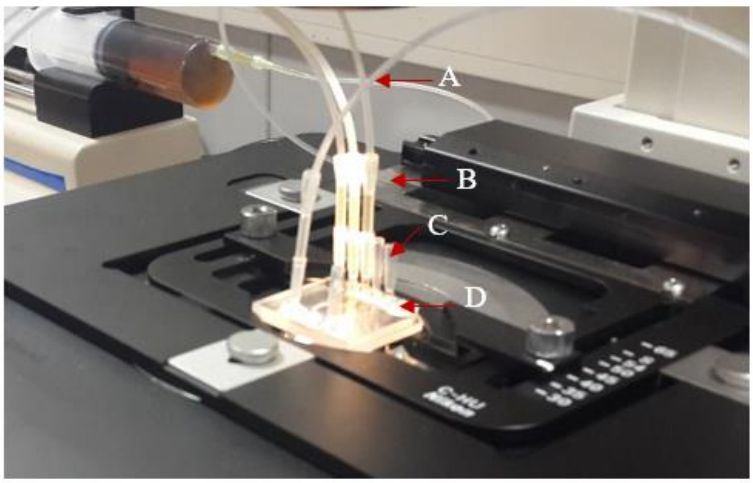

Figure 4.30. The inlet and outlet connections (a) silicon tubing (b) pipette tip to connect the silicon tubings to inlets (c) fixed pipette tips on holes (d) epoxy connection.

Table 4.3. Timing.

Process	Steps	Time (h)
Fabrication	All process	6-7
	Photolithography	3-4
	Electrochemical Wet Etching	1
	Hot embossing (includes cleaning step)	0.5
	Drilling and cleaning before bonding	0.75
	Bonding	1
Setting up auxilliary equipment (connections by using epoxy and pipette tips)		3
Preparing yeast strains and media		2-3
Preparing an inverted fluorescence microscopy experiment		1

There were approximately 100 chips fabricated with this design. Unfortunately, 80% of them were discarded due the problems occurred during the fabrication process. About 20 chips could be tested on the microscope stage, i.e. on Lab-on-a-Chip platform. Nevertheless, each time the process had to be stopped some time after the medium loading. Proper medium flow could not be achieved due to leakage or clogging problems.

Several problems encountered during the experiments are exemplified in following text. In the fabrication process, it was difficult to control all the heights throughout the microfluidic device during the bonding process. Some wider sections of the channels extending either from the inlet to the first chamber or from the last chamber to the outlet were collapsed during bonding and the flow cannot pass through these sections. The height of the microbioreactor in some sections was lowered too much, i.e. more than half of its original height (z-direction 8 μm), especially in the channels towards the outlets (collapses occur in these channels), and the outlet of the reactor behaved as a close system (not open to atmosphere) and this caused a very big pressure difference during the experiment. The collapsed area in outlet channel is shown in Figure 4.31.

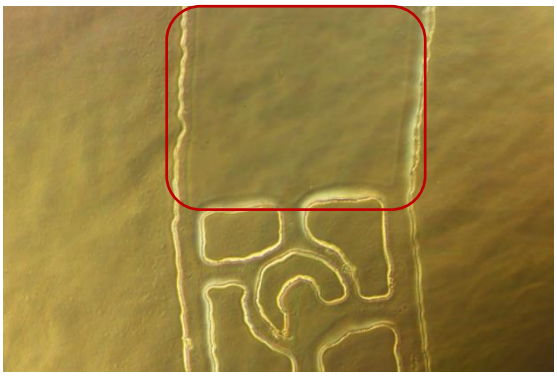

Figure 4.31. The collapsed area in the middle of the outlet channel.

Moreover, during the experiments, the visualization of all the chambers had to be done to monitor yeast cells. When the microscope stage was moved sideways or forward or backward, the silicon tubings (shown in Figure 4.32) were pulled and stretched, that in turn pulled the pipette connections, and the case generally ended up with the damage of epoxy connection. Hence, the inlet and outlet connections shown in Figure 4.32 were the major source of failure (damp squib).

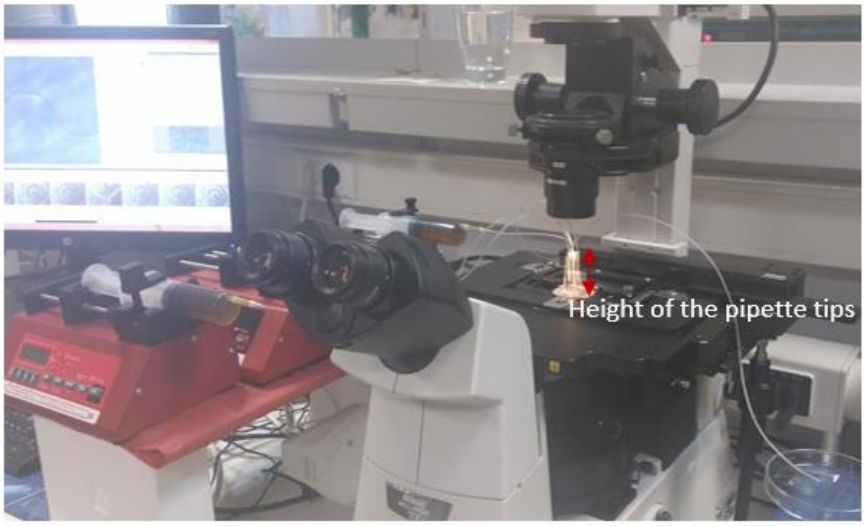

Figure 4.32. The distance between pipette tips and the condenser.

The epoxy connections were damaged and they broke up during the medium loading process. This situation caused the leakage of the medium through the intersection of epoxy

and the polymer piece. Also, the distance between the end of the pipette tips and the condenser was not high enough to zoom in the image. When the condenser was fully zoomed in to capture the images via 40X objective, the microbioreactor could not be moved easily to sideways. Figure 4.33 shows the distance between condenser and pipette tips. The inlet tubing system needed to be revised for proper visualization via the inverted microscope. The critical points for the proper design and fabrication process (electrochemical wet etching, cleaning, drilling and bonding) are given in detail in the following section.

4.5. Critical Points of the Fabrication Process

The chemical properties of the different polymers used in this study affect the bonding process and the flow in the channels and chambers of the microbioreactor. Several problems needed to be resolved during the bonding process of PMMA, COP and PEN polymers, in order to avoid the clogging of the channels as well as the leakage.

4.5.1. Cleaning Process

An important point during the fabrication process is the cleaning procedure of the pieces to be bonded. As the first step of this process, chemical resistances of the polymers need to be known. The chemical resistances of COP, PMMA and PEN polymers to most commonly used chemicals are listed in Table 4.4.

Table 4.4. The chemical resistance properties of the polymers.

Polymer Name	2-propanol, pure (Isopropyl alcohol)	Acetone, pure	Ethanol	Chloroform, pure
PMMA	Not resistive	Not resistive	Not resistive	Not resistive
COP	Resistive	Resistive	Resistive	Resistive
PEN	Resistive	Resistive	Resistive	Resistive

Before the bonding process the surface cleaning of three different polymers were varied. For the cleaning of the PMMA polymer pieces, as the first trial, cleaning was done by washing with 2-propanol and distilled water. There were still some contaminations on the polymer piece. After a while the cleaning procedure was started by baby shampoo to clean the oil like particles on the surface caused by hand or environment. After the optimization process, baby shampoo, water, 2-propanol and distilled water were used, respectively (Table 4.5).

After drilling, solvent treatment was done using various solvents such as 2-propanol, dimethyl sulfoxide, acetone and chloroform. For acetone and chloroform, the solvent was evaporated through the polymer surface for a short time to achieve a uniform solvent distribution on the surface. As a result of these experiments, 2-propanol was selected as the most effective solvent for the solvent treatment and the polymer pieces were submerged in 2-propanol for 2 minutes before bonding. Eventually, for a better bonding strength after the drilling of the inlets, two PMMA pieces were washed following the same steps as explained above and submerged in 2-propanol for 2 minutes.

Table 4.5. Cleaning agents for polymers.

Polymer	**Cleaning agents used sequentially before drilling process**	**Treatment after drilling**
PMMA	Baby shampoo, water, 2-propanol and distilled water	Repeat cleaning steps and submerge in 2-propanol for 2 min
COP	Acetone, 2-propanol and distilled water	Repeat cleaning steps, then put into ultrasonic bath for 15 min, put on a 80°C heated hot plate for 15 minutes, clean remaining residual flakes by pincer
PEN	Acetone, 2-propanol, distilled water	Chloroform-Ethanol solution (1:1 by volume)

The COP pieces are more resistant to alcohols. The cleaning process of COP was done by washing with acetone, isopropanol and distilled water before drilling the inlets. There were some polymer residuals near the inlet and outlet holes owing to the drilling. The cleaning step was repeated and the drilled piece was put into ultrasonic bath for 15 minutes to flake of these residuals, and after that the visible residuals were cleared by the help of a pincer. The polymer pieces were dried by pressurized nitrogen and put on a hot plate heated at 80°C for 15 minutes to evaporate all the solvents on the surface.

For the PEN pieces, the cleaning procedure was optimized by washing with acetone, 2-propanol and distilled water. Then, a solvent treatment was applied by submerging the PEN polymer into Ethanol:Chloroform (1:1) mixture for 5 minutes, and then PEN pieces dried by pressurized nitrogen (Table 4.5).

4.5.2. Drilling Process

The drilling direction was a problem while working with COP pieces. The COP material was prone to melt by the heat appeared in the drilling bit. As a result of this melting, polymer made bulges appeared on the inlets. These bulges on the inlets were obstacles for the thermo-compression bonding. If the inlets were drilled from the upper side of the reactor piece, the bonding was started from these bulge sides, which caused a clogging at the inlets and no flow was observed in this closed channel (Figure 4.33).

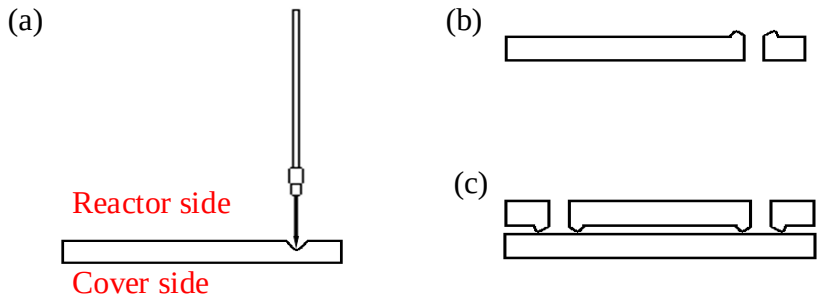

Figure 4.33. Drilling process (a) drilling of the polymer pieces from the reactor side (b) the polymer bulges appeared after drilling (c) the bonding started from the inlets.

This bulge problem was solved by changing the drilling direction of the polymer piece. The problem appeared on the reactor side of the polymer (the side where the shape was appeared after hot embossing) hence the drilling direction was changed to the cover side of the reactor.

4.5.3. Optimization of Temperature and Pressure for Bonding

After the optimization of cleaning and solvent treatment steps, to optimize the bonding parameters, different temperature, pressure and duration times were tested.

4.5.3.1. PMMA. The bonding parameters were needed to be optimized to achieve a strong bonding. The parameters tested in hot embossing press (carver) and in oven for the optimization of the temperature and pressure are listed in Table 4.6 and Table 4.7, respectively. For our hydraulic press system, 2 bar equals to 95 lbs.

Table 4.6. Bonding parameters tested for PMMA in hot embossing press.

Sample #	Cleaning & Pretreatment			Bonding				Results
	Cleaner	Solvents used for surface treatment	Time (min)	T (°C)	Load (lb)	Time (min)	Comments	
1	IPA + Distilled water	IPA	2	85	600	10	Solvent remained in device, shape deformation	-
2		IPA applied by brush	-	85	500	10	Shape deformation	-
4		3 min IPA, 5 min DMSO dried by N_2	-	85	500	10	No deformation, weak bonding	Leakage
5		Acetone	5	85	400	10	Surface is whitened, channels are deleted	-
6		Acetone evaporation on channel side	3	85	400	10	Weak bonding	Leakage
7		Chloroform evaporation on channel side	2	85	400	10	Weak bonding	Leakage
8		-	-	95	500	45	No leakage on one side, strong bonding	Flow is not observed
9		-	-	95	400	45	Weak bonding	Leakage
10		Chloroform evaporation on two sides	2	95	400	30	Weak bonding	-

Table 4.6. Bonding parameters tested for PMMA in hot embossing press (cont.).

11	Baby shampoo +IPA + Distilled water	IPA	2	105	750	120	All shapes are deleted, good bonding strength	-
12		IPA	2	105	500	120		-
13		IPA	2	105	500	90		-
14		IPA	2	105	500	75	Shape is blurred	No leakage or flow
16		IPA	2	105	500	60	Shape is blurred, bonding strength is still good	-
17		IPA	2	105	500	45	Shape is good, bonding strength is weak	Leakage
18		IPA	2	115	500	30	All shape is deleted	-
19		IPA	2	105	95	15	Strong bonding, shape is blurred	Water flow was not observed

Table 4.7. Bonding parameters tested in oven for PMMA.

Sample #	**Cleaning & Pretreatment**			**Bonding**				**Results**
	Cleaner	**Solvents used for surface treatment**	**Time (min)**	**T (°C)**	**Load (lb)**	**Time (min)**	**Comments**	
1	Baby shampoo +IPA + Distilled water	IPA	2	95	4 clamps	45	Shape is OK but weak bonding	
2				95		60	Weak bonding	
3				95		45	Weak bonding	
4				100		120	Weak bonding	
5				105		60	Shape is blurred	
6				105		55	Good bonding strength, shape is not blurred, can not to be opened by hand	Flow is not observed by syringe and pump
7				105		50	Good bonding strength, shape is not blurred, can not to be opened by hand	Flow is observed at one side but not repeatable

The glass transition temperature of PMMA is almost 105°C and the trials on the bonding temperature were started from 85°C by using the hydraulic press machine (Carver). The bonding operation was done by using two 3cm x 4cm PMMA polymer

pieces. As the first step of this process, cleaning was done as described in Table 4.6. Then, the two clean polymer pieces were aligned between two 2 mm thick glass pieces to achieve a uniform heat distribution and covered by aluminum foil, and put between two plates of Carver machine. The initial temperature values tested were between 85-95°C after the solvent treatment. After many trials listed in Table 4.7, the best results were achieved at 105°C under 500 lbs pressure for 45 minutes. Unfortunately, the leakage was still observed and the heat distribution was not uniform enough.

In order to achieve more uniform heat distribution, the two clean polymer pieces to be bonded were aligned between the two 2 mm thick glass pieces, covered by aluminum foil and pressurized by 4 clamps at each side and this system was put into oven to test several temperature and duration times (Table 4.7). The duration time was optimized as 50 minute at the temperature of 105°C. After the fabrication of the microfluidic device (microbioreactor), the channels need to be tested whether they are open or clogged. The PMMA made devices were tested by water. The water flow through the channels is shown in Figure 4.34.

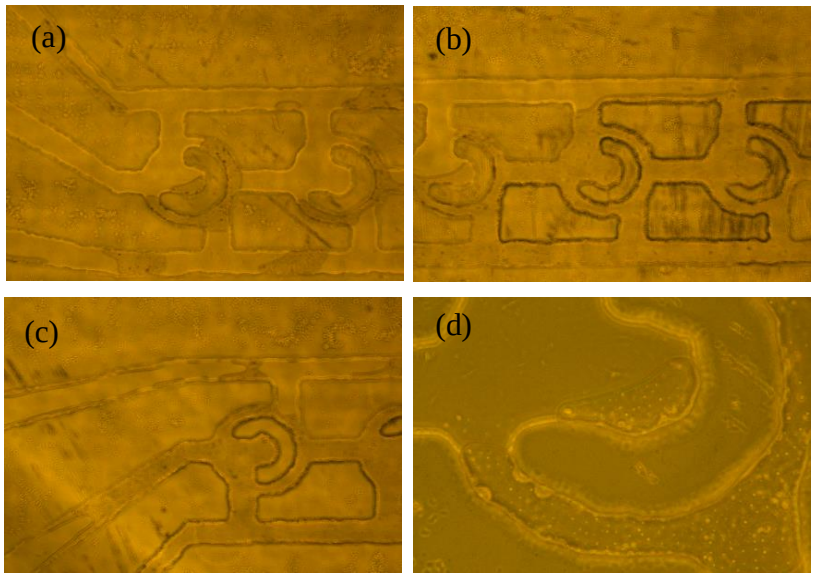

Figure 4.34. The water flow in the PMMA made microbioreactor (a) left side inlets (b) filling the channels by water (c) right side inlets (d) the water droplet in the c-shaped region.

4.5.3.2. COP. The bonding parameters for two COP polymer pieces needed to be optimized again because of the different characteristics of this polymer. The temperature and pressure parameters tested to optimize the bonding process are given in Table 4.8.

Table 4.8. Bonding parameters tested for COP.

Sample #	Cleaning & Pretreatment			Bonding				Results
	Cleaner	Solvent	Time (min)	Temp (°C)	Load (bar)	Time (min)	Comments	
1	Acetone + IPA + Distilled water	No solvent treatment	-	95	9	30	Parameters were determined by using reference [29]	No bonding
2				135	4	5	Parameters were determined by using reference [30]	Good bonding strength but shape is blurred
3				135	2	5	Shape is blurred	-
4				130	4	5	Bonded but opened after a while	-
5				130	2	5	Bonded but opened after a while	-
6				130	2	30	Bonding strength is good, shape is not blurred	Flow is observed at one side, only leakage at outlet
7				130	2	30	Inlets are corrected by knife before bonding (to avoid the clogging because of inlets)	Weak bonding
8				130	2	30	Inlets are opened at cover slide and corrected by knife	Weak bonding
9				90	10	30	No bonding	-
10				110	20	10	No bonding	-
11				110	20	30	No bonding	-
12				130	10	10	Strong bonding, channels are also bonded (tried with a dummy sample)	-

Table 4.8. Bonding parameters tested for COP (cont.).

Sample #	Cleaning & Pretreatment			Bonding				Results
	Cleaner	**Solvent**	**Time (min)**	**Temp (°C)**	**Load (bar)**	**Time (min)**	**Comments**	
13	Acetone + IPA + Distilled water	No solvent treatment		130	8	10	Strong bonding, channels are also bonded (dummy sample)	-
14		Ethanol	10	130	2	30	Weak bonding	Acetone leakage
15				130	2	30	Treated by O2 plasma-180 W / 20 Torr / 13.56 MHz / 4 min	Good hydrophilic properties, water leakage
16				130	10	30	Bonding strength is OK, C-shapes cannot be cleared under microscope (dummy sample)	Acetone flow without leakage, no water flow
17		Ethanol	10	130	9	30	Bonding strength is OK, C-shapes cannot be cleared under microscope (dummy sample)	Acetone and water flow are observed without leakage
18			10	130	10	30	Bonding strength is OK, shape cannot be seen clearly under microscope (new sample)	Shape cannot be seen clearly
19			10	130	8	30	Bonding strength is OK, shape cannot be seen clearly under microscope (new sample)	Shape cannot be seen clearly

Table 4.8. Bonding parameters tested for COP (cont.).

Sample #	Cleaning & Pretreatment			Bonding				Results
	Cleaner	Solvent	Time (min)	Temp (°C)	Load (bar)	Time (min)	Comments	
20	Acetone + IPA + Distilled water + Ultrasonic bath 15 min + hot plate	No solvent treatment	-	130	6	30	Bonding was done between two glass pieces.	Shape is clear. Channels and c-shapes are also bonded.
21					4	30		Shape is clear. Channels are also bonded.
22					4	30		Shape is clear. Channels are also bonded.
23					2	15		Shape is clear. Acetone flow is observed. Some inlets may also bonded.
24	Acetone + IPA + Distilled water + Ultrasonic bath 15 min + hot plate	No solvent treatment	-	130	2	15		Shape is clear. Acetone flow is observed in all three channels. (triangle piece)
25					2	30	Bonding was done between two glass pieces.	Acetone flow was observed in all channels wo leakage (bigger triangle piece)
26					4	45		Acetone flow was observed (rectangular piece)
27				120	50	60		Acetone flow without leakage Middle channels collapsed
28					45	60		Acetone flow without leakage Some channels collapsed
29					35	60		Acetone flow without leakage Some channels collapsed
30					25-30	60		Acetone flow without leakage Open and not collapsed channels

The solvent treatment was not used for COP polymers because of their high resistance to chemicals. The chemicals do not change their surface properties easily. The most important beginning step was the cleaning procedure and it was optimized. Both hot embossed and cover pieces were cleaned by acetone, 2-propanol and distilled water respectively and put into ultrasonic bath for 15 minutes, dried on the hot plate heated at 80°C. Two polymer pieces were aligned between two glass pieces as shown in Figure 4.35.

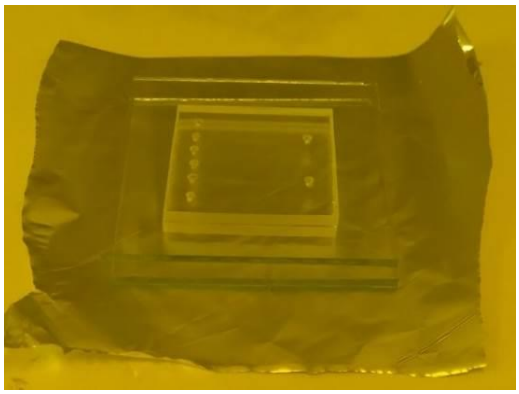

Figure 4.35. The alignment of two to be bonded COP polymer pieces.

The optimized temperature for the bonding process of two COP pieces (2 mm thickness each) is 130°C, no bonding was materialized at 125°C and the channels were collapsed at 135°C. Therefore, the temperature is a very critical parameter for the bonding of two COP pieces. The dimension of the polymer piece is also critical. The bonding of small triangular pieces with dimensions of 4cm x 3cm x 3cm (2 mm thickness) were optimized at 130°C by applying 2-4 bar for 30 minutes. The bonding of rectangular COP pieces (area of 3cm x 4cm, thickness of 2 mm) were optimized at 130°C by applying 4-6 bar for 45 minutes. The bonding of square COP pieces (area of 3cm x 3cm, thickness of 1.5 mm) were optimized at 120°C by applying 25-30 bar for 60 minutes. The uniform heat distribution through a big surface area is more difficult.

The COP polymer showed very high hydrophobicity and because of this reason, the flow in the channels was tested by injecting acetone through the inlets. The acetone flow in the microbioreactor and the empty and filled sides of COP made microbioreactor are

shown Figure 4.36. The devices, in which acetone flow occurred in channels without leakage, were then tested with water by inserting the tubings to inlets and outlets (Figure 4.37).

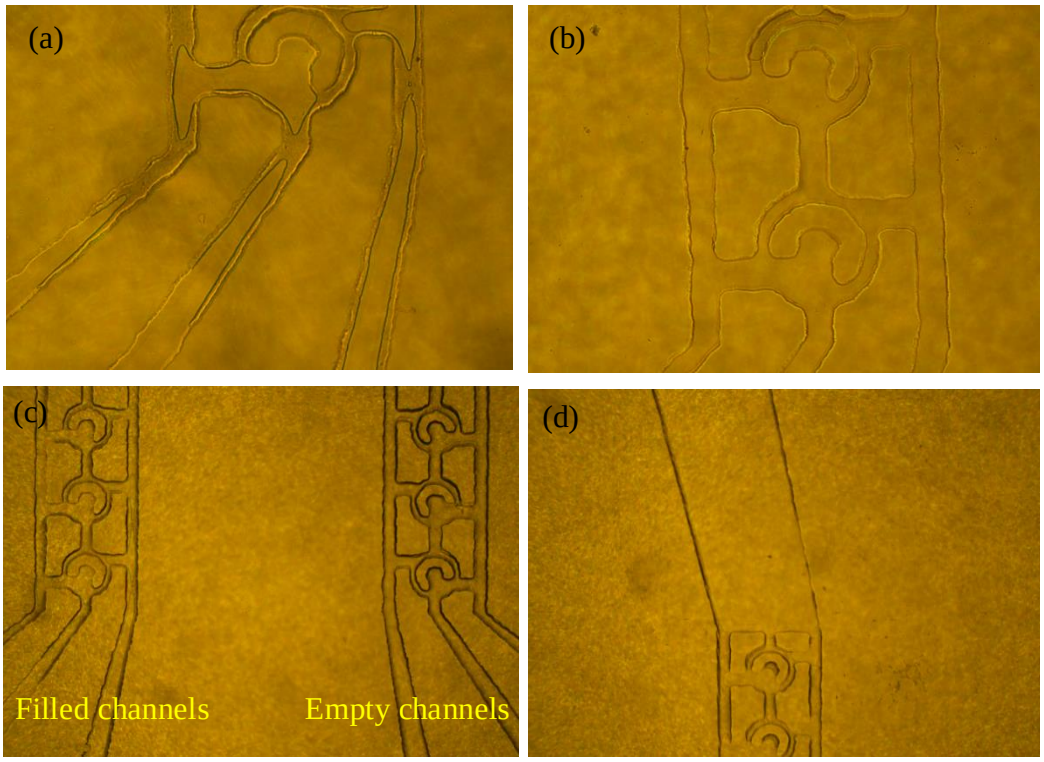

Figure 4.36. The COP made microbioreactor after acetone injection (a) the parabolic flow in inlets at the beginning (b) the first two channels loaded with acetone (c) the difference between a filled and an empty channel (d) the outlet of the device.

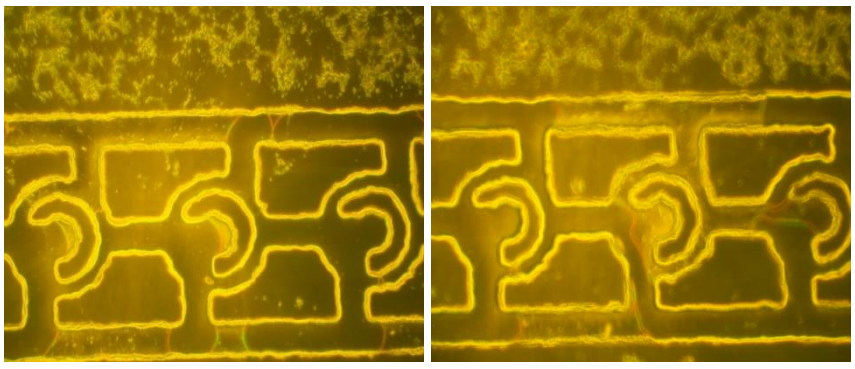

Figure 4.37. Filling of the channels of the COP made microbioreactor with water.

4.5.3.3. PEN. The parameters tested to bond 3cm x 4cm PEN polymer pieces are shown in Table 4.9. The solvent cleaning procedure was first optimized as washing with acetone, 2-propanol and distilled water. The solvent treatment was applied by submerging into Ethanol:Chloroform (1:1) mixture for 5 minutes. The optimized temperature, pressure and duration times are 135°C, 1500 lbs and 90 minutes, respectively. The PEN made microbioreactor's channels were also tested by injecting acetone through the inlets. The thickness of PEN sheets were 125 micron and keeping the pieces clean was more difficult because of the charging of PEN surface by the environment. Figure 4.38 shows the acetone flow in the PEN made microfluidic channels.

Table 4.9. Bonding parameters tested for PEN.

Sample #	Cleaning & Pretreatment			Bonding				Results
	Cleaner	Solvent	Time (min)	T (°C)	Load (lbs)	Time (min)	Comments	
1	IPA + Distilled water	Ethanol+Chloroform(1:1)	5	120	2350	150	Solvent procedure repeated.	Bonding ok, collapse at inlets & outlets, acetone flow is observed.
2			5	120	1800	180	-	Bonding ok, collapse at inlets & outlets, acetone flow is observed.
3			5	120	1200	180	-	Leakage observed (acetone)
4	Acetone + IPA + Distilled water		5	120	1500	210	Load >2500 at the end of the process (unknown reason)	Bonding ok, big bubble is observed at the center of the chip.
5			5	125	1800	180	-	Bonding ok, collapse at inlets & outlets, acetone flow is observed.
6			5	125	1200	120	-	Bonding ok acetone flow is observed (less collapsed area)
7			5	125	1200	240	-	Bonding ok acetone flow is observed (less collapsed area)
8			5	125	1200	360	-	Bonding ok, collapse at inlets & outlets, acetone flow is observed.

Table 4.9. Bonding parameters tested for PEN (cont.).

Sample #	Cleaning & Pretreatment			Bonding				Results
	Cleaner	Solvent	Time (min)	T (°C)	Load (lbs)	Time (min)	Comments	
9	Acetone + IPA + Distilled water	Ethanol+Chloroform(1:1)	5	125	1200	420	load >2000 at the end of the process (unknown reason)	Nonhomogeneous bonding, leakage observed (acetone)
10			5	125	1500	90	-	Bonding ok, collapse at inlets & outlets, acetone flow is observed.
11			5	135	500	60	-	Nonhomogeneous bonding, leakage observed (acetone)

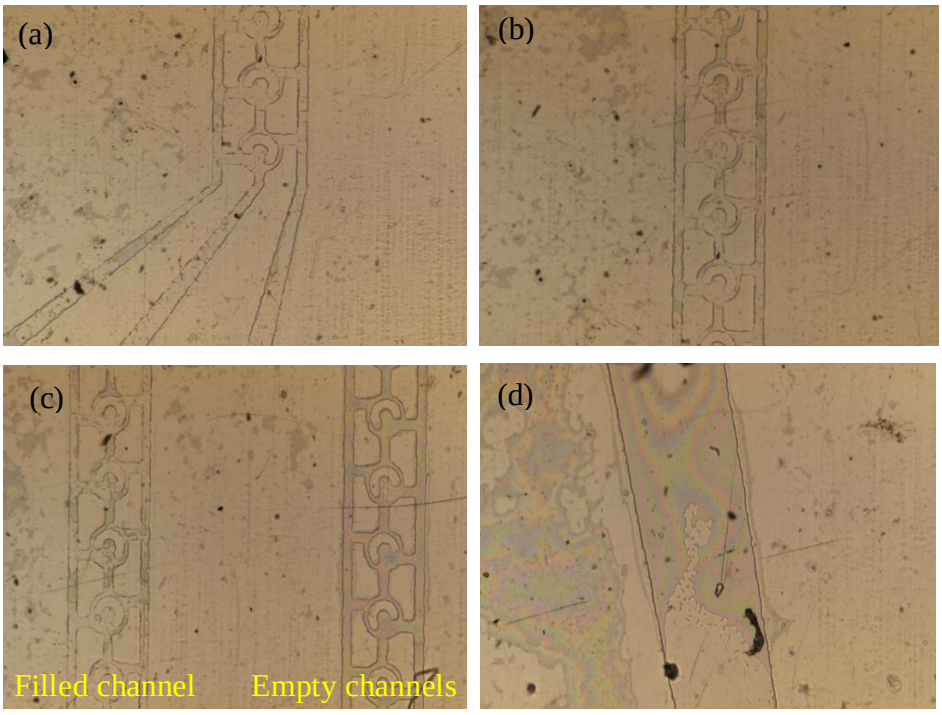

Figure 4.38. The inlets of the PEN made microbioreactor after acetone injection (a) filling of the channels after injection (b) the acetone filled c-shapes (c) a filled and an empty channel (d) the outlet of the device (4X objective).

4.5.4. Clogging Problem

After testing the channels with acetone, experimental setup was established. As the first step of loading, acetone and ethanol were perfused to channels to remove the air bubbles. First acetone was introduced through the inlets and when the microbioreactor was fully filled with acetone, ethanol perfusion was done through the channels in order to remove acetone so that it did not harm the COP and PEN polymer pieces and sterilized the microbioreactor. The acetone and ethanol were loaded through all inlets at a rate of 20 µL/min for 30 minutes to fill all the channels and remove the air bubbles. The acetone flow and air bubble formation are shown in Figure 4.39. Acetone and also ethanol filled the first c-shaped region and then continuously filled all the chambers including c-shapes one by one (Figure 4.40).

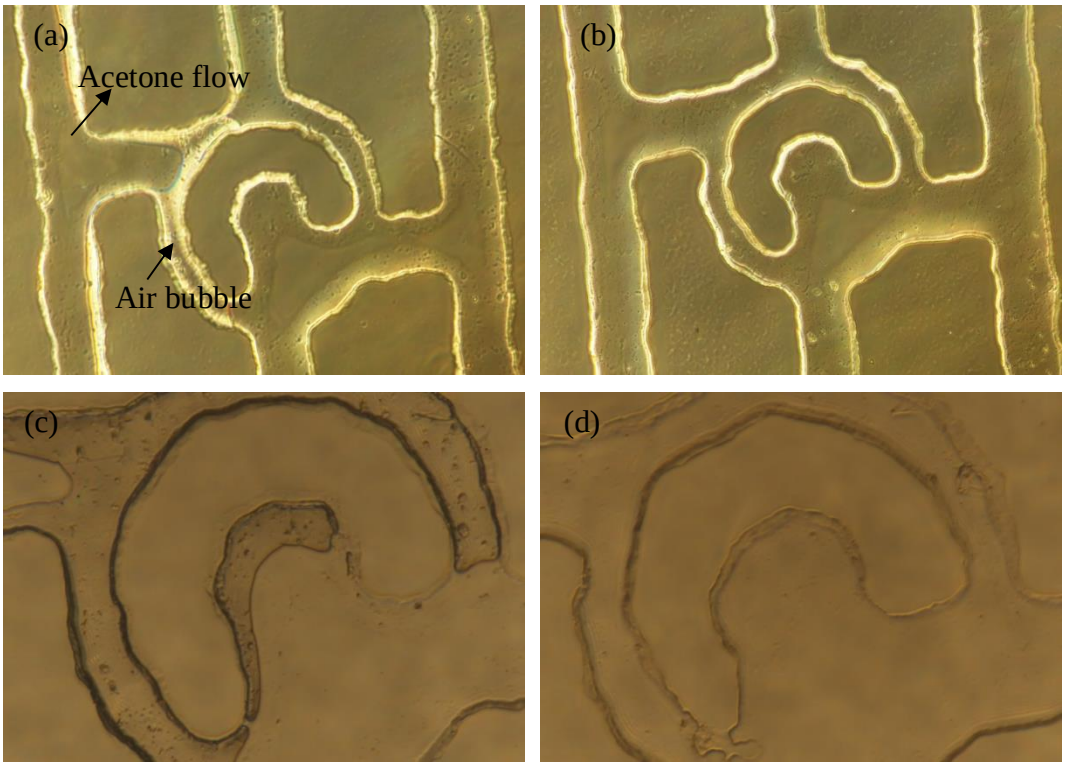

Figure 4.39. The acetone flow in the COP made channels (a) air bubbles occured in the cell perimeter (b) a fully filled channel (20X objective) (c) the first c-shaped region (d) the last c-shaped region (40X objective).

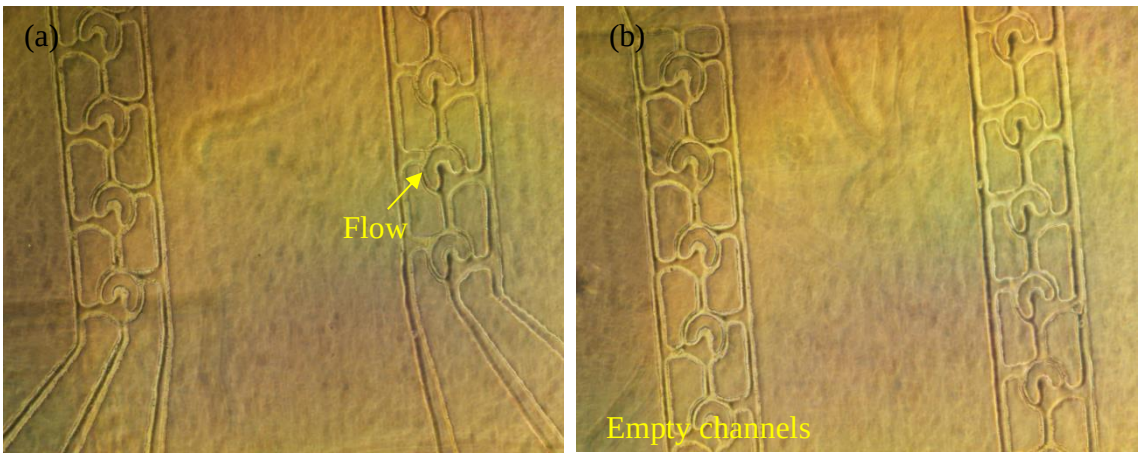

Figure 4.40. The COP made microbioreactor (a) channels started to fill with ethanol (b) empty and filled channels (4X objective).

The air bubbles in the device was also removed by the perfusion of ethanol in PEN made microfluidic device. Figure 4.41 shows the auto white images of the empty and filled PEN made channels with ethanol.

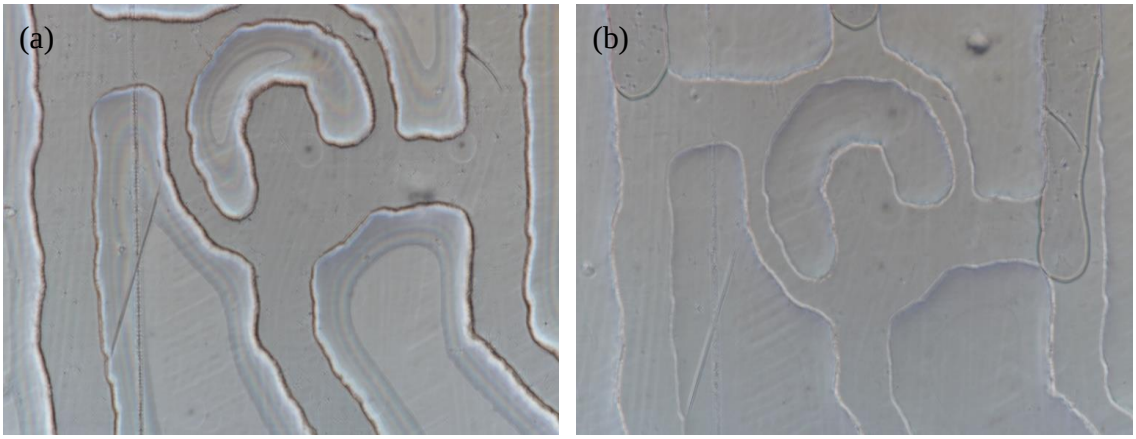

Figure 4.41. The ethanol flow in the PEN made channels (a) the empty channels (b) ethanol flow in the first chamber (20X objective).

After this perfusion process, the syringes containing liquid medium were connected to three inlets of COP made microbioreactor and medium loading was started. When the liquid medium was forced by the syringe pump at a rate of 5-20 µL/min through the inlets,

a very high pressure difference occurred in the microfluidic device and no medium flow can be observed. This could be because of the high resistance caused by the hydrodynamic pressure difference in the 8 µm depth channels. Due to high pressure drop through the channels, the fluid started to flow in the opposite direction, backflow occurred. As it can be seen in Figure 4.42, the fluid flow was divided into two parts because of the backflow in the COP made microbioreactor.

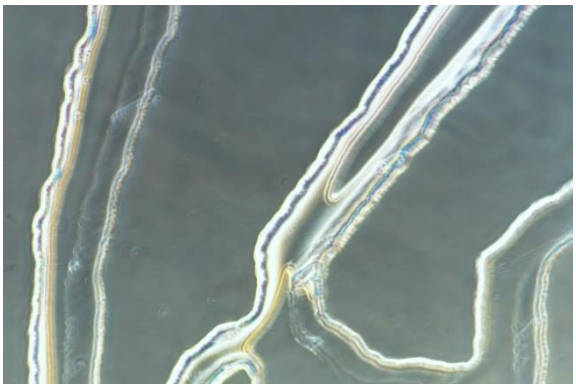

Figure 4.42. The auto white image of the backflow in the middle inlet channel of COP made device (20X objective).

Considering these problems, the microbioreactor height was increased from 8 µm to 17 µm enable proper flow in the channels and consequently to visualize the cells. Also the inlet and outlet channels' shapes were changed to avoid the clogging possibility of the wider sections. For this aim, a new mask was created by using the L-Edit software. The problems and their solutions are given in Table 4.10.

4.6. The Second New Design

4.6.1. Creating the Second Mask

The previous design was found to be not appropriate for cell and nutrient loading. Hence, a new design was created by taking the problems mentioned in Section 4.5 into consideration.

Table 4.10. Troubleshooting Table.

Step	Problem	Possible Reason	Solution
Design	The entire c-shaped region cannot be seen under Nikon inverted Ti-microscope by using 40X objective	The inappropriate dimensions of the design	A 40X objective stage micrometer was set and measured by using 40X objective. New dimensions were specified for seeing all area of the c-shaped region. The possible undercuts appeared during the etching process were also considered.
Electrochemical Wet Etching	Thicker c-shape dimensions than expected	Longer electrochemical etching duration than needed Etching of the perimeter of c-shaped region more than expected	The electrochemical etching duration is optimized for different depths individually.
Cleaning	Unexpected dust or contamination on the polymer surface and difficulty in imaging step	Insufficient cleaning steps or solvents for a clear surface	The most proper solvent was chosen for each polymers cleaning specifically. Ultrasonic bath was used to clean the COP pieces.
Drilling	The bulges appeared during the opening of inlet and outlet ports Inefficient bonding of the channel side	Melting of the COP polymer because of the heat of the drilling bit	The bulges were appeared on the side where drilling bit first touches. The drilling was done from the opposite side of the COP polymer piece.
Bonding	Non uniform heat distribution	Not enough uniform heat spreading in the polymer by carver's upper and lower plates	The polymers were aligned between 2 mm thick glass pieces.
Bonding	The clogging of the channel walls	Too much temperature or pressure	Lower pressure and temperatures were applied for longer times.
Loading	Leakage from the inlets during fluid loading	Insufficient bonding or weak sticking of polymer piece and the inlet ports	The tubings were safely attached by using more epoxy to strengthen the access.

Furthermore, the inlet and outlet channels' polygonal shape causes some clogging in the middle of the inlet and outlet channels leading to chambers. Therefore the channels were designed as straight lines to eliminate this problem (Figure 4.44). Another problem was the narrow channels around the perimeter of the c-shaped region. The fluid could not

pass through these channels easily. The diameters were reconsidered in the new design, by estimating the reduction in these areas resulted by electrochemical wet etching process. Also, because of the new height of the microbioreactor expected to be 20µm, consequently the dimensions were changed as shown in Table 4.11. The new dimensions are shown in Figure 4.43.

Table 4.11. Dimensions of design-1 and new design-2.

Dimensions (microns)	**New design-1**	**New design-2**
R1 (radius of the inner chamber)	60	100
R2 (radius of the middle chamber)	110	150
R3 (radius of the outer chamber)	160	310
w (widths of the channels)	90	160
Height of the reactor	10	20
C-shape thickness	50	50

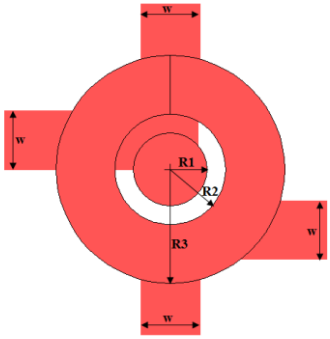

Figure 4.43. The dimensions of a chamber for new design-2.

The new design again consists of 8 chambers along 2 columns with 6 inlet and 2 outlet channels. The diameter of the trapping region is 200 µm and c-shape thickness is 50 µm. The inlet channels for yeast and nutrient supply, outlet channels for waste and side channels for carrying the excess flow to main channels, all have 160 µm width and 20 µm depth. The design modelled by L-Edit software program in two dimensional form is shown in Figure 4.44 and the microscope images of mask is shown in Figure 4.45.

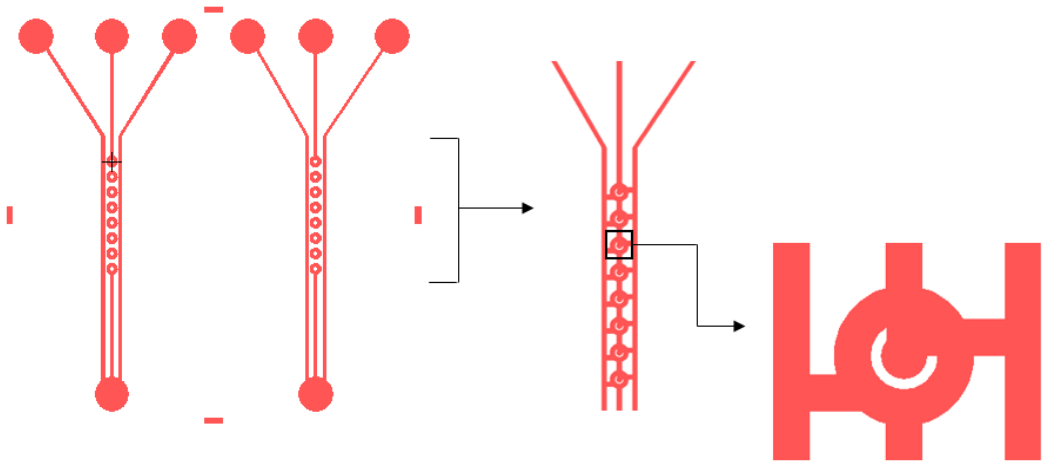

Figure 4.44. General view of mask and chambers for new design-2.

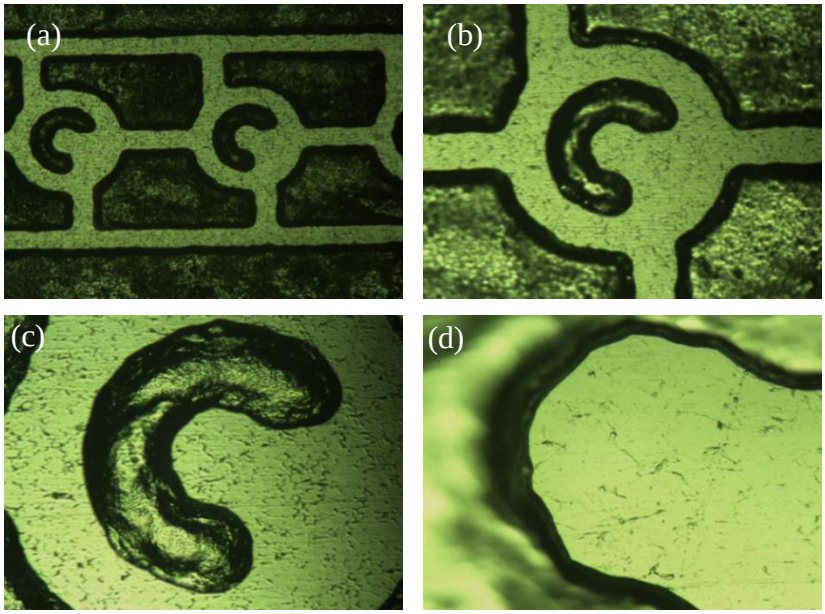

Figure 4.45. Microscope images of second etched steel plate (a) channels by 5X objective (b) one entire c-shaped region by 10X objective (c) 20X objective (d) 50X objective (captured by Nikon Measuring Microscope MM-400).

The mask was printed on an acetate paper and used to shape the steel plate with this new design by following the same procedure in Section 3.1.3. The wet etching setup was

prepared to create a 20 µm depth in the steel plate. DC power supply was set to 22.5A to provide the current for electrochemical etching and applied for 60 seconds. The steel mask was then formed and its depth was measured as 17-20 µm as shown in Figure 4.45.

The microfluidic device with its channels was produced by using the stainless steel mask via hot embossing. The hot embossing process was carried out at 130°C. The 3cm x 3cm polymer piece was put on the steel mask and pressurized at 30 bar. The stainless steel mask used for hot embossing is shown in Figure 4.46.

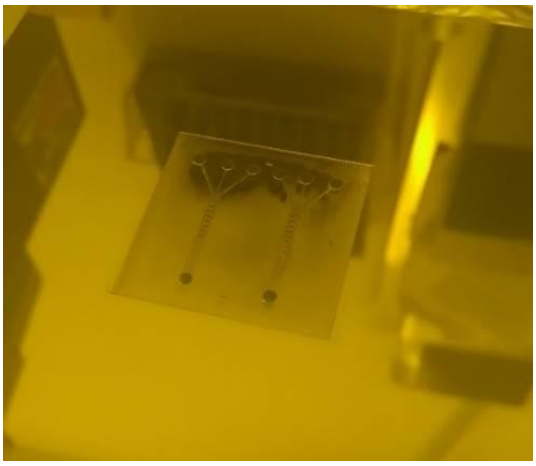

Figure 4.46. The stainless steel mask used for hot embossing.

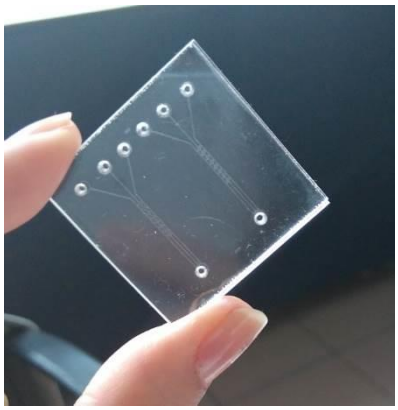

Figure 4.47. The COP made microbioreactor after bonding.

The inlets and outlets were drilled and polymer pieces were cleaned by following the same cleaning procedure as mentioned before in Section 4.5. The bonding parameters were also optimized for this new design. The two COP pieces were aligned between two glass pieces, pressurized at 50 bar (2375 lbs) and 120℃. The microbioreactor's channels were tested after bonding (Figure 4.47), by injecting acetone through the inlets. Acetone flow in channels is shown in Figure 4.48.

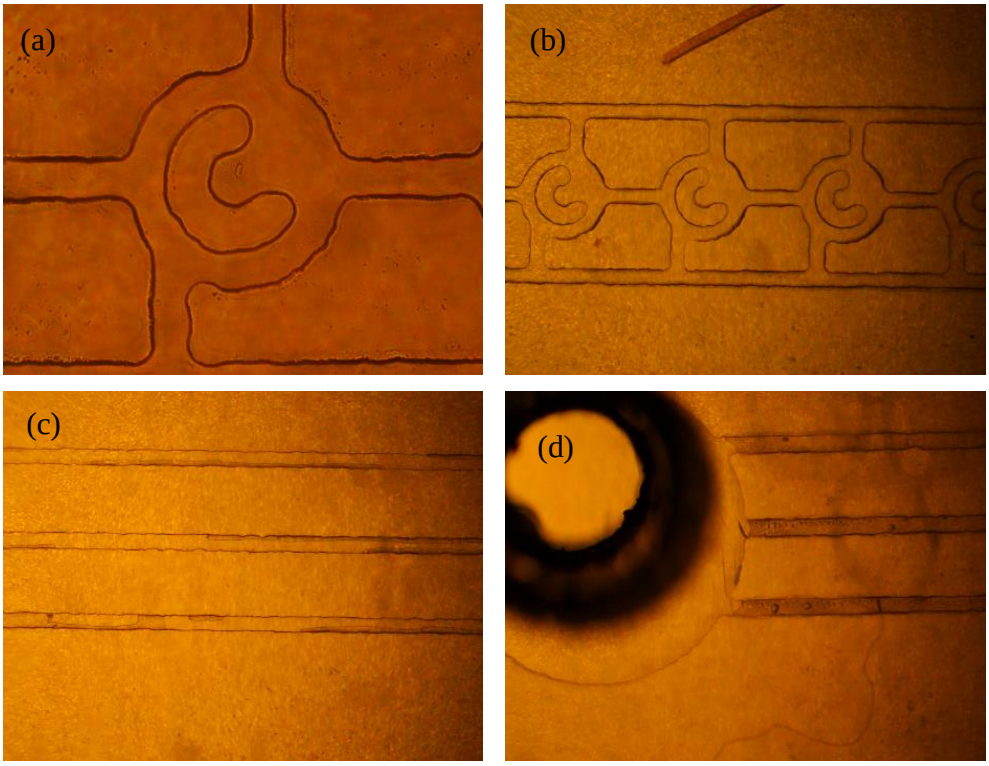

Figure 4.48. Acetone flow in the COP microbioreactor (a) an empty chamber (b) the channels filling with acetone (c) the outlet channels (d) acetone flow at the outlet.

4.6.2. Determination of Optimum Inlet Flowrates for Design-2

The aim of this simulation was to find the efficient inlet flow rates to trap the yeast cells in all c-shaped regions. In order to achieve this aim, several inlet flow rates were tested and the flow profile inside the second revised design was analyzed. Table 4.12 shows the summary of flow rates which were tested to determine the optimum velocity values in the middle and the side channels.

Table 4.12. Summary of inlet flow rates and velocities in the simulated models for new design-2.

Model	Flow rate in the middle channel (µL/min)	Flow rate in side channels (µL/min)	Chamber 8 velocity at the middle of the chamber (m/s)	Flow in C-shaped region
1	1	1	2.2×10^{-4}	Rapid
2	0.1	0.1	1.92×10^{-5}	Rapid
3	0.1	0.01	5×10^{-6}	Irregular
4	1	0.1	7.6×10^{-5}	Efficient
5	10	1	0.00126	Efficient

In the first model, same inlet velocities of 1 µL/min were used for all the three inlets. The general velocity field, first and last chambers' velocity distribution and the velocities inside the c-shaped region of the chambers are shown in Figures 4.49, 4.50 and 4.51, respectively.

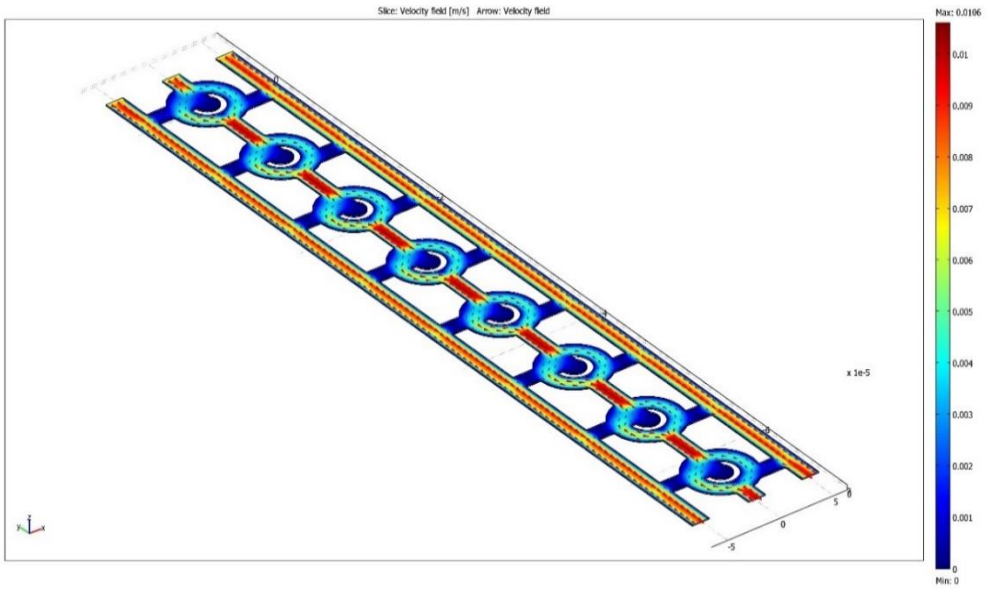

Figure 4.49. Velocity field of model 1 for new design-2.

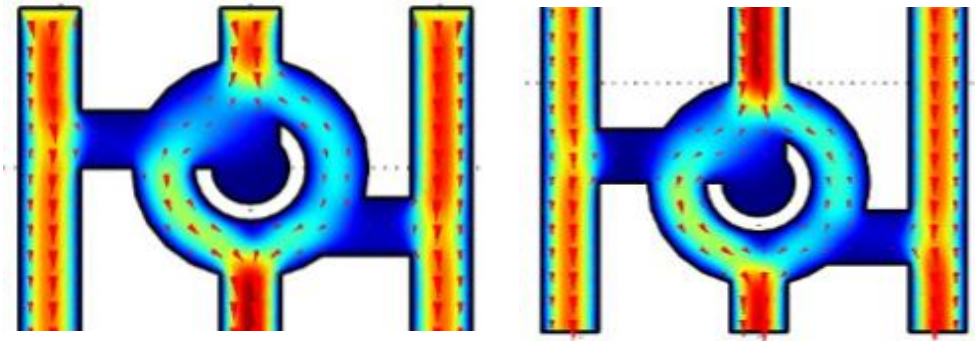

Figure 4.50. Velocity field of the first and the last chambers of model 1 for new design-2.

The color distribution through the microbioreactor showed that the flow in two side channels, between the chambers and around the perimeter of the c-shape were very rapid. The velocity in all the chambers showed the same behavior and these rapid velocity values may cause the cells to be flushed away from the trapping region. In Model 2, the inlet velocity values were decreased by 10 fold and entered as 0.1 µL/min. Model 2 had similar velocity profile as Model 1 (Figure 4.51 and 4.52). Again, the high velocity values throughout the microbioreactor appeared in all sections continuously.

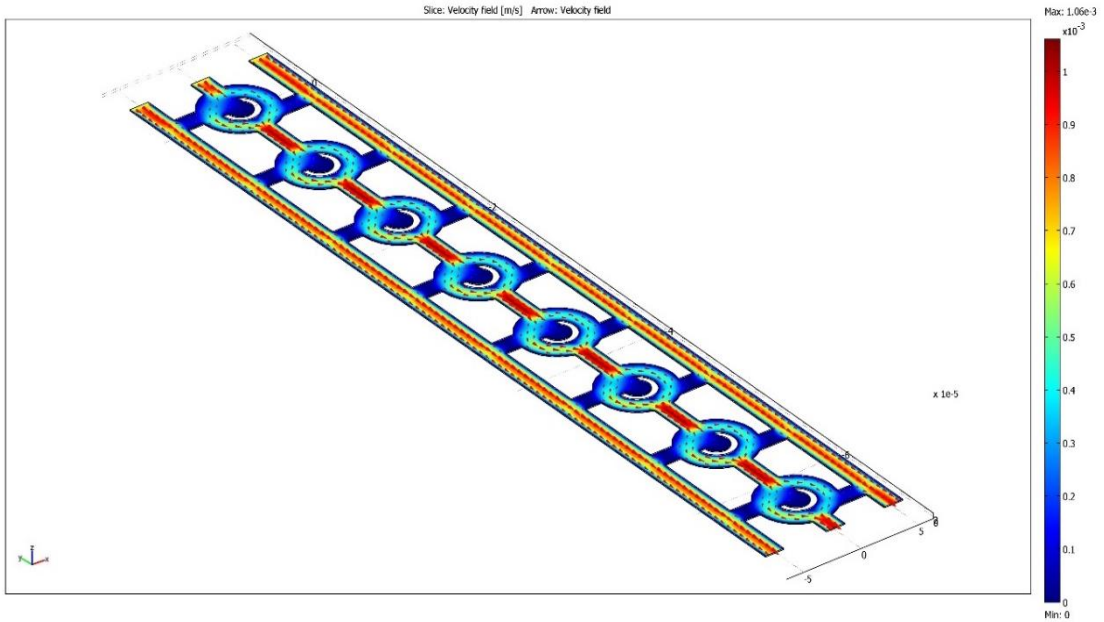

Figure 4.51. Velocity field of model 2 for new design-2.

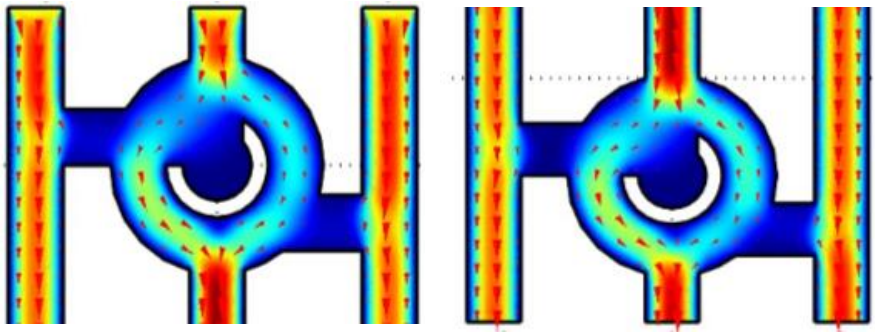

Figure 4.52. Velocity field of the first and the last chambers of model 2 for new design-2.

The velocities inside the c-shaped regions of the chambers for Models 1 and 2 are given in Figure 4.53. The velocity curves showed the same trend for these models. In model 1, the speed value at the center of the first chamber (x=0) was $1.8x10^{-4}$ m/s and higher speeds were seen in other seven chambers ($2.2x10^{-4}$ m/s). In model 2, the speed value at the center of the first chamber (x=0) was $1.59x10^{-5}$ m/s and higher velocities were seen in other seven chambers ($1.92x10^{-5}$ m/s). These proportionally rapid flows may cause inefficient trapping in the first c-shaped regions of the first chambers.

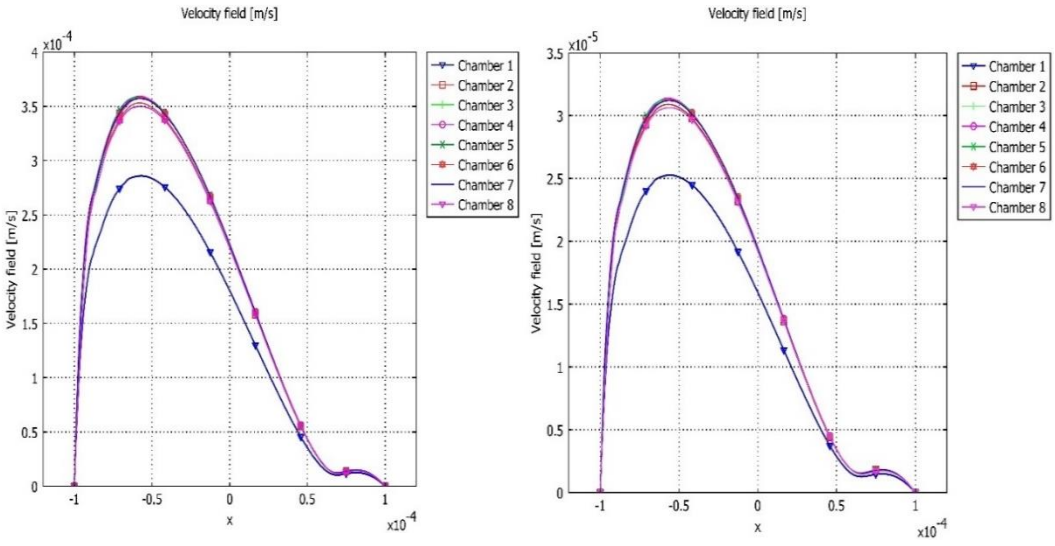

Figure 4.53. The velocities inside the c-shaped regions of the chambers of model 1 and model 2 for new design-2.

In Model 3, the inlet velocities of side channels were decreased by 10 fold. The inlet velocity values for middle and side channels were determined as 0.1 and 0.01 μL/min. The velocity profile given in Figure 4.54 showed that the velocity values in side channels were slower than those obtained by first two models. Also, flow was not so rapid in connection channels and around the perimeter of the c-shaped region (Figure 4.55). The velocity in the first chamber was higher than those in other seven chambers, though, there was not a significant velocity difference among all chambers. In Model 4, the inlet velocities of Model 3 were increased by 10 fold and almost same velocity profiles were obtained as those in Model 3 (Figure 4.56). Also, the velocity fields of first and the last chambers showed the same trend in two models.

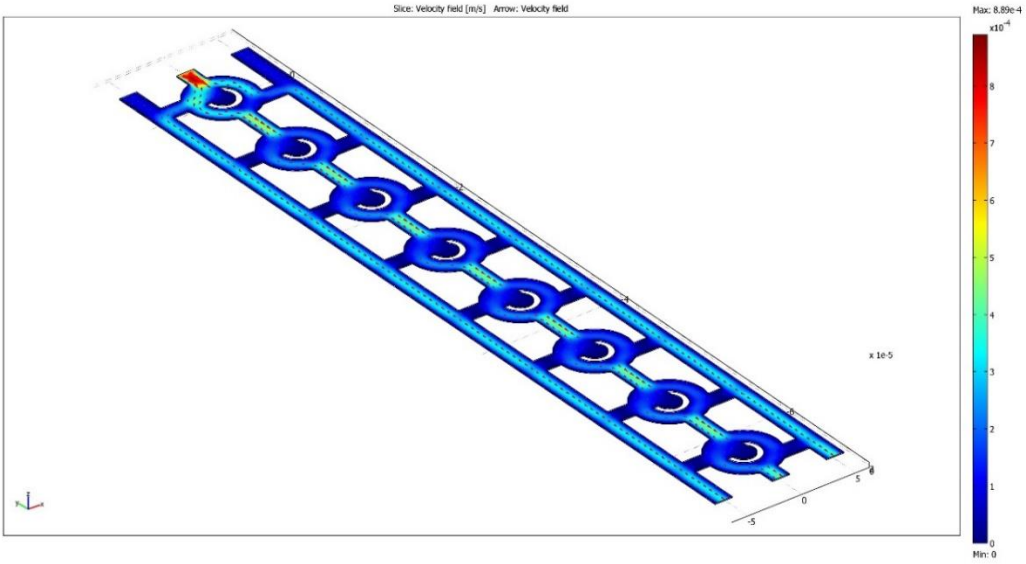

Figure 4.54. Velocity field of Model 3 for new design-2.

In Model 3, the velocity inside the first c-shaped region was irregular (Figure 5.57 and 5.58). The velocity showed a meaningless decrease from the center towards the walls of the c-shaped region. Also, it reached zero in some region ($x=-0.65x10^{-4}$ m) which may cause inefficient trapping. The speed values at the center of other seven chambers (x=0) were nearly 5×10^{-6} m/s and almost zero, which shows that cells could not reach the trapping region. In Model 4, the speed at the center of the first chamber (x=0) was $2x10^{-4}$ m/s and lower speeds were seen in other seven chambers ($8x10^{-5}$ m/s). The velocity values

were convenient for an efficient cell trapping. Also, the colors showed that the flow was not as rapid as in other models, which may prevent the flushing out.

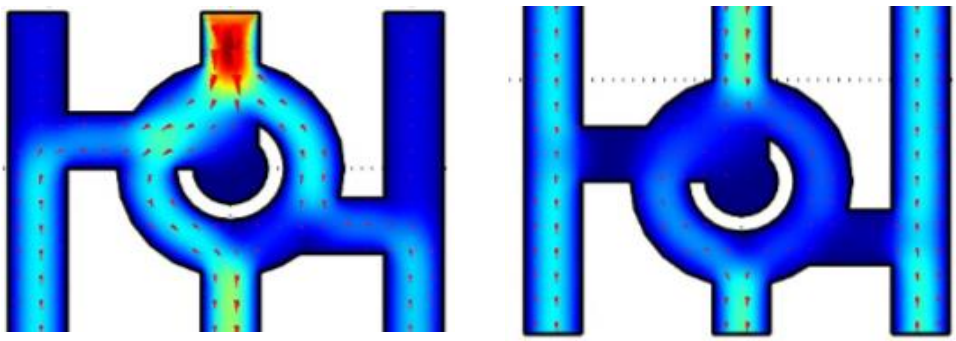

Figure 4.55. Velocity field of the first and the last chambers of model 3 for new design-2.

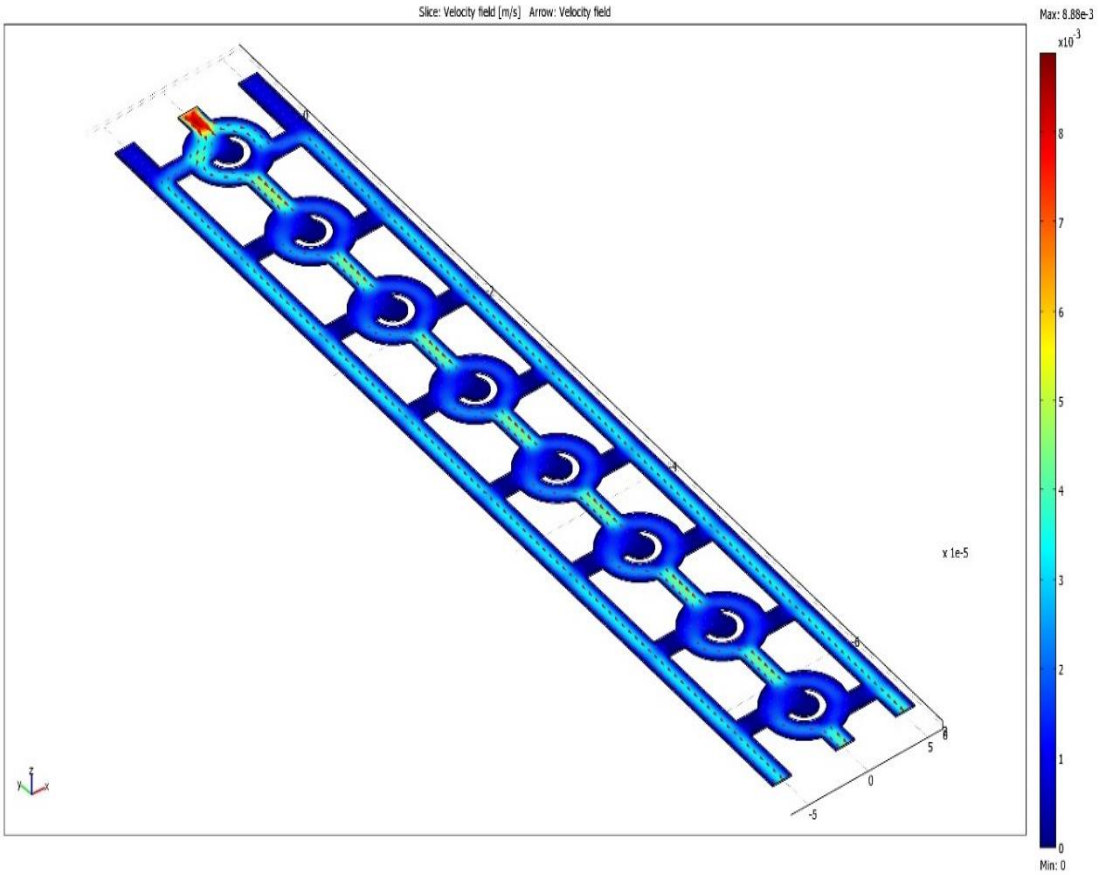

Figure 4.56. Velocity field of model 4 for new design-2.

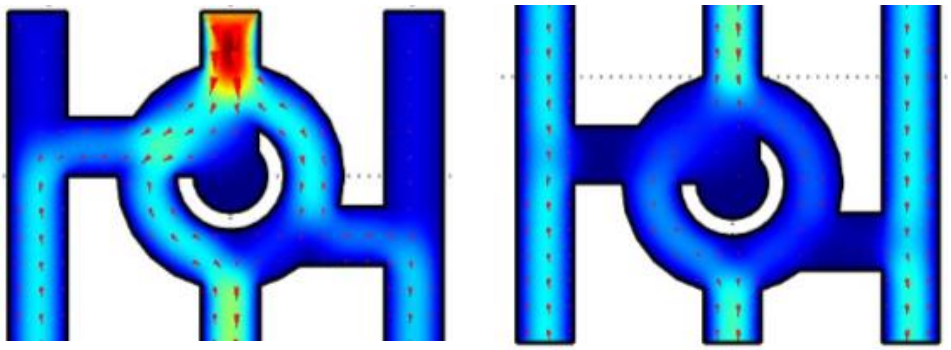

Figure 4.57. Velocity field of the first and the last chambers of model 4 for new design-2.

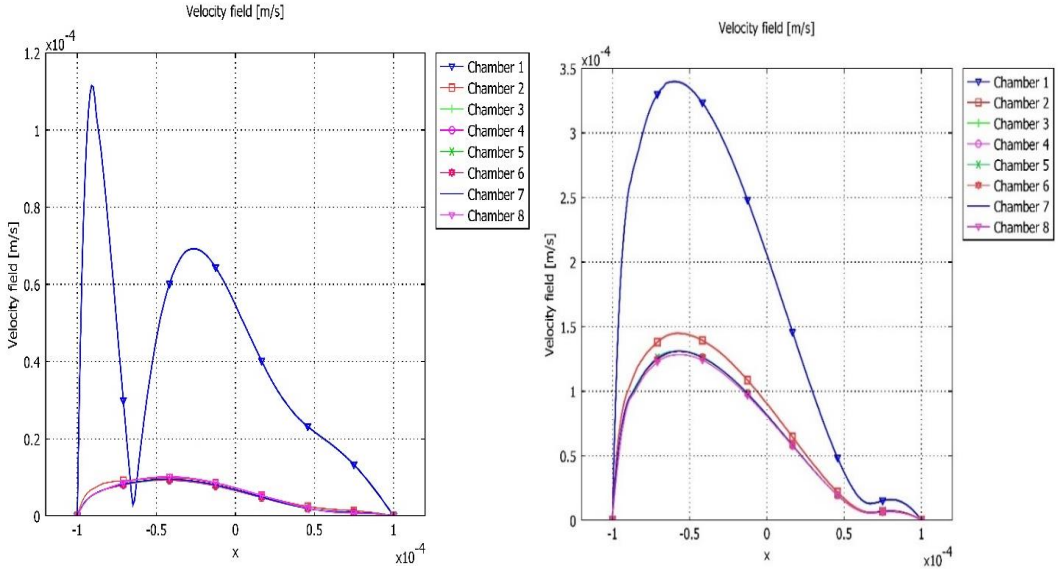

Figure 4.58. The velocities inside the c-shaped regions of the chambers of model 3 and model 4 for new design-2.

In Model 5, the inlet velocity values of Model 4 were increased by 10 fold. The general velocity field, first and last chambers' velocity distribution and the velocities inside the c-shaped regions of the chambers for Model 5 are shown in Figures 4.59-4.61. The speed at the center of the first chamber (x=0) was almost 0.0042 m/s which was higher than those obtained in other seven chambers (0.00126 m/s). The velocity profiles in chambers were same in Model 4 and 5 and selected as suitable models for an efficient cell

trapping. In the light of the simulations of velocity, pressure and concentration profiles, Model 4 (inlet velocities of 1 µL/min and 0.1 µL/min for cell and nutrient loading, respectively) is selected as the best model for efficient cell trapping. The nutrient concentration value was decreased from 111 mol/m^3 to only 107.68 mol/m^3 (2.99% decrease) and the profile was as expected. Pressure distribution and nutrient distribution graphs of Model 4 are given in Appendix B.

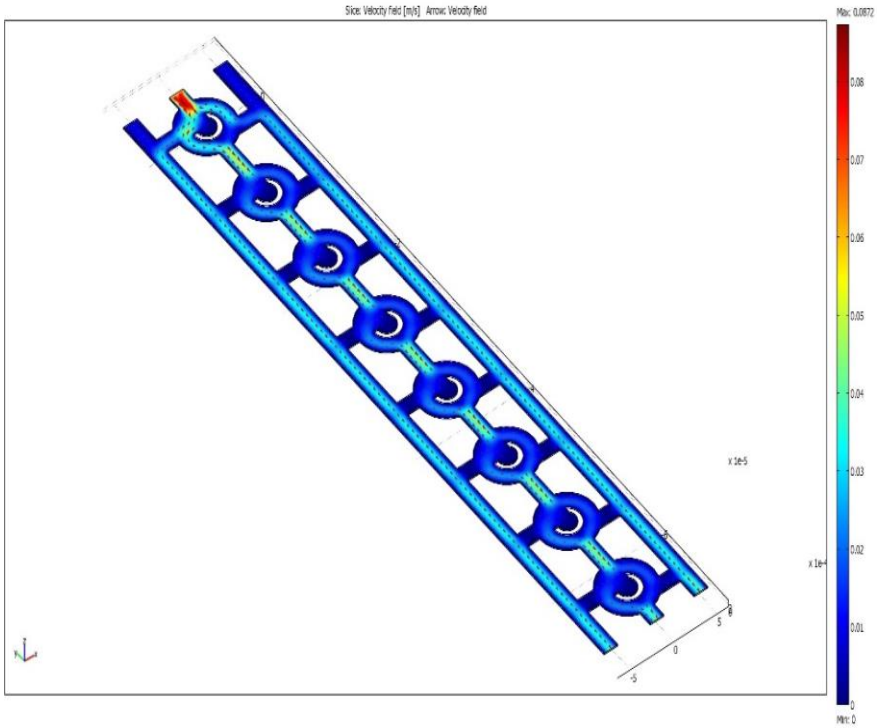

Figure 4.59. Velocity field of model 5 for new design-2.

Figure 4.60. Velocity field of the first and the last chambers of model 5 for new design-2.

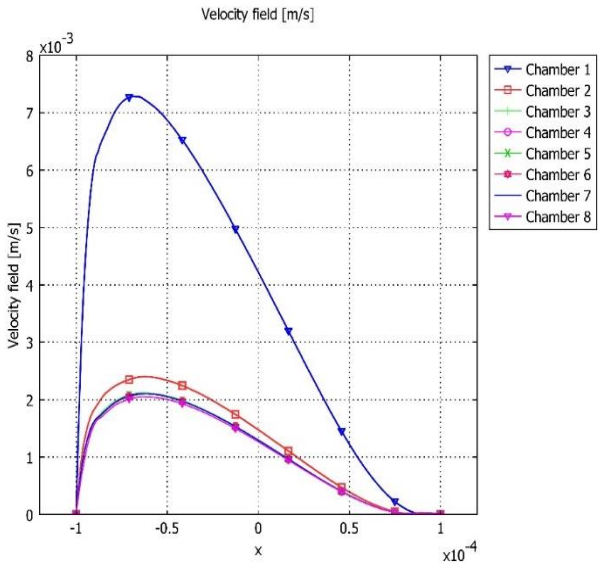

Figure 4.61. The velocities inside the c-shaped regions of the chambers of model 5 for new design-2.

4.7. Yeast Culturing in Microfluidic Device (Microbioreactor)

In order to visualize the cell culturing in the home-made microfluidic device, GFP tagged YOR060C strain (*Saccharomyces cerevisiae*) was used for the experiments and medium types were varied for each experiment.

4.7.1. Growth Experiments with Rich YPD Medium (E1Y)

The Lab-on-a chip platform was prepared for yeast experiments. The microfluidic device (consists of chambers of 0.13 nL volume) was mounted on the stage of Nikon Eclipse Ti inverted fluorescence microscope. 4 connection tubings for inlet and outlet ports were inserted by using epoxy and dried at room temperature for 3 hours. The syringe pumps were prepared for yeast cell and media loading. Diluted yeast preculture (Optical Density=0.5) was filled into 5 mL syringe. Three 50 mL syringes were filled with YPD medium. Tubings connected to the device were located on the microscope stage. The three YPD medium filled syringes were located in the syringe pumps and their rates (1μL/min) and diameters were set and perfusion through the chip was started. When all the chambers

were filled with YPD medium, yeast cell loading was initiated through the middle inlet at a rate of 0.1μL/min. After cell loading, nutrient feeding at a rate of 1 μL/min through all channels was done for 12 hours. The experimental setup is shown in Figure 4.62.

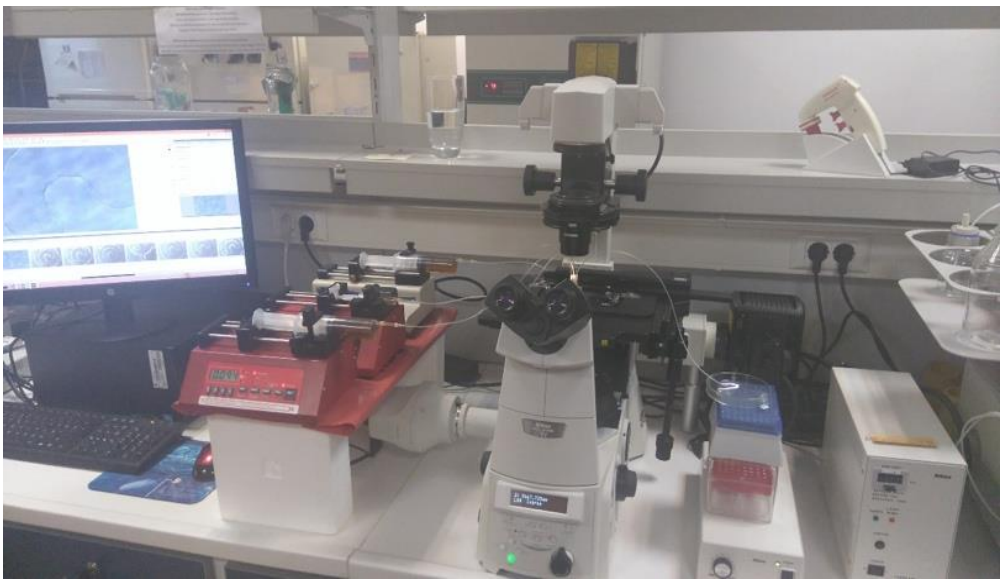

Figure 4.62. Experimental setup.

The yeast cells were imaged under 40X objective by using Ph2 condenser filter and both bright field and fluorescence images were taken at one hour time intervals. All the taken photos were processed by using Fiji/ImageJ software and the parameters such as cell count, cell area and cell perimeter of GFP tagged yeast strain (YOR060-GFP) were determined and the results are given in the following sections. The integrated density values obtained from fluorescence images were used to obtain the amount of luminescence for cell concentration.

The duration of experiment was 20 hours. Approximately, 15 chips of Design-2 were used in this experiment (E1Y). The preparation of inlet connections took 3 hours. After the connections were done, the first chamber was filled with YPD medium in 1 hour and perfusion of the whole microbioreactor approximately took 5 hours. After the perfusion, the yeast cells were loaded through the middle inlet and the experiment was stopped after 12 hours. The problem in this setup was the leakage of the medium from inlets through the intersection of the epoxy and polymer. Because of the leakage, direction of flow changed

after 10 hours and some air bubbles appeared in the channels. After a while, yeast cells were started to flow back and the experiment had to be finished.

4.7.1.1. Chamber 1. Most of the yeast cells were efficiently trapped in the first chamber. Because of the narrow gap between the c-shape and the cover, medium also filled on top of the c-shape and some cells were trapped in this area beside the determined trapping region. Here, Figure 4.63 shows the initial yeast cells started to be trapped in the first chamber after one hour from the start of the cell loading. Figure 4.64 shows the perfectly trapped cells at 60^{th}, 120^{th} and 180^{th} minutes of the experiment.

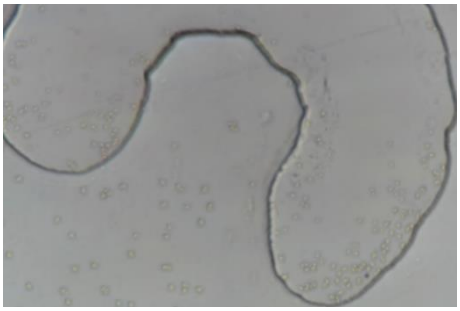

Figure 4.63. The yeast cells in the first chamber.

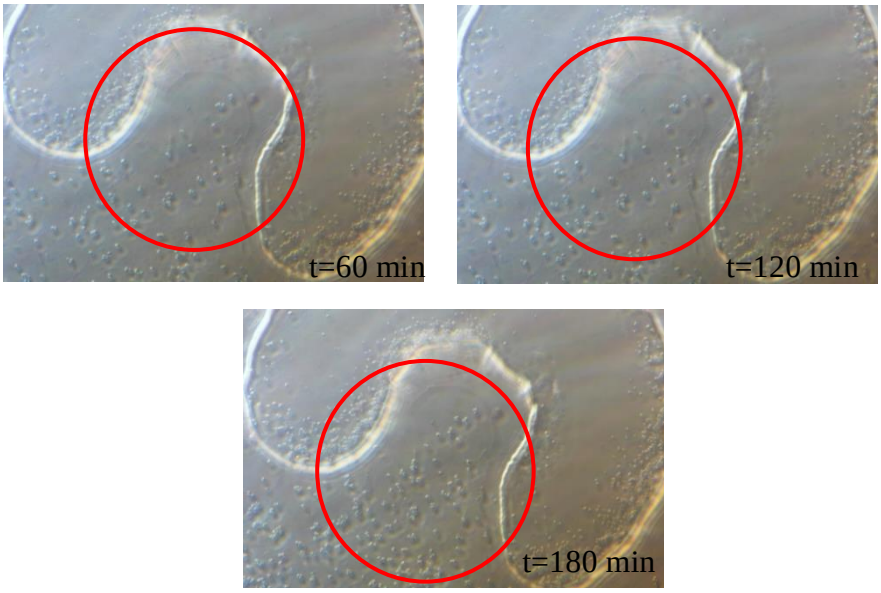

Figure 4.64. The trapped yeast cells in the trapping region of chamber 1.

The yeast cells in the images were processed by taking the area of trap region without considering the cells trapped on top of the c-shape. The cell count, cell area and cell perimeter were determined for each chamber respectively (Figure 4.65 and 4.66). According to Figure 4.65a, the cell number was zero at the beginning of the yeast cell loading experiment. After 60 minutes, cells were started to fill in the c-shaped trapping region. The cell number started to increase slowly between 60th and 240th minutes and sharply increased between 240th and 360th minutes.

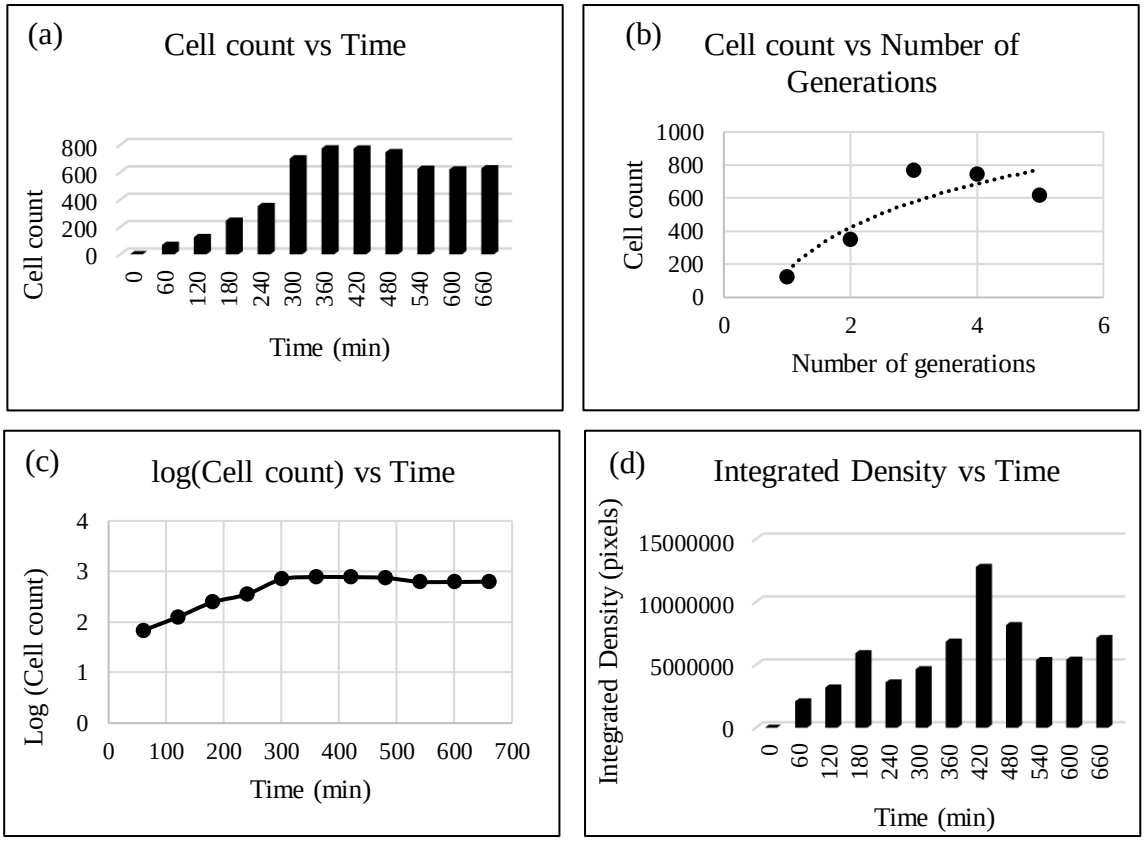

Figure 4.65. Graphical display of processed data for chamber 1 (a) cell count vs time graph (b) cell count vs number of generations graph (c) log(cell count) vs time graph (brightfield images) (d) integrated density vs time graph (fluorescence image)-E1Y.

The cell cumber was increased from nearly 200 to 800 throughout 5 generations (Figure 4.65b). Here the exponential growth of the GFP tagged YOR060C yeasts can clearly be seen in Figure 4.65c. At the time interval of 300 to 480 minutes, the cell number

remained same which showed the stationary phase of the cell growth. After 480th minute, cell number started to decrease and remained same until the end of the experiment. Yeast culturing was performed successfully in the first chamber. The integrated density of GFP tagged cells were also analyzed to see the change in the amount of luminescence during the culturing. The fluorescence images were processed and results are shown in Figure 4.65d. The integrated density vs time graph showed similar behavior as cell count. At 420th minute, a sharp increase was also seen. This may be because of the distribution of fluorescence signals of yeast cells. In some cases, while the cells started to form clusters, the signals come closer and seen as one big signal point. In Figure 4.66a, the change in cell area with time is given for the first chamber. The behavior of the area change was very similar to that of cell count change.

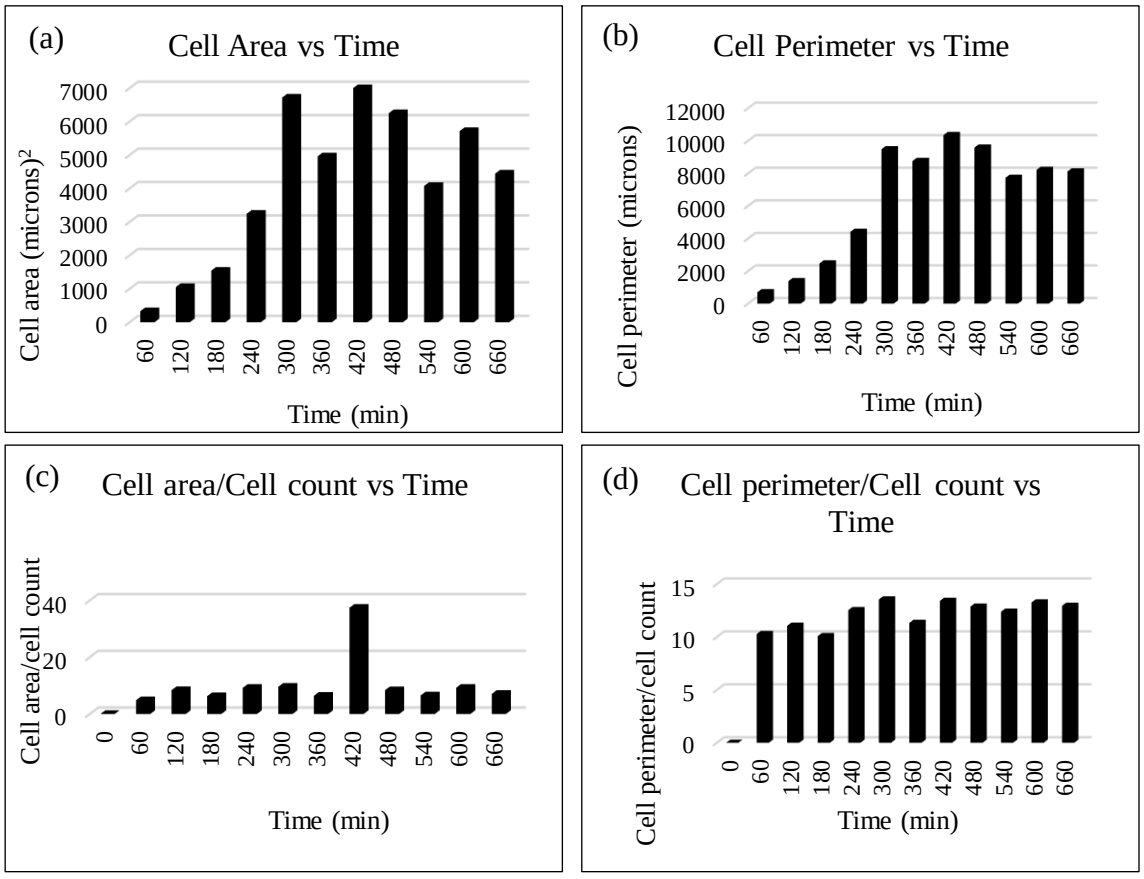

Figure 4.66. Graphical display of processed data for chamber 1 (a) cell area vs time graph (b) cell perimeter vs time graph (c) cell area/cell count vs time graph (d) cell perimeter/cell count vs time graph (brightfield images)-E1Y.

The cell area was started to increase from 60th to 240th minutes and sharply increased between 300th and 480th minutes. The cell area difference between 420th and 480th minutes was greater than those in other intervals. This may be due to the aggregation of the cells and the separation of these cells in image processing was more difficult. The cell perimeter for the first chamber showed an increase through at the experiment. After 480th minute, cell perimeter started to decrease and remained same. The cell perimeter/cell count vs time graph is given in Figure 4.66d. As cell number increases the cell perimeter should also increase and this ratio need to remain same for all time. The cell area/cell count values at 60th, 180th and 360th minutes were smaller than others, the values almost remained same at all times (Figure 4.66c).

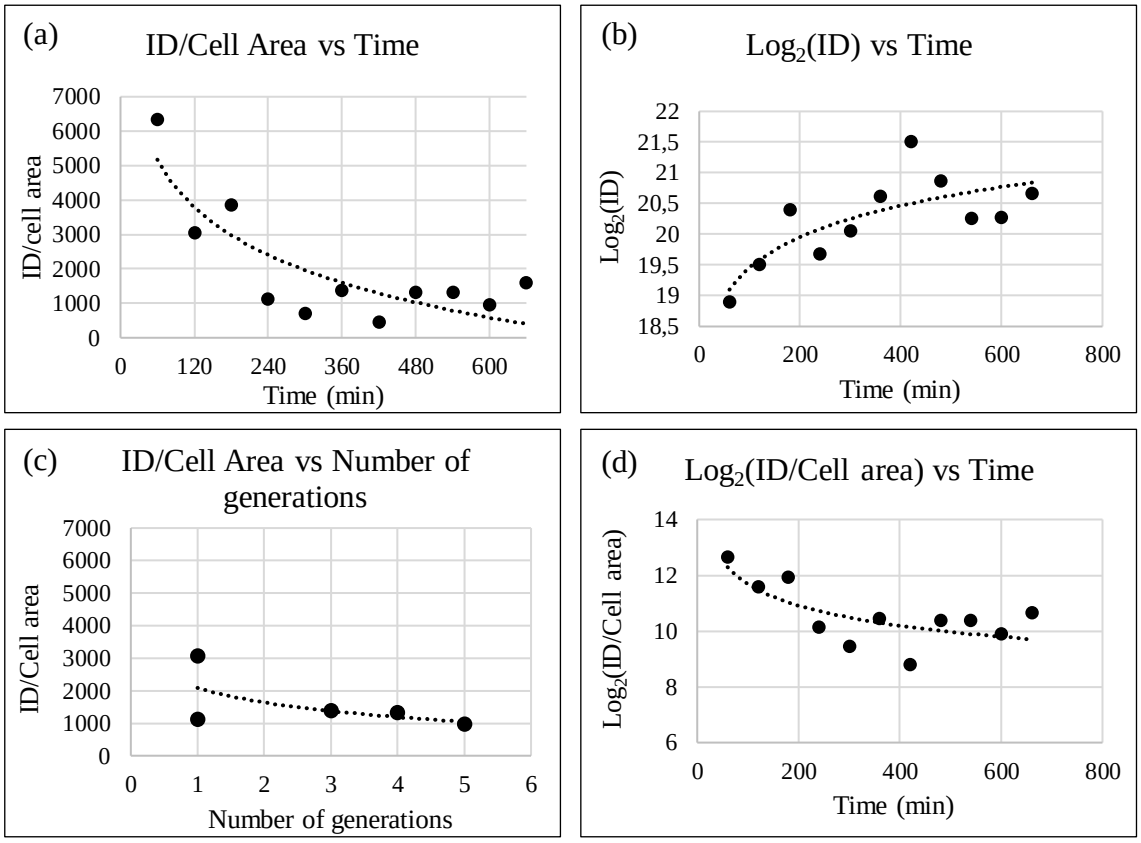

Figure 4.67. Graphical display of processed data for chamber 1 (a) integrated density/cell area vs time graph (b) log(integrated density) vs time graph (c) integrated density/cell area vs number of generations (d) log(integrated density)/cell area vs time graph-E1Y.

As the cell numbers increase by time, the total cell area is expected to increase like cell perimeter/cell count relation. The cell area/cell count ratio was almost same but at the 420th minute there was a sharp increase. As the cell number was increased during the experiment, area of the cells was also increased and fluorescence signals become more detectable. According to Figure 4.67c, integrated density/cell area ratio was shown a constant trend along the generations.

4.7.1.2. Chamber 2. The cells were trapped in the c-shaped region of the second chamber efficiently. Figure 4.68 shows the perfectly trapped cells at 300th, 360th and 420th minutes of the experiment.

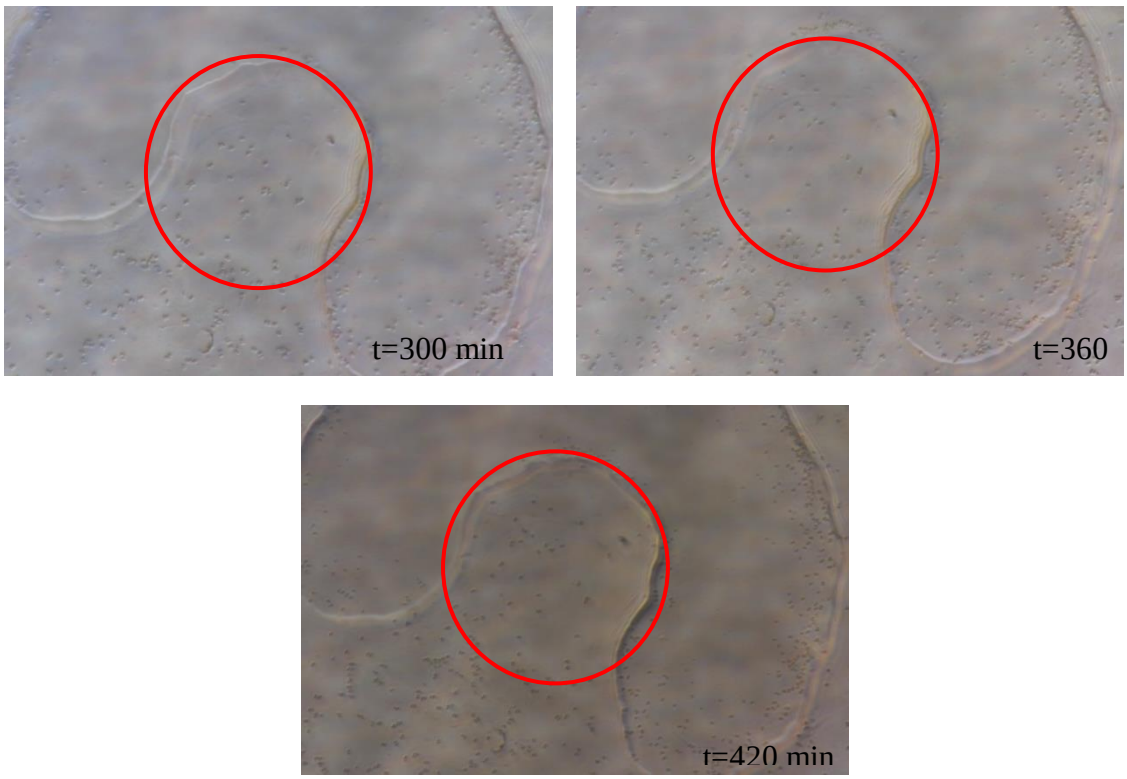

Figure 4.68. The trapped yeast cells in the trapping region of chamber 2.

The brightfield images of Chamber 2 were processed and cell count, cell perimeter, cell area and integrated density graphs are given in Figure 4.69. The cell number was zero at the beginning and first cells were started to be trapped in the c-shaped region at about

120th minute. Cell number increased slowly in 3 hours, between 120th and 360th minutes. There was a sharp increase in cell number from 240th to 300th minute interval. The cell number almost remained same between 360th and 660th minutes (Figure 4.69a). The logarithmic change in cell number with time is shown in Figure 4.69c. Here, at first two hours, no cells were trapped in the trapping region. From the 120th minute onwards, the cell number started to increase exponentially (exponential growth phase) and remained same until the experiment stopped (stationary phase). The cells were first trapped at 120th minute and number of cells were reached almost 400 during 5 generations (Figure 4.69b).

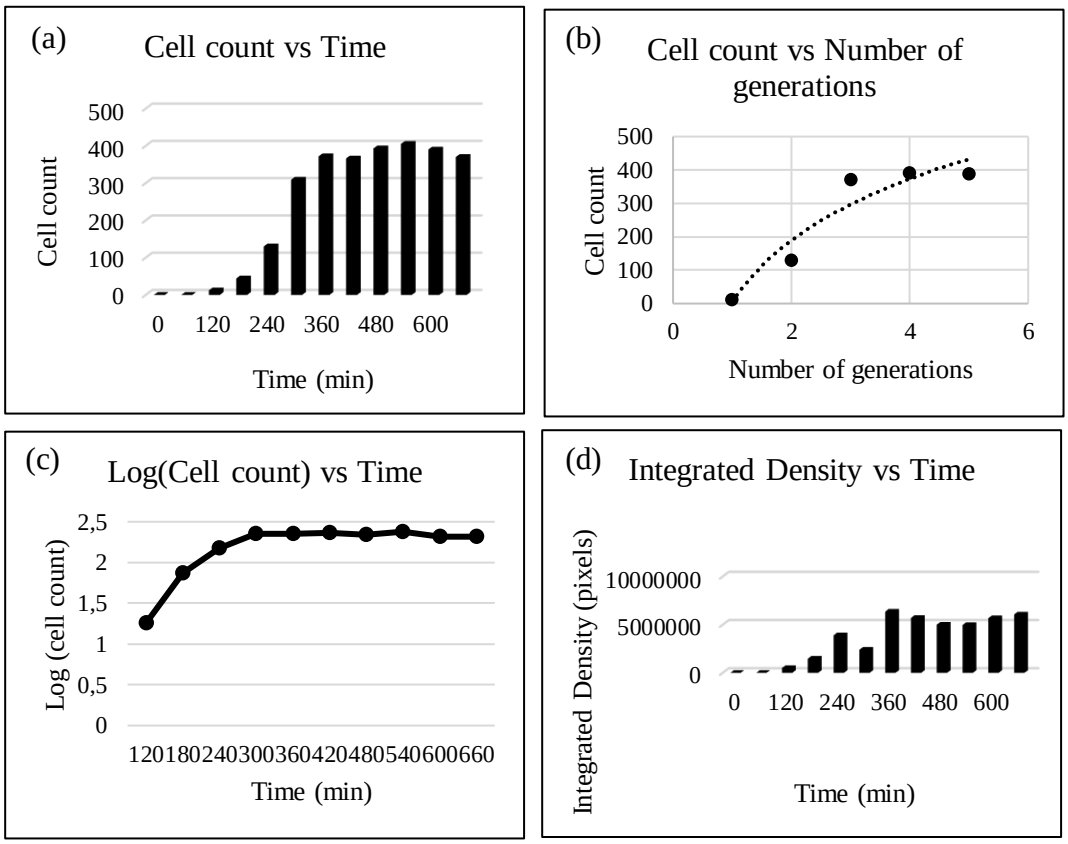

Figure 4.69. Graphical display of processed data for chamber 2 (a,b) cell count vs time graph (c) log(cell count) vs time graph (brightfield images) (d) integrated density vs time graph (fluorescence image)-E1Y.

The fluorescence images were also processed to see the integrated density change during the experiment. When the cells started to grow and divide, the integrated density is

expected to increase by the increasing fluorescence signals. The integrated density was found to increase until 360th minute in agreement with cell count, but there was a degradation at 300th minute (Figure 4.69d). Some signals might become invisible under microscope because of the sedimentation of cells. After 300th minute, integrated density again started to increase as expected. The cell area was increased as the cell number increased which was as expected result (Figure 4.70a). At the 480th minute of the experiment, the increment in cell area was bigger than those obtained in other time intervals. This may be because of the aggregated cells in this region and while processing, the cells could not be divided more than twice. The cell perimeter was expected to increase by time and Figure 4.70b supports this. Same as cell area graph, at 480th minute the perimeter increased more than those in other time intervals. This may also be explained by aggregated cells with bigger area and perimeter.

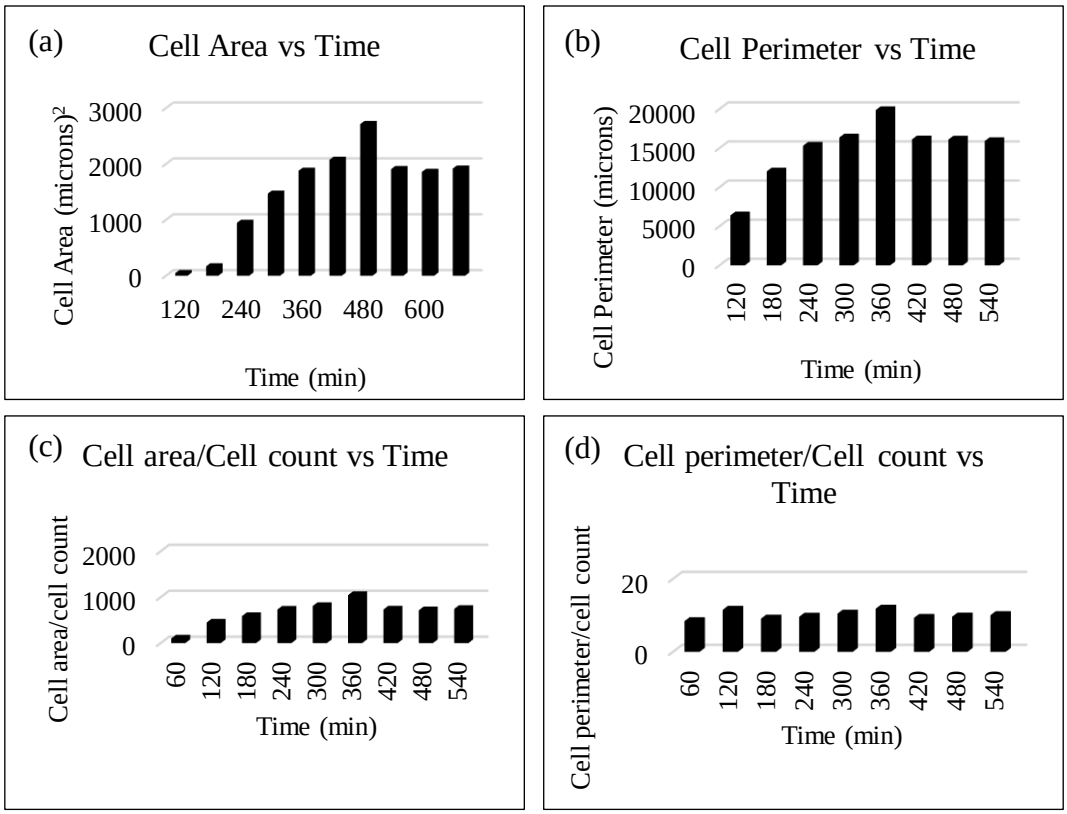

Figure 4.70. Graphical display of processed data for chamber 2 (a) cell area vs time graph (b) cell perimeter vs time graph (c) cell area/cell count vs time graph (d) cell perimeter/cell count vs time graph (brightfield images)-E1Y.

Cell area/cell count change by time was also analyzed for chamber 2. As shown in Figure 4.70c, there was a constant ratio seen after the cells started to be trapped in the determined c-shaped region. Also, cell area/cell count ratio remained almost same during the experiment. The cell perimeter/cell count vs time graph is shown in Figure 4.70d. The ratio was higher at 240th and 480th minutes but the difference among all data points was not significant. According to Figure 4.71, log2 based values of integrated density were remained constant at the value of nearly 22.5 throughout the generations.

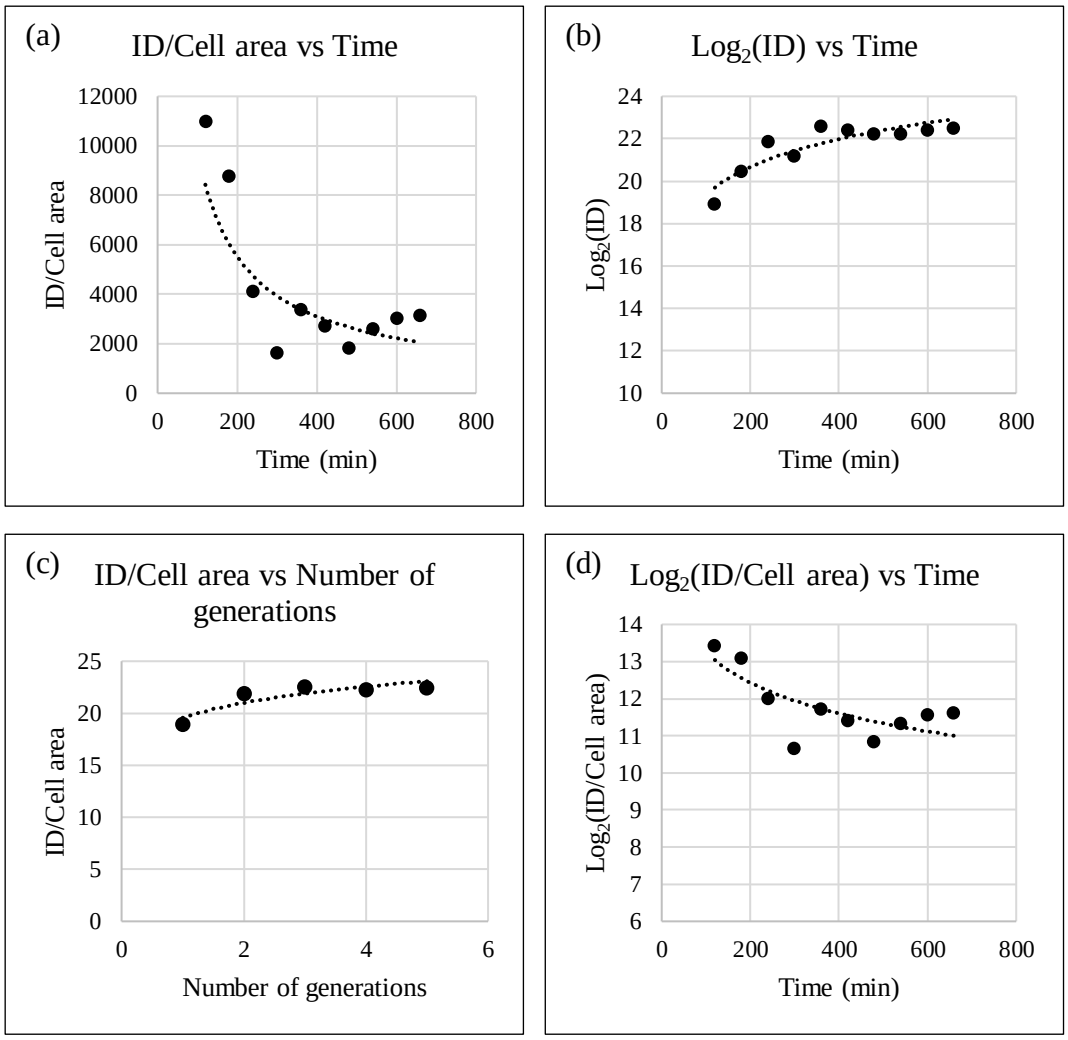

Figure 4.71. Graphical display of processed data for chamber 2 (a) integrated density/cell area vs time graph (b) log(integrated density) vs time graph (c) integrated density/cell area vs number of generations (d) log(integrated density)/cell area vs time graph-E1Y.

4.7.1.3. Chamber 3. The brightfield and fluorescence images of the third chamber were also analyzed. The cell count, cell area and cell perimeter graphs are given in Figure 4.72 and Figure 4.73. According to cell count vs time graph, the cells started to be trapped at about 120th minute. Integrated density changes with time graph (Figure 4.72d) also supports this. The decrements in Figure 4.72a may be because of the sedimentation of the cells. The number of cells trapped in the third chamber was less than those of first two chambers. The backflow, happened after a while, may cause the forward flowing cells to go in opposite direction and may lead to cell loss in chamber 3. Therefore, a very low number of cells were trapped in the fourth chamber and the cells could not reach beyond 4th chamber. First cells were trapped in the c-shaped region at 120th minute and counted cell number was 100 at the 5th generation (Figure 4.72b). Figure 4.72c shows the logarithmic change in cell number with time.

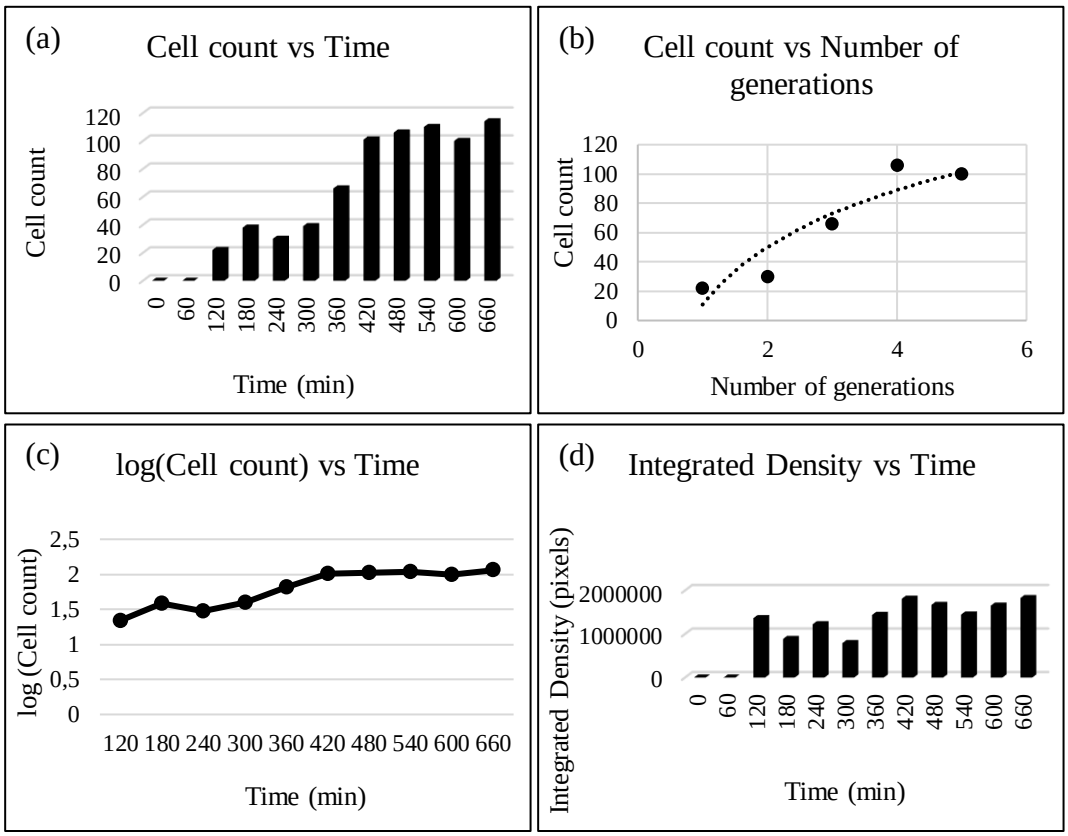

Figure 4.72. Graphical display of processed data for chamber 3 (a,b) cell count vs time graph (c) log(cell count) vs time graph (brightfield images) (d) integrated density vs time graph (fluorescence image)-E1Y.

The changes in cell area and cell perimeter with time were expected to increase with increasing cell number in the c-shaped region. Figure 4.73a and 4.73b also show that, the cell area and perimeter started to increase at 120th minute and there was an increasing trend in the area during the experiment. Some small fluctuations may be due to the image processing step. The cell area / cell count and cell perimeter / cell count graphs were plotted to see whether the ratios were constant or not (Figure 4.73c and d).

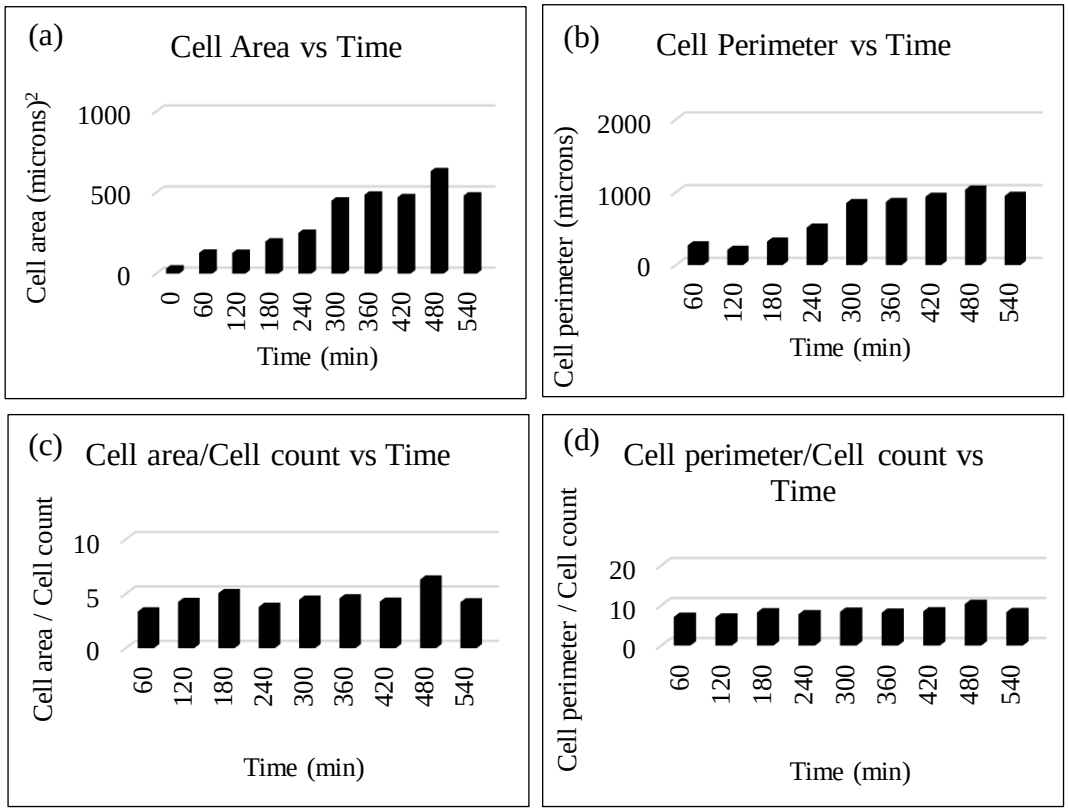

Figure 4.73. Graphical display of processed data of chamber 3 (a) cell area vs time graph (b) cell perimeter vs time graph (c) cell area/cell count vs time graph (d) cell perimeter/cell count vs time graph (brightfield images)-E1Y.

While cells were started to be trapped and budding, some budded cells were seen as one big cell in the processing step. The cells could be divided mostly twice in the imaging software but it was not possible to portion the cells as much as we want. Therefore, the cell clusters were sometimes counted as one big cell. The change in the ratio of cell perimeter/cell count with time was almost constant during the experiment, as shown in

Figure 4.73. The log2 based integrated density to cell area ratio was high at the beginning of the experiment. After 240th minutes, the grown daughter cells were started to separate from mother cells and their area were also taken into account. The ratio almost remained constant after this point (Figure 4.74d). Integrated density / cell count change by time graphs are given in Appendix C.

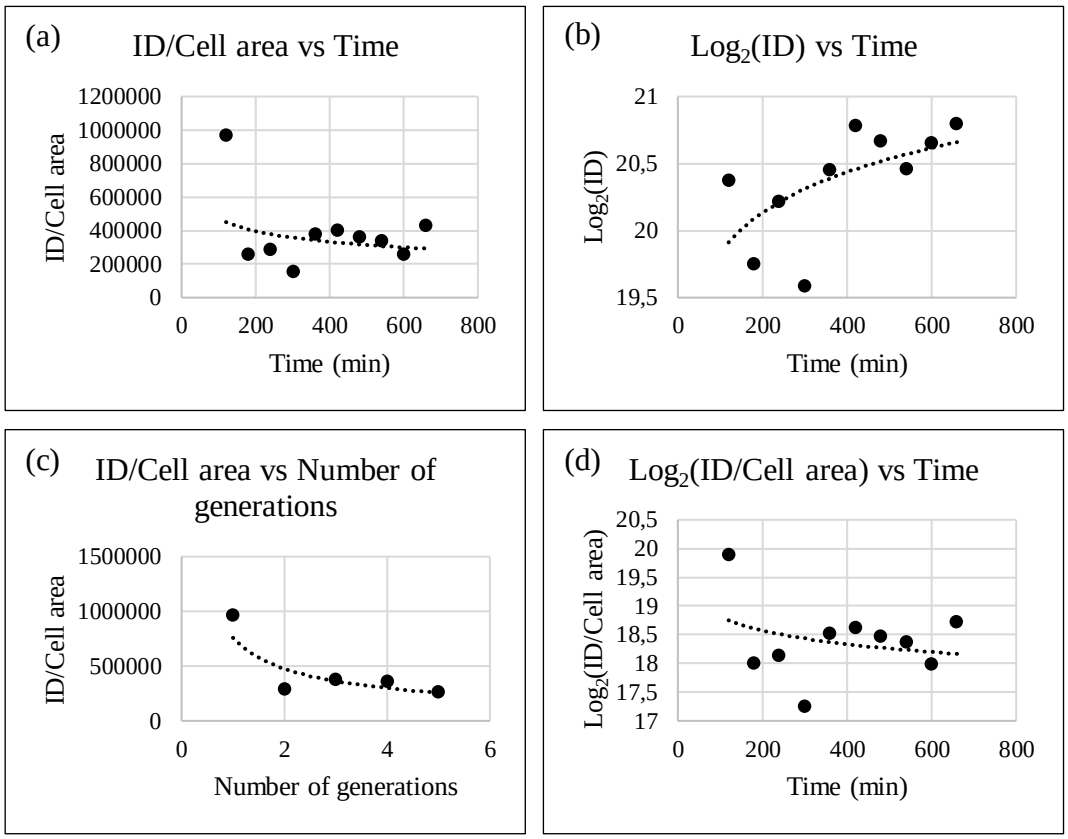

Figure 4.74. Graphical display of processed data for chamber 3 (a) integrated density/cell area vs time graph (b) log(integrated density) vs time graph (c) integrated density/cell area vs number of generations (d) log(integrated density)/cell area vs time graph –E1Y.

4.7.2. Growth Experiments on Caloric Restriction with YPD medium (E2Y)

The second type of experiments were done via using the chips bonded at different parameters. The chips bonded at 125 °C by applying different pressures (45, 35, 30 and 25 bars) were tested. Approximately, 15 chips of Design-2 were used in this experiment

(E2Y). The medium loading was started at an inlet flow rate of 1 µL/min and continued until all channels were filled with 0.2% glucose containing medium.

For the chips bonded at 45, 35 and 30 bars, after a while leakage of the medium from the inlets through the intersection of the epoxy and surface of the polymer piece occurred. The flow could not reach to outlet of the microfluidic device because of this leakage problem. The chip which was bonded at 25 bar was filled with medium faster than other three chips and no leakage occurred. Also, the excess flow was collected from outlet ports continuously during the experiment. After all the channels were filled with medium, the diluted yeast culture started to be introduced through the middle channel at a rate of 1 µL/min. The cells reached the first chamber rapidly and filled in all chambers one by one. Unfortunately, a vortex flow occurred in the c-shaped regions and the cells left the c-shaped regions immediately. The flow rate was decreased to 0.1 µL/min and the medium flow was stopped to get rid of this vortex. Rapid removal of the cells slowed down, but the vortex flow was still not prevented by the 10 folds decrease in flow rate. The medium loading was continued for 8 hours to reach steady state. After 8 hours, the vortex flow did not stop and this experiment had to finish. The leaving path of the cells is shown in Figure 4.75.

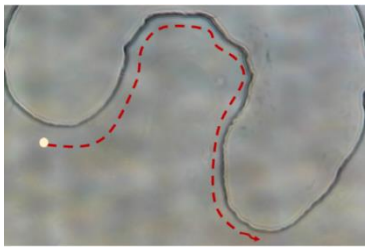

Figure 4.75. The leaving path of the cells.

4.7.3. Growth Experiments with Low Auto-fluorescence YNB medium (E3Y)

The third set of experiments were done by the chips (microbioreactors) bonded at 25-30 bar. Approximately 10 chips of Design-2 were used in this experiment (E3Y). The YNB medium (2% glucose) without histidine was used for both cell culturing and medium

loading steps. At the medium loading step, the flow rates were set to 5 μL/min and the medium was observed to fill all the channels. The leakage of the medium from the intersection of the polymer and epoxy occurred in some devices. The cell size used in this set of experiments (E3Y) was larger than the cells used in first two experiments (E1Y and E2Y). Yeast cells were at their exponential phase of growth when they were introduced into the microfluidic device.

The cell culture was filled into a 5 mL syringe. In yeast loading step, at the beginning very low flow rates were used for the middle inlet (0.01 μL/min). Even at very low flow rates, the cells started to trap at the wall of the inlet hole. The rate was increased step-wise. At the flow rate of 0.1 μL/min, the cells still could not overcome this wall barrier. The cells then forced to flow at the flow rate of 1 μL/min through the channel. Nevertheless, they could not pass the inlet of the first chamber and caused a clogging in this region. The explanation of the problems faced during the experiments up to now and possible reasons are discussed in Section 4.8. After clearing out all the problems, a new set of experiments using YNB medium (2% glucose) without histidine was performed and explained in the following section.

4.7.4. Growth Experiments with rich YNB medium (E4Y)

The device (microbioreactor) was revised by integrating a new inlet unit. The yeast cells were again cultured in rich (%2) YNB medium without histidine. After all the channels were filled with YNB medium, yeast loading was started through the middle inlet. The yeast cells were trapped in the first four chambers efficiently. The growth of yeast cells and the expression of Sld7p-GFP fusion protein were monitored. After 15 hours, air bubbles appeared in the channels and these air bubbles started to sweep away the cells from their trapping regions. The experiment was stopped at this point and collected images of all chambers were processed.

4.7.4.1. Chamber 1. The yeast cells started to be trapped at the c-shaped region of the first chamber after 30 minutes. The image of the colony of yeast cells after 240 minutes is shown in Figure 4.76. As the behavior of yeast cells was similar to those of previous

experiments, the results of first chamber were analyzed for this experiments. Except some deviations, the cell count was increasing with respect to time over about 4 generations (Figure 4.77). The integrated density also showed an increasing trend with respect to time (Figure 4.77d).

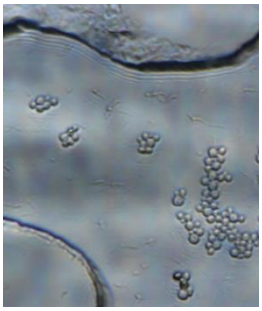

Figure 4.76. The colonies of yeast cells-E4Y (40X objective).

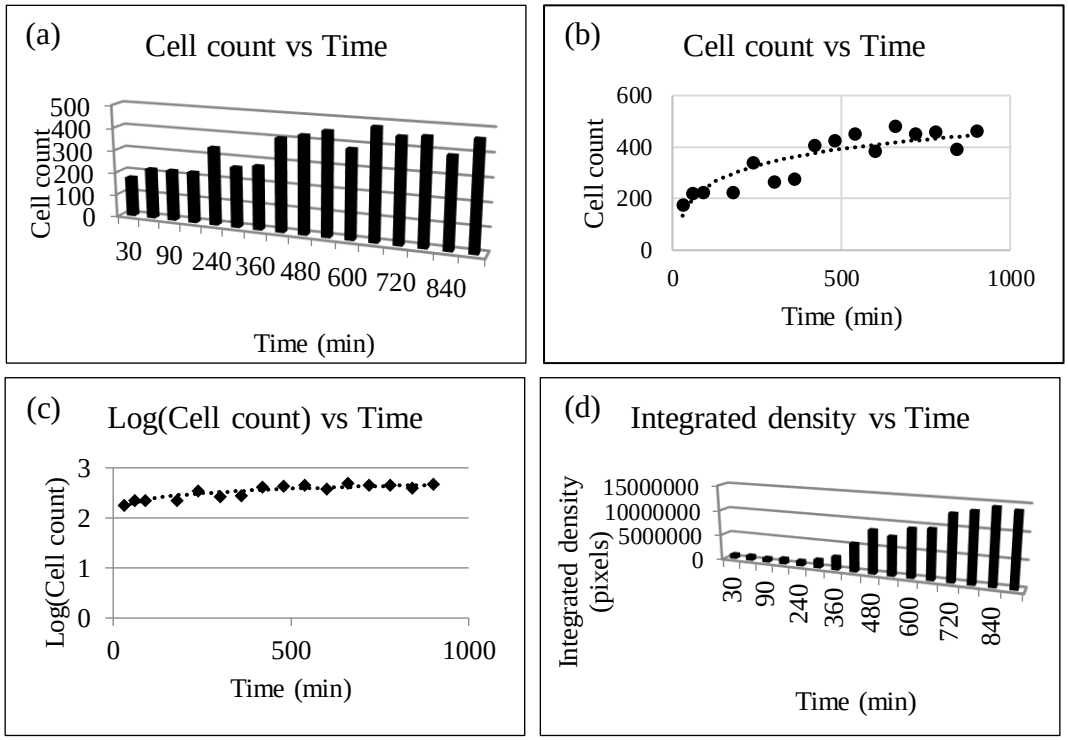

Figure 4.77. Graphical display of processed data for chamber 1 (a,b) cell count vs time graph (c) log(cell count) vs time graph (brightfield images) (d) integrated density vs time graph (fluorescence image)–E4Y.

The time profiles of cell area and cell perimeter also showed the same trend as the cell count (Figure 4.78a and Figure 4.78b). Thereafter, no significant change was observed for cell count. Except the fluctuation at some points, the cell area/cell count and cell perimeter/cell count results showed almost constant trends during the experiment (Figure 4.78c and Figure 4.78d).

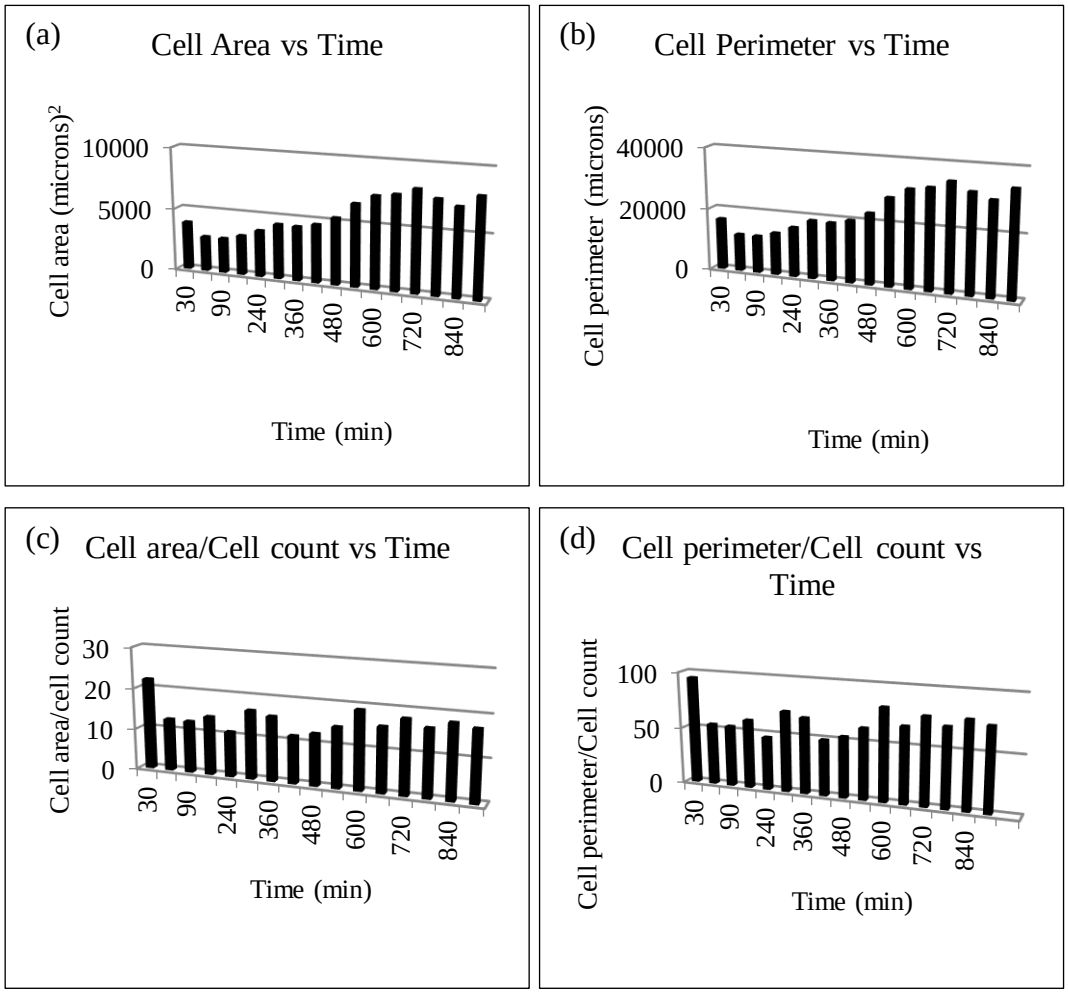

Figure 4.78. Graphical display of processed data of chamber 1 (a) cell area vs time graph (b) cell perimeter vs time graph (c) cell area/cell count vs time graph (d) cell perimeter/cell count vs time graph (brightfield images)-E4Y.

When the change in integrated density/cell area with respect to time was analyzed, there was an increasing trend in expression of Sld7p-GFP fusion till the 400th minute which corresponds to duplication time and end of budding phase (Figure 4.79a). After 400th

minute, the signal appeared to increase up to 800th minute, which corresponds to the end of second budding phase.

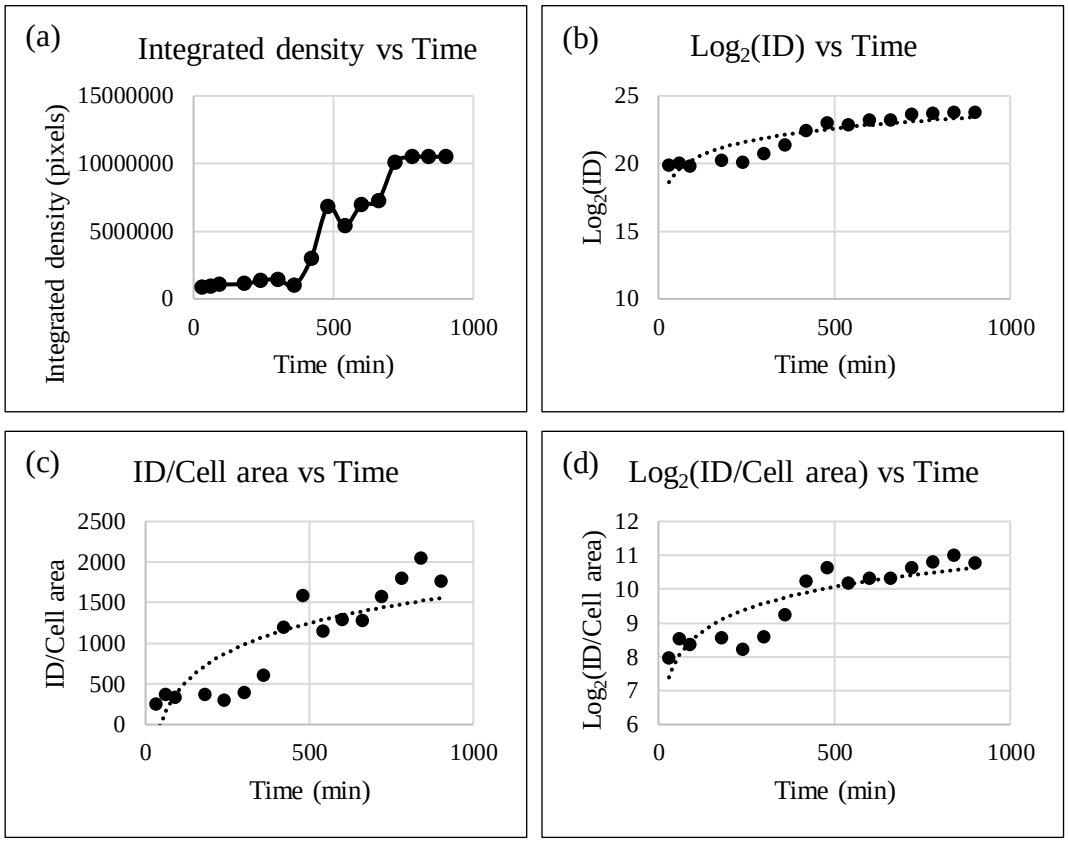

Figure 4.79. Graphical display of processed data for chamber 1 (a) integrated density vs time graph (b) $\log_2$(integrated density) vs time graph (c) integrated density/cell area vs time graph (d) $\log_2$(integrated density)/cell area vs time graph-E4Y.

4.7.4.2. Chamber 2. The number of trapped cells also increased by time in the second chamber for 7 generations (Figure 4.80b). When the logarithm of cell count was analyzed, the cells did not show a strong increment as shown in Figure 4.80c. The integrated density was very small for first 360 minutes, then radically increased until the end of the experiment (Figure 4.80d). The area and perimeter of the cells showed the same behavior as that of cell count. The ratios of cell area/cell count and cell perimeter/cell count remained almost constant as expected (Figure 4.81c and Figure 4.81d).

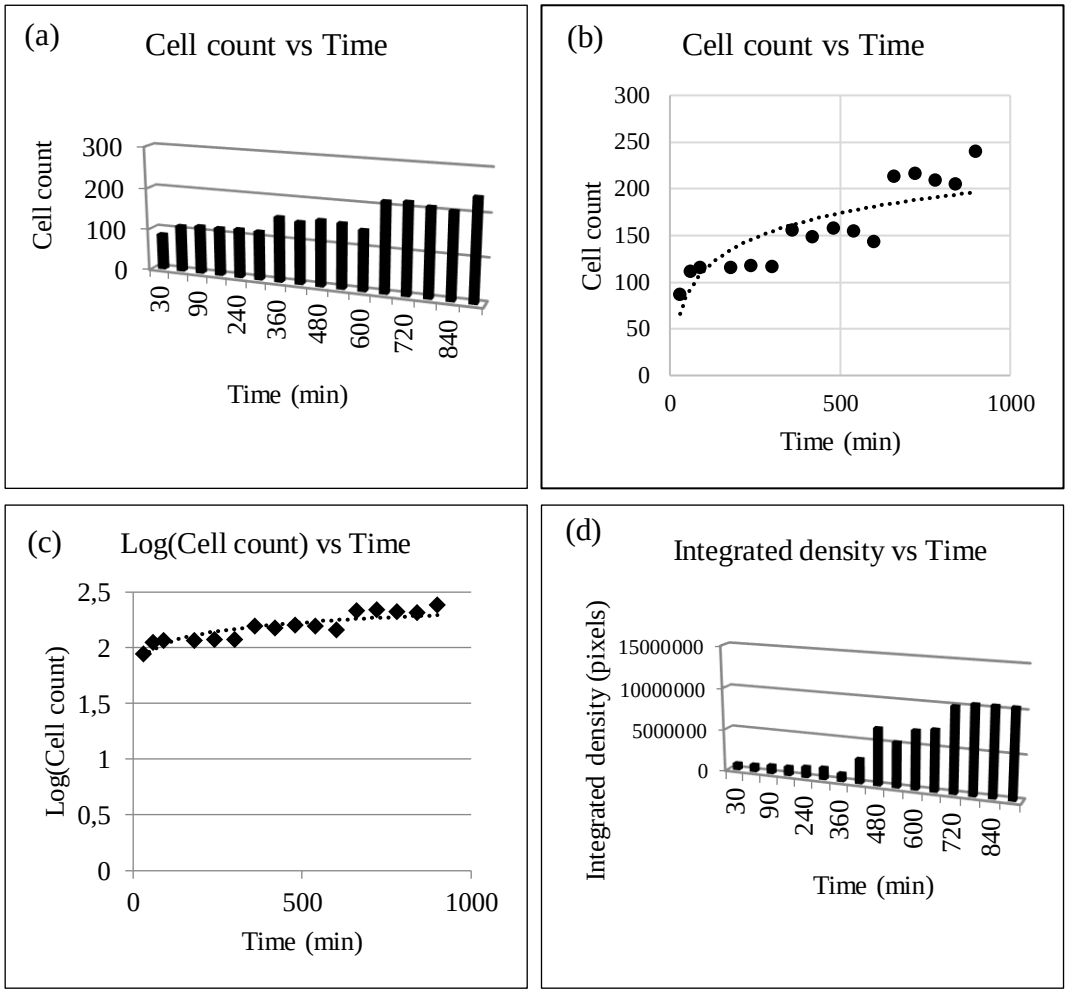

Figure 4.80. Graphical display of processed data for chamber 2 (a,b) cell count vs time graph (c) log(cell count) vs time graph (brightfield images) (d) integrated density vs time graph (fluorescence image)-E4Y.

The changes in integrated density/cell area and log-2 based integrated density with respect to time were very similar to the first chamber. The log-2 based integrated density was at a range between 20 and 25 during the experiment (Figure 4.82b).

4.7.4.3. Chamber 3. In the third chamber, the number of yeast cells trapped at the c-shaped region was smaller than those of first two chambers. The number of cells slightly increased from about 10 to 100 in 15 hours (Figure 4.83a). Likewise, the integrated density increased very slowly in the first 360 minutes, and thereafter integrated density increased significantly till the end of experiment (Figure 4.83d). This may be because of very few

number of cells trapped at the region. As the cells grew, their area and perimeters also rised simultaneously as shown in Figure 4.84. Except some fluctuations at some points, cell area/cell count and cell perimeter/cell count were almost constant for 7 generations (Figure 4.84 c and Figure 4.84 d).

The change in integrated density were also figured out by taking the cell area into account. For the third chamber, there were slightly increasing trends in expression of Sld7p-GFP fusion at intervals of about 200 minute which corresponds to duplication time and end of budding phase (Figure 4.85b). After 5th generation, the signal appeared to be constant till the end of experiment. As the other chambers showed similar behavior, the results were in Appendix C but not discussed.

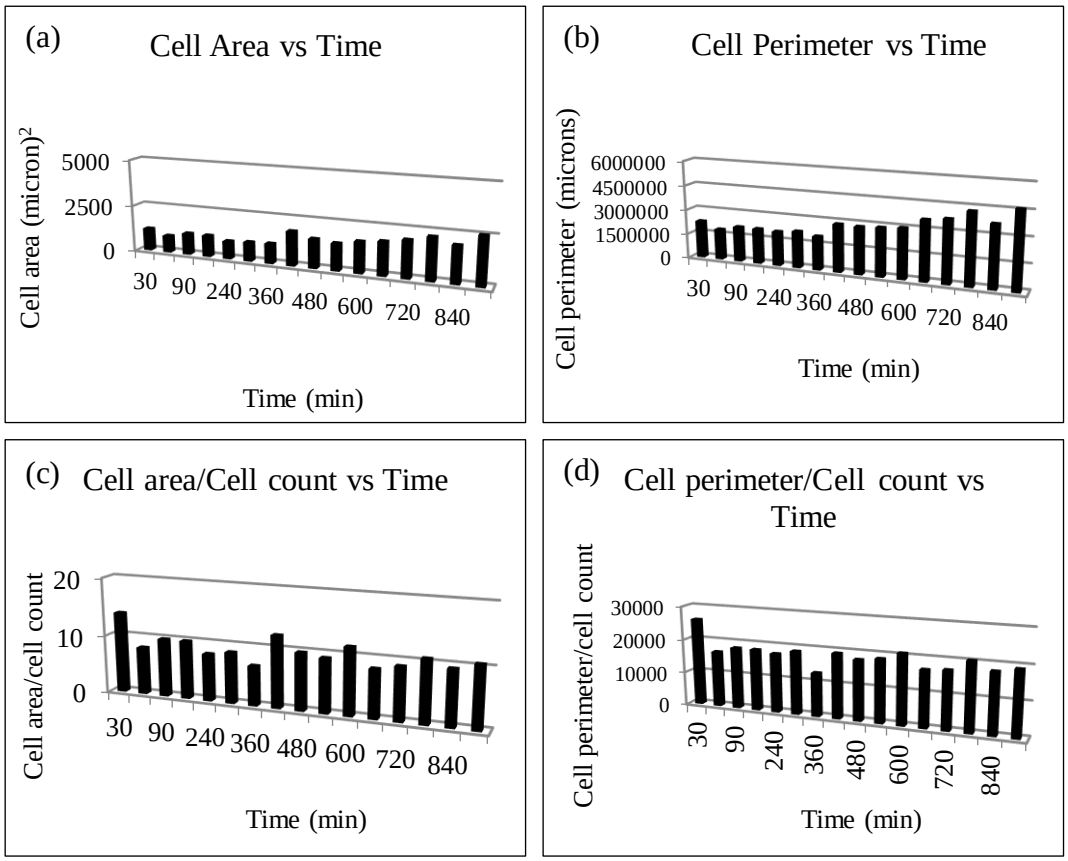

Figure 4.81. Graphical display of processed data of chamber 2 (a) cell area vs time graph (b) cell perimeter vs time graph (c) cell area/cell count vs time graph (d) cell perimeter/cell count vs time graph (brightfield images)-E4Y.

4.7.5. Experiments on Caloric Restriction- YNB medium (E5Y)

In this experiment, culturing of yeast cells in glucose limited (0.2%) YNB medium without histidine was observed. The experimental setup was prepared as mentioned in Section 7.7.1. All the channels were filled with YNB medium in 2 hours. Then yeast cell loading was started at a rate of 1 μL/min through all channels and the experiment was stopped after 60 hours. After 12 hours, some leakage from inlets through the intersection of the epoxy was observed. However, the medium flow was continuously collected from outlet port which showed that medium was still continuously fed to the chambers.

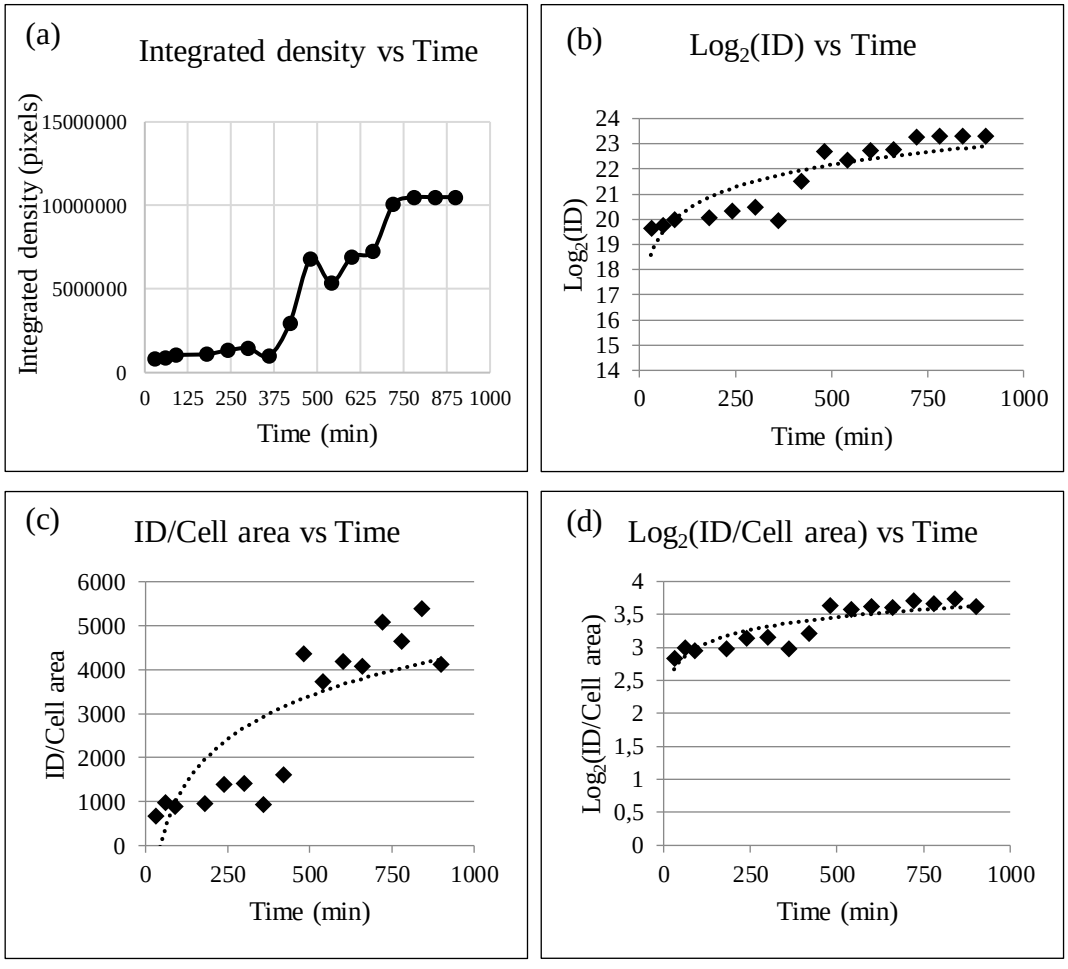

Figure 4.82. Graphical display of processed data for chamber 2 (a) integrated density vs time graph (b) $\log_2$(integrated density) vs time graph (c) integrated density/cell area vs time graph (d) $\log_2$(integrated density)/cell area vs time graph-E4Y.

4.7.5.1. Chamber 1. The yeast cells were efficiently trapped at the first c-shaped region. Figure 4.86 shows budding of some immobilized yeasts in the first chamber.

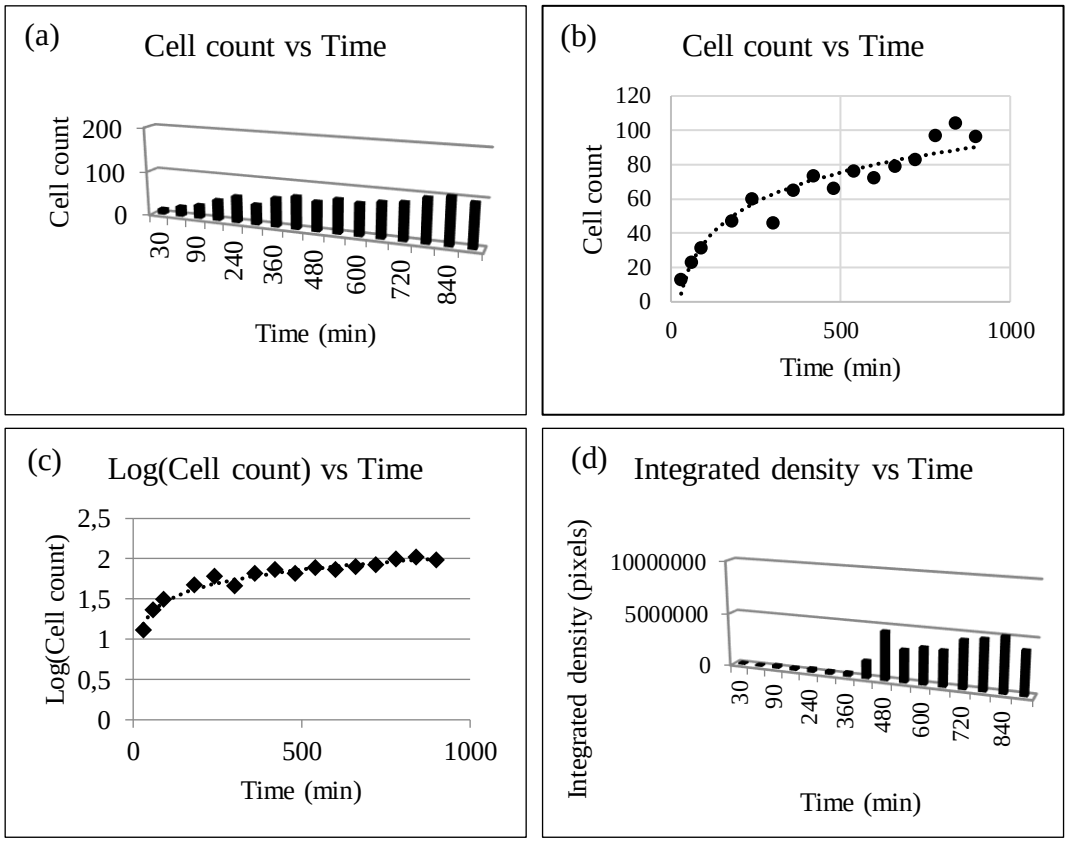

Figure 4.83. Graphical display of processed data for chamber 3 (a,b) cell count vs time graph (c) log(cell count) vs time graph (brightfield images) (d) integrated density vs time graph (fluorescence image)-E4Y.

The yeast cells were processed and cell count, cell area, perimeter and integrated density results of first chamber were analyzed. The cells were started to trap in the first chamber after 30 minutes. The cell number was increased slowly between 30th to 1530th minutes and increased faster between 1530th to 3510th minutes in first chamber (Figure 4.87a). According to Figure 4.87b, the cell division continued for 29 generations. Exponential growth of yeast cells was seen in low glucose containing YNB medium (Figure 4.87c). The integrated density (fluorescence intensity) was followed and increasing trend in fluorescence signal of Sld7p-GFP fusion was observed (Figure 4.87d). Sharp

increases at certain time points may be because of the position of cells, which caused higher signal intensity.

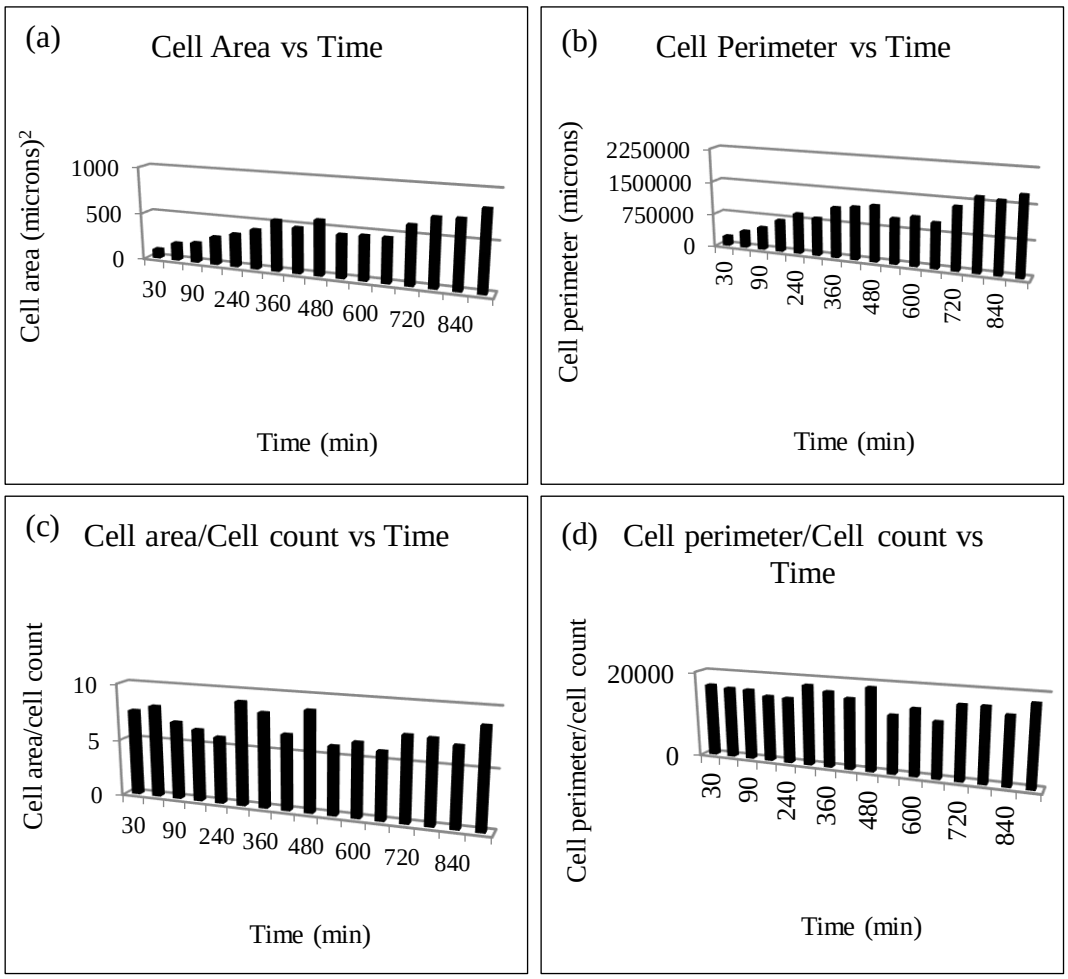

Figure 4.84. Graphical display of processed data of chamber 3 (a) cell area vs time graph (b) cell perimeter vs time graph (c) cell area/cell count vs time graph (d) cell perimeter/cell count vs time graph (brightfield images)-E4Y.

The cell area and cell perimeter profiles matched with the profiles of cell count (Figure 4.88a and Figure 4.88b). Similar to the cell count, the cell area and cell perimeter were slowly increasing between 30th and 1530th minutes, followed by a strong rise between 1530th to 3510th minutes (between 23th and 29th generations). The values of cell area/cell count and cell perimeter/cell count remained almost same throughout the experiment (Figure 4.88c and Figure 4.88d). When the change in integrated density/cell area with time

was analyzed, it can be seen that the ratio stayed almost constant at a value of 3000 throughout the experiment (Figure 4.89). As cell area increased, the fluorescence signal also increased regularly.

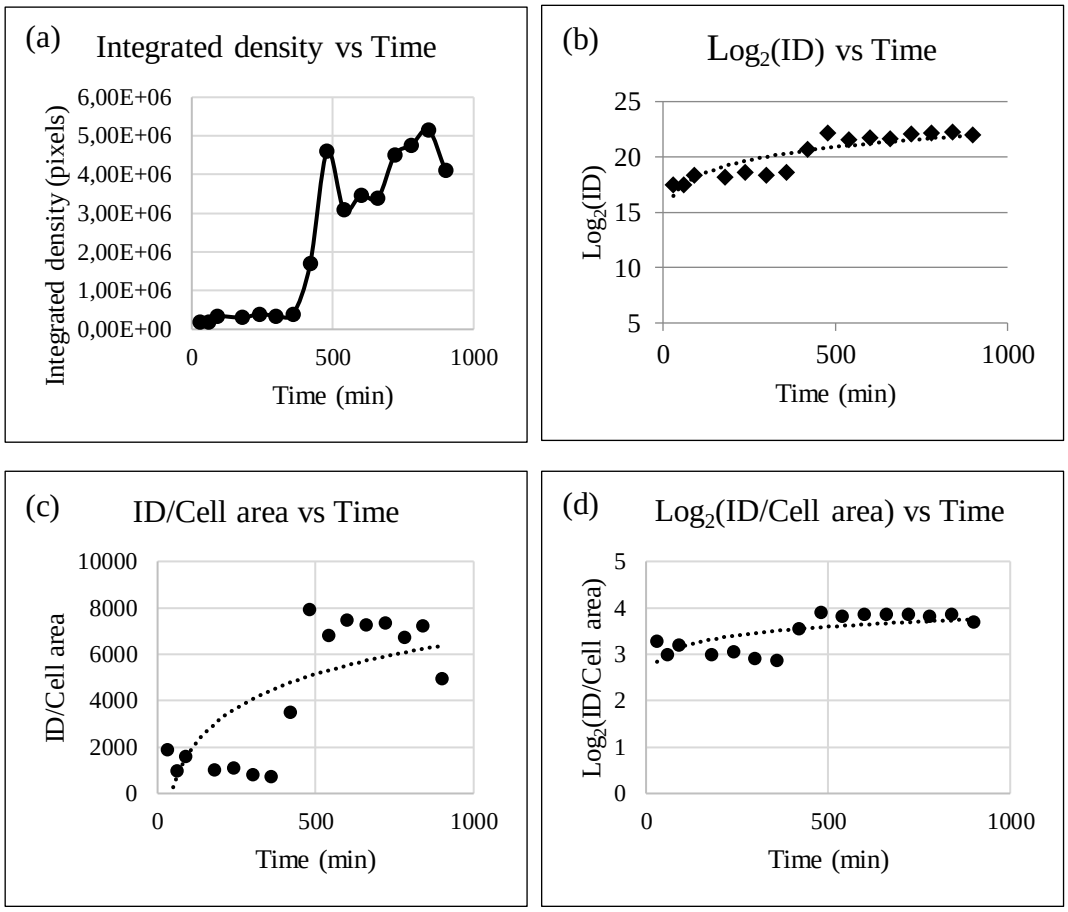

Figure 4.85. Graphical display of processed data for chamber 3 (a) integrated density vs time graph (b) $\log_2$(integrated density) vs time graph (c) integrated density/cell area vs time graph (d) $\log_2$(integrated density)/cell area vs time graph-E4Y.

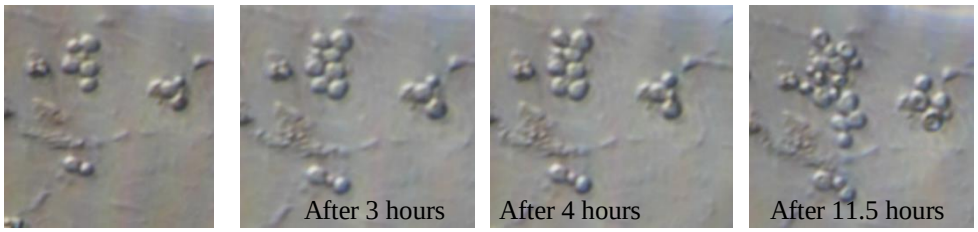

Figure 4.86. Budding yeast cells (40X objective).

4.7.5.2. Chamber 2. The cells started to get trapped in the second chamber at the same time as first chamber. Figure 4.90 shows the formation of a colony of yeast cells by time in the second chamber. Yeast cells increased exponentially in the second chamber from 30th to 2520th minute interval. After this point, the cell number remained same (Figure 4.91a). First cell was trapped in the c-shaped region after 30th minute and cell growth continued for 30 generations (Figure 4.91b). The integrated density (fluorescence intensity) showed an increasing trend up to 2310th minute (Figure 4.91d), i.e. almost same behavior was followed as the cell number.

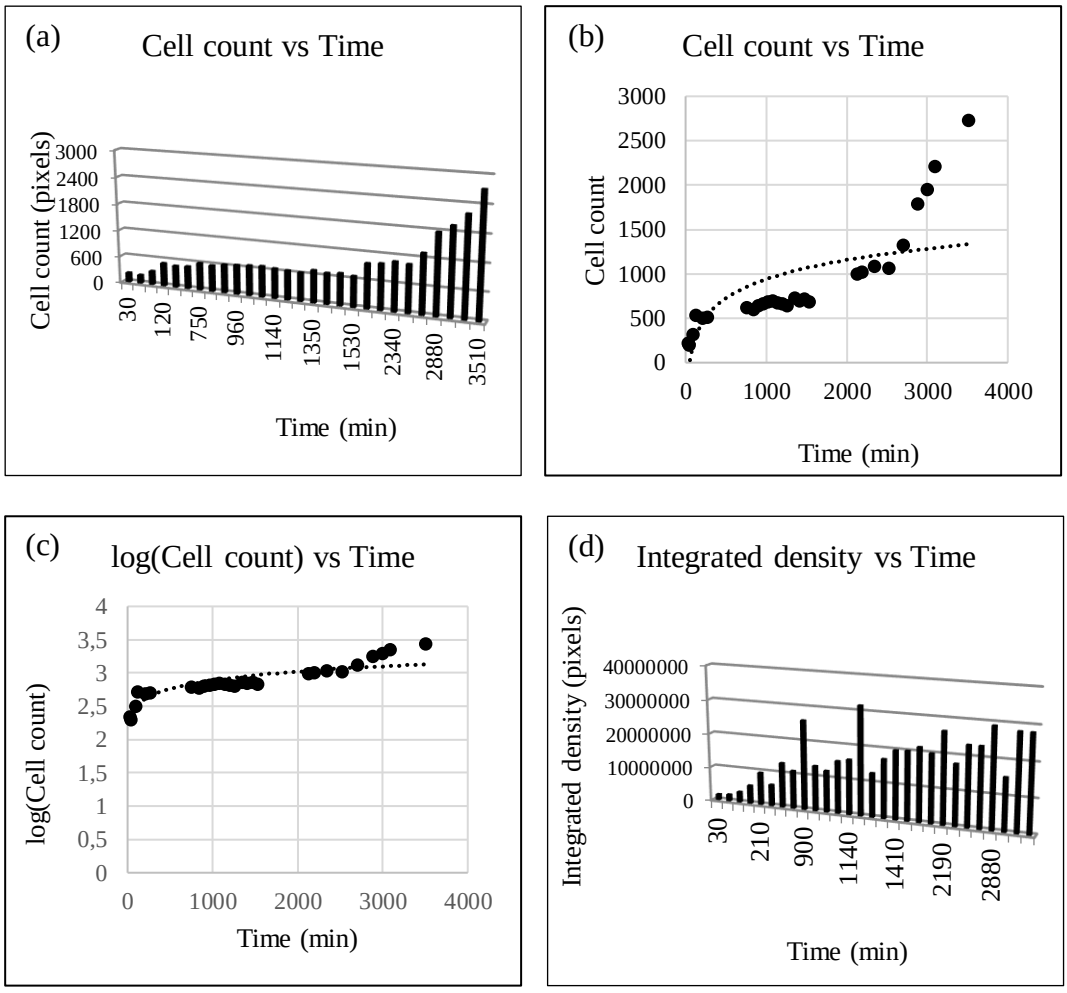

Figure 4.87. Graphical display of processed data for chamber 1 (a,b) cell count vs time graph (c) log(cell count) vs time graph (brightfield images) (d) integrated density vs time graph (fluorescence image)-E5Y.

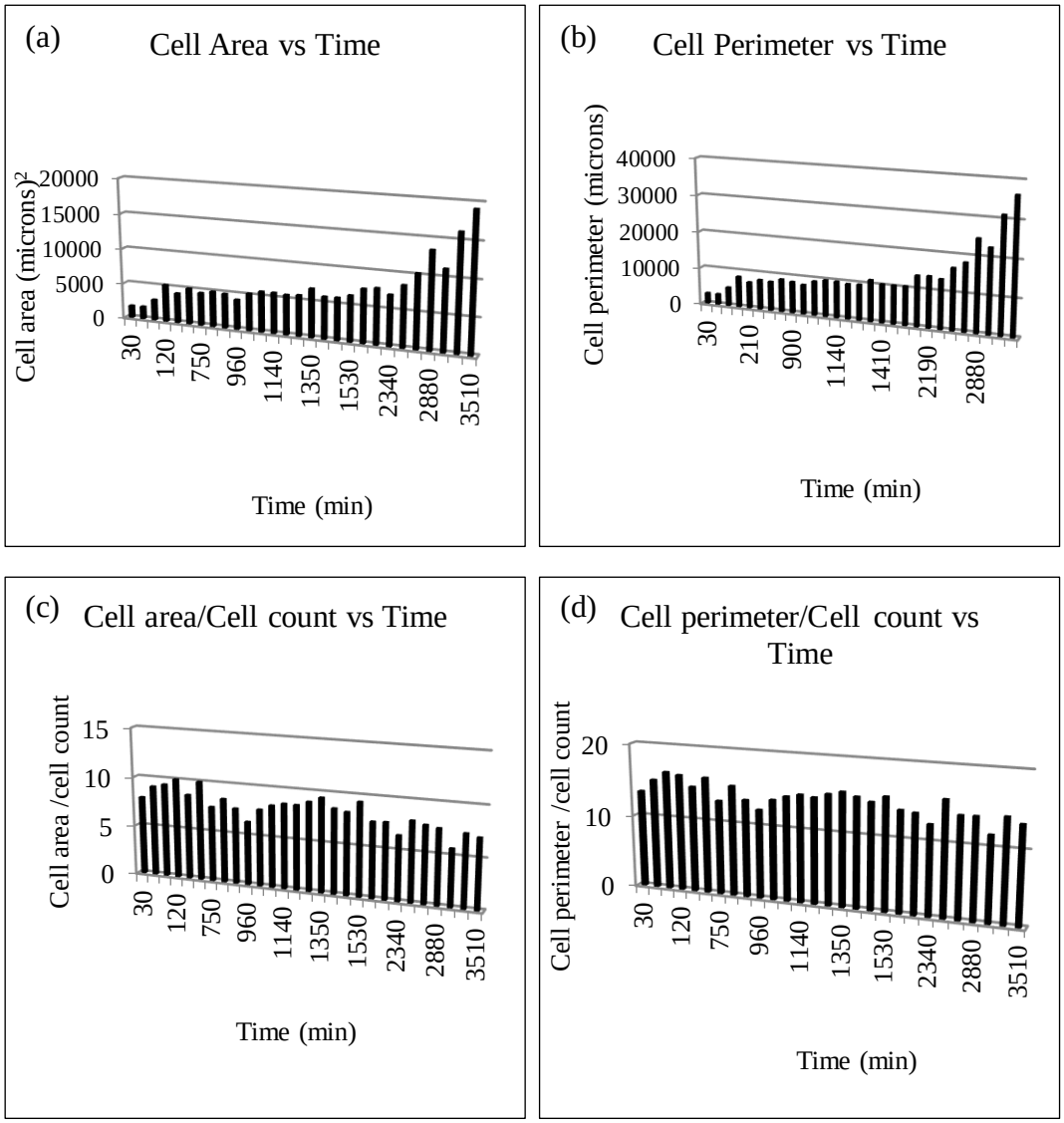

Figure 4.88. Graphical display of processed data of chamber 1 (a) cell area vs time graph (b) cell perimeter vs time graph (c) cell area/cell count vs time graph (d) cell perimeter/cell count vs time graph (brightfield images)-E5Y.

The changes in values of cell area and cell perimeter are shown in Figure 4.92. As expected, the cell area and cell perimeter were concurrently increased by increasing cell count (Figure 4.92a and Figure 4.92b). Cell area/cell count and cell perimeter/cell count were almost same throughout the experiment. When the integrated density/cell area ratio was analyzed (Figure 4.93), as cell area was increased by time, the ratio remained constant at a value of 4000.

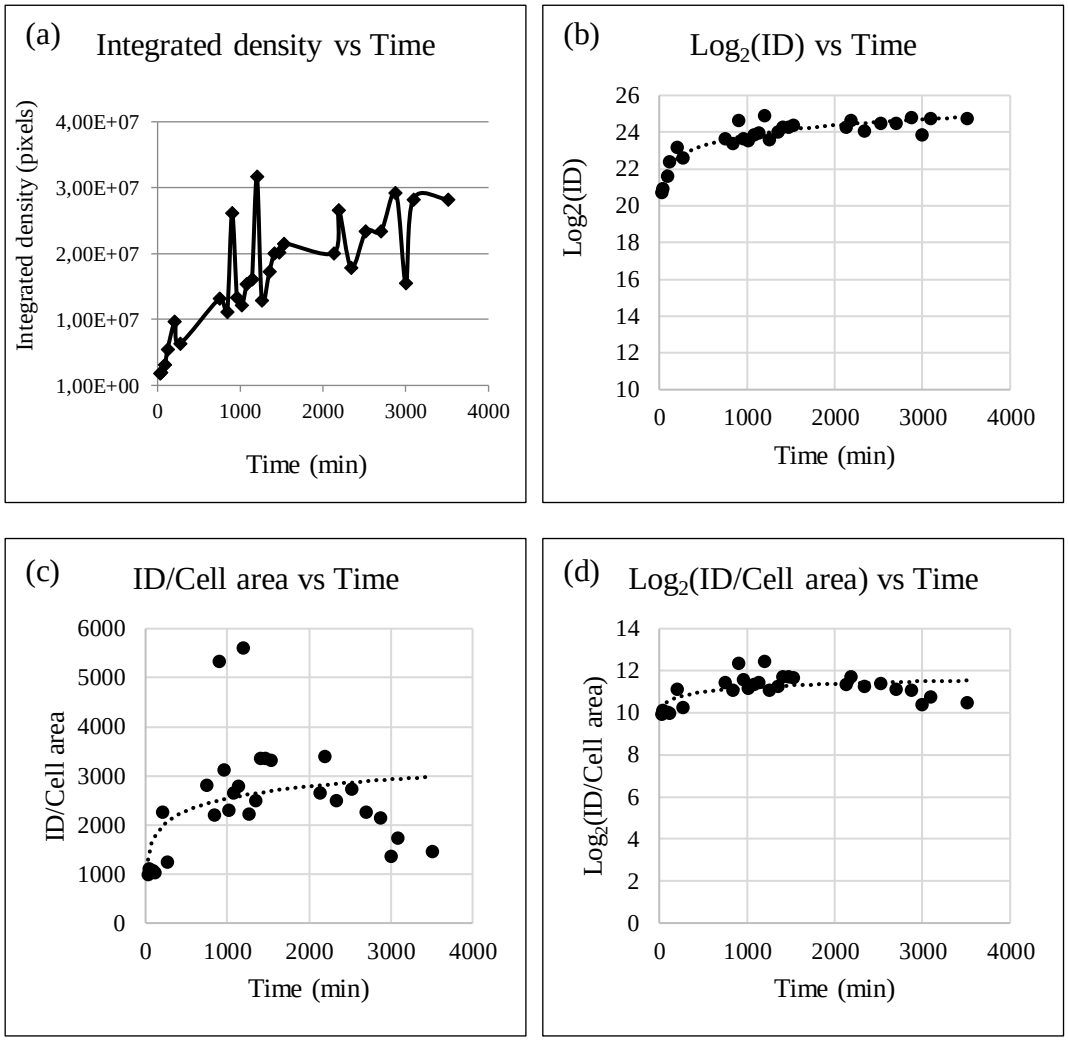

Figure 4.89. Graphical display of processed data for chamber 1 (a) integrated density vs time graph (b) $\log_2$(integrated density) vs time graph (c) integrated density/cell area vs time graph (d) $\log_2$(integrated density)/cell area vs time graph-E5Y.

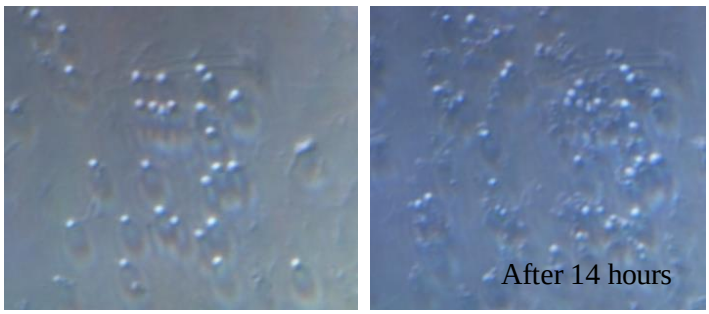

Figure 4.90. Yeast colony in the second chamber (40X objective).

4.7.5.3. Chamber 3. The brightfield and fluorescence images of the third chamber were also analyzed. Cell numbers were increased at a slower rate than those in first two chambers (Figure 4.94a). In the third chamber, first cell was trapped after 40 minutes and almost 160 cells were grown throughout 20 generations (Figure 4.94b). Also, the number of trapped cells were less than those of first two chambers. According to Figure 4.94d, there was a fluctuating trend in integrated density with time. The highest fluorescence signals were obtained at 2190th and 2340th minutes.

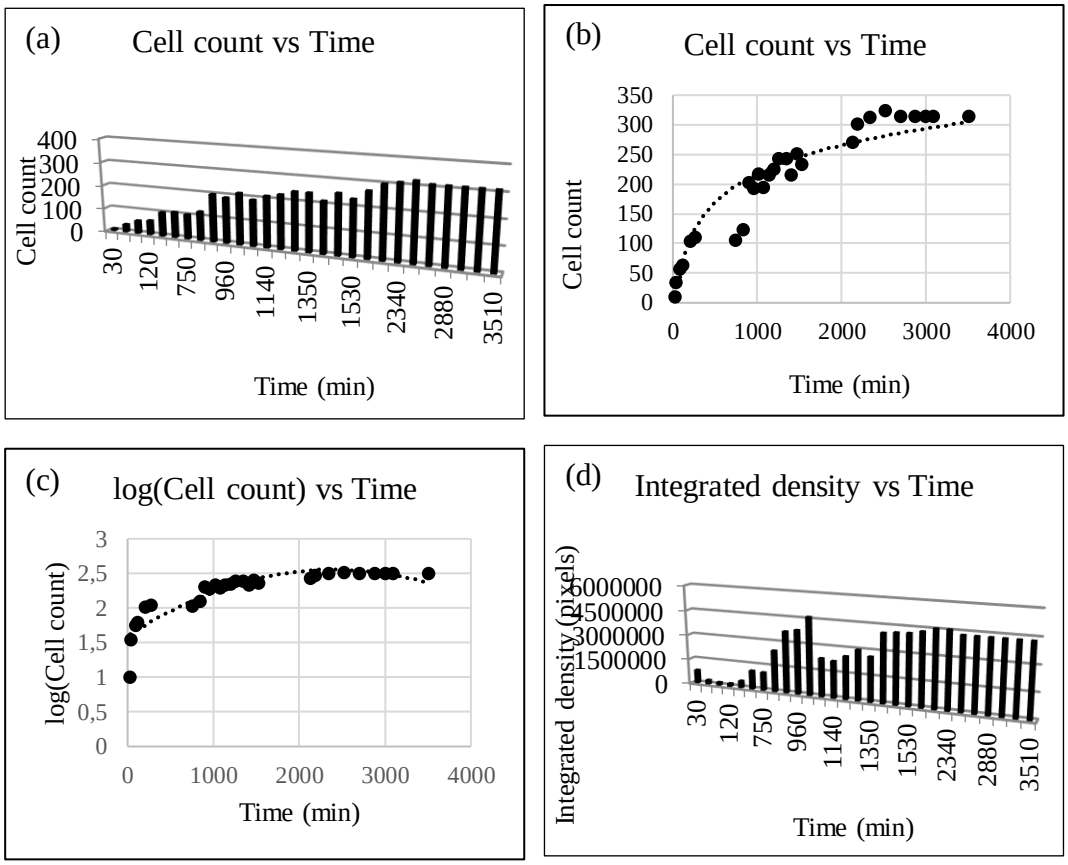

Figure 4.91. Graphical display of processed data for chamber 2 (a,b) cell count vs time graph (c) log(cell count) vs time graph (brightfield images) (d) integrated density vs time graph (fluorescence image)-E5Y.

The cell area and cell perimeter changes with time are given in Figure 4.95a and 4.95b, respectively. The cell area and perimeter increased properly between 40th to 1140th minutes and the increments were not considerable after this point. The ratio of cell area/cell

count was lowest at the 40th minute. After this point, it sharply increased and remained almost constant (Figure 4.95c). According to Figure 4.95d, the cell perimeter/cell count vs time graph also followed the same trend. The small values at 40th minute were because of the very small number of cells initially trapped. When cells grew and started to form daughter cells, their areas also increased. At the same time, the expression of fluorescence signal continued and integrated density increased. As a result of this concurrent increment of cell area and integrated density, the ratio of integrated density/cell area remained almost constant at a value of 2000 throughout 20 generations (Figure 4.96). As the remaining chambers showed similar behavior, the results were presented in Appendix C but not discussed.

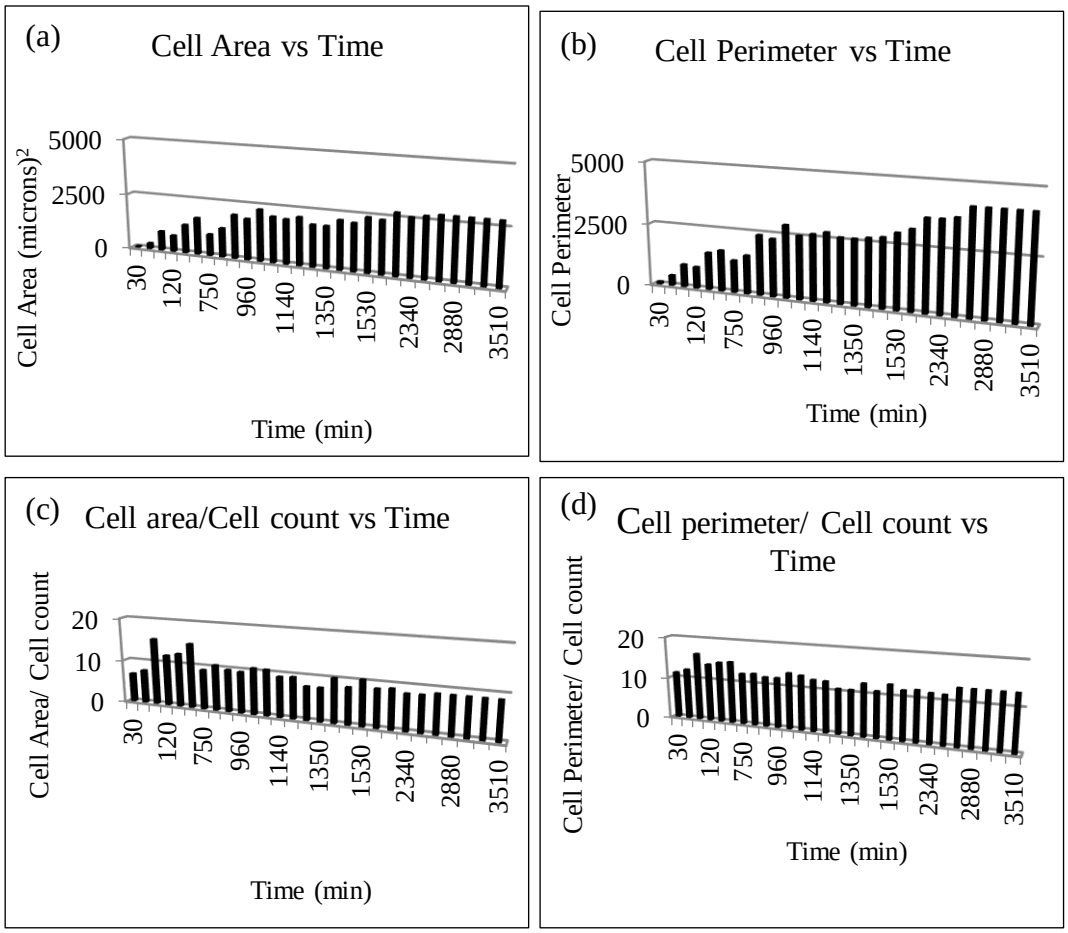

Figure 4.92. Graphical display of processed data of chamber 2 (a) cell area vs time graph (b) cell perimeter vs time graph (c) cell area/cell count vs time graph (d) cell perimeter/cell count vs time graph (brightfield images)-E5Y.

In all these experiments there was no constant decrease either in cell perimeter or cell area, so we understand that the yeast cells did not enter death phase after 2500 hours of operation and they were living perfectly well in microfluidic system of 1nL volume.

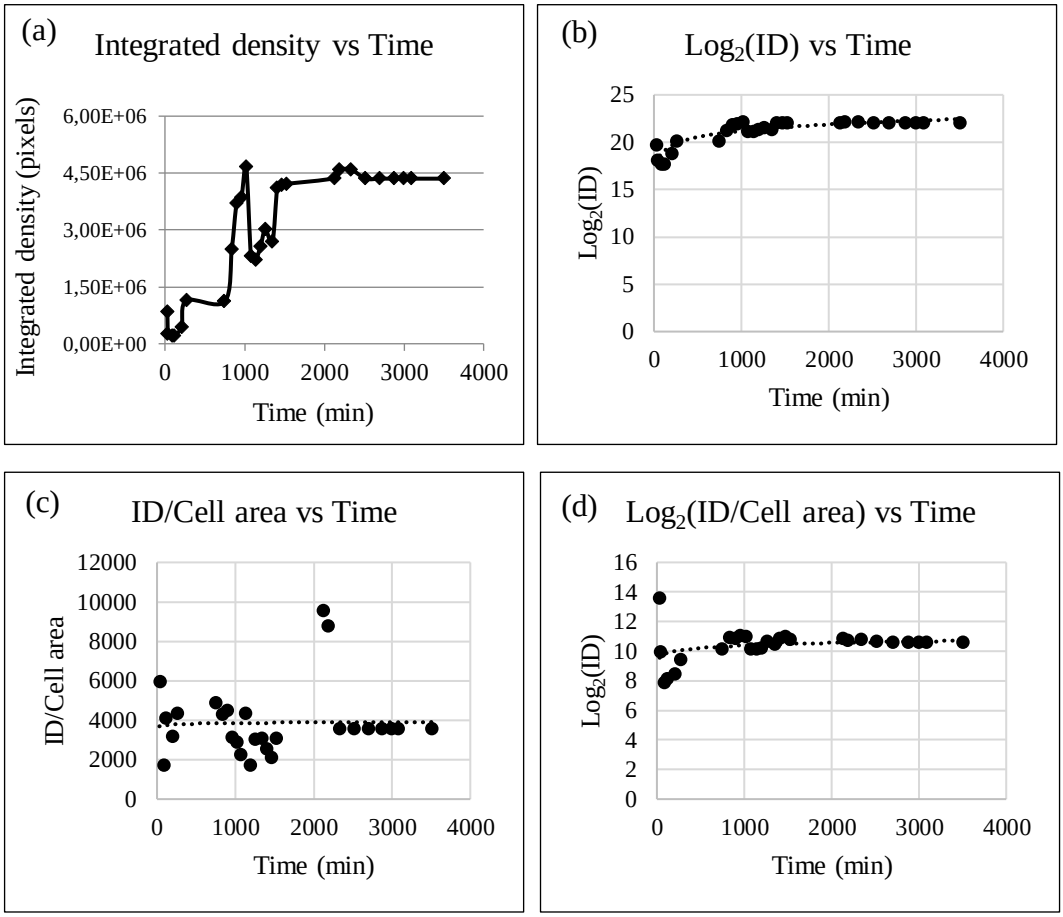

Figure 4.93. Graphical display of processed data for chamber 2 (a) integrated density vs time graph (b) $\log_2$(integrated density) vs time graph (c) integrated density/cell area vs time graph (d) $\log_2$(integrated density)/cell area vs time graph-E5Y.

4.8. Insights from the Experiments

Approximately 40 chips of Design-2 were used in experiments for yeast culturing up to this point. There are several problems needed to be solved which are repeated in most of the experiments. Some of the problems are exemplified via the images taken during an experiment (E3Y) are given in follows.

When all of the microfluidic system (from inlet to outlet) was filled with medium, yeast cell flow was started. In most of the chips, cells started to trap and accumulate at the inlet wall (Figure 4.97). This may be because of opening of the inlets with drill by hand. Laser micromachining might be needed for improvement [31].

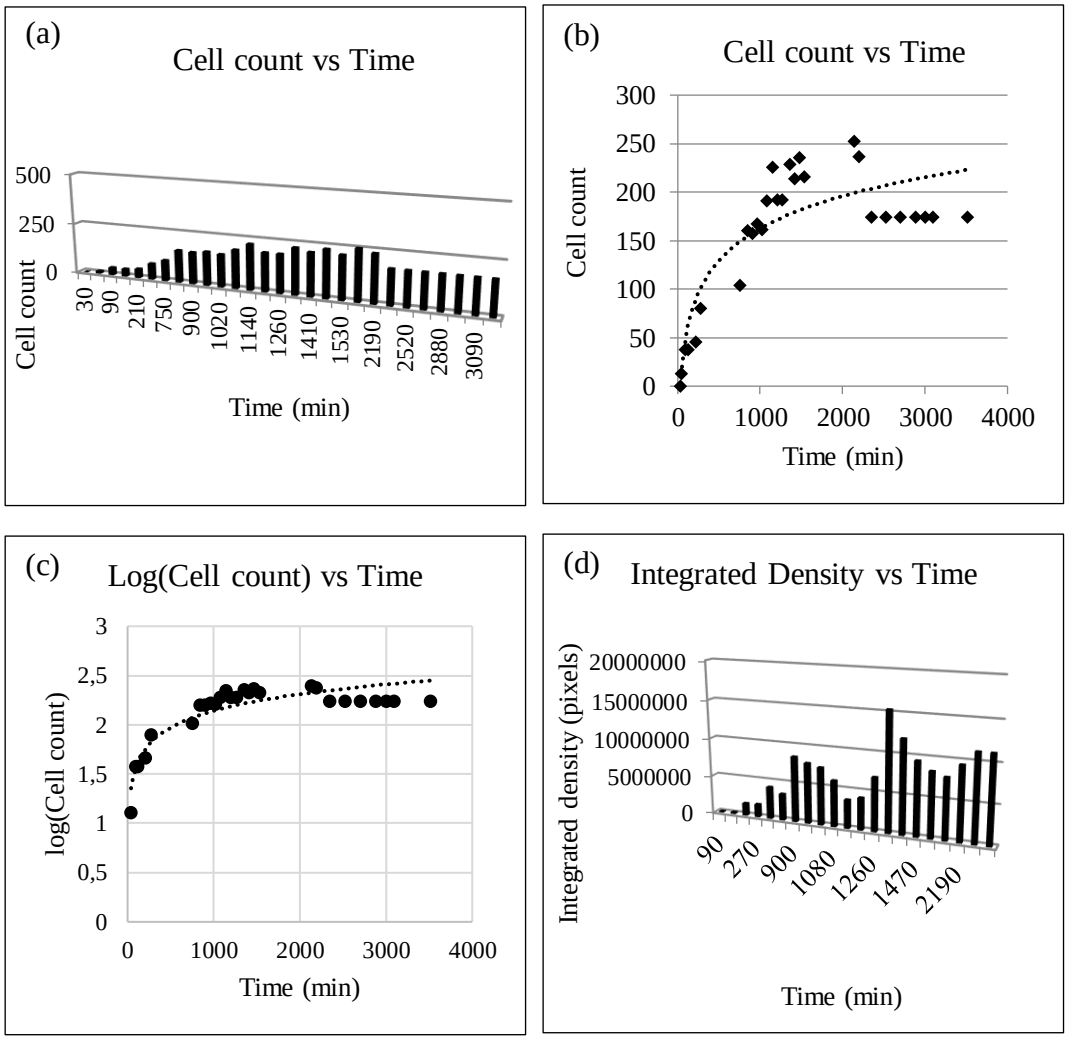

Figure 4.94. Graphical display of processed data for chamber 3 (a,b) cell count vs time graph (c) log(cell count) vs time graph (brightfield images) (d) integrated density vs time graph (fluorescence image)-E5Y.

Even at low flow rates (0.01 µL/min, syringe diameter : 15 cm), the flow of cells was very fast at the inlet of the channels, then started to slow down in the channel before the first chamber, and the cells accumulated at the inlet of the first chamber as shown below.

This may be because of the design and collapse of channel. Therefore, the depth differences throughout the microbioreactor were measured (Figure 4.99, Table 4.13). As it can be seen from Table 4.40, the depth was dramatically reduced at the entrance of the first chamber, preventing the passage of yeast cells. Flow profile is not uniform through the channels. At the inlet of the channels, the yeast flow was generally too fast, but when it reached the first chamber, the flow started to slow down and it took extremely long time (about 15-30 minutes to pass Region 2) to enter into the chambers. This may be because of the depth differences (the depth values belong to the chips, into which yeast cells were loaded). The collapse of channels were given in Figure 4.98. The flow was mainly staggered (Figure 4.100).

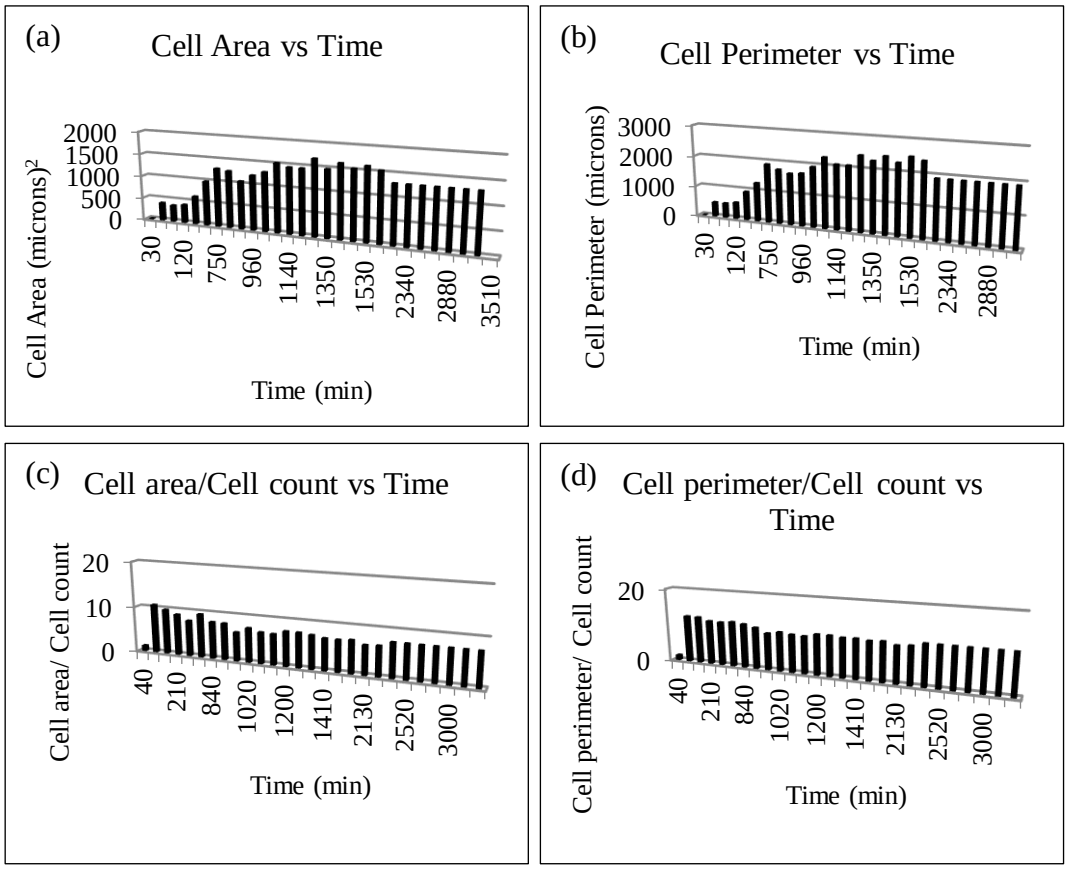

Figure 4.95. Graphical display of processed data of chamber 3 (a) cell area vs time graph (b) cell perimeter vs time graph (c) cell area/cell count vs time graph (d) cell perimeter/cell count vs time graph (brightfield images)-E5Y.

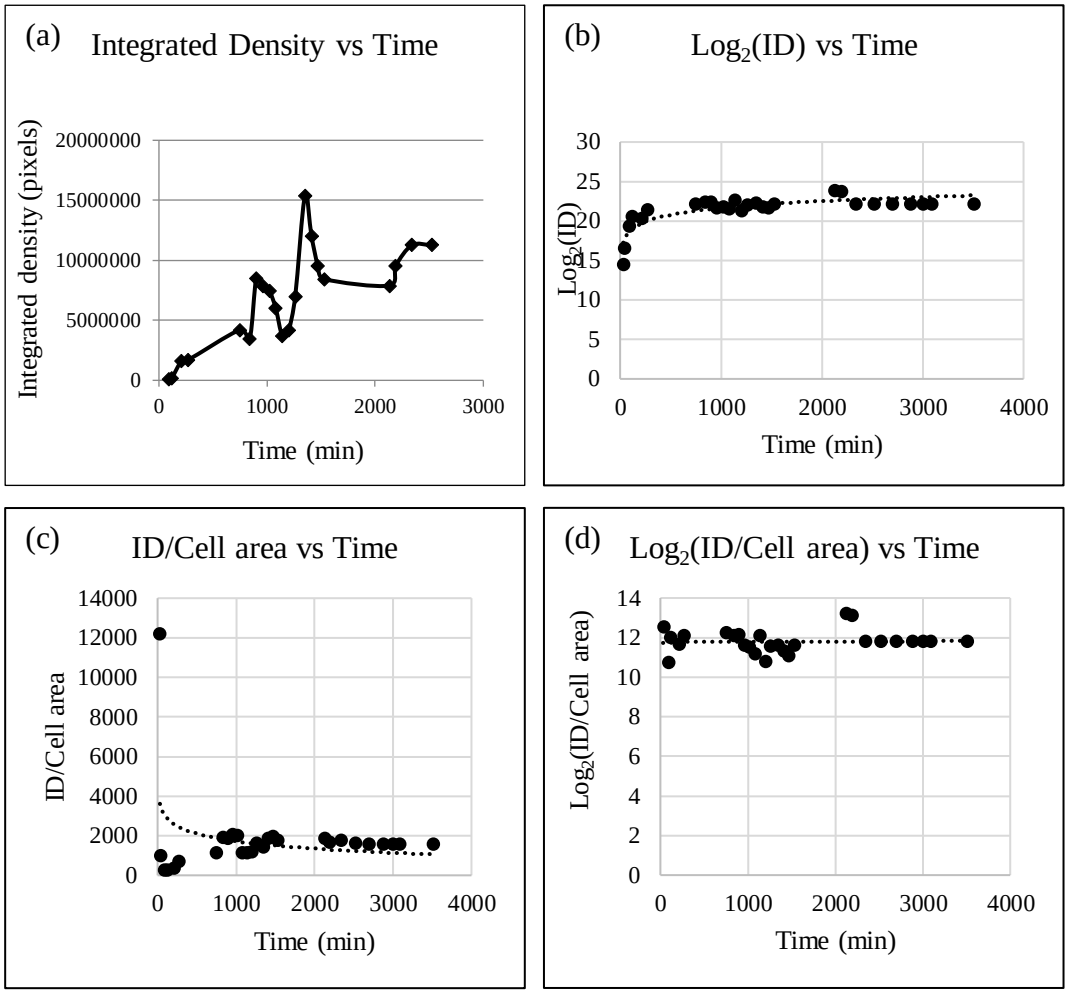

Figure 4.96. Graphical display of processed data for chamber 3 (a) integrated density vs time graph (b) $\log_2$(integrated density) vs time graph (c) integrated density/cell area vs time graph (d) $\log_2$(integrated density)/cell area vs time graph-E5Y.

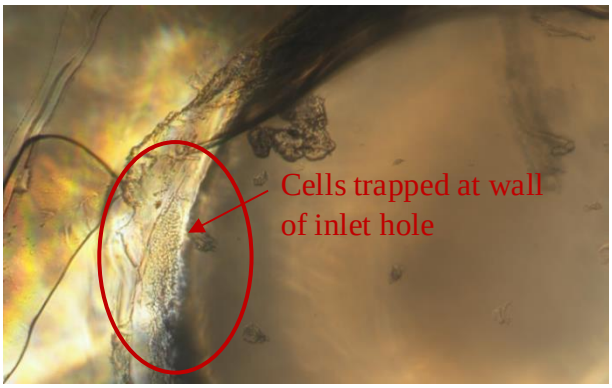

Figure 4.97. Cells trapped at the wall of inlet hole.

Flow profile is not uniform through the channels. At the inlet of the channels, the yeast flow was generally too fast, but when it reached the first chamber, the flow started to slow down and it took extremely long time (about 15-30 minutes to pass Region 2) to enter into the chambers. This may be because of the depth differences (the depth values belong to the chips, into which yeast cells were loaded). The collapse of channels were given in Figure 4.98. The flow was mainly staggered as shown in Figure 4.100.

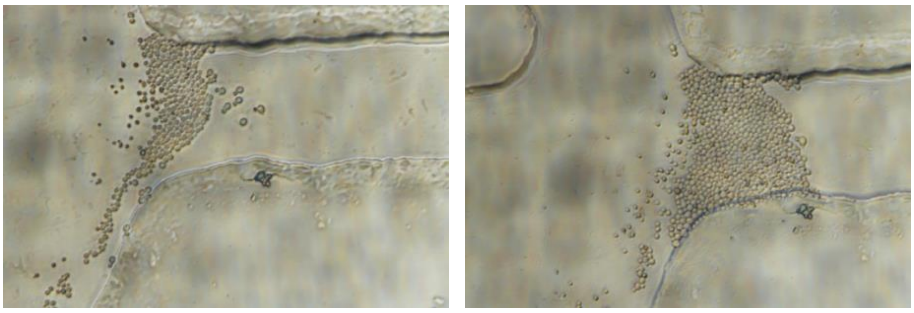

Figure 4.98. Cells trapped at inlet of the first chamber.

Leakage through the epoxy and polymer intersection occurred in almost all chips. After the yeast loading, the flow was generally stopped due to the leakage. A new inlet was designed and fabricated to prevent leakage and connection problems which were mentioned in Section 4.4. A PMMA block was drilled from right and bottom sides and a path was created for fluid flow. This block was attached on the inlet holes by the help of double-sided tape. Then pipette tips were inserted into the holes at the right side of the block and consolidated by the help of epoxy. The design of new inlet is shown in Figure 4.101. The summary of all experiments is given in Table 4.14.

Table 4.13. Depth differences along the microbioreactor.

Chip	Inlet of Middle channel (μm) 3	Inlet of First Chamber (μm) 2	Middle of the trapping region (μm) 1
1	10.47	3	7.87
2	8	3.5	8.2

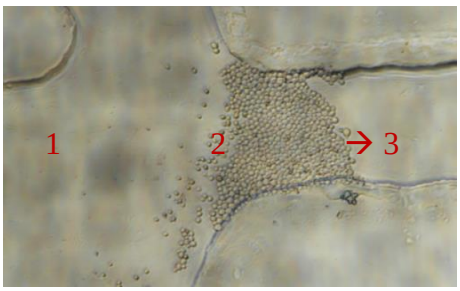

Figure 4.99. Regions selected to measure depth differences along the microbioreactor.

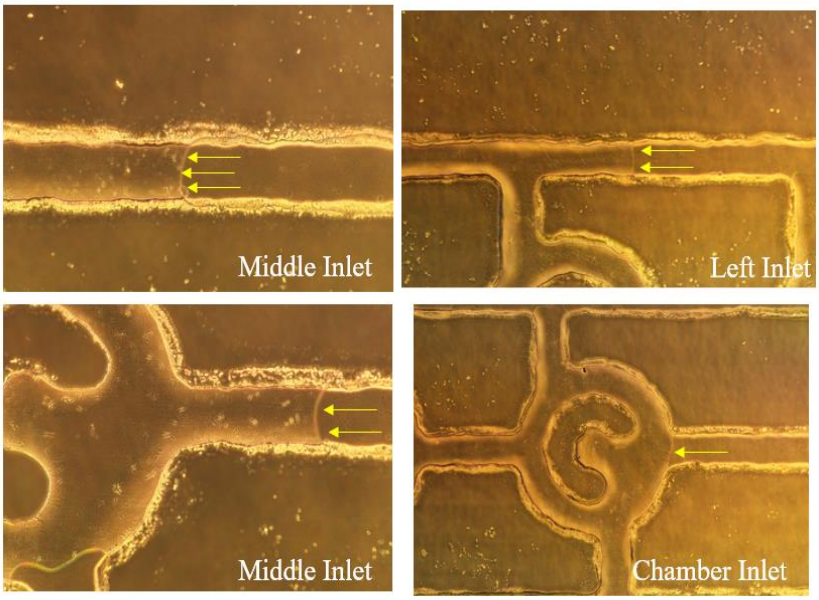

Figure 4.100. Flow profiles in microbioreactor.

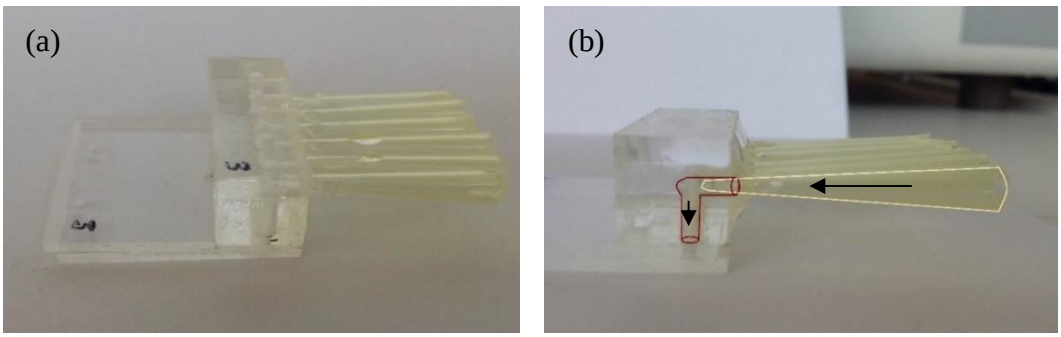

Figure 4.101. The design of new inlet (a) The inlet apparatus fixed on the chip (b) Flow direction through the created path.

Table 4.14. Summary of experiments.

Design	Bonding parameters	Situation
D1 E1	130 °C 2-4 bar 1 hour	Acetone and water flow were observed. High pressure differences and back flow occurred. Channels were collapsed too much (8µm height mask) Yeast could not be loaded.
D2 E1Y	125 °C 50 bar 1 hour	Acetone and medium flow observed. Back flow and leakage of medium from inlets through the intersection of epoxy and the polymer occurred. Flow filled this area instead of channels and chambers. Air bubbles occurred. Yeast cells trapped in first three chambers. The size of cells were not big, most likely they were at their early growth phase. No outlet flow was observed.
D2 E2	125 °C 35-40-45-50 bar 1 hour	Back flow and leakage of medium from inlets through the intersection of epoxy and the polymer occurred. Same problems seen as chips bonded at 50 bar. Yeast could not be loaded.
D2 E2Y	125 °C 25 bar 1 hour	Channels filled with medium without any problem. Outlet flow collected continuously (19 hours) Yeast cells introduced and they reached all chambers (1 µL/min) A vortex flow occurred in all chambers. The vortex cannot be prevented even though liquid flow rate slowed down to 0.1 µL/min or stopped and continued for 8 hours and outlet flow observed continuously. The size of cells were not big enough to be trapped.
D2 E3Y	125 °C 25-28 bar 1 hour	The medium filled channels easily. The flow was slower in chambers rather than inlet channels. Flow profile was not uniform. Yeast was introduced to middle channel, started to be trapped at walls of inlet hole. The size of cells were big enough. At even low flow rates (0.01 µL/min), cells were trapped at the intersection of middle channel and inlet of the first chamber. Leakage of medium from inlets through the intersection of epoxy and the polymer occurred (generally after cell loading). (10 chips were tested)
D2 E4Y	125 °C 25-28 bar 1 hour	The medium filled channels easily. The flow was slower in chambers rather than inlet channels. Cells were trapped at first four chambers efficiently. After 15 hours, experiment was stopped because of the air bubbles appeared in channels. Air bubbles were started to sweep away the trapped cells.
D2 E5Y	125 °C 25-28 bar 1 hour	The medium filled channels easily. Cells were trapped and grown at first seven chambers efficiently. Experiment was stopped after 60 hours.

4.9. Discussion

4.9.1. Choice of Materials for Fabrication Process

The polymers have important properties, that must taken into account, as chemical, optical, thermal and mechanical properties, biological inertness and optical transparency. In the light of these properties, three polymers were chosen to study, PMMA (polymethyl methacrylate), COP (cyclo olefin polymer) and PEN (polyethylene naphthalate) and to fabricate the microbioreactor for yeast cell culturing. The properties of polymers given in Table 4.15 need to be considered to construct a high-performance microfluidic chip. The chemical properties of the polymers were important for the steps of surface treatment and loading test of the channels. Because of the low chemical resistance of PMMA polymer to solvents, the solvent treatment was applied to PMMA substrates before bonding to strengthen the bonding of two pieces. PMMA is a polar and amorphous polymer and its surface properties change by most of the solvents easily. 2-propanol was here used as a polar solvent to change the surface properties of PMMA and to achieve a strong bonding [34].

Table 4.15. Properties of materials used for the fabrication of the microbioreactor [32,33].

Property		COP	PMMA	PEN
Chemical Resistance	Acids, bases (medium conc.)	Good	Poor	Good
	Alcohols, acetone	Good	Poor	Good
	Esters	Good	Poor	Good
	Ketones	Moderate	Poor	Good
Optical Transparency		Good	Good	Good
Low Fluorescence		Good	Moderate	Moderate
Moisture barrier		Good	Poor	Good
Dimensional stability		Good	Moderate	Good
Processing (macro/nano scale)		Good	Moderate	Good
Break resistance		Good	Good	Good
Water adsorption		Poor	Moderate	Moderate

The solvent treatment was not used for COP and PEN because of their good chemical resistance properties to polar solvents, strong acids and bases. To modify the surface of COP polymer, oxygen plasma or UV radiation exposure methods are commonly used. The solvents were only used for cleaning of COP and PEN. The dimensional stability of the polymer is another important point for the fabrication step. The water absorption of COP polymer is 10 times less than that of PMMA and this provides excellent dimensional stability in changing environmental conditions (Figure 4.102). The high moisture barrier of COP is beneficial when working with cell cultures, the cells are consuming oxygen of water more instead of its absorption onto the surface of the polymers [31]. The low water absorption is also directly related to the high dimensional stability of the COP polymer (Figure 4.102). The glass transition temperatures of COP and PMMA are close, but their Young's modulus values are different. COP polymer has smaller Young's modulus than PMMA and its rigidity and strength are higher. This also makes the dimensional stability property of COP polymer better.

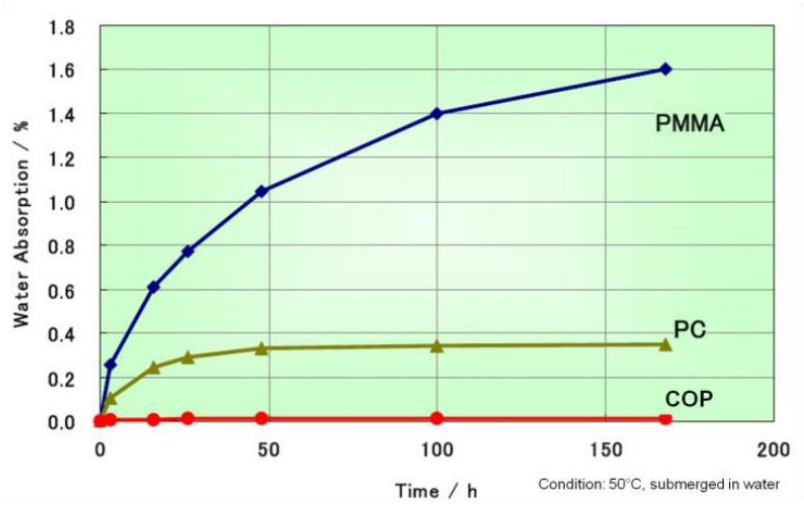

Figure 4.102. Moisture absorption of COP and other optical polymers [33].

The COP made microfluidic devices have been used for analysis of biological materials such as blood and DNA [33]. The COP is a fully saturated olefin polymer and it shows very little interaction with various proteins. The materials' ring structure provide high stability and COP material shows an inert low binding surface property. Therefore, the materials' reaction chemistry show stability against various proteins. The zeta potential

change is not significant at different pH values and protein types (i.e. BSA, lysozyme). The low adsorption on COP is shown via comparing with polypropylene (PP) in Figure 4.103. High transparency and low fluorescence characteristics of the material are required to visualize the cells under microscope and to process the images. The optical transmission properties and the low fluorescence background signal of COP is good enough to visualize the fluorescently tagged cells. Figure 4.104 shows the excitation emission sweeps of COP polymer. High background fluorescence can cover up the fluorescence signals of the GFP tagged cells and cause inefficient imaging. In the light of the advantages of COP polymer, the COP made microfluidic devices were used for yeast cell trapping and imaging experiments [32].

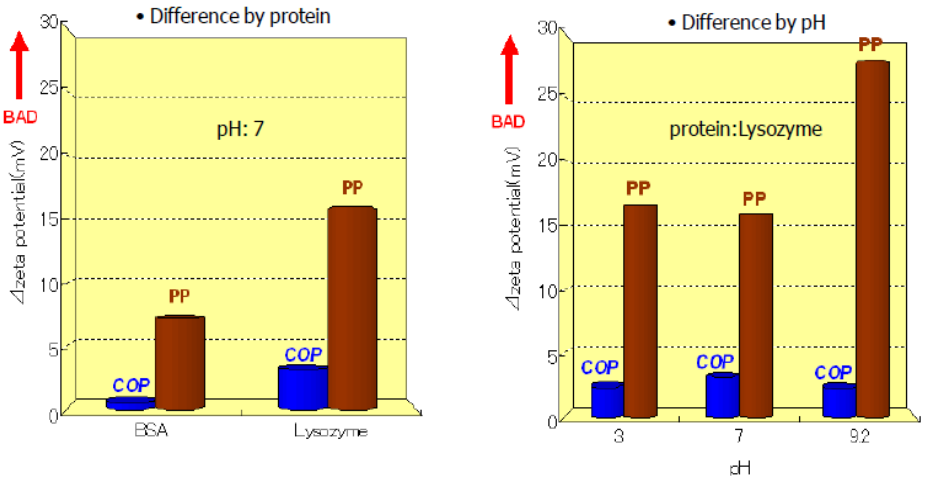

Figure 4.103. Low absorption properties of COP [33].

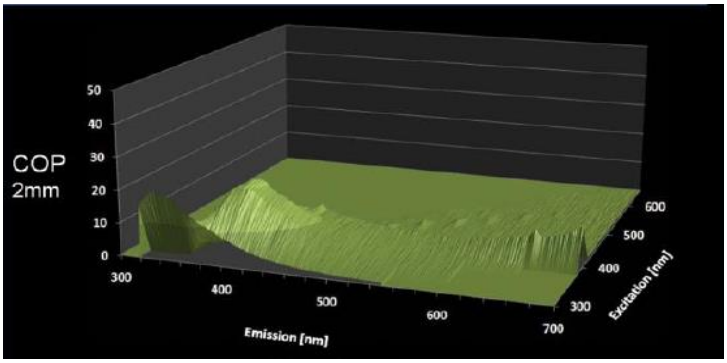

Figure 4.104. Excitation emission sweeps of non-polar optical polymer (COP).

4.9.2. Fabrication Steps

The reliability of the in house fabricated device was tested over 300 replications of single mold. Lee *et al.* (2008) reported a value of 30 replications of a single mold [34]. Replication of the channel by hot embossing and thermal bonding of polymer pieces were performed by using Carver Hydraulic Press Machine. The thickness of the polymer sheets were 3 mm, 2 mm and 125 μm PMMA, COP and PEN, respectively. The surface areas of these polymers were 3 cm x 4 cm for PMMA, 3 cm x 5 cm for PEN and 3 cm x 3 cm square, 3 cm x 4 cm rectangular and 3 cm x 4 cm x 3cm triangular shape for COP polymers.

In literature, hot embossing and thermal bonding methods are used by optimizing the parameters by considering the specific polymeric properties, structure of the design, height of the channels and surface area of the polymer pieces. The fabrication of polymeric microstructures via hot embossing method is widely used in the last 10 years because of the simplicity of the process, the low cost of master structures and the large range of suitable polymer materials [35]. The thermal bonding (to bond the thermoplastic structures by heat and pressure) can also be done by same machine used for hot embossing. The bonding quality can be improved by surface treatment (i.e. solvent treatment, UV/ozone, oxygen plasma) [34].

Depending on the material of the master molds, design and the type of the polymer, process parameters need to be optimized. The channel formation via hot embossing can be performed about 20-30°C above the glass transition temperature of the plastic resin [36]. Kricka *et al.* (2002) performed the replication of channels using PMMA polymer. The replication of the polymer was performed about 20°C above the glass transition temperature of PMMA by applying 3 N/mm^2 pressure. After hot embossing, each plastic piece was drilled from the inlet and outlet positions of the channels and 1 mm holes were created. Each polymer piece was covered using the same material via a proprietary method. The micropart was tested with an aqueous dye solution to investigate whether the channels were open or clogged [36]. The replication accuracy of the hot embossed part was measured to find the optimum hot embossing parameters [37]. The PMMA of 3 mm thickness was used to create 27 μm depth and 110 μm width channels. Several temperature

(160, 180, 200, 220, 240°C) and pressure (10, 15, 20, 25, 30 kN) values were tested, and the chosen parameters were 20 kN applied force, 180°C temperature and 5 min embossing time. The polymer was cooled down and separated from the mold at 80°C.

Table 4.16. Fabrication parameters for polymers in literature.

Reference	Material	Tg	Area	Hot Embossing Parameters	Surface Treatment	Bonding Parameters	Cleaning Procedure
[29]	Zeonor ZF14	136	110 x 110 mm^2	190°C 3.125 MPa 120 sec	-	126°C 0.9 MPa 30 min	Not announced
[36]	Zeonor 1020R	105	3.3 x 3.3 cm^2	138°C 667 N 5 min	-	107°C 448 N 10 min Anneal at 115 C for 10 min	Not announced
[37]	PMMA	105	NA	180°C 20 kN 5 min	-	-	-
[38]	Zeonor 1020	105	4 x 2 cm^2	130°C 2.50 MPa 7 min	-	85°C 200 psi 10-15 min	Cleaned by acetone for 2 minutes in ultrasonic bath
[39]	Zeonor 1020R	105	3 x 3 cm^2	-	UV ozone 30 min vapor-phase cyclohexane container for 6 min	3.45 MPa for 1 min at room temperature	Sonication for 30 min in ultrapure water, sequential rinsing using methanol, 2-propanol, and ultrapure water, dried with N2 and deaerated at 50 °C in vacuum oven for 8 h

Another study was done by Kameoka *et al.* (2001), the embossing of Zeonor pieces occurred at 130°C at a pressure of 1.7 MPa applied for 7 min. Two pieces to be bonded were cleaned by acetone for 2 minutes in an ultrasonic bath. The capillary electrophoresis

chips having 60 µm wide and 20 µm high channels were bonded at 85°C under 200 psi pressure for 10-15 minutes [38]. Chen *et al.* (2015) used another cleaning procedure, i.e. they sonicate the Zeonor 1020R polymer pieces in ultrapure water to remove the debris, sequential rinsing using methanol, 2-propanol and ultrapure water, drying with pressurized N_2 and deaeration at 50°C in vacuum oven for 8 hours [39]. The microembossing parameters of 0.8 mm thick Zeonor ZF14 COP pieces were optimized by *Pemg et al.* (2010). Several temperatures (170, 180, 190°C), embossing pressures (1.875, 2.5, 3.125 MPa), duration (60, 90, 120 seconds) and de-molding temperatures (40, 60, 80°C) were tested. The optimized hot embossing parameters were 190°C, 3.125 MPa and 120 seconds, demolding temperature of 80°C [29]. Some of the hot embossing and bonding parameters tested in literature are given in Table 4.16.

The fabrication steps of PMMA made microbioreactor is as follows; first the polymer piece was cleaned by baby shampoo, 2-propanol and distilled water, dried by pressurized nitrogen. Then the microchannel formation was done at 120°C (Tg = 105 °C) under 1250 lbs pressure for 10 minutes. The polymer was demolded at 65°C. After replication, the microchannel featured 3 mm thick PMMA piece was drilled at the inlet and outlet positions of each channel. The 1 mm thick cover piece and featured piece were again washed by the same cleaning procedure and solvent treated by rinsing into 2-propanol for 2 minutes and dried by pressurized nitrogen. For the bonding process, these two pieces were aligned between glass pieces of 3 cm x 4 cm and 1.5 mm thickness and clamped from four sides. The optimized bonding for oven was done at 105°C for 50 minutes. The bonded device was tested with distilled water to investigate the ease of the channels and the effectiveness of bonding of the hot embossed and the cover part.

The fabrication of COP made microbioreactor was also optimized effectively. The COP polymer piece was cleaned by acetone, 2-propanol and distilled water, and dried by pressurized nitrogen. Then the hot embossing was done at 130°C (Tg = 102°C) under 1330 lbs pressure for 10 minutes and demolded at 65-80°C. The inlet and outlet holes were drilled on the microchannel featured COP piece. Two pieces were then washed by same cleaning procedure and ultrasonicated in ultrasonic bath for 15 minutes, dried by nitrogen and annealed at a 80°C hot plate for 15 minutes. The two pieces were aligned between two

glass pieces. The bonding parameters were optimized for each size. The 2 mm thick, 3 cm x 4 cm x 3 cm triangular pieces were bonded at 130°C under pressure of 190 lbs for 30 minutes. The 2 mm thick, 3 cm x 4 cm rectangular pieces were bonded at 130°C and 380 lbs for 45 minutes. The 2 mm thick, 3 cm x 3 cm square pieces were bonded at 125°C and 2375 lbs for 1 hour. The COP polymers were bonded between 2 mm thick glass pieces. Because of the heat transfer time from the glass to the polymer piece, the bonding of rectangular and square pieces took longer than that of small triangular pieces. Also pressure values needed for bonding were varied for different sizes. The bonded chip was tested with acetone to investigate the channels whether open or clogged. Because of the high hydrophobicity of COP polymer, water cannot easily enter the channels, it must be forced by syringe pump.

The fabrication of PEN made microbioreactor was started by cleaning with Chloroform:Ethanol (1:1 volume/volume) mixture and followed by drying by pressurized N_2. The 125 μm thick, 3 cm x 5 cm PEN polymer piece was hot embossed at 135°C under 3800 lbs for 10 minutes, demolded at 60°C. The inlet and outlet holes were opened by laser before hot embossing of the polymer piece. Two pieces were then cleaned by acetone, 2-propanol and distilled water and submerged into Chloroform-Ethanol solution (1:1 volume/volume) for 5 minutes. The optimized temperature, pressure and duration times for the bonding was 135°C, 1500 lbs and 90 minutes, respectively. The PEN made microbioreactor was also tested by acetone to see the effectiveness of the bonding.

4.9.3. Growth Kinetics in the Microbioreactor

Growth has been considered as one of the most important performance indicators in biotechnological production processes [40]. In the present study, the behavior of *S. cerevisiae* cells was followed in Lab-on-a-Chip platform under environmental stress conditions, i.e. rich YPD medium and low auto-fluorescence YNB media containing both 2% and 0.2% glucose as the primary carbon source.

In this section, the behavior of the trapped cells in all the chambers were analyzed via cell count and integrated density/cell area values and compared with those of other experiments. For the first experiment (E1Y), cells were grown in 2% glucose containing

YPD medium for 15 hours. As the medium was continuously supplied to the reactor, the environment was favorable for cell culturing, i.e. enough nutrient supply. The cells were trapped in first three chambers and the number of cells was highest in the first chamber. Figure 4.105a shows that the number of cells trapped decreased from the first to third chamber. After 420th minute (7 hours) of the experiment, the number of cells showed a constant trend in all chambers. When the integrated density/cell area results were analyzed (Figure 4.105b), the ratio was high at the beginning for all chambers because of the very small starting areas of cells. The value of the integrated density/cell area became constant after 120th minute of the experiment. With the growth of the cells by time, the expression of fluorescence signal of Sld7p-GFP also increased. This parallel trend of integrated density and cell area resulted in a constant ratio throughout the experiment.

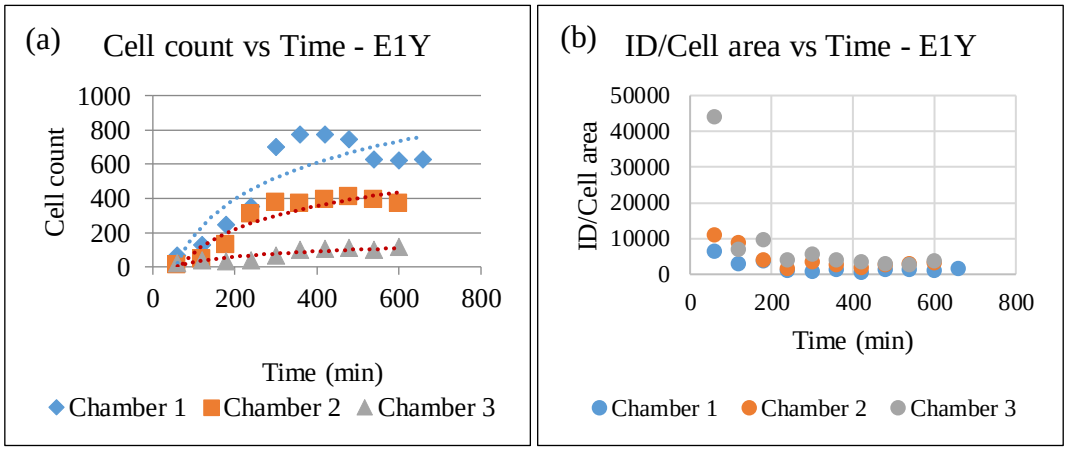

Figure 4.105. Results for E1Y (a) cell count vs time graph (b) integrated density/cell area vs time graph for all chambers.

The results were then analyzed for the experiment done by 2% YNB medium without histidine (E4Y). The cells were trapped in first four chambers and grown under continuous medium supply for 15 hours. The number of cells trapped in the c-shaped region of the first chamber was around 200 at the beginning (Figure 4.106a). There was an increasing trend for the first chamber and the number of cells was around 500 at the end of the experiment. The number of cells trapped decreased from the first to the third chamber. The variance of counted cells through the experiment was around 100 for the second and third chambers. The medium has a low auto-fluorescence characteristic and the fluorescence

signals of cells were observed more clearly during image processing. The ratio of the integrated density/cell area in all the chambers reached constant values after 400th minute of the experiment as shown in Figure 4.106b.

For the experiment E5Y (caloric restriction, 0.2% glucose containing YNB medium without histidine), the number of cells trapped from the first to seventh chamber showed a decreasing trend same as first two experiments (E1Y and E4Y). Most of the cells were trapped in the c-shaped region of the first chamber and no cell was trapped at the eighth chamber. According to Figure 4.107, the cell number was around 2600 after 60 hours of operation for the first chamber and cells were alive for almost 60 hours. Between 2700th and 3510th minutes, a sharp increase of cell count was observed. After 2500th minute, there was a radical increase in cell number and that cannot be explained by ordinary nutrient supply.

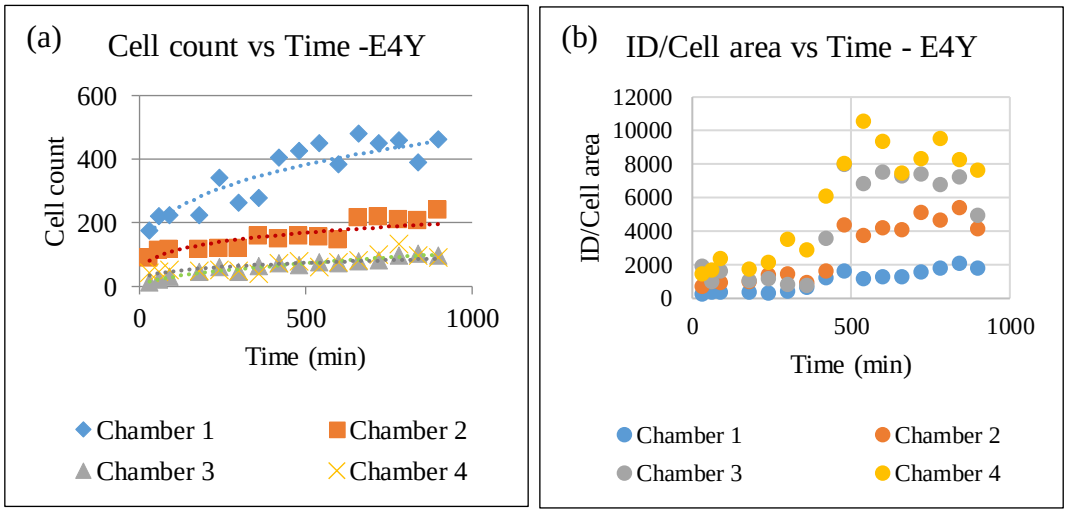

Figure 4.106. Results for E4Y (a) cell count vs time graph (b) integrated density/cell area vs time graph for all chambers.

The number of cells was around 1500 at this point, which indicated huge colonies of cells. Yeast cells consume glucose and prefer any fermentable carbon source over any source such as glycerol, ethanol or acetate [41]. At anaerobic growth 90% of the glucose carbon was converted into ethanol and carbon dioxide [42]. In our system, *S.cerevisiae* cells were grown anaerobically in a glucose limited environment for 60 hours. This sudden

increase at the end of the experiment can be correlated with the ethanol production of cells and consumption of this product for cell growth. Actually, this radical increment can be due to growth of cells on products and byproducts (ethanol and glycerol respectively), which were produced and secreted into the medium. There were high number of cells trapped and grown in the first chamber and the production of ethanol, glycerol etc. might be high during the first 45 hours. Cells may consume these products for their growth between 2700th and 3510th minutes resulting in 2.5 fold increase in cell number. The number of cells trapped in the c-shaped region of the second chamber was significantly lower, i.e. it decreased from 2600 cells (1st chamber) to 300 cells (2nd chamber), but all the cells were alive for 60 hours. According to Figure 4.107, the number of cells increased by time in each chamber, but the total cell count decreased towards the last chambers. The number of cells reached a constant value after 2000th minute except the first chamber (Figure 4.107b).

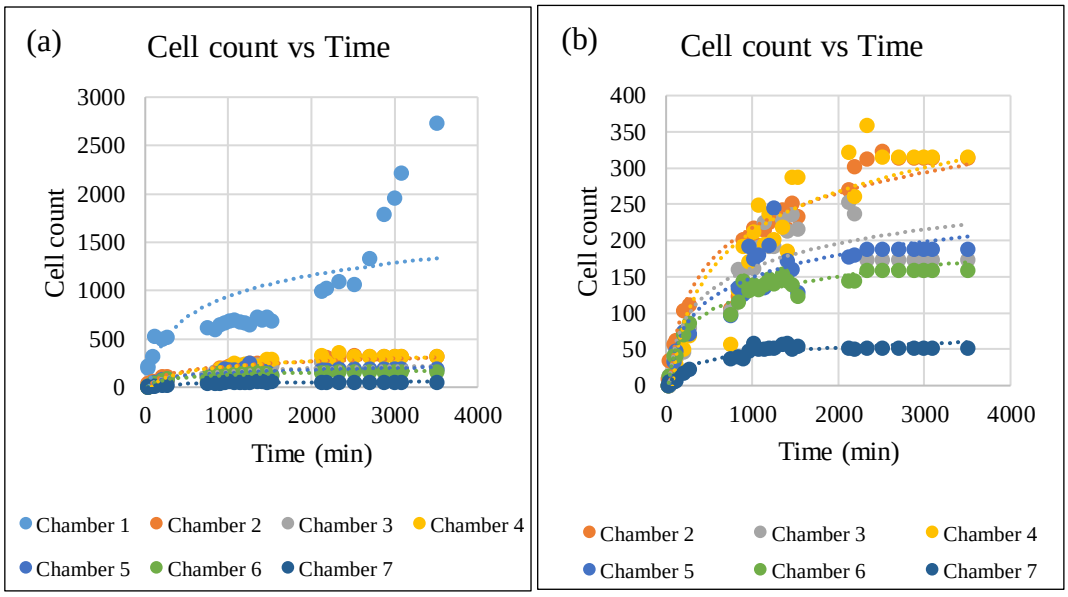

Figure 4.107. Cell count vs time graphs of E5Y (a) for all chambers and (b) for last six chambers.

As there was no constant decrease either in cell perimeter or cell area, we understand that the yeast cells did not enter death phase (shrinkage of cell volume) after 15-60 hours of operation and they were living perfectly well in the in house fabricated microchemostat.

The number of cells per chamber (cultivation volume) gets smaller towards the 7th or 8th chamber, that allows us to control the environment around the cells more accurately, as it was mentioned in Grünberger *et al.* (2004) [40]. As the areas of cells were increasing by time, the expression of fluorescence signals were also increasing in parallel to it. The expectation was a constant ratio throughout the experiment. The ratio in all the chambers reached a constant value as shown in Figure 4.108. The protein level of Sld7p:GFP fusion did not increase with age. Similar behavior was observed for Gsh1p by Xie *et al.* (2012) [43]. The number of cells and the ratios of integrated density/cell area are given at steady state for all the chambers in Table 4.17.

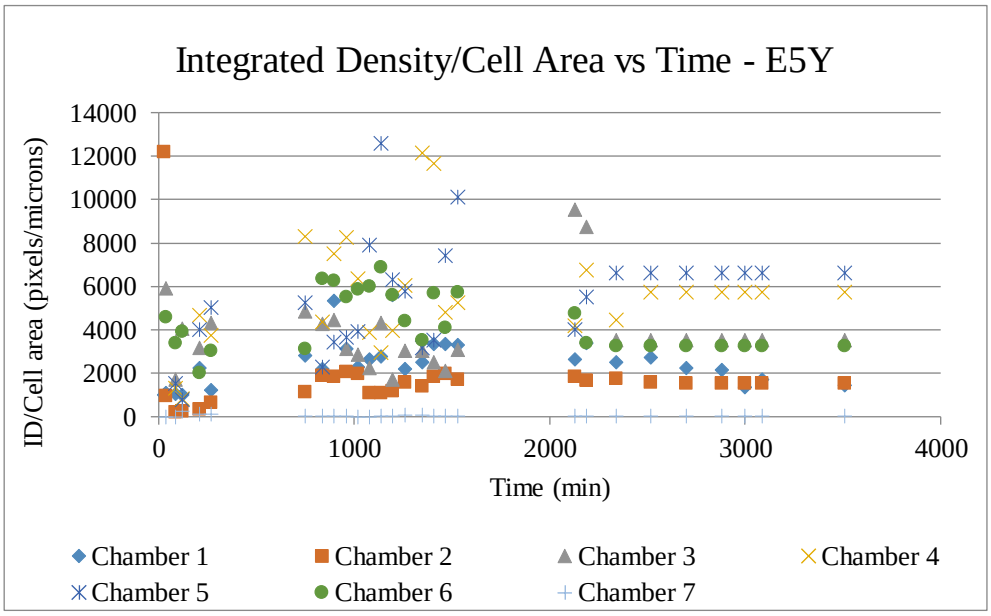

Figure 4.108. ID/Cell area vs time graph of all chambers for E5Y.

The growth trends of cells in different media were compared by plotting the time profiles for the first chambers (Figure 4.109). For all experiments, in first 5-6 hours, the number of cells increased exponentially and reached at steady state. The experiments E1Y and E4Y were ended after 11 and 15 hours, respectively, due to the leakage appeared through the intersection of epoxy and the polymer as well as air bubbles in channels. The experiment E5Y was carried out for approximately 60 hours and even after that time no contamination was observed within the chip. The ratio of integrated density to cell area showed the same trend as the growth profile for experiments done using YNB medium.

The time profiles were constant after a slight increment at the beginning. However, for experiment E1Y, which was done using YPD medium, the ratio decreased by time and stayed constant after 125th minute. This can be linked to the volume of the cells in experiments. The diameter of the cells grown in YPD medium were around 2-3 μm but the cells (new strain) in experiment done by YNB medium were around 4-5 μm. The typical haploid cell was reported to have 5+/- 0.5 micrometer in diameter [34]. When the volumes of the cells were small at the beginning, in E1Y the data points were at higher values in first 125 minute.

Table 4.17. Cell count and integrated density/cell area at steady state.

Experiment	**Chamber**	**Cell count (Steady State)**	**ID/Cell area (Steady State)**
E1Y	1	700-800	50-100
	2	400	100-150
	3	100	100-150
E5Y	1	400-500	75-100
	2	200-250	200-300
	3	80-100	300-400
	4	80-100	400-500
E4Y	1	1250-1500	100-200
	2	275-300	75-100
	3	200-250	200
	4	300-350	300-400
	5	175-200	300-400
	6	150-200	200-300
	7	50-75	50-100

On the other hand, in the experiments done using YNB medium, the ratio of integrated density to cell area slightly increased in the first 270 minute and stayed constant until the end of the experiment. Nevertheless, similar expression values of Sld7p:GFP (300-400 A.U) were obtained in YNB medium without histidine independent of glucose concentration. Rich YPD medium with 2% glucose resulted in higher cell number, but lower Sld7p:GFP (100-150 A.U) expression compared to YNB medium with 2% glucose.

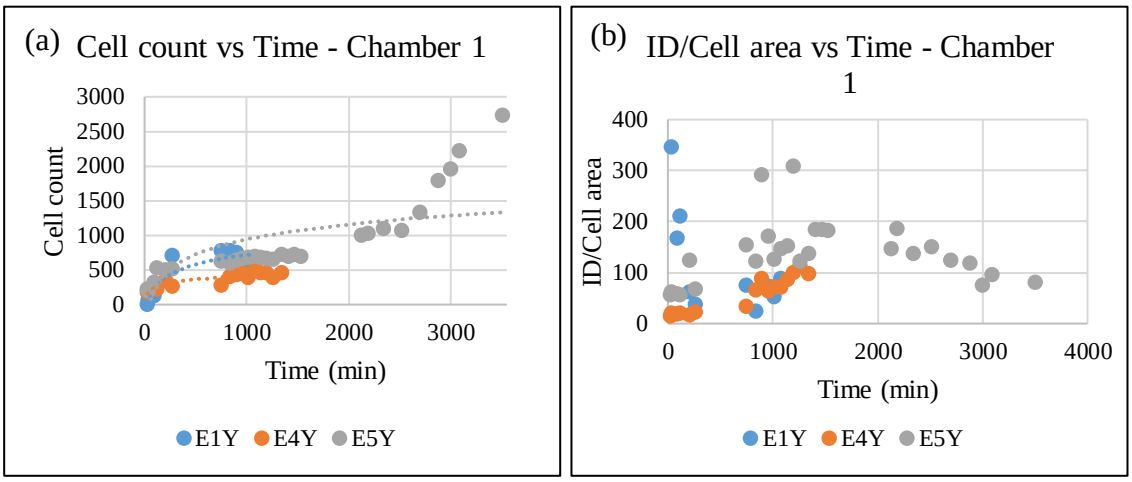

Figure 4.109. Results of the first chamber for all chambers (a) cell count vs time graph (b) integrated density/cell area vs time graph.

4.9.4. Determination of Maximum Specific Growth Rates

The specific growth rates of *S. cerevisiae* cells and product formation kinetics of Sld7p:GFP fusion protein were estimated using the data collected from image processing. After selecting the time intervals for unsteady and steady state, the maximum specific growth rates were calculated for all chambers in each experiment. The cells in the continuous microfluidic system had a growth profile which fits the Monod kinetics (Figure 4.110). The specific growth rate was estimated by the slope of the semi-logarithmic growth curve, according to the equation below,

$$\mu = \frac{1}{X}\frac{dX}{dt} \quad \rightarrow \quad ln\frac{X}{X_0} = \mu . \Delta t \qquad (4.3)$$

Here, μ is specific growth rate (h^{-1}), X is the cell count at this time, X_0 is the cell count at previous time and Δt is the time difference between two consecutive time points. Table 4.18 shows the specific growth rates in all chambers in each experiment. In experiment E4Y, apparent growth of cells were mostly observed in the first and third chambers and their specific growth rates were determined as 0.117 and 0.200 (h^{-1}), respectively. For the second and fourth chambers, the number of cells did not increase

more than 1% fold and growth rates were determined as 0.017 and 0.05 h^{-1}. For the experiment done using 0.2% glucose containing YNB medium (E5Y), the maximum specific growth rate was between 0.142-0.256 h^{-1}. These values (0.1-0.2 h^{-1}) are in agreement with literature reports for *S. cerevisiae* [46]. The group of Alberghina (1998) studied the growth of yeast cells by controlling the nutrients. In this pioneering study, 2% glucose containing YNB medium was used and μ_{max} was obtained in a range of 0.156 – 0.327 h^{-1} for daughter cell populations of *S.cerevisiae* cells [47]. In the study of Govindaswamy *et al.* (2006), *S.cerevisiae* 424A strain was used for the fermentation using YPD medium containing 2% glucose and a maximum specific growth rate (μ_{max}) of 0.291 h^{-1} was obtained [45].

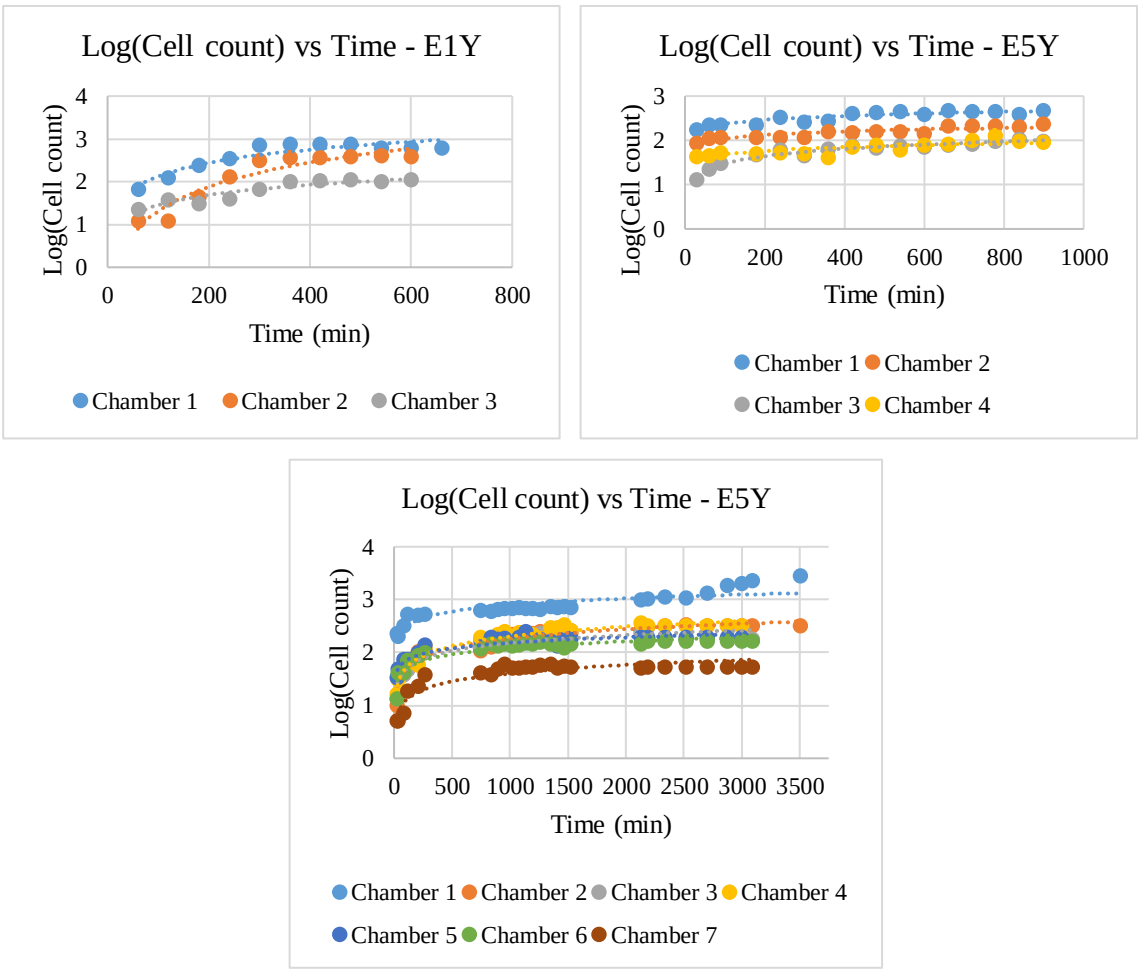

Figure 4.110. Log (cell count) vs time graphs for all experiments.

In another study done by Oliveria *et al.* (2015), a diffusion-based microfluidic device was used to investigate the yeast (*S.cerevisiae ATCC 7754*) growth by generating concentration gradients in a microchannel. The specific growth rate was 0.24 h^{-1} at an initial glucose concentration of 2% in YPD medium. In this study, the maximum specific growth rate values were between 0.234-0.330 h^{-1} in YPD medium containing 2% glucose [46] . The dilution rate is defined as the flowrate of medium per time (F) over the volume of culture (V) in the bioreactor. The flow rate of fluid was as follows (COMSOL simulations, Model 4): 1 µL/min for middle inlet and 0.1 µL/min for side inlets. The volume of one chamber is 15.6 $x10^{-6}$ μm^3 (diameter of 310 µm). The dilution rate gives the growth rate of cells in a chemostat at steady state.

Table 4.18. The specific growth rates in all experiments.

Experiment	**Chamber**	**Exponential Growth Phase (min)**	**μ_{max} (h^{-1})**
E1Y	1	60-300	0.225
	2	120-300	0.330
	3	240-420	0.234
E4Y	1	60-240	0.117
	2	60-240	0.017
	3	60-240	0.200
	4	60-240	0.050
E5Y	1	40-270	0.142
	2	40-270	0.227
	3	40-270	0.218
	4	90-270	0.256
	5	90-270	0.180
	6	40-270	0.221
	7	40-270	0.204

A lead study was done by Verduyn *et al.* (1989) to observe the physiology of *S. cerevisiae* in anaerobic glucose-limited chemostat cultures. At a 0.1 h^{-1} dilution rate, the microorganism had a μ_{max} of 0.31 h^{-1} in 2.3% glucose containing medium [47]. Boender *et al.* (2009) also researched about the physiology of *S. cerevisiae* at near-zero specific growth rates, i.e at dilution rates below 0.025 h^{-1}. In their anaerobic glucose limited system, the value of μ_{max} decreased from 0.2 to 0.001 (h^{-1}) after 22 days of experiment. In chemostat studies on *S. cerevisiae*, the steady state specific growth rate were usually between 0.03 – 0.4 h^{-1} [43]. When the results of specific growth rates were compared with those in literature, our results were all in agreement.

4.9.5. Product Formation Kinetics

The rates of growth and product formation of viable cells were calculated and the graphs were plotted for all experiments. The growth associated product formation was also analyzed via using the equations given below.

$$Cell\ growth \quad r_x = \mu . x_v \tag{4.4}$$

$$Product\ formation\ r_p = \alpha . r_x\ (growth\ associated) \tag{4.5}$$

The rate of formation of viable cells (r_x) and rate of formation of simple energy-producing product (r_p) for each time interval were calculated for unsteady state phase and the results are given in following figures. At the exponential growth phase, μ decreased linearly with increasing product concentration (log-2 based integrated density) until it reached the steady state (E1Y). The product formation rate, r_p = dP/dt, showed an increasing trend with cell formation rate, dX/dt during the initial unsteady state phase (Figure 4.111). However, a uniform trend cannot be obtained for all the chambers (Appendix D) using the data after image processing. Some opposite behavior may be because of the loss of fluorescence signals, which cannot be processed properly.

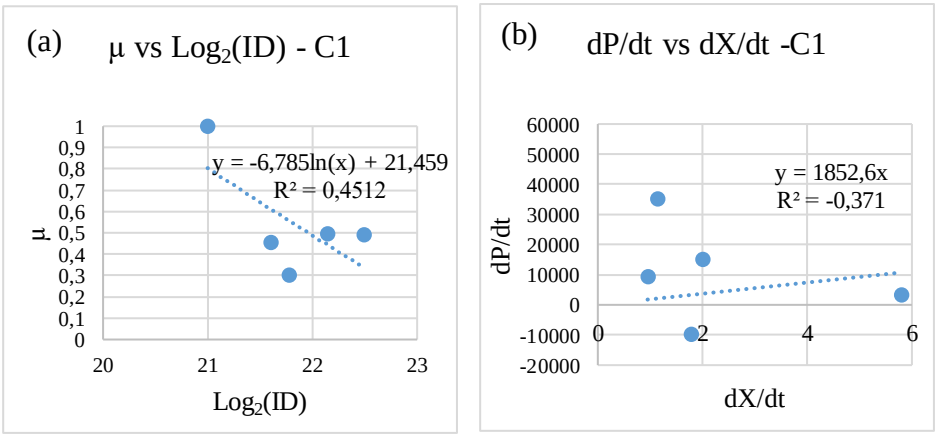

Figure 4.111. Product formation kinetics (a) μ vs $\log_2$(ID) graph (b) dP/dt vs dX/dt graph of chamber 1 for E1Y.

4.9.6. Cell Cycle Mechanism of Sld7p

The budding yeast *S. cerevisiae* is commonly used for studying DNA replication because the average firing time of each phases has been mapped and the initiation of DNA replication has been described [48]. Sld7 protein in *Saccharomyces cerevisiae* is an uncharacterized protein with a putative role in chromosomal DNA replication. Sld7 protein has genetic interactions with other proteins of DNA synthesis including Sld3 and Cdc45 (Sld4) as shown in Figure 4.112, and that creates the question on the role of Sld7 in cell cycle process. Although, Sld7p protein is found at a limited amount in yeast, its depletion slowed down the growth of cells by causing a delay in S-phase [49]. Sld3 protein is known to play a role in DNA replication and it is a required replication protein at the origins of the replication process. Sld7p binds to the domain in the N-terminal side of Sld3p, stabilizes it, reduces its binding affinity to Cdc45 (cell division cycle protein) protein, which is a DNA replication initiation factor.

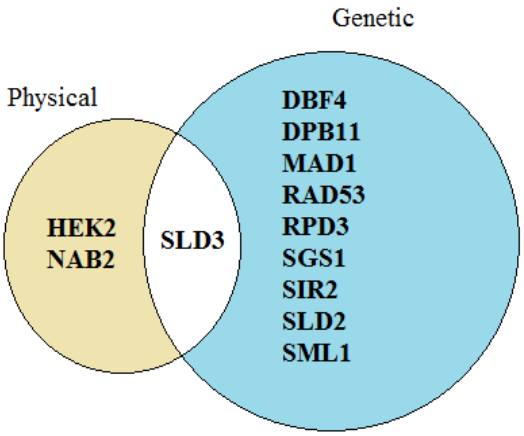

Figure 4.112. Physical and genetic interactions of Sld7p.

The role of Sld mutations (-2,-3 and -5) in the mechanism of eukaryotic chromosomal DNA replication was determined. In the study of Tanaka et al (2011), the role of Sld7 protein in cell cycle was studied and Sld7p was found to function in cooperation with Dpb11 and other Sld proteins during cell cycle [50]. The initiation of DNA replication delayed when Sld7 protein was deleted. The characteristics and close features of Sld7 protein given in literature are summarized in Table 4.19.

Table 4.19. Characteristic features of Sld7 in *S. cerevisiae* [51].

Feature		SLD7
Systematic Name		YOR060C
Molecular Function		Unknown
Biological Process	**Manually curated**	Regulation of DNA-dependent DNA replication initiation
Cellular Component	**Manually curated**	Chromosome, centromeric region, DNA replication preinitiation complex
	High-throughput	Cytoplasm, endoplasmic reticulum, nuclear envelope, nucleus, co-localized with spindle body

In the present study, the fraction of total budded cells (FBC) was assumed as 0.3 for all experiments. The duration of budding phase during the balanced growth period or the time of budding (Tb), comprising the S, G2, M phases and the duration of G1 phase were calculated from the equation below [44];

$$Tb = [\ln(1 + FBC)]Td/ln2 \tag{4.6}$$

Here, Td refers to the duplication time ($Td = \ln2/\mu_{max}$). Duplication times, budded and G1-phase durations are given in Table 4.20.

In budding yeast, the main control of the cell division cycle takes place late in the G1 phase and essential processes as budding, DNA replication and spindle-body duplication begin. The duration of G1 phase is longer than the budding phase for cells born during exponential growth phase on glucose. At the initial stages of chemostat operation, duplication time, duration of G1 phase and budding phase were changing in ranges of 2.10-5.90, 1.30-3.67 and 0.79-2.23 hours, respectively. These values were in agreement with literature data published by Alberghina *et al.* (1998) [44]. Z-score values of product concentration were estimated to find the high expression intervals of Sld7p:GFP fusion protein (Figure 4.113). Although the product expression signals per cell volume were more or less constant within each chamber, they increase above the mean value at steady state operation in all the experiments.

Table 4.20. Duplication time, budded and G1 phase durations at exponential growth phase.

Experiment	Chamber	Duplication time (hr)	G1 phase	Budding phase (S, G2, M)
E1Y	1	3.08	1.91	1.16
	2	2.10	1.30	0.79
	3	2.96	1.84	1.12
E5Y	1	5.90	3.67	2.23
	2	40.77	25.34	15.43
	3	3.46	2.15	1.31
	4	13.86	8.61	5.24
E4Y	1	4.88	3.03	1.84
	2	3.05	1.89	1.15
	3	3.17	1.97	1.20
	4	2.70	1.68	1.02
	5	3.85	2.39	1.45
	6	3.13	1.95	1.18
	7	3.39	2.11	1.28

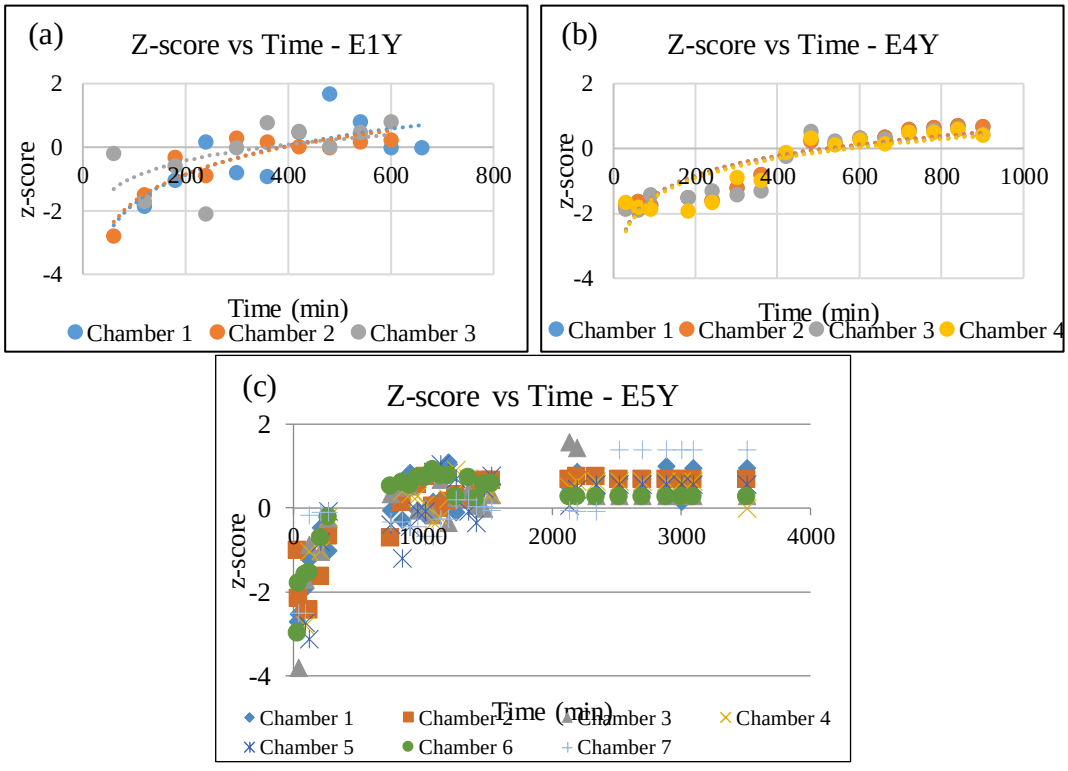

Figure 4.113. Z-score vs time graphs for experiments (a) E1Y (b) E4Y (c) E5Y.

4.9.7. Diffusion phenomena of cells and nutrients and shear stress

In order to achieve an efficient cell culture experiment in a microfluidic device, the cells need to be trapped in the determined regions and fed by nutrient flow continuously. The flow phenomena is used to determine the characteristics of the device. The Reynolds Number (Re) is the most commonly used dimensionless number which defines the flow regime being laminar or turbulent [52]. The Reynolds number is defined as follows;

$$Re = \frac{\rho . u . D}{\eta} = \frac{inertial\ forces}{viscous\ forces} \tag{4.7}$$

In this equation, ρ is the density (1013.2 kg/m^3), u is the inlet velocity (6.127 x 10^{-3} m/s), D is the diameter of the c-shape (200 μm) and η is the viscosity of the fluid (0.000894 Pa.s). By this calculation, Reynold number is estimated as 1.38 which dictates that flow regime is laminar and no mixing was occurring in the fabricated microbioreactor. Also at the center of the first c-shape, Re number is equal to 0.04, which supports the laminar flow behavior.

Another most commonly used number in microfluidics is the Peclet number. This number represents the relative strength of convection over diffusion and defined as;

$$Pe = u.\frac{L}{D} = \frac{convective\ forces}{diffusive\ forces} \tag{4.8}$$

The Peclet number is calculated to determine whether sufficient glucose is reaching the first chamber by convection or diffusion process. The length (L) from the inlet hole to the entrance of the first c-shape is 6000 μm and Peclet number is calculated as approximately 58000 through this path. The transportation of the glucose molecules mainly depends on diffusive forces, which are created via syringe pump in the experiments. The diffusion time is defined as the time taken by a molecule to travel distance x by diffusive process as shown in Equation 4.9 and calculated as 16 hours. The calculated

diffusion time indicates that glucose molecules directly reach the chambers by advection without diffusing in the channels.

$$t = \frac{x^2}{D} \tag{4.9}$$

The statistical movement of a molecule (y) is characterized as random and described by Einstein-Smoluchowski relation as given below.

$$y = \sqrt{2.D.t} \tag{4.10}$$

According to equation 4.10, after 3 hours one glucose molecule is transported for approximately 30 micrometers by diffusion. This value shows that a significant diffusion of glucose molecule cannot be obtained through the channels. The molecular transport occurs via diffusive transport.

While studying cell culturing on microfluidic platforms, shear stress need to be kept below a level to avoid the trapped cells washed off from the surface. The local shear stress is a function of the device geometry, volumetric flow rate and viscosity. Wall shear stress can be manipulated by controlling the inlet flow rate and calculated by following equation,

$$\tau = \frac{6\,\eta\,Q}{w\,h^2} \tag{4.11}$$

When the wall shear stress is estimated at the velocity of 0.1 μL/min (at the middle of the first chamber), it is found as 2.62 dyne/cm^2. This low value of the wall shear stress in the c-shaped region shows that the cells were trapped in this region efficiently and were not flushed away by fluid flow. *Park et al.* (2015) reported that at maximum wall shear stress of 8.2 dyne/cm^2, all cells were flushed off from the surface [53].

5. CONCLUSION

5.1. Conclusions

This thesis described the work on culturing yeast cells in well-designed home-made microbioreactor. The following achievements were obtained from this study:

- The previous design of the microfluidic device was successfully scaled down for the visualization of the trapping region along the C-shape during the experiment.
- The new designed microfluidic device was successfully produced via hot embossing and thermal bonding techniques from PMMA, COP and PEN polymers.
- The simulations of velocity, concentration and pressure profiles were executed via COMSOL Multiphysics program and the favorable inlet velocities were obtained for the nutrient feeding and cell loading steps of the experiments.
- Yeast cells were trapped and cultured in predetermined c-shaped regions (0.13 nL volume) within the chip as it was purposed.
- The yeast cell experiments were performed by rich YPD medium and low auto-fluorescence YNB media containing both 2% and 0.2% glucose as the primary carbon source. The longest experiment lasted for about 60 hours and cells were visualized successfully.
- The brightfield and fluorescence images of the cells were captured by Nikon Eclipse-T inverted microscope at regular time intervals during the experiments. The images were processed via ImageJ-Fiji software by use of the macros written for brightfield and fluorescence images. The change on cell count, cell area, cell perimeter and integrated density parameters in each experiment were analyzed for all chambers of the microbioreactor. Despite the low protein abundance of Sld7 protein, the fluorescence signals were processed successfully.
- The behavior of GFP tagged Sld7p (YOR060C) of *S. cerevisiae* cells was followed in the fabricated Lab-on-a-Chip platform under environmental stress conditions. The maximum specific growth rates were calculated by using the results of processed images and were compared with those in literature, the results were all

in agreement. The product concentration (Sld7p:GFP expression) was found to increase in accordance with cell count, cell area and perimeter.

- The durations of G1 phase and budded phase in cell cycle were determined. The duration of G1 phase was found to be longer than the budded phase for cells born during exponential growth phase on glucose. The application of caloric restriction on yeast cells caused a decrease both in time of budding (S, G2, M phases) as well as G1 cell cycle phase.

5.2. Recommendations

The ultimate aim of this study was to fabricate a microfluidic device from different polymers and visualize the growth of green fluorescently tagged *S. cerevisiae* yeast cells by applying environmental stress via changing nutrient media and concentration. The results were used to get an insight on expression behavior of Sld7p which has a role in DNA replication of the cell cycle process. Nevertheless, some additional studies should be done to annotate a function to uncharacterized Sld7p (YOR060C) protein by using the fabricated microbioreactor.

- To get an insight about the molecular function of Sld7 protein, another protein (e.g. Sld3p), which has an interaction with Sld7, can be used. The localization of GFP tagged Sld7p protein and RFP tagged Sld3p can be followed and their expression profiles can be compared.
- In order to have a deeper understanding of the role of Sld7 protein in DNA replication step of the cell cycle, the abundance changes of GFP tagged Sld7 protein in yeast can be followed by applying replication inhibitors such as HU or MMS. The analyses done in absence and presence of inhibitor should be compared to figure out the DNA damage response of the cells.
- Since the optical transparency and biological inertness of COP and PMMA polymers were good, they were advantageous for the fabrication of a microbioreactor. The experiments were mainly performed in the COP made microfluidic device (microbioreactor). In order to compare the effects of different

polymers (used for fabrication of the device) on cell growth, additional experiments can be done using polystyrene (PS) made microfluidic devices.

- As long as the created microfluidic platform provides efficient cell trapping, it can be used for other type of cell experiments except yeast cells.

REFERENCES

1. Whitesides, G. M., "The Origins and the Future of Microfluidics'', *Nature*, Vol. 442, pp. 368–373, 2006.

2. Yeo, L. Y., H. C., Chang., P. P. Y. Chan, and J. R. Friend, "Microfluidic Devices for Bioapplications'', *Small*, Vol. *7*, pp. 12–48, 2011.

3. Sia, S. K., and G. M. Whitesides, "Microfluidic Devices Fabricated in Poly(dimethylsiloxane) for Biological Studies'', *Electrophoresis*, Vol. 24, pp. 3563–3576, 2003.

4. Halldorsson, S., E. Lucumi, R. Gómez-Sjöberg and R. M. T. Fleming, "Advantages and Challenges of Microfluidic Cell Culture in Polydimethylsiloxane Devices", Biosensors and Bioelectronics, Vol. 63, pp. 218–231, 2015.

5. Patel, S., D. Showers, P. Vedantam, and T. Tzeng, "Microfluidic Separation of Live and Dead Yeast Cells Using Reservoir-based Dielectrophoresis'', *Biomicrofluidics*, Vol. 6, pp. 1–12, 2012.

6. Ferry, M. S., I. A. Razinkov and J. Hasty, "*Microfluidics for Synthetic Biology*. *Synthetic Biology, Part A*", 1st ed., Vol. 497, pp. 295-372, Elsevier Inc., 2011.

7. Groisman, A., C. Lobo, H. Cho, J. K. Campbell, Y. S. Dufour, A. M. Stevens, and A. Levchenko, "A Microfluidic Chemostat for Experiments with Bacterial and Yeast cells'', *Nature Methods*, Vol. 2, pp. 685–689, 2005.

8. Cookson, S., N. Ostroff, W. L. Pang, D. Volfson, and J Hasty, "Monitoring Dynamics of Single-cell Gene Expression Over Multiple Cell Cycles'', *Molecular Systems Biology*, Vol. 1, 2005.

9. Ryley, J., and O. Pereira-Smith, "Microfluidics Device for Single Cell Gene Expression Analysis in Saccharomyces Cerevisiae'', *Yeast*, pp. 1065-1073, 2006.

10. Luo, C., L. Jiang, S. Liang, Q. Ouyang, H. Ji, and Y. Chen, "High-throughput Microfluidic System for Monitoring Diffusion-based Monolayer Yeast Cell Culture Over Long Time Periods'', *Biomedical Microdevices*, Vol. 11, pp. 981–986, 2009.

11. Falconnet, D., A. Niemistö, R. Taylor, M. Ricicova, T. Galitski, I. Shmulevich, and C. Hansen, "High-throughput Tracking of Single Yeast Cells in a Microfluidic Imaging Matrix'', *Lab Chip*, pp. 466-473, 2011.

12. Lee, S. S., P. Horvath, S. Pelet, B. Hegenmann, L. P. Lee, and M. Peter, "Quantitative and Dynamic Assay of Single Cell Chemotaxis'', *Integrative Biology*, Vol. 4, pp. 381, 2012.

13. Zhang, Y., C. Luo, K. Zuo, Z. Xie, O. Brandman, Q. Ouyang, and H. Li, "Single Cell Analysis of Yeast Replicative Aging Using a New Generation of Microfluidic Device'', *PLoS ONE*, Vol. *7*, pp.11, 2012.

14. Dénervaud, N., J. Becker, R. Delgado-Gonzalo, P. Damay, A. S. Rajkumar, M. Unser, and S. J. Maerkl, "A Chemostat Array Enables The Spatio-temporal Analysis of the Yeast Proteome'', *Proceedings of the National Academy of Sciences of the United States of America*, Vol. 110, pp. 15842–15847, 2013.

15. Park, J., J. Wu, M. Polymenis, and A. Han, "Microchemostat Array with Small-volume Fraction Replenishment for Steady-state Microbial Culture'', *Lab on a Chip*, Vol. 13, pp. 4217–24, 2013.

16. Crane, M. M., I. B. N. Clark, E. Bakker, S. Smith, and P. S. Swain, "A Microfluidic System for Studying Ageing and Dynamic Single-cell Responses in Budding yeast'', *PLoS ONE*, Vol.9, pp. 1–10, 2014.

17. Jo, M. C., W. Liu, L. Gu, W. Dang, and L. Qin, "High-throughput Analysis of Yeast Replicative Aging Using a Microfluidic System'', *Proceedings of the National Academy of Sciences*, Vol.112, pp. 9364-9369, 2015.

18. Hansen, A. S., N. Hao, and E. K. O. Shea, "High-throughput Microfluidics to Control and Measure Signaling Dynamics in Single Yeast Cells'', *Nature Protocols*, Vol. 10, pp. 1181–1197, 2015.

19. Bell, L., A. Seshia, D. Lando, E. Laue, M. Palayret, S. F. Lee, and D. Klenermn, "A Microfluidic Device for the Hydrodynamic İmmobilization of Living Fission Yeast Cells for Super-resolution Imaging'', *Sensors and Actuators B: Chemical*, Vol. 192, pp. 36–41, 2014.

20. Bouchez, I., M. Pouteaux, M. Canonge, M. Genet, T. Chardot, A. Guillot, and M. Froissard, "Regulation of Lipid Droplet Dynamics in Saccharomyces Cerevisiae Depends on the Rab7-like Ypt7p, HOPS Complex and V1-ATPase'', *Biology Open*, pp. 1–12, 2015.

21. Breker, M., M. Gymrek, and M. Schuldiner, "A Novel Single-cell Screening Platform Reveals Proteome Plasticity During Yeast Stress Responses'', *Journal of Cell Biology*, Vol. 200, pp. 839–850, 2013.

22. Becker, H., and C. Gärtner, “Polymer Microfabrication Technologies for Microfluidic Systems’’, *Analytical and Bioanalytical Chemistry*, Vol. 390, pp. 89–111, 2008.

23. Alrifaiy, A., O. A. Lindahl, and K. Ramser, “Polymer-based Microfluidic Devices for Pharmacy, Biology and Tissue engineering’’, *Polymers*, Vol. 4, pp. 1349–1398, 2012.

24. Yi, L., W. Xiaodong, and Y. Fan, “Microfluidic Chip made of COP (cyclo-olefin polymer) and Comparison to PMMA (Polymethylmethacrylate) Microfluidic Chip’’, *Journal of Materials Processing Technology*, Vol. 208, pp. 63–69, 2008.

25. Goodfellow, “Polyethylene naphthalate (PEN)-Film-Material Information’’, http://www.goodfellow.com/E/Polyethylene-naphthalate.html, accessed at July 2016.

26. Gençtürk, E., “Design and Fabrication of a Microbioreactor for Yeast Culturing”, M.Sc. Thesis, Boğaziçi University, 2015.

27. Nam-Trung N., and T. W. Steven, 2006, *Fundamentals and Applications of Microfluidics*, 2nd edition, Artech House, Boston.

28. Bellah, M. M., S. M. Christensen, and S. M. Iqbal, “Nanostructures for Medical Diagnostics’’, *Journal of Nanomaterials*, pp. 1–21, 2012.

29. Pemg, B. Y., C. W. Wu, Y. K. Shen, and Y. Lin, “Microfluidic Chip Fabrication Using Hot Embossing and Thermal Bonding of COP’’, *Polymers for Advanced Technologies*, Vol. 21, pp. 457–466, 2010.

30. Kosse D., M. Focke, C. Müller, F. von Stetten and R. Zengerle, "Microthermoforming and Sealing of COP Films to Form Thin Walled Lab-on-a-chip Cartridges", *8th International Conference on Multi-Material Micro Manufacture*, Stuttgart, Germany, 2011.

31. McCann, R., K. Bagga, A. Stalcup, M. Vazquez, and D. Brabazon, "Laser Micro-engineering of Functionalized Cyclic Olefin Polymers for Microfluidic Applications'', *Proceedings of SPIE - The International Society for Optical Engineering*, Vol. 9351, pp. 0–7, 2015.

32. Nunes, P. S., P. D. Ohlsson, O. Ordeig, and J. P. Kutter, "Cyclic Olefin Polymers: Emerging Materials for Lab-on-a-chip Applications'', *Microfluidics and Nanofluidics*, Vol. 9, pp. 145–161, 2010.

33. Nevitt, M., "Selecting and Designing with the Right Thermoplastic Polymer for Your Microfluidic Chip: A Close Look into Cyclo-olefin Polymer'', *Proc. Of SPIE*, Vol. 8615, pp. 1–11, 2013.

34. Lee, P. J., N. C. Helman, W. A. Lim, and P. J. Hung, "A Microfluidic System for Dynamic Yeast Cell Imaging''. *BioTechniques*, Vol. 44, pp. 91–95, 2008.

35. Becker, H., and L. E Locascio, "Polymer Microfluidic Devices'' *Talanta*, Vol. 56, pp. 267–287, 2002.

36. Kricka, L. J., P. Fortina, N. J. Panaro, P. Wilding, Alonso-Amigo, and H. Becker, "Fabrication of Plastic Microchips by Hot Embossing'', *Lab on a Chip*, Vol. 2, pp. 1–4, 2002.

37. Chien, R.-D., "Hot Embossing of Microfluidic Platform'', *International Communications in Heat and Mass Transfer*, Vol. 33, pp. 645–653, 2006.

38. Kameoka, J., H. G. Craighead, H. Zhang, and J. Henion, “Articles A Polymeric Microfluidic Chip for CE / MS Determination of Small Molecules’’, *Analytical Chemistry*, Vol. 73, pp. 1935–1941, 2001.

39. Chen, J. Y., Y.T. Huang, H. H. Chou, C.P. Wang, and C. F. Chen, “Rapid and Inexpensive Blood Typing on Thermoplastic Chips’’ *Lab on a Chip*, Vol. 15, pp. 4533–4541, 2015.

40. Grünberger, A., J. van Ooyen, N. Paczia, P. Rohe, G. Schiendzielorz, L. Eggeling, and S. Noack, “Beyond Growth Rate 0.6: Corynebacterium Glutamicum Cultivated in Highly Diluted Environments’’, *Biotechnology and Bioengineering*, Vol. 110, 2013.

41. Broach, J. R., “Nutritional Control of Growth and Development in Yeast’’, *Genetics*, Vol. 192, pp. 73–105, 2012.

42. Boender, L. G. M., E. A. F. De Hulster, A. J. A. Van Maris, P. A. S. Daran-Lapujade, and Pronk, J. T. Pronk, “Quantitative Physiology of Saccharomyces Cerevisiae at Near-zero Specific Growth Rates’’, *Applied and Environmental Microbiology*, Vol. 75, pp. 5607–5614, 2009.

43. Xie, Z., Y. Zhang, K. Zou, O. Brandman, C. Luo, Q.Ouyang, and H. Li, “ Molecular Phenotyping of Aging in Single Yeast Cells Using a Novel Microfluidic Device’’, *Aging Cell*, Vol. 11, pp. 599–606, 2012.

44. Alberghina, L., C. Smeraldi, and B. M. Ranzi, “Control by Nutrients of Growth and Cell Cycle Progression in Budding Yeast, Analyzed by Double-Tag Flow Cytometry Control by Nutrients of Growth and Cell Cycle Progression in Budding Yeast, Analyzed by Double-Tag Flow Cytometry’’, *Journal of Bacteriology*, Vol. 180, pp. 3864–3872, 1998.

45. Govindaswamy, S., and L. M. Vane, “Kinetics of Growth and Ethanol Production on Different Carbon Substrates Using Genetically Engineered Xylose-fermenting Yeast’’, *Bioresource Technology*, Vol. 98, pp. 677–685, 2007.

46. Oliveira, A. F., V. B. Pelegati, H. F. Carvalho, C. L. Cesar, R. G. Bastos, and L. G. de la Torre, “Cultivation of yeast in diffusion-based microfluidic device’’, *Biochemical Engineering Journal*, Vol. 105, pp. 288–295, 2016.

47. Verduyn, C., E. Postma, W. A. Scheffers, and J. P. Van Dijken, “Physiology of Saccharomyces Cerevisiae in Anerobic Glucose-Limited Chemostats’’, *Journal of General Microbiology*, Vol. 136, pp. 395–403, 2015.

48. Tanaka, S., R. Nakato, Y. Katou, K. Shirahige, and H. Araki, “Origin Association of Sld3, Sld7, and Cdc45 Proteins is a Key Step for Determination of Origin-firing Timing’’, *Current Biology*, Vol. 21, pp. 2055–2063, 2011.

49. Itou, H., Y. Shirakihara, and H. Araki, “The Quaternary Structure of the Eukaryotic DNA Replication Proteins Sld7 and Sld3’’, *Acta Crystallographica Section D: Biological Crystallography*, Vol. 71, pp. 1649–1656, 2015.

50. 50. Tanaka T., T. Umemori, S. Endo, S. Muramatsu, M. Kanemaki, Y. Kamimura, and H. Araki, “Sld7, an Sld3-associated Protein Required for Efficient Chromosomal DNA Replication in Budding Yeast’’, *EMBO J* Vol. 30, pp. 2019-30, 2011.

51. Saccharomyces Genome Database, “SLD7/YOR060C Protein”, http://www.yeastgenome.org/, accessed at July 2016.

52. Yildiz-Ozturk, E., O. Yesil-Celiktas, “Diffusion phenomena of cells and biomolecules in microfluidic devices”, *Biomicrofluidics*, Vol. *9*(5), 2015.

53. Park, J. W., S. C. Na, T. Q. Nguyen, S. M. Paik, M. Kang, D. Hong, N.L. Jeon, "Live cell imaging compatible immobilization of Chlamydomonas reinhardtii in microfluidic platform for biodiesel research", *Biotechnology and Bioengineering*, Vol. *112*(3), pp. 494–501, 2015.

54. Ribeiro, A. C. F., O. Ortona, S. M. N. Simoes, C. I. A. V. Santos, P. M. R. A. Prazeres, A. J. M. Valente, V. M. M. Lobo, and H. D. Burrows, "Binary Mutual Diffusion Coefficients of Aqueous Solutions of Sucrose, Lactose, Glucose, and Fructose in the Temperature Range from (298.15 to 328.15) K", *Journal of Chemical & Engineering Data*, Vol. 51, pp. 1836-1840, 2006.

APPENDIX A: DENSITY AND DIFFUSION CONSTANT CALCULATIONS

A.1. Density Calculation for CFD Simulations

The density value for COMSOL simulations were calculated by using the equation A.1 via considering 2% glucose solution was used as nutrient:

$$\rho_{mix} = \frac{1}{x_1/\rho_1 + x_2/\rho_2} \tag{A.1}$$

In the equation, density of the mixture is defined as ρ_{mix}, x_1 and x_2 represents weight fractions of the components and ρ_1 and ρ_2 are densities of components.

A.2. Diffusion Constant Calculation for CFD Simulations

The diffusion constant was calculated by using the following equation and selecting the constants given in the paper of Ribeiro *et al.* (2006). The concentration depence on diffusion coefficient and other equation for dilute solutions ($c < 0.1$ mol.dm^{-3}) are given as follows;

$$D = D^0 . 10^{-9} \left(1 + B(\frac{c}{mol} . dm^{-3}\right)_{T,P} \tag{A.2}$$

Here, D is the diffusion coefficient ($m^2.s^{-1}$), D^0 is the diffusion coefficient at infinite solution, c is concentration, γ is the thermodynamic activity coefficient of the solute and B is a constant(c/mol.dm^{-3}). Here ln γ equals to B and the value of γ constant was selected as 0.9734 for the glucose concentration of 0.1 mol.dm^{-3} at 303.15 K. By using this value, B is calculated as 2.64 and D^0 is taken as 0.767 for the glucose and water solution [54].

APPENDIX B: OPTIMUM CONCENTRATION AND PRESSURE PROFILES OF DESIGN-2

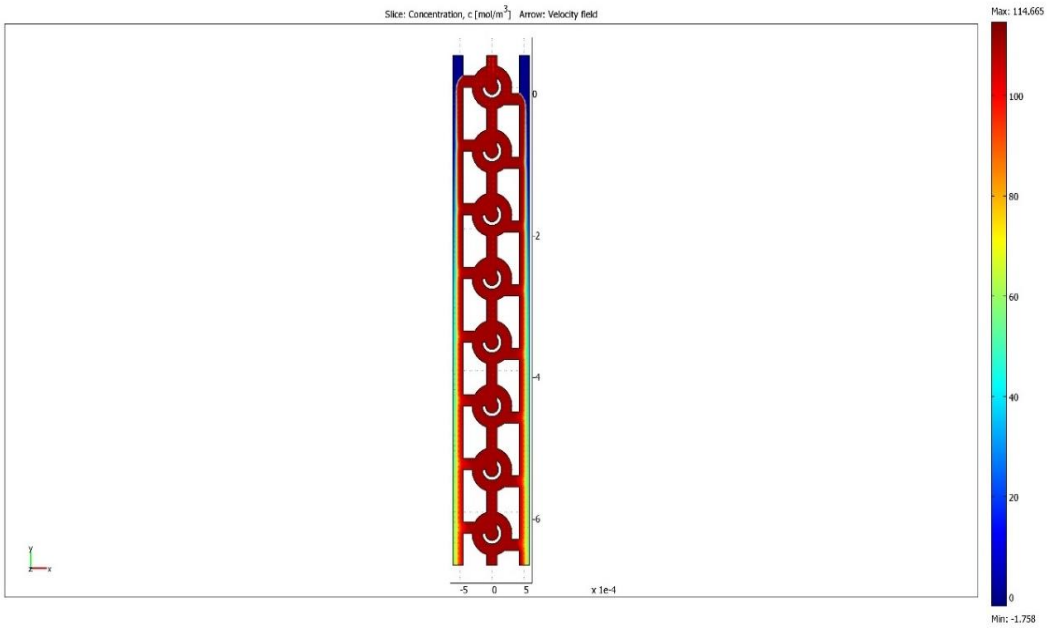

Figure B.1. Concentration profile of model 4 for new design-2.

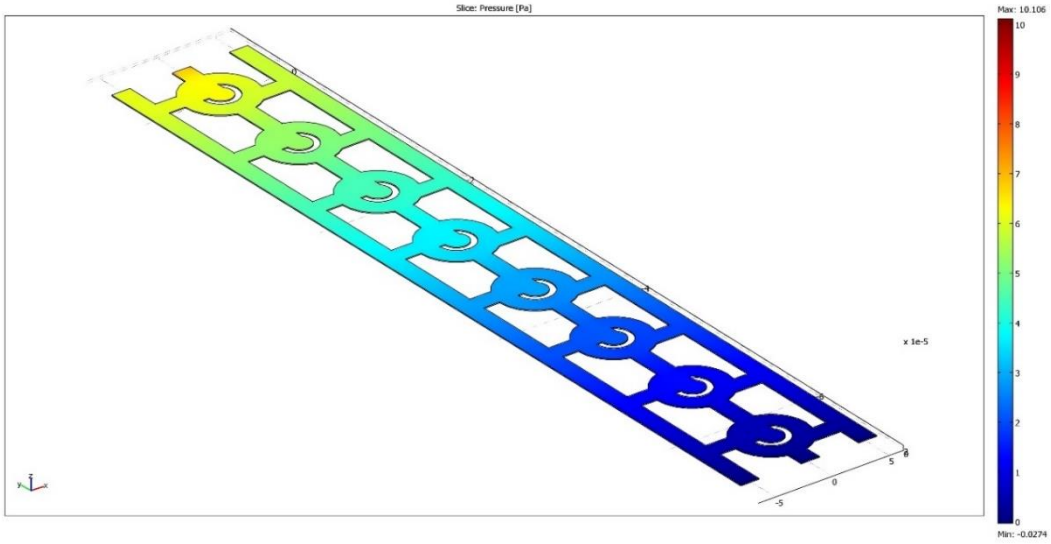

Figure B.2. Pressure profile of model 4 for new design-2.

APPENDIX C: RESULTS OF EXPERIMENTS

C.1. Results of Integrated Density/Cell Count for E1Y

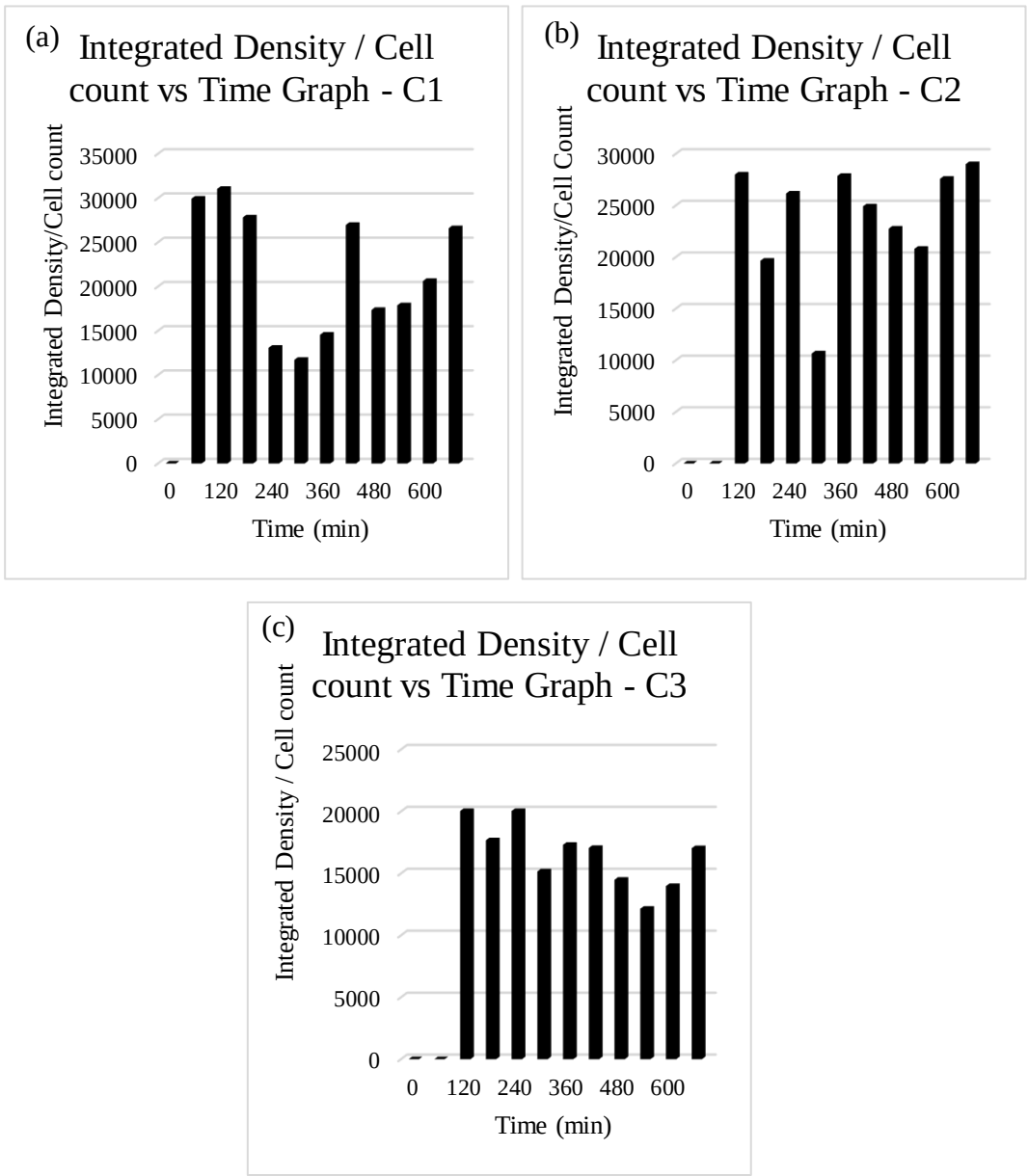

Figure C.1. Integrated density/cell count vs time graphs for (a) chamber 1 (b) chamber 2 (c) chamber 3.

C.2. Results of Chamber 4 in Experiment E4Y

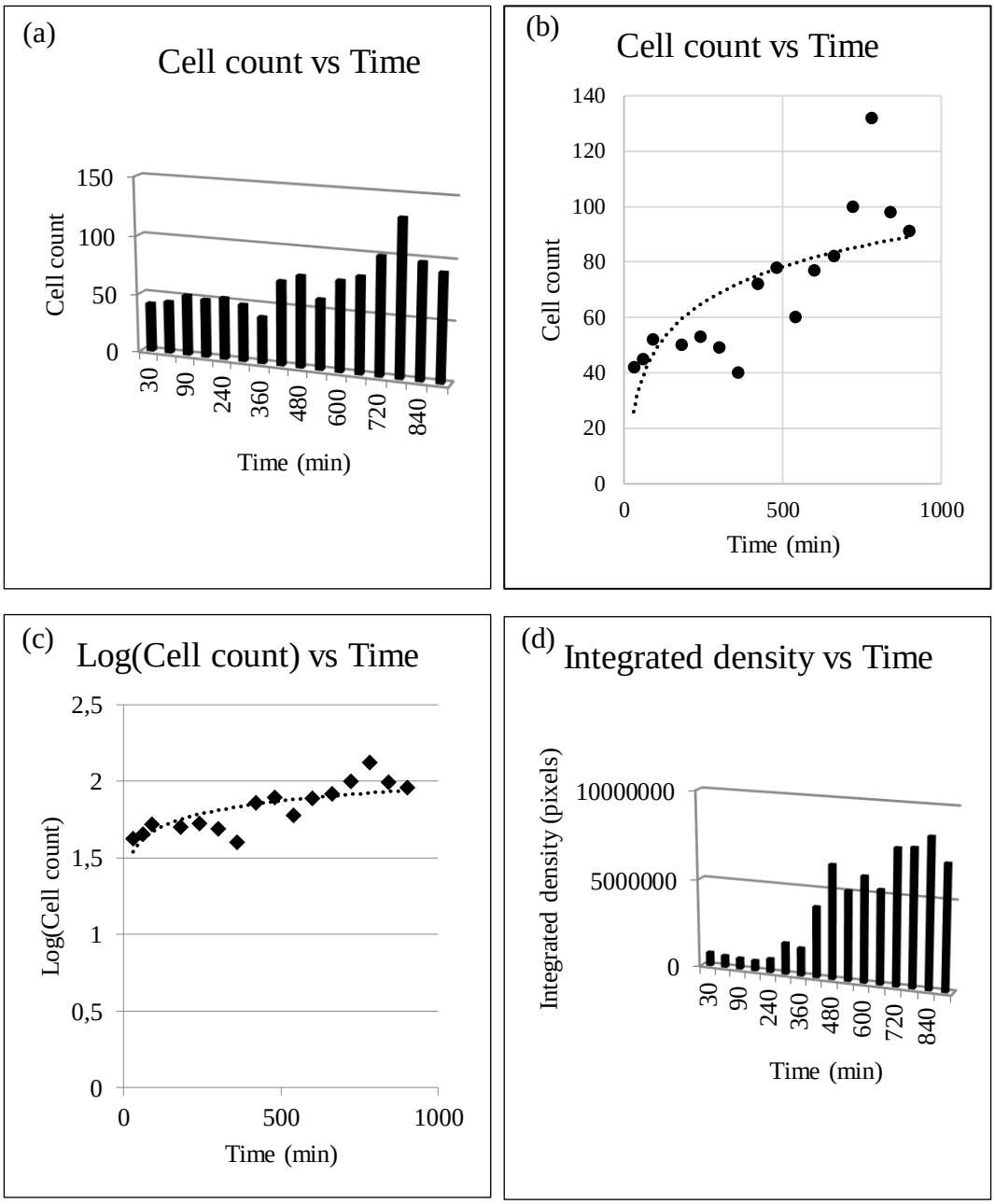

Figure C.2. Graphical display of processed data for chamber 4 (a,b) cell count vs time graph (c) log(cell count) vs time graph (brightfield images) (d) integrated density vs time graph (fluorescence image)-E4Y.

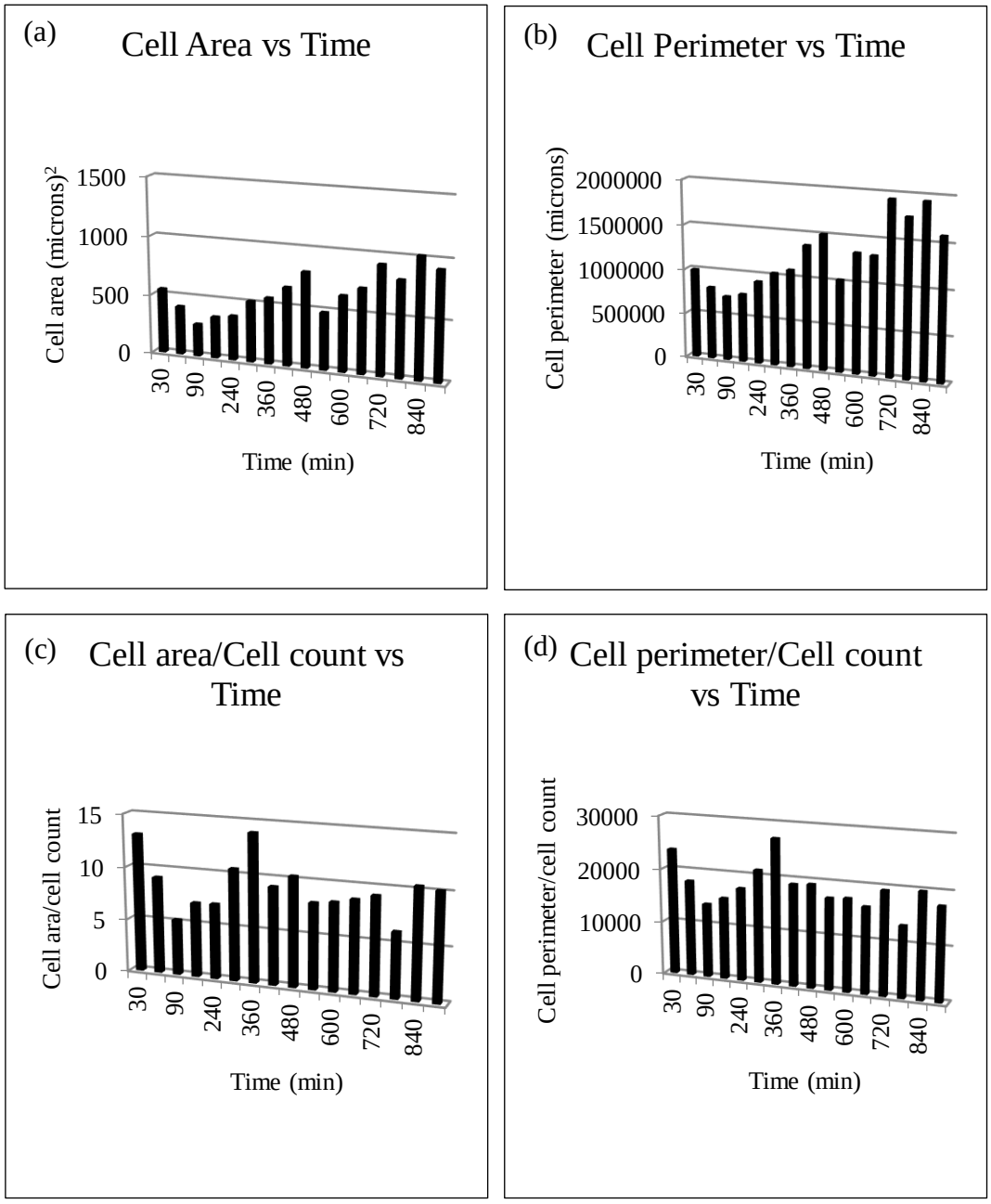

Figure C.3. Graphical display of processed data of chamber 4 (a) cell area vs time graph (b) cell perimeter vs time graph (c) cell area/cell count vs time graph (d) cell perimeter/cell count vs time graph (brightfield images)-E4Y.

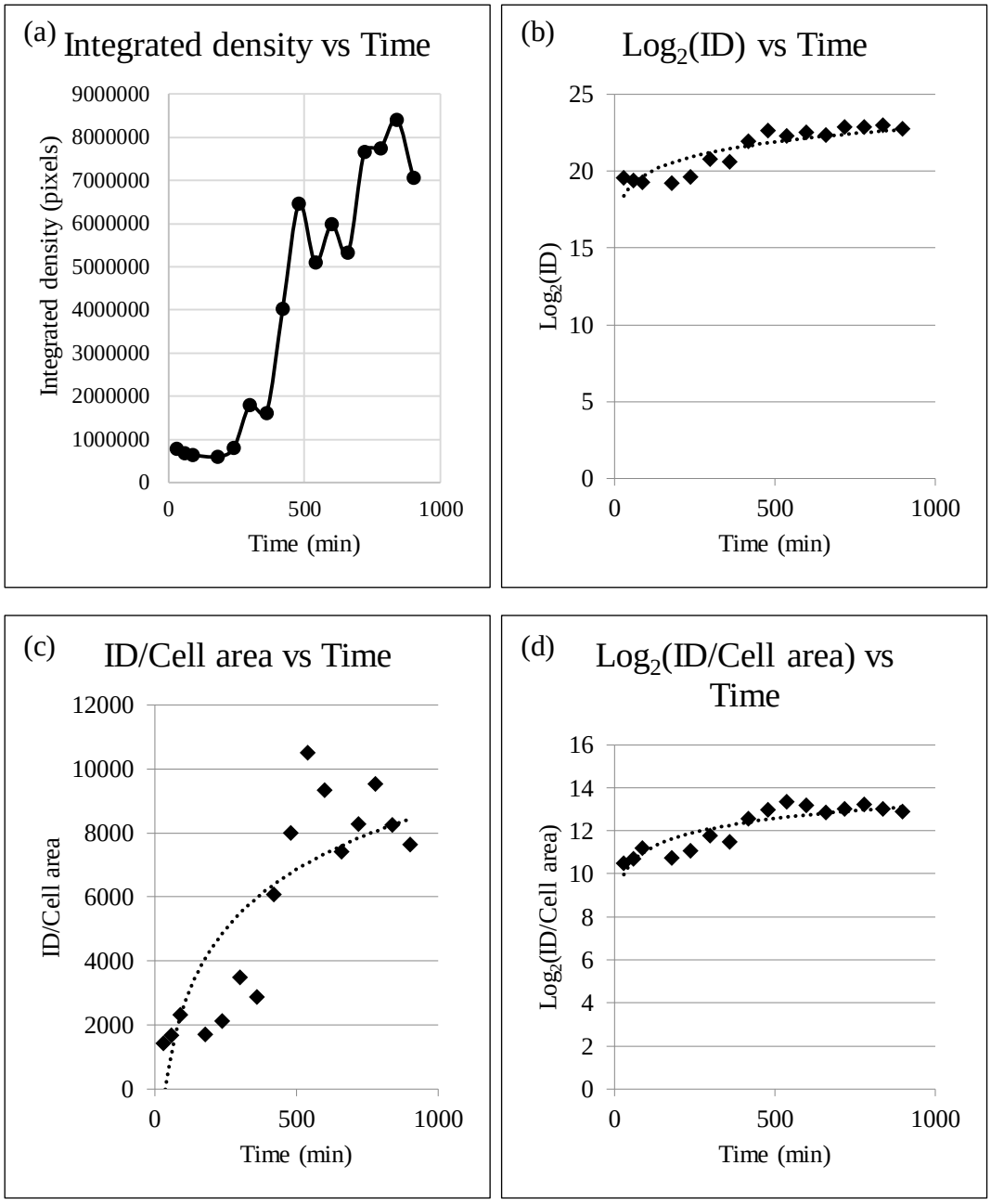

Figure C.4. Graphical display of processed data for chamber 4 (a) integrated density vs time graph (b) $\log_2$(integrated density) vs time graph (c) integrated density/cell area vs time graph (d) $\log_2$(integrated density)/cell area vs time graph-E4Y.

C.3. Results of Chamber 4 in Experiment E5Y

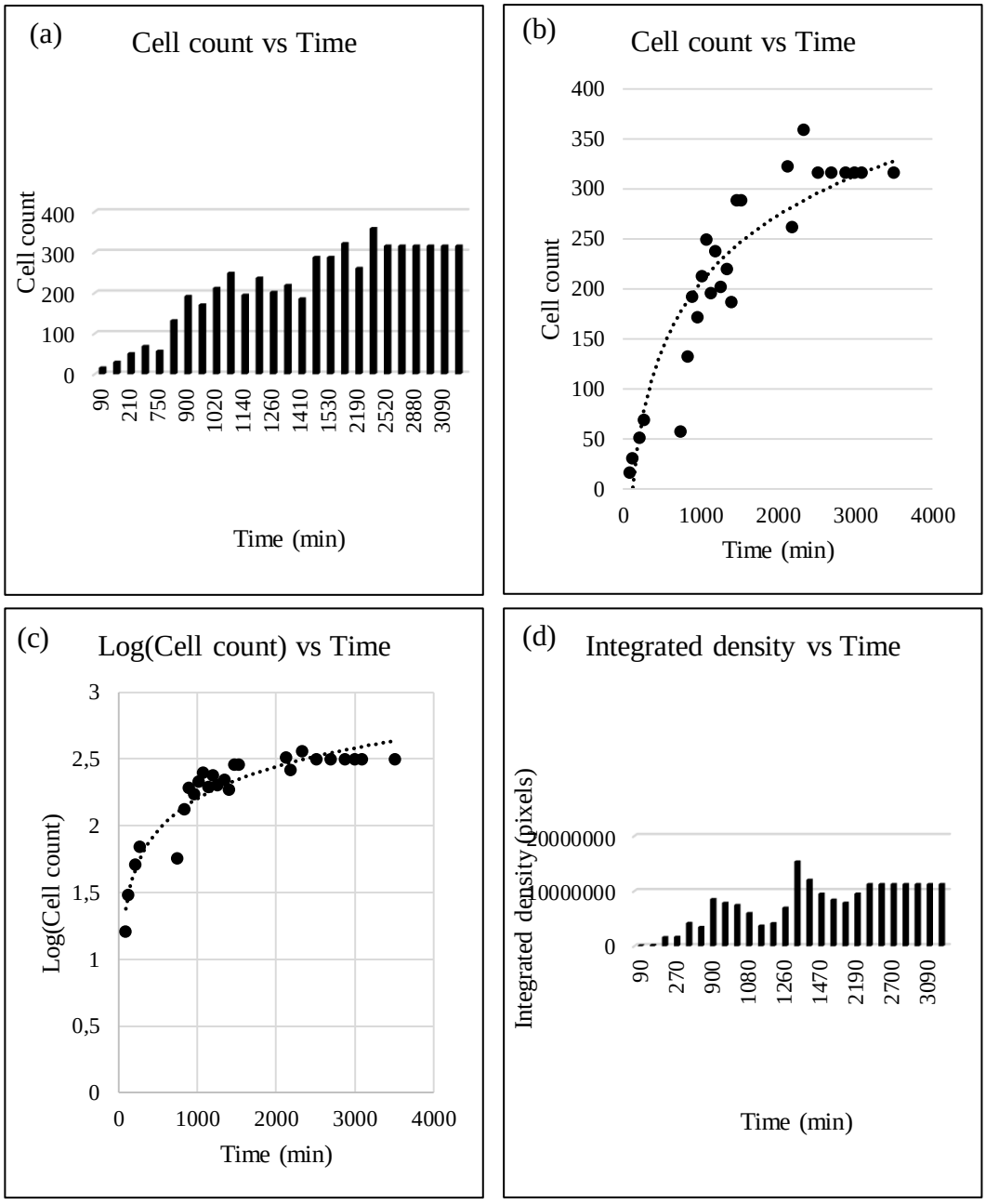

Figure C.5. Graphical display of processed data for chamber 4 (a,b) cell count vs time graph (c) log(cell count) vs time graph (brightfield images) (d) integrated density vs time graph (fluorescence image)-E5Y.

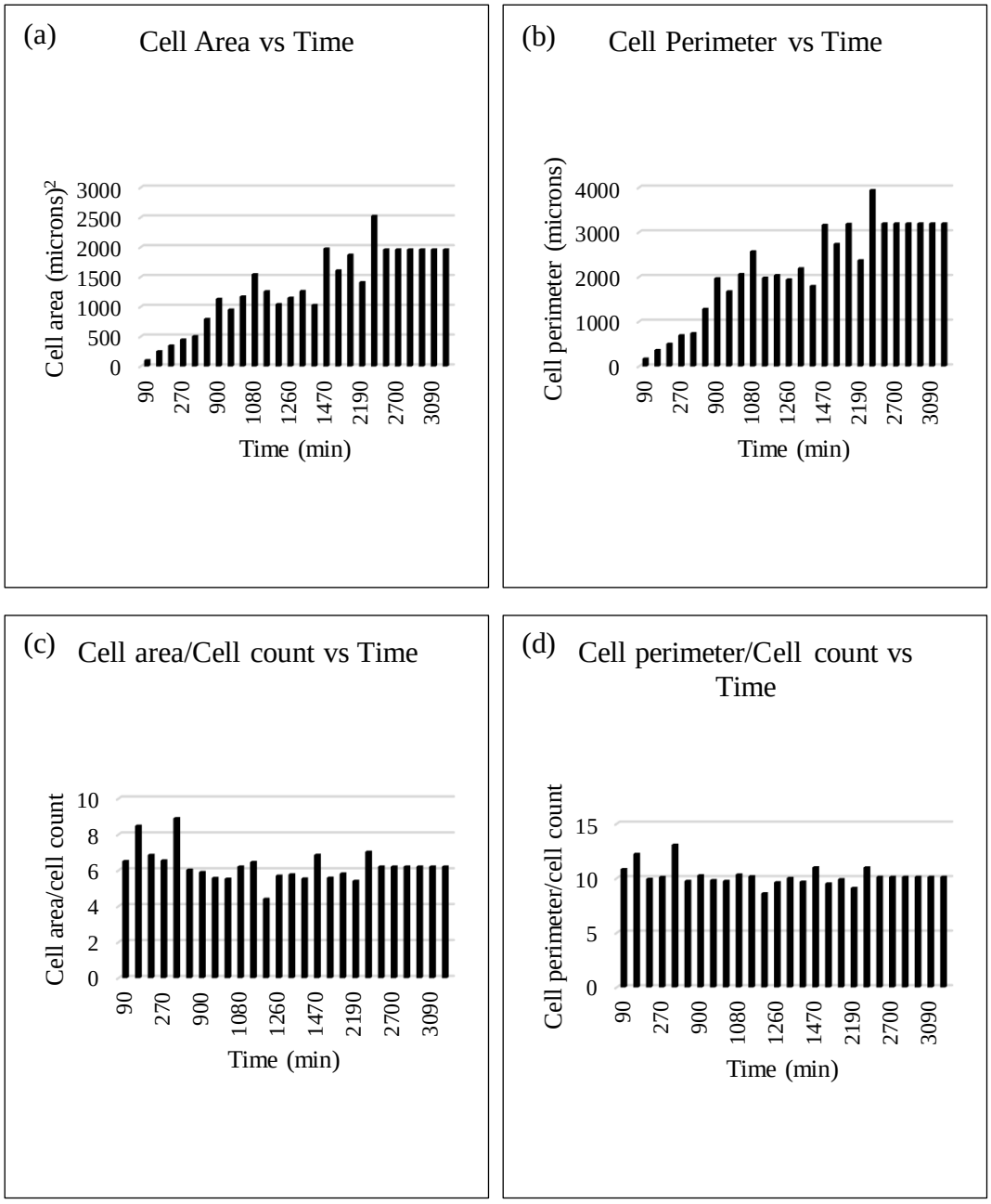

Figure C.6. Graphs of processed data of chamber 4 (a) cell area vs time graph (b) cell perimeter vs time graph (c) cell perimeter/cell count vs time graph (d) cell area/cell count vs time graph (brightfield images)-E5Y.

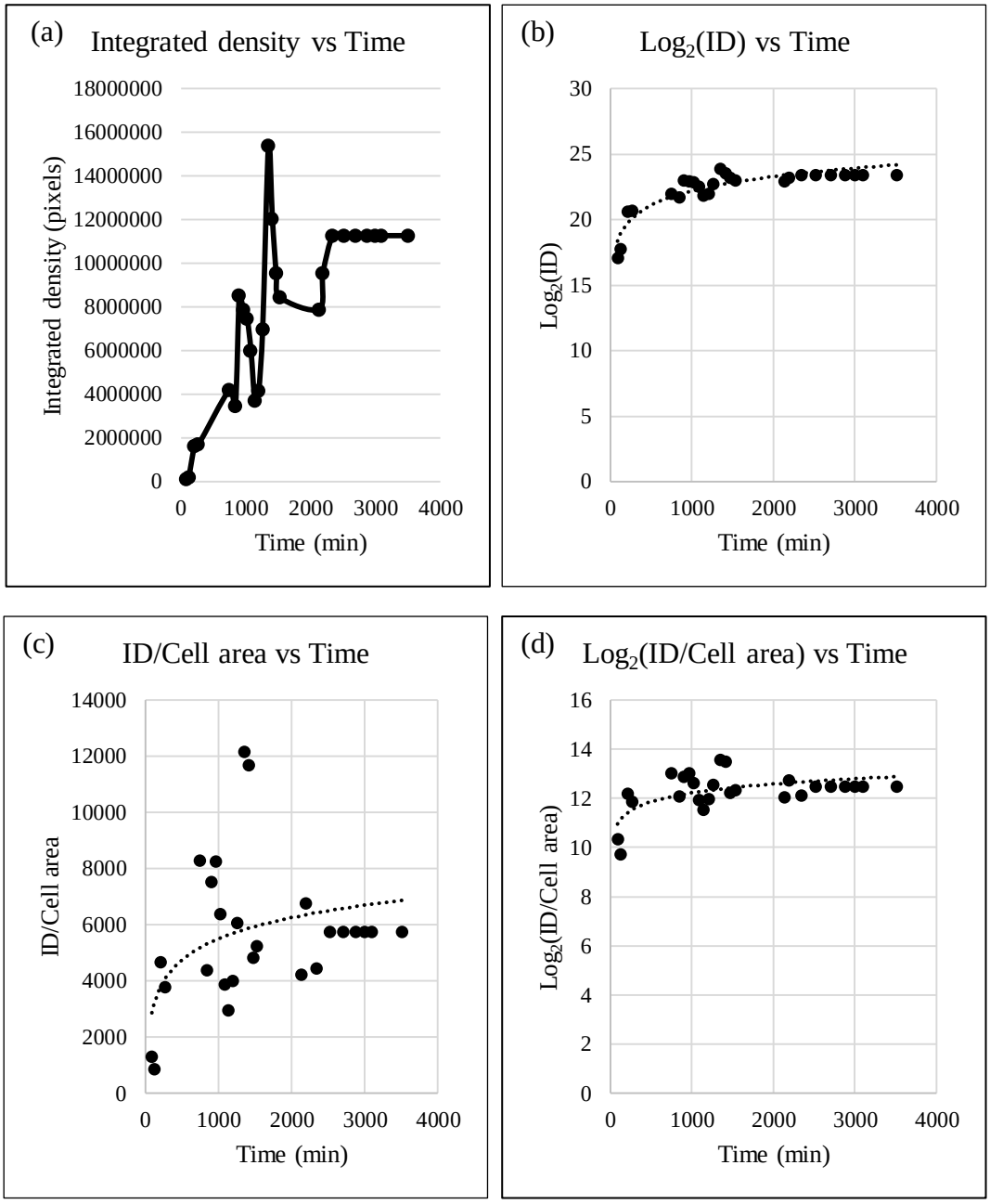

Figure C.7. Graphical display of processed data for chamber 4 (a) integrated density vs time graph (b) $\log_2$(integrated density) vs time graph (c) integrated density/cell area vs time graph (d) $\log_2$(integrated density)/cell area vs time graph-E5Y.

C.4. Results of Chamber 5 in Experiment E5Y

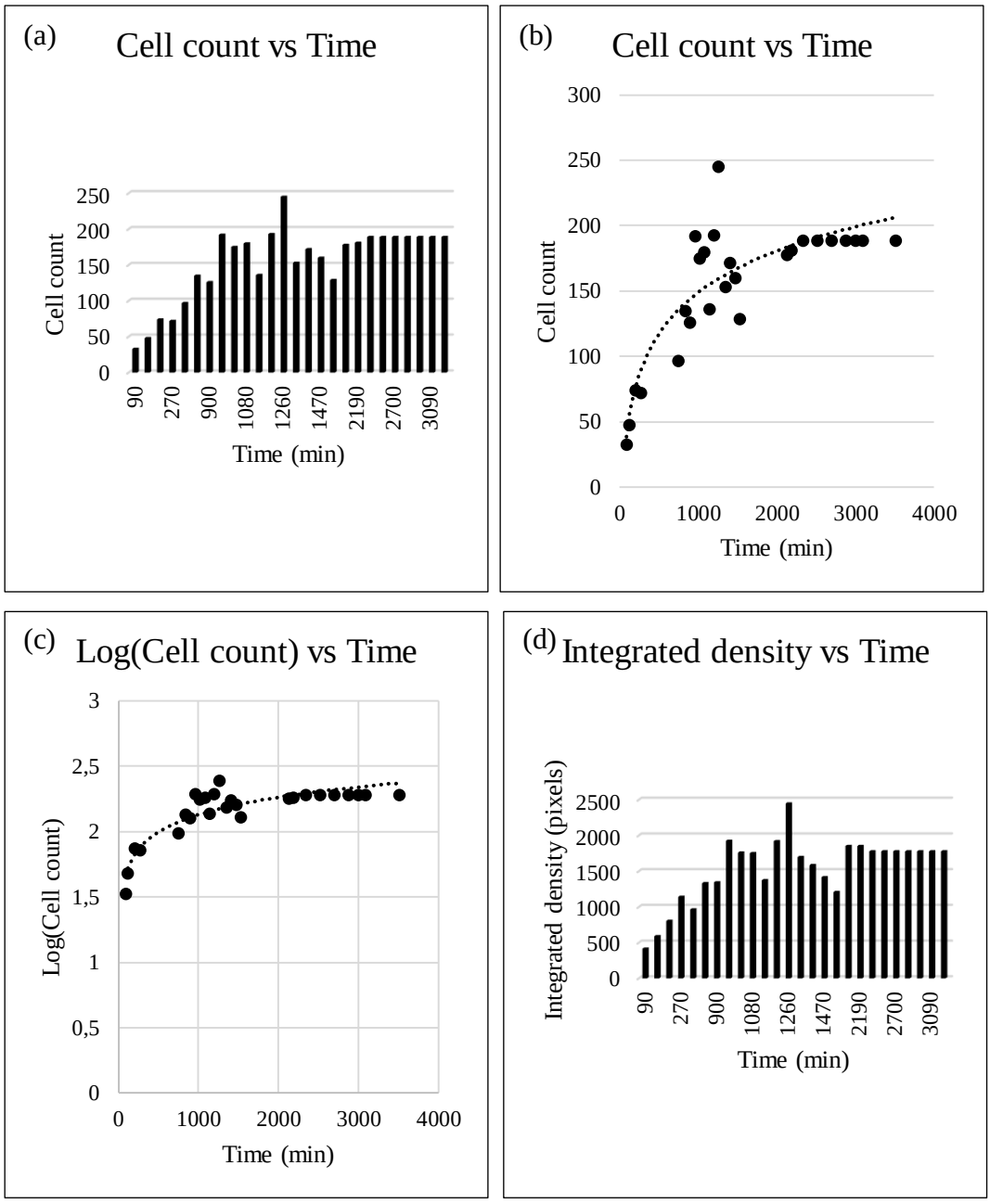

Figure C.8. Graphical display of processed data for chamber 5 (a,b) cell count vs time graph (c) log(cell count) vs time graph (brightfield images) (d) integrated density vs time graph (fluorescence image)-E5Y.

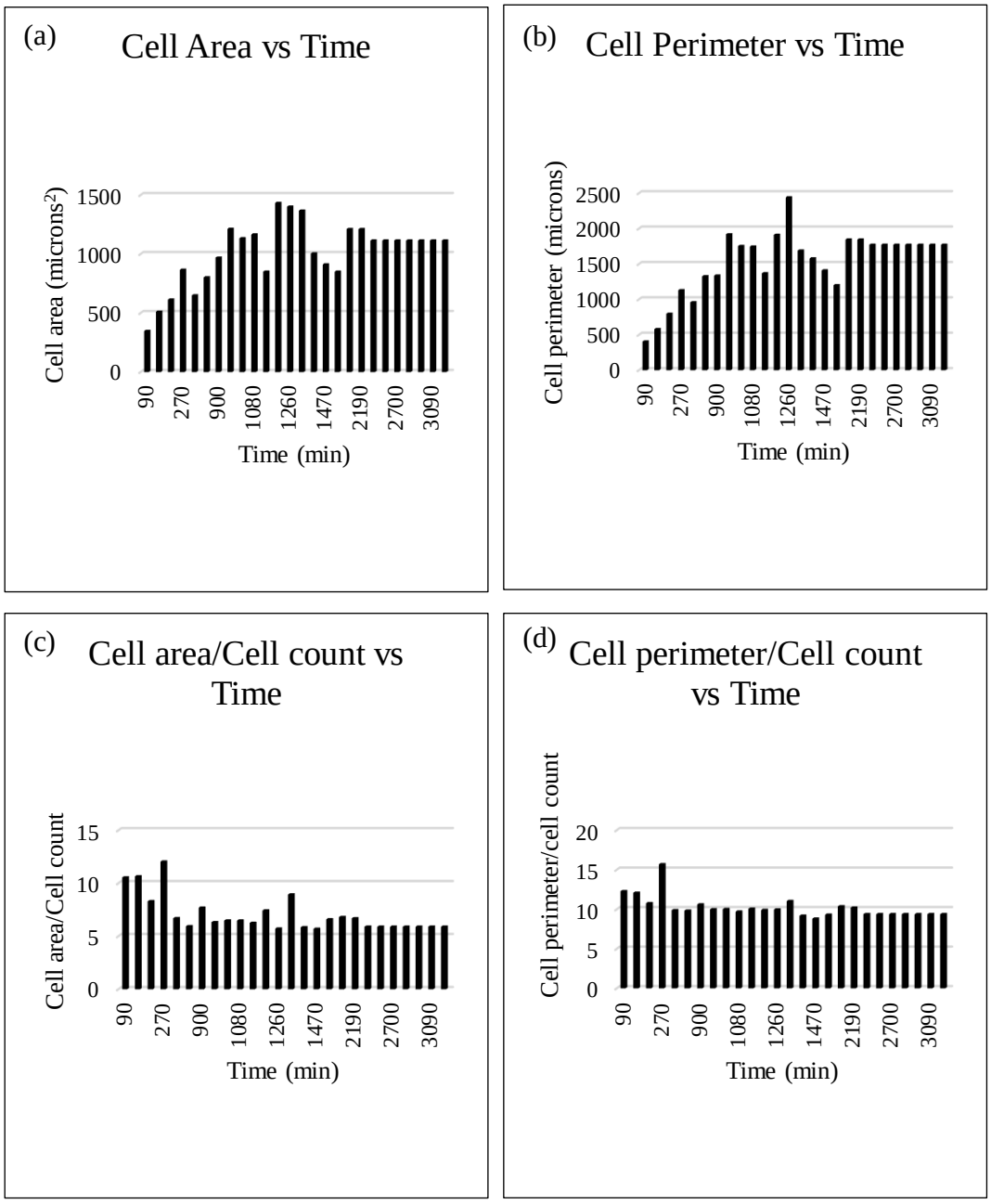

Figure C.9. Graphs of processed data of chamber 5 (a) cell area vs time graph (b) cell perimeter vs time graph (c) cell perimeter/cell count vs time graph (d) cell area/cell count vs time graph (brightfield images)-E5Y.

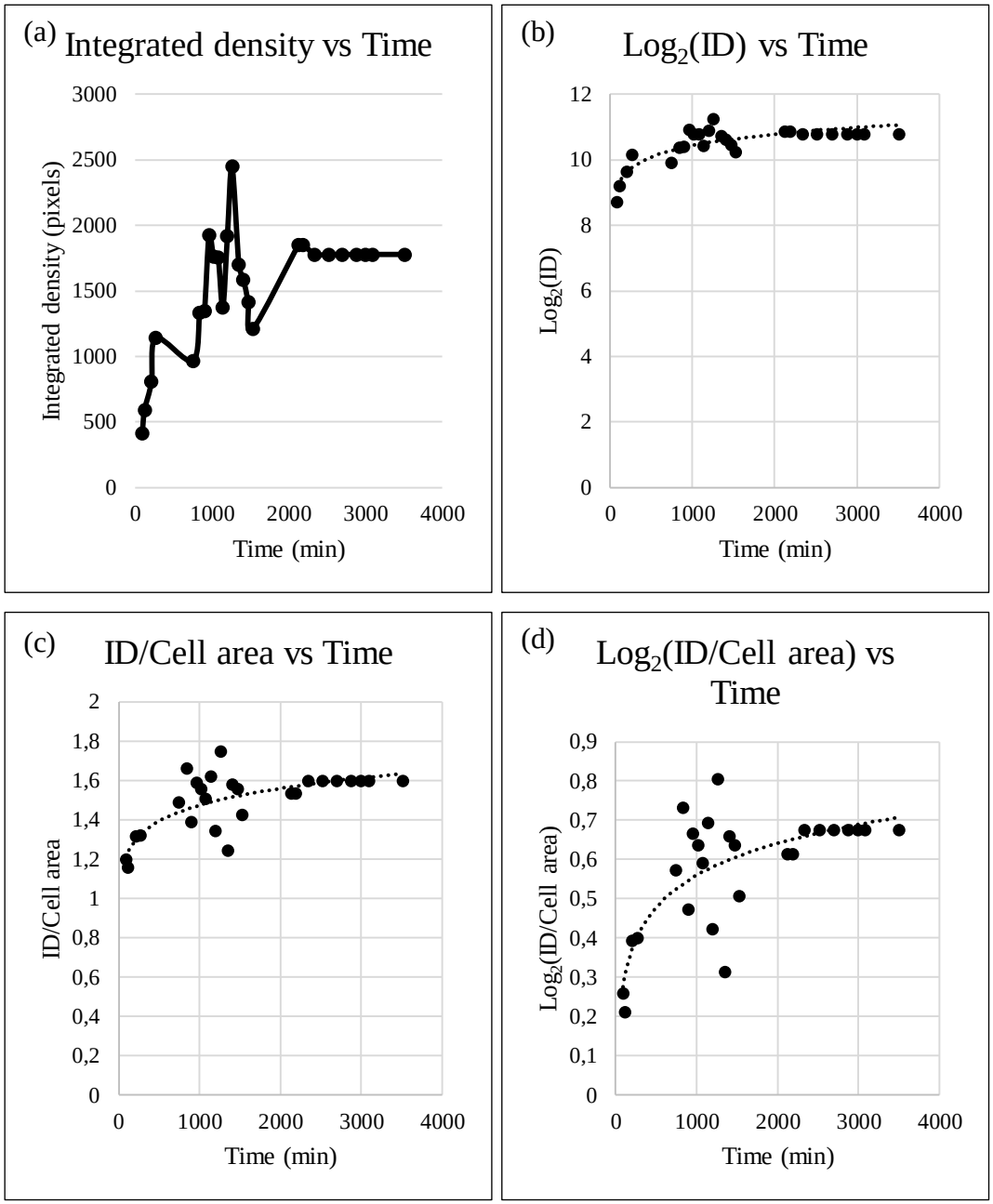

Figure C.10. Graphical display of processed data for chamber 5 (a) integrated density vs time graph (b) $\log_2$(integrated density) vs time graph (c) integrated density/cell area vs time graph (d) $\log_2$(integrated density)/cell area vs time graph-E5Y.

C.5. Results of Chamber 6 in Experiment E5Y

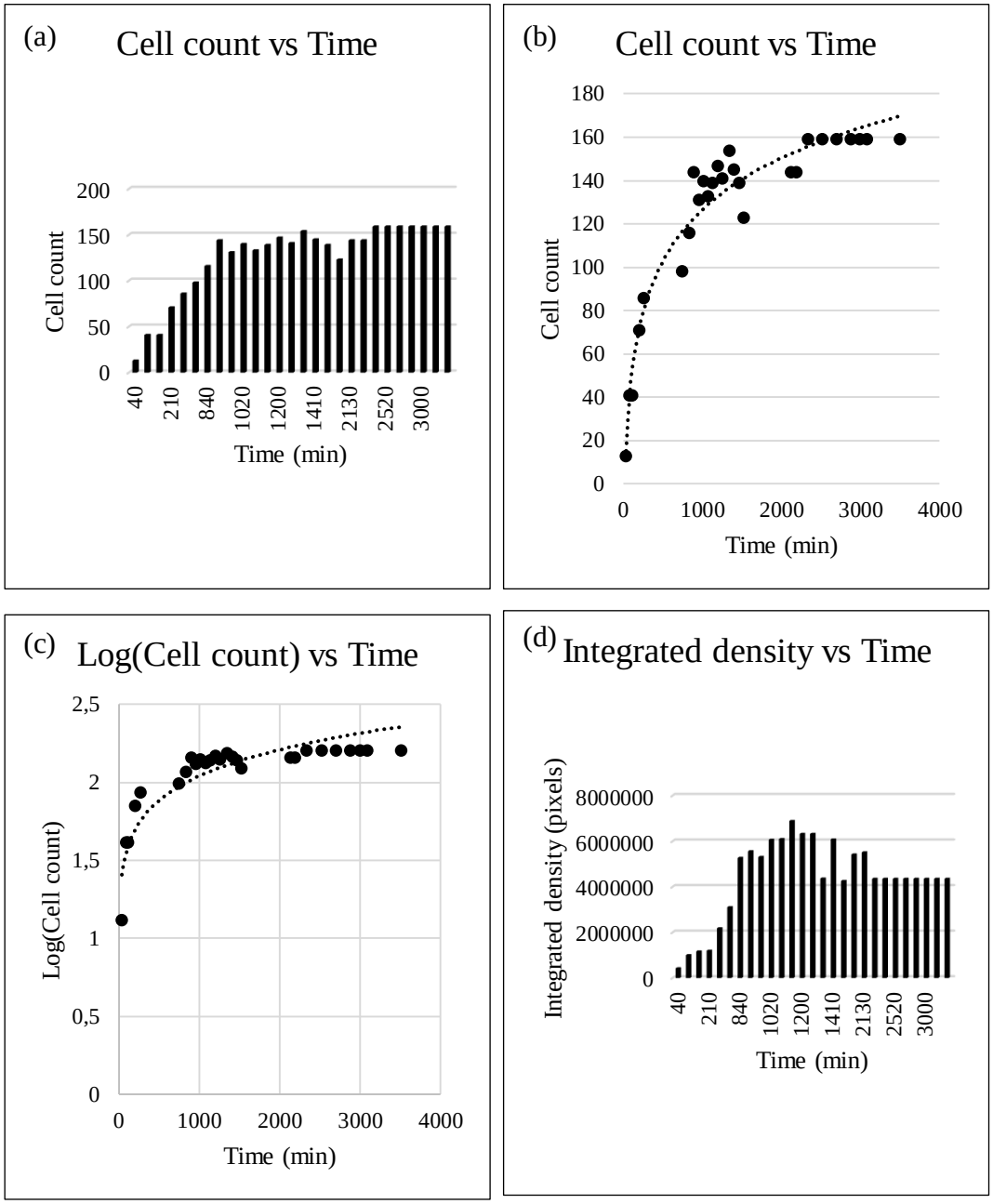

Figure C.11. Graphical display of processed data for chamber 6 (a,b) cell count vs time graph (c) log(cell count) vs time graph (brightfield images) (d) integrated density vs time graph (fluorescence image)-E5Y.

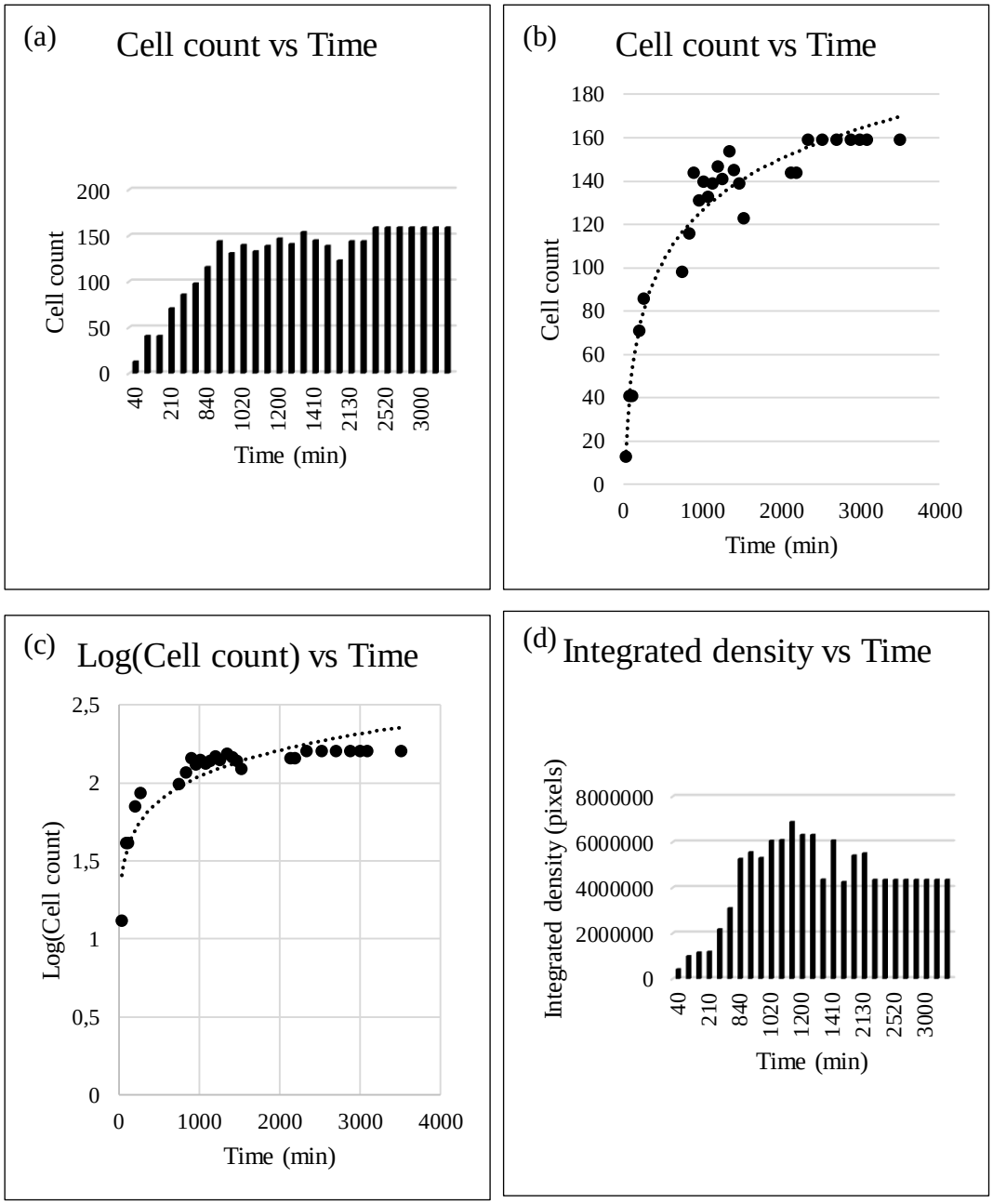

Figure C.12. Graphs of processed data of chamber 6 (a) cell area vs time graph (b) cell perimeter vs time graph (c) cell perimeter/cell count vs time graph (d) cell area/cell count vs time graph (brightfield images)-E5Y.

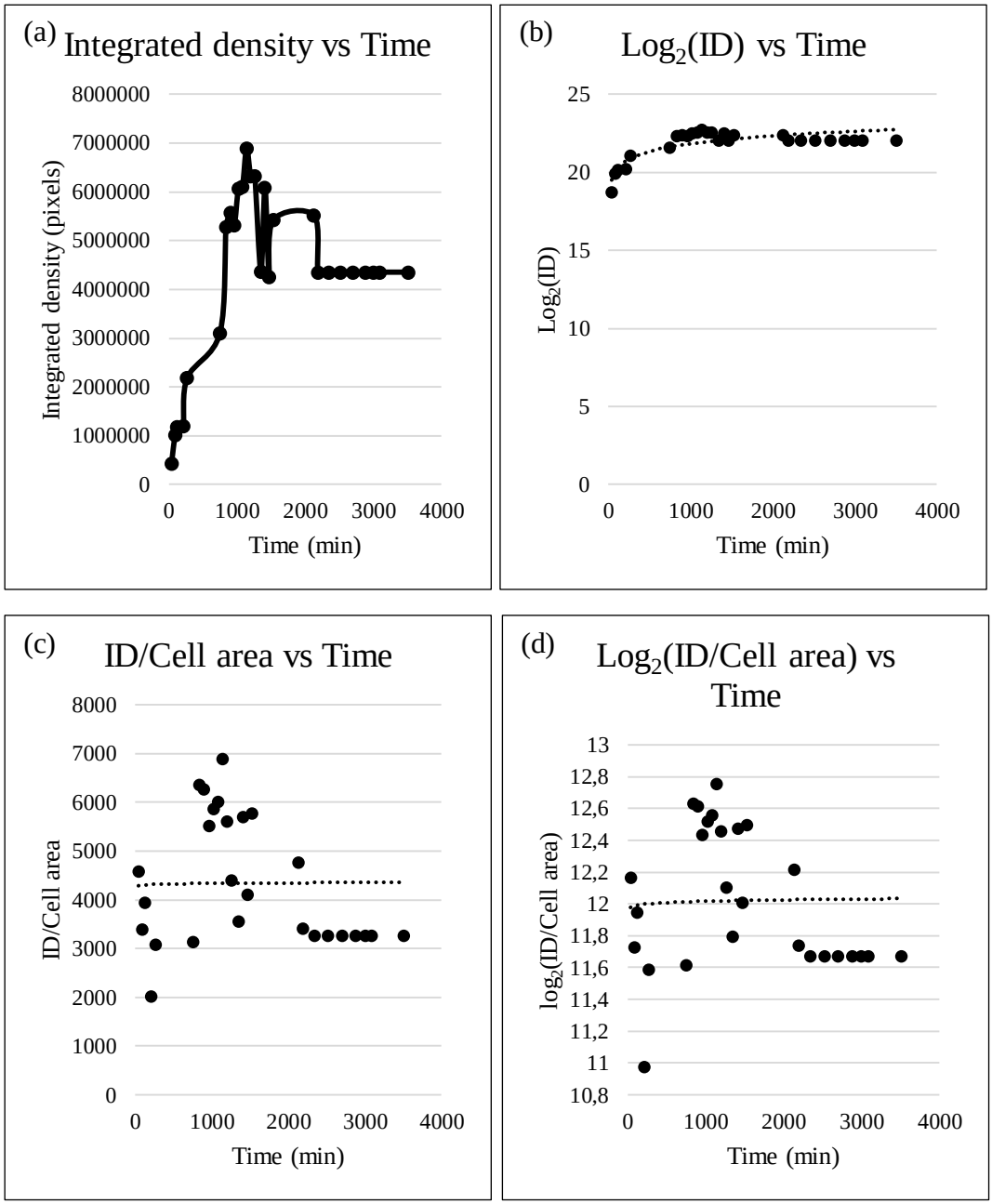

Figure C.13. Graphical display of processed data for chamber 6 (a) integrated density vs time graph (b) $\log_2$(integrated density) vs time graph (c) integrated density/cell area vs time graph (d) $\log_2$(integrated density)/cell area vs time graph-E5Y.

C.6. Results of Chamber 7 in Experiment E5Y

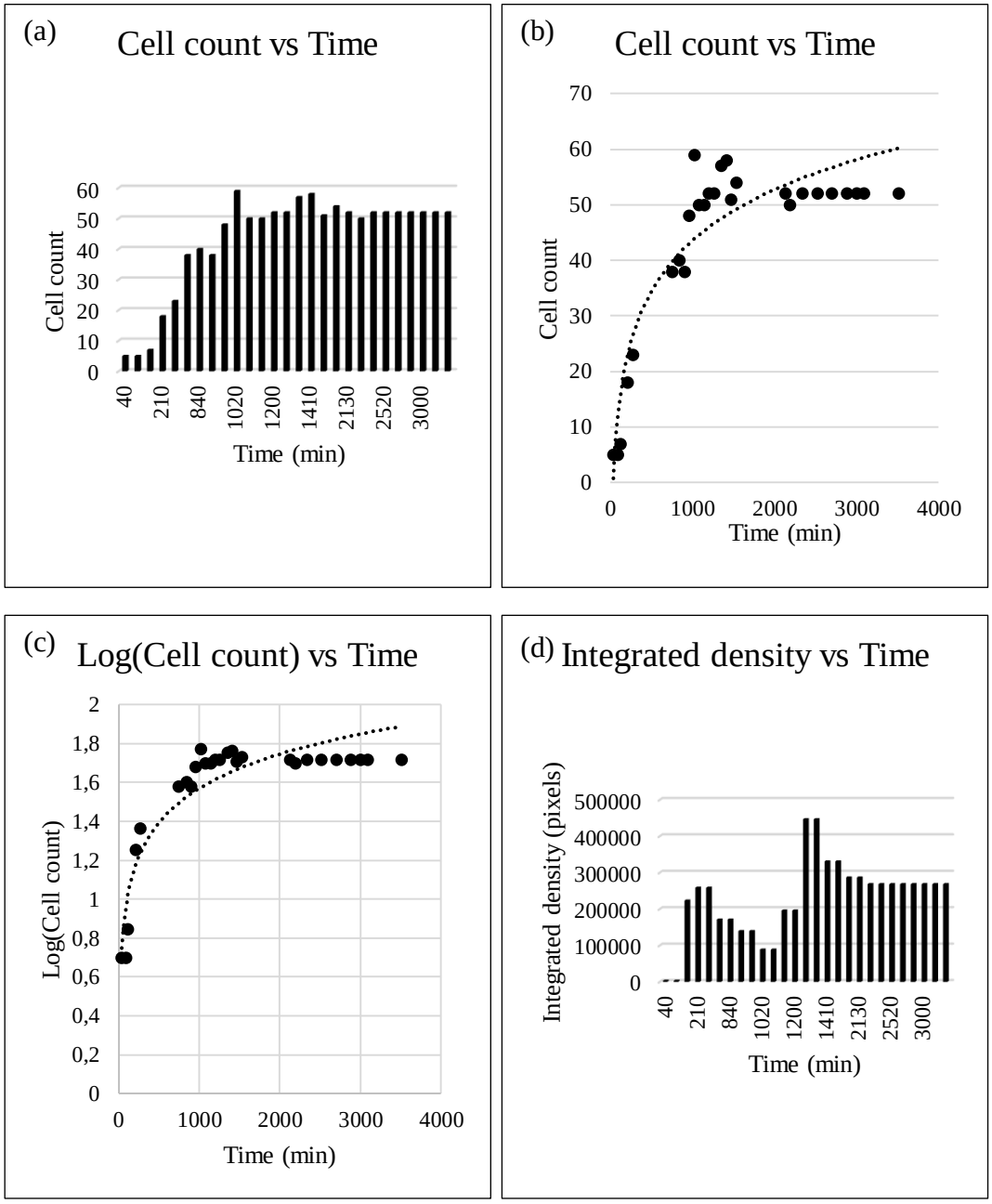

Figure C.14. Graphical display of processed data for chamber 7 (a,b) cell count vs time graph (c) log(cell count) vs time graph (brightfield images) (d) integrated density vs time graph (fluorescence image)-E5Y.

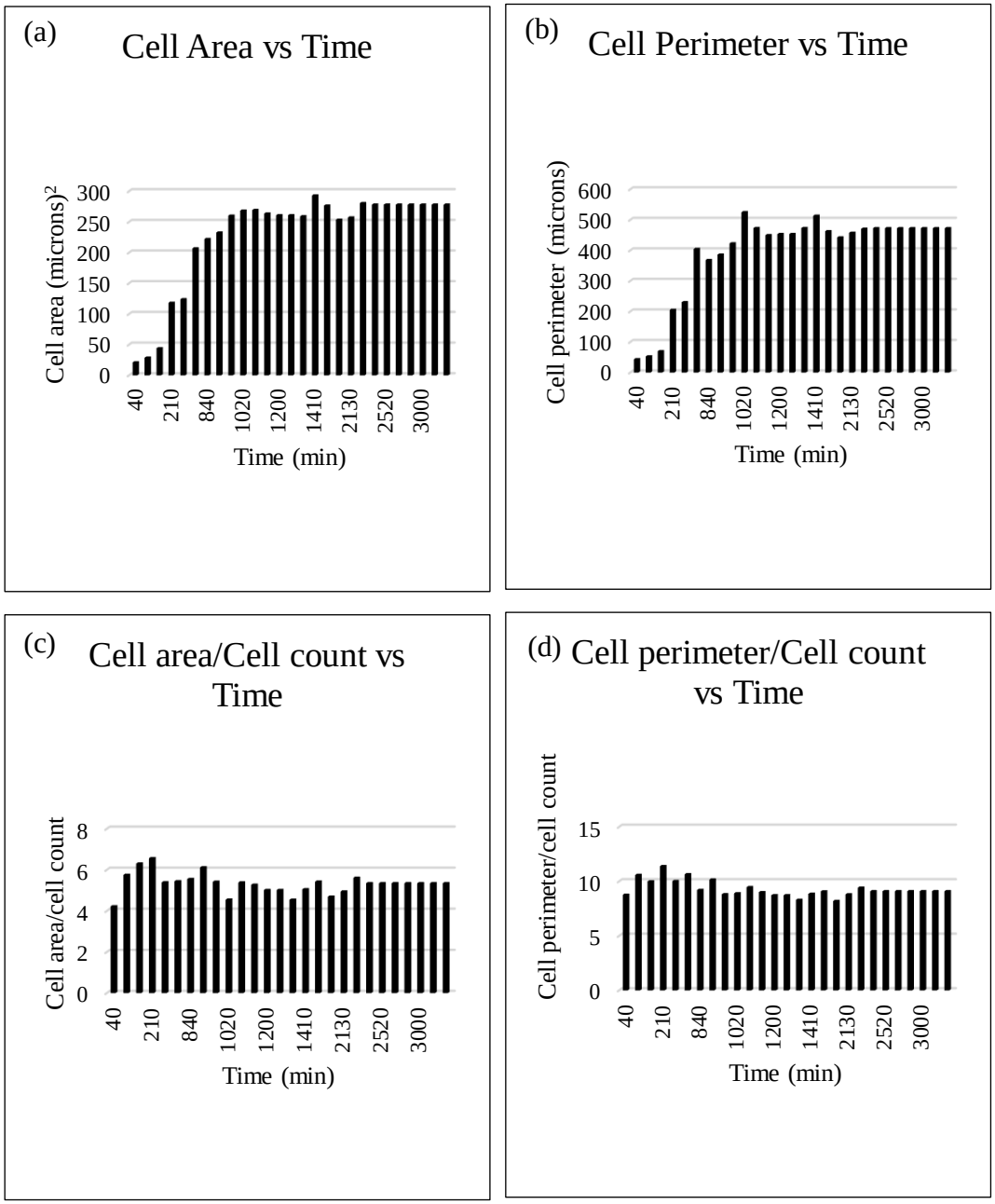

Figure C.15. Graphs of processed data of chamber 7 (a) cell area vs time graph (b) cell perimeter vs time graph (c) cell perimeter/cell count vs time graph (d) cell area/cell count vs time graph (brightfield images)-E5Y.

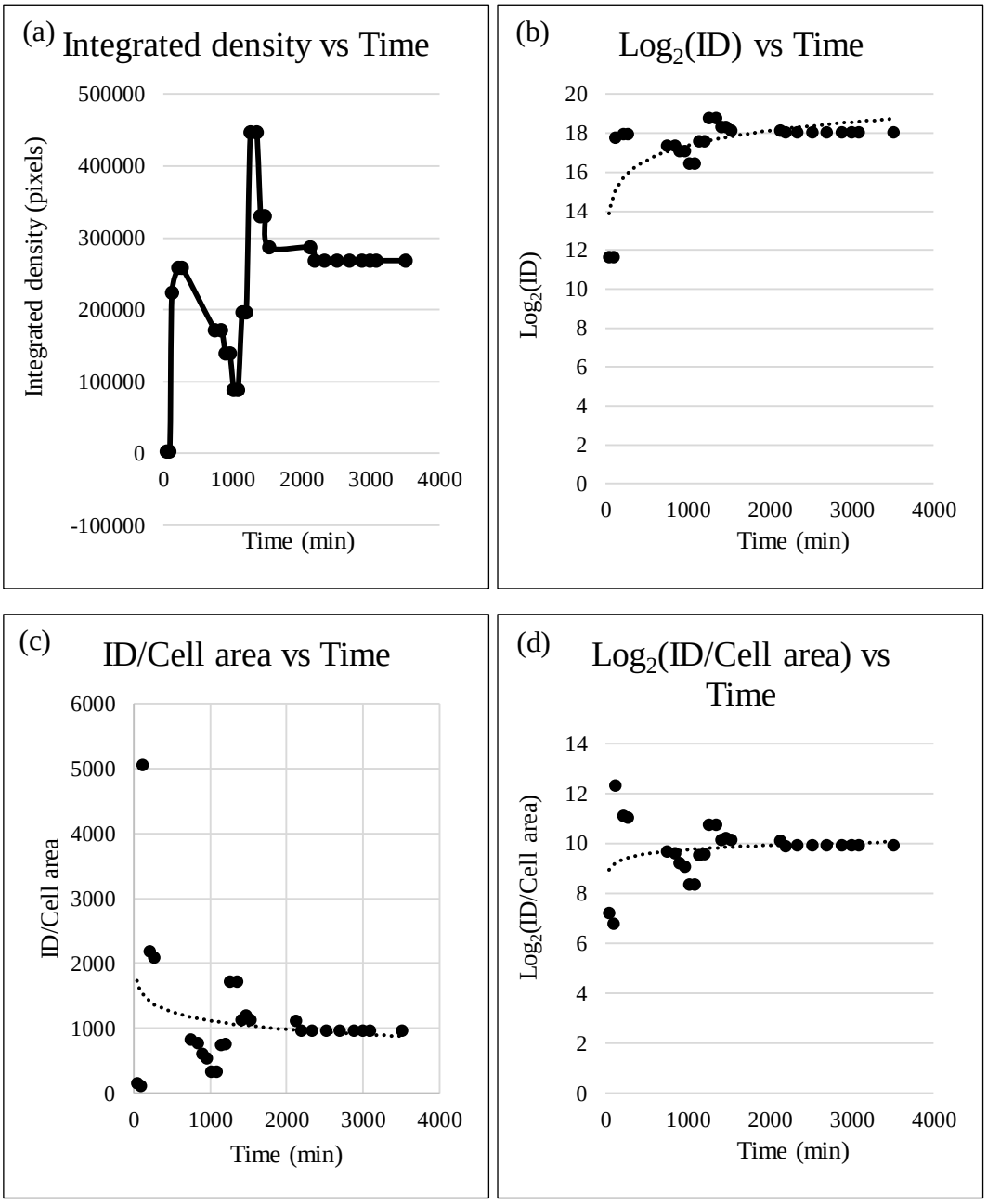

Figure C.16. Graphical display of processed data for chamber 7 (a) integrated density vs time graph (b) $\log_2$(integrated density) vs time graph (c) integrated density/cell area vs time graph (d) $\log_2$(Integrated density)/cell area vs time graph-E5Y.

APPENDIX D: RESULTS OF PRODUCT FORMATION KINETICS

D.1. Results of Product Formation Kinetics for E1Y

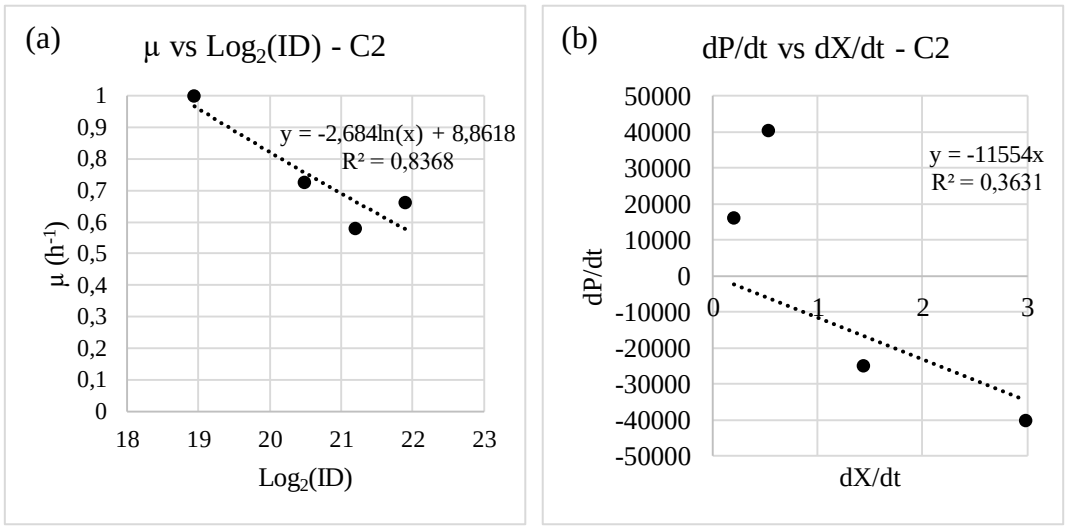

Figure D.1. Product formation kinetics (a) μ vs $\log_2$(ID) graph (b) dP/dt vs dX/dt graph of chamber 2 for E1Y.

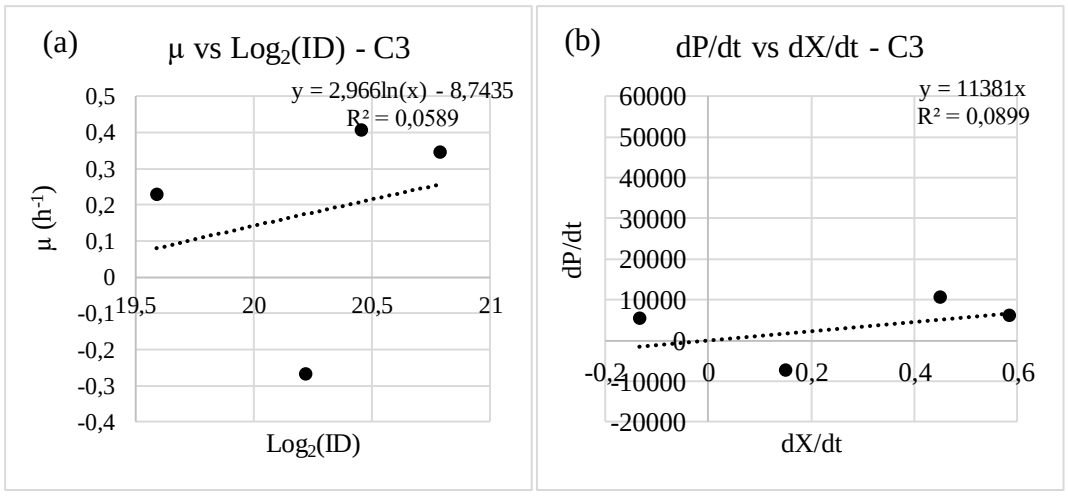

Figure D.2. Product formation kinetics (a) μ vs $\log_2$(ID) graph (b) dP/dt vs dX/dt graph of chamber 3 for E1Y.

D.2. Results of Product Formation Kinetics for E4Y

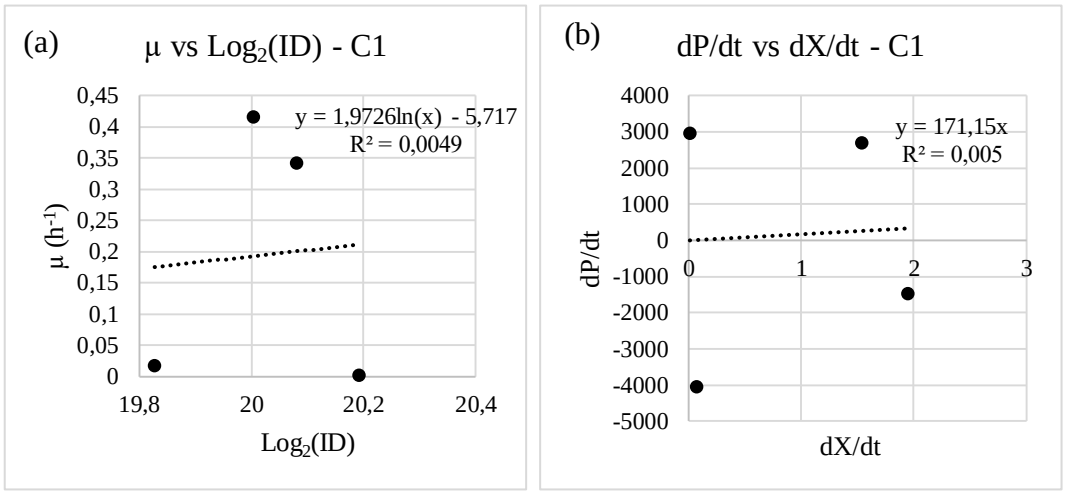

Figure D.3. Product formation kinetics (a) μ vs $\log_2$(ID) graph (b) dP/dt vs dX/dt graph of chamber 1 for E4Y.

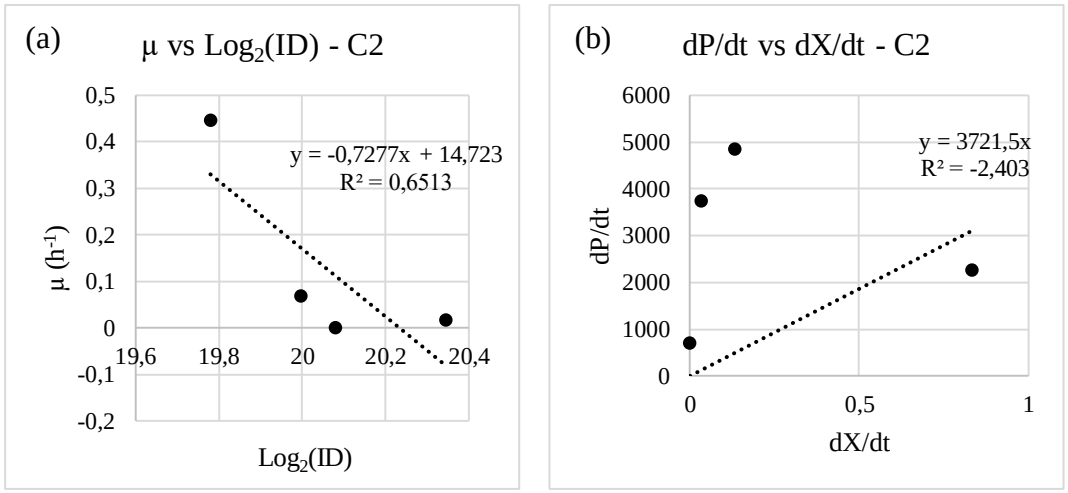

Figure D.4. Product formation kinetics (a) μ vs $\log_2$(ID) graph (b) dP/dt vs dX/dt graph of chamber 2 for E4Y.

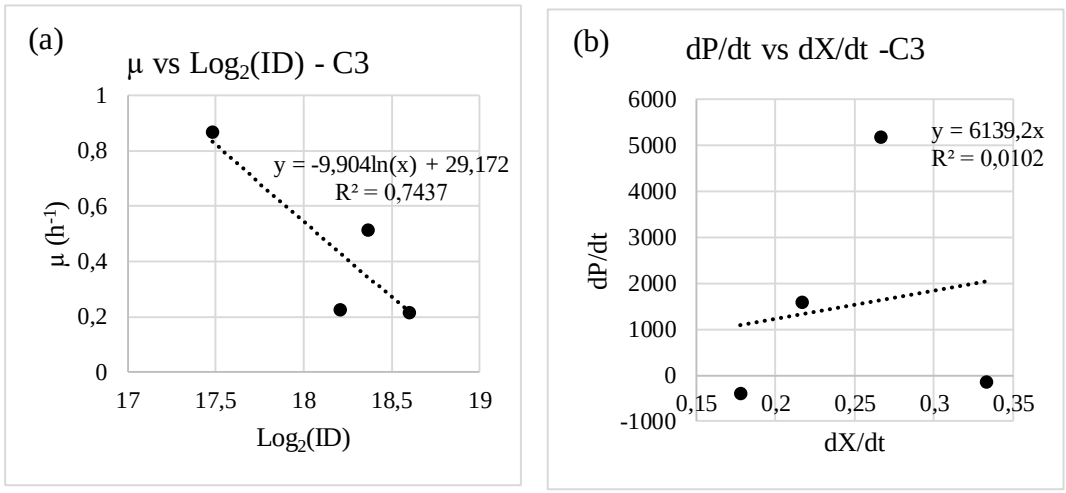

Figure D.5. Product formation kinetics (a) μ vs $\log_2$(ID) graph (b) dP/dt vs dX/dt graph of chamber 3 for E4Y.

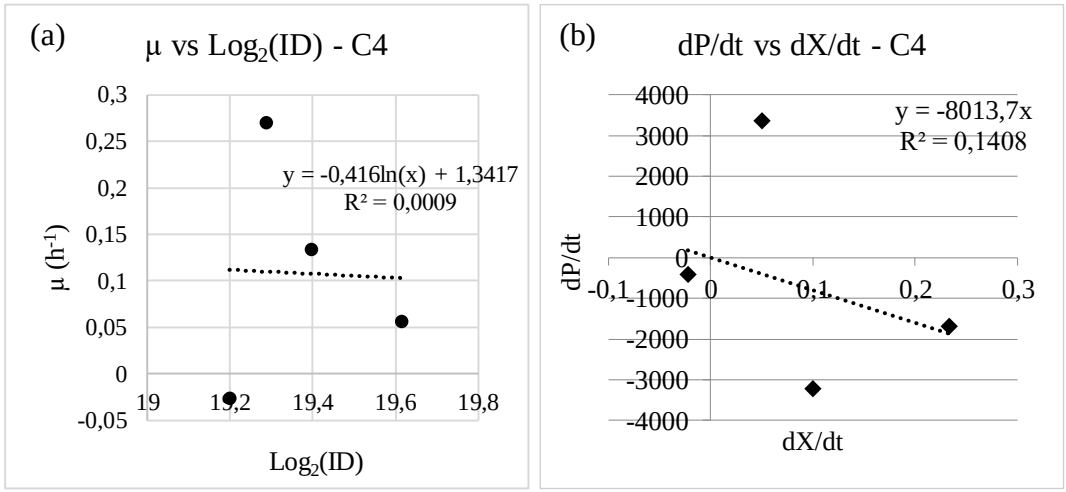

Figure D.6. Product formation kinetics (a) μ vs $\log_2$(ID) graph (b) dP/dt vs dX/dt graph of chamber 4 for E4Y.

D.3. Results of Product Formation Kinetics for E5Y

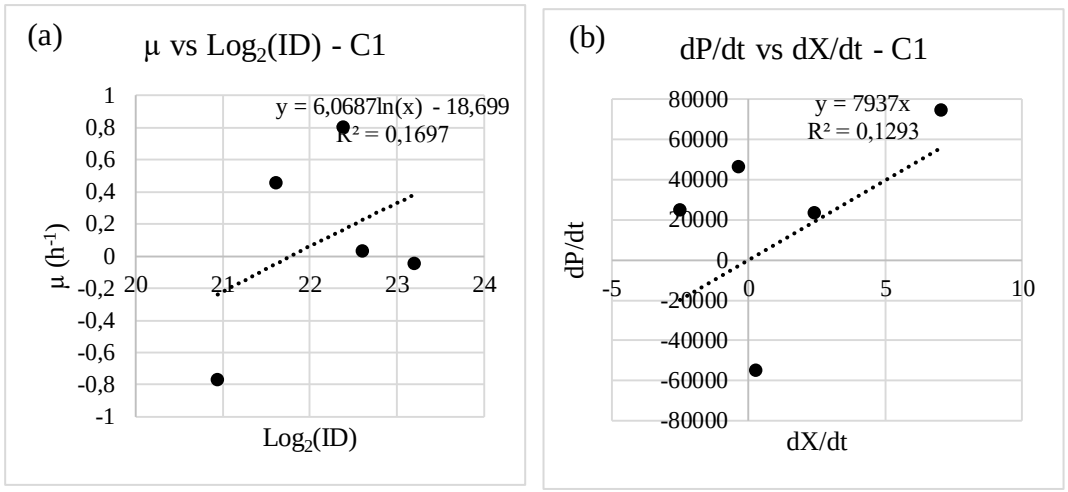

Figure D.7. Product formation kinetics (a) μ vs $\log_2$(ID) graph (b) dP/dt vs dX/dt graph of chamber 1 for E5Y.

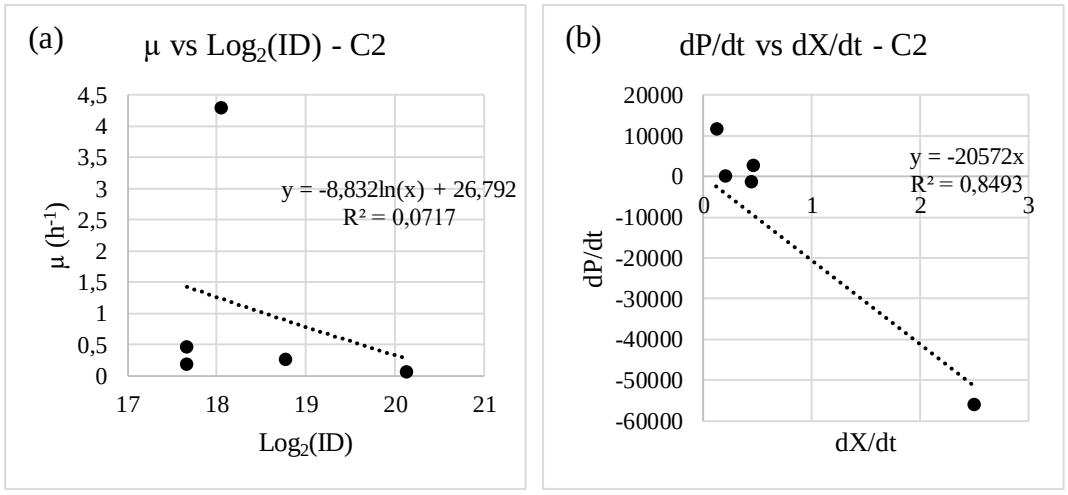

Figure D.8. Product formation kinetics (a) μ vs $\log_2$(ID) graph (b) dP/dt vs dX/dt graph of chamber 2 for E5Y.

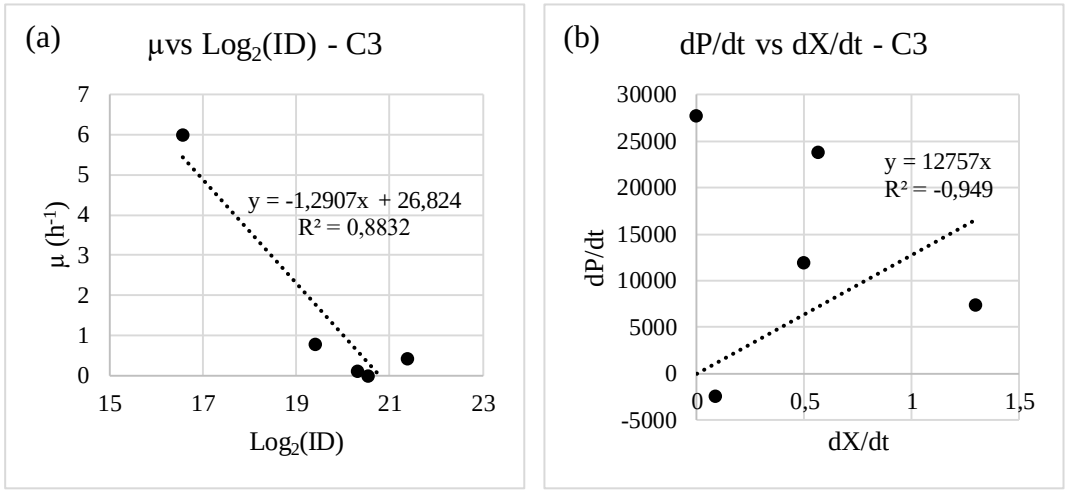

Figure D.9. Product formation kinetics (a) μ vs $\log_2$ (ID) graph (b) dP/dt vs dX/dt graph of chamber 3 for E5Y.

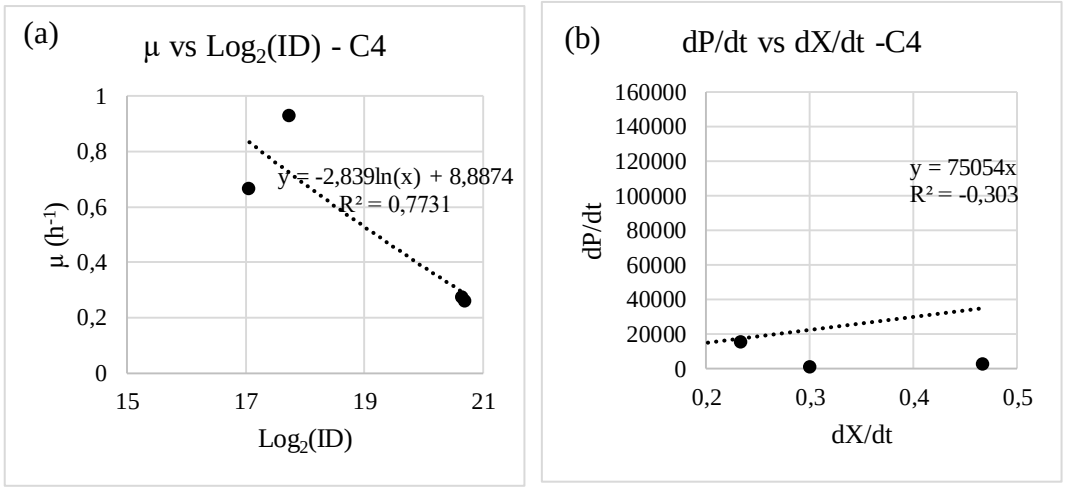

Figure D.10. Product formation kinetics (a) μ vs $\log_2$ (ID) graph (b) dP/dt vs dX/dt graph of chamber 4 for E5Y.

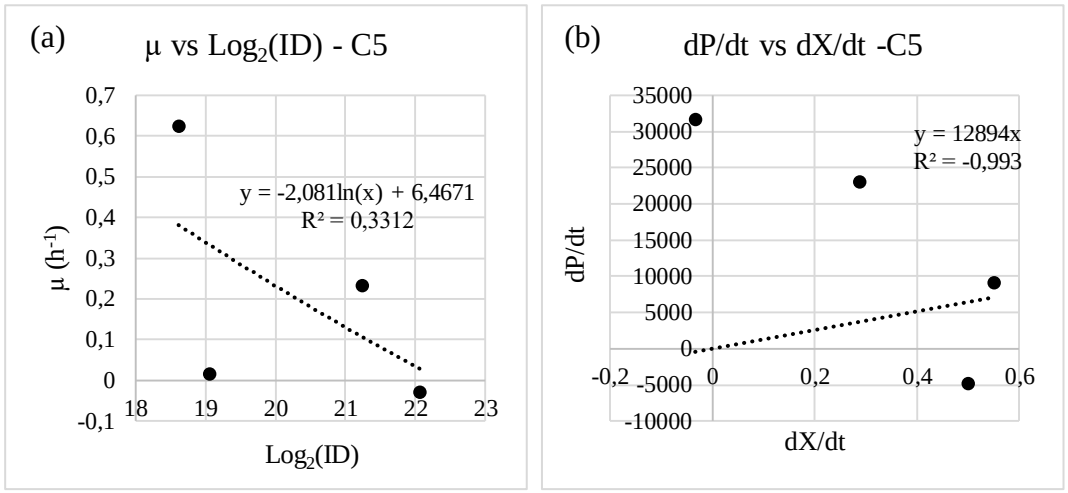

Figure D.11. Product formation kinetics (a) μ vs $\log_2$ (ID) graph (b) dP/dt vs dX/dt graph of chamber 5 for E5Y.

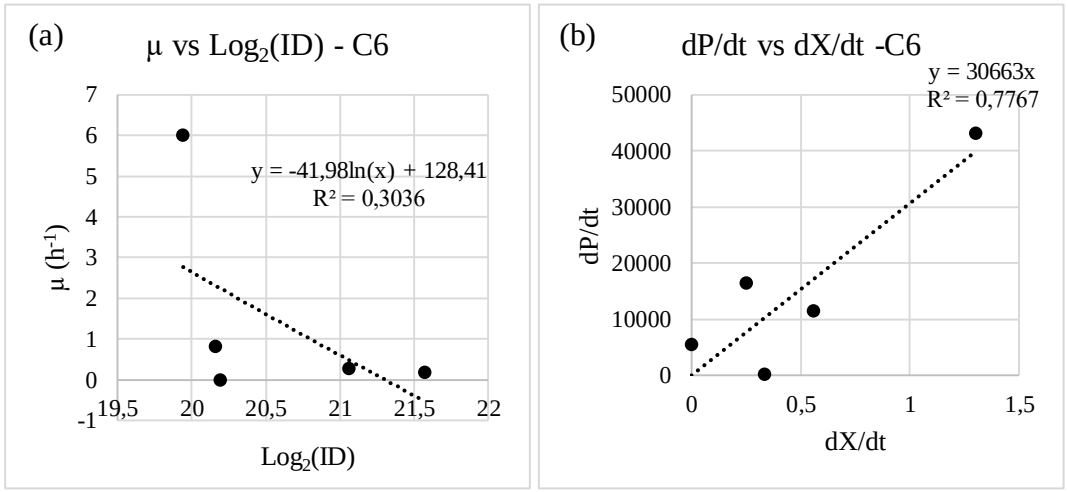

Figure D.12. Product formation kinetics A) μ vs $\log_2$(ID) graph B) dP/dt vs dX/dt graph of chamber 6 for E5Y.

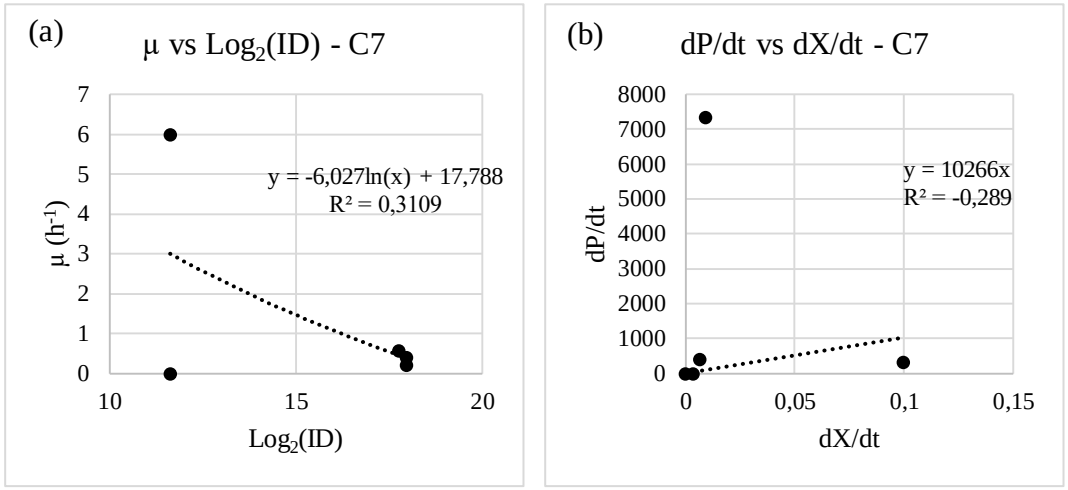

Figure D.13. Product formation kinetics (a) μ vs $\log_2$(ID) graph (b) dP/dt vs dX/dt graph of chamber 7 for E5Y.